STUDY OF FLUID BEHAVIOR AND PVT PROPERTIES OF HYDROCARBONS IN SHALE RESERVOIRS USING MOLECULAR SIMULATIONS

A Thesis

by

TERMPAN PITAKBUNKATE

Submitted to the Office of Graduate and Professional Studies of
Texas A&M University
in partial fulfillment of the requirements for the degree of

DOCTOR OF PHILOSOPHY

Chair of Committee,	Thomas A. Blasingame
Co-Chair of Committee,	George J. Moridis
Committee Members,	Peter P. Valkó
	Perla B. Balbuena
Head of Department,	A. Daniel Hill

August 2015

Major Subject: Petroleum Engineering

ABSTRACT

Reservoir studies are crucial for field development plans. The level of the studies ranges from analogies to fully integrated production modeling. Numerical reservoir simulation is a tool to predict how fluid will flow in the reservoirs. It is developed based on the continuity equation, flow equation, and equation of state. The continuity equation is basically conservation of mass. Darcy's law is a fundamental equation to describe fluid flow in a porous media (i.e. oil and gas reservoirs). Fluid properties in the reservoirs are calculated from the equation of state. This concept has been implemented to predict reservoir performance for over centuries and it works flawlessly for conventional reservoirs (i.e. sandstone and carbonate reservoirs).

In the past decade, shale reservoirs became resources of future energy in the U.S. Shale reservoirs are unconventional reservoirs as their permeability is ultra-low and common pore sizes are in nanoscale level. Recent studies/research in the oil and gas industry mainly focus on explaining fluid flow behavior in the shale reservoirs. Some studies have been done in the oil and gas industry to describe how hydrocarbons are stored and flow through ultra-small pores in the shale reservoirs. Most of these studies were derived by borrowing and modifying techniques used for conventional reservoirs.

Fluid properties in shale reservoirs are one of the keys to improve the accuracy of reservoir simulators. The common pore size distribution of the shale reservoirs is approximately 1-20 nm. In such confined spaces the interactions between the walls of the container (i.e. the shale and kerogen) and the contained fluids (i.e. the hydrocarbon fluids and water) may exert significant influence on the localized phase behavior. We believe this is due to the fact that the orientation and distribution of fluid molecules in the confined space are different from those of the bulk fluid; causing changes in the localized thermodynamic properties.

This study provides a detailed account of the changes of PVT properties and phase behavior in a synthetic shale reservoir for pure hydrocarbons and their mixtures. Grand Canonical Monte Carlo (GCMC) simulations are performed to study the effect of confinement on the fluid properties and Molecular Dynamics (MD) simulations are performed to simulate movements of fluid molecules in a confined system and validate the conclusions obtained from the GCMC simulations. A graphite slab made of two layers is used to represent kerogen in the shale reservoirs. The separation between the two layers,

representing a kerogen pore, is varied from 1 nm to 10 nm to observe the changes in the hydrocarbon fluid properties.

We delivered phase diagrams and critical properties of pure hydrocarbons and phase diagrams of their mixtures. In addition, the deviations in the fluid densities in the confined space from those of the bulk fluids at reservoirs conditions were provided.

DEDICATION

To my parents Roongroaj Pitakboonkate and Sunetta Iamklad,
who never stopped believing in me and for their unconditional love and support.

To my brother, Chaiyaphant, and my sisters, Thanyarat and Jantrarat Pitakboonkate,
for taking care of our parents while I was away.

To the Buengers, my adoptive family,
for their encouragement and moral support during my graduate school years.

ACKNOWLEDGEMENTS

I would like to express my gratitude to Dr. Tom Blasingame and Dr. George Moridis, my academic co-advisors and committee co-chairs, for providing financial support, warm advice, and strong encouragement. They taught me how to solve engineering problems from the fundamentals, and this has led me to the point where I have figured out the physics of shale flow using molecular thermodynamics. They have trained me to be the best at my work and to think professionally. They are my role models for helping, encouraging, and mentoring new graduate students. They have always been understanding and supportive. All the experience and knowledge I obtained from them are invaluable and have become a strong asset for my professional life.

I would like to thank Dr. Perla Balbuena and Dr. Peter Valko for serving me on my dissertation committee. Dr. Balbuena has been providing guidance and support. Her invaluable knowledge in molecular thermodynamics is a key factor in my Ph.D. dissertation. Even though she is only technically serving on my Ph.D. committee, I see her as one of my academic advisors. Dr. Peter Valko taught me a lot when I was a student in his group for my Master's degree. He has continued giving me very good advice and support. He has always been open to my questions. The knowledge I obtained from him has been useful for my Ph.D. study.

Also, I would like to thank Dr. Randall Q. Snurr and Dr. Shaji Chempath at Northwestern University for granting me the permission to use the MUSIC software and valuable discussions about the software. I also thank Dr. Lisa Perez, Graduate Faculty in the Chemistry Department at Texas A&M University, as well as Jose Leonardo and Jamie Yu – Dr. Balbuena's students – for their advice on molecular simulations.

I also acknowledge and appreciate the Crisman Institute for Petroleum Research in the Harold Vance Department of Petroleum Engineering at Texas A&M University for funding this work. Computer time from the CAT cluster at the Texas A&M Department of Chemical Engineering and time in the TAMU supercomputer facilities are duly acknowledged.

This research is also supported in part by the Materials Simulation Center of the Materials Research Institute, the Research Computing and Cyberinfrastructure unit of Information Technology Services, Penn-State Center for Nanoscale Science, the Theoretical and Computational Biophysics Group at the

Beckman Institute for Advanced Science and Technology at the University of Illinois at Urbana-Champaign, and Daresbury Laboratory granted me permission to use their Material Studio, VMD, and DL_POLY software.

Special thanks go to my smart Chemistry Ph.D. student roommates, Dr. Anyanee Kamkaew, Dr. Kantapat Chansaenpak, soon to be Dr. Jakkrit Suriboot, and soon to be Dr. Peerada Samanual, for their understanding, encouragement, and their help for me to go through the hardship of the Ph.D. student life.

TABLE OF CONTENTS

Page

LIST OF FIGURES

LIST OF TABLES

Page

CHAPTER I

INTRODUCTION

1.1 Motivation

Numerical reservoir simulation has been used as a tool for reservoir studies to predict reservoir performance and consequently yield the best field development plan. Most of the commercial reservoir simulators available in the oil and gas industry are developed based on continuity equations, flow equations, and conventional equations of state. The continuity equation describes conservation of mass, where the difference between mass flow in and mass flow out equals mass accumulations. The fundamental flow equation that is used to state fluid flow in petroleum reservoirs is Darcy's law. The equation of state (e.g. Van der Waal EOS, Redlich-Kwong EOS, and Peng-Robinson EOS) is a thermodynamic equation defining the state of matter under a given set of conditions (i.e. temperature and pressure). According to reservoir simulations, equations of state are useful in determining the fluid properties.

The current commercial numerical reservoir simulation software works flawlessly for conventional reservoirs ─ sandstone and carbonate reservoirs ─ whose common pore size is relatively large compared to the size of their contained fluid molecules. As a result, the effect of confinement is negligible. However, this concept may not be able to predict the flow performance of shale reservoirs, which is the main focus of current studies in the petroleum industry. Many studies have been done in the past decade trying to forecast the production profiles of shale reservoirs using conventional reservoir simulators. None of those studies give the results within an acceptable range of error when compared with the actual production profile. It implies that fluid flow in shale reservoirs violates one or more assumptions required for conventional reservoir simulation.

Unlike conventional sandstone and carbonate reservoirs, shale reservoirs have a unique rock property — in particular, ultra-low in-situ permeability (on the order of 1-100 nd is very common). Shale reservoirs contain nanoscale sized pores, which lead to ultra-low permeabilities but also unusual phase behavior caused by "confinement" in very small pores. As noted, numerous studies have been performed to describe the storage and transport of hydrocarbons in shale reservoirs; in particular to improve reserves estimation and production forecasts. Desorption-adsorption models (e.g. the Langmuir model) are added in numerical reservoir simulation and gas-in-place calculation to account for adsorbed gas in shales (Shabro et al. 2011;

Ambrose et al. 2011; Ambrose et al. 2012; Das et al.). In ultra-small pores, turbulent flow may develop and cause deviation from the conventional models (i.e. Darcy's equation). Knudsen's number is used to characterize slip and no-slip flow and Knudsen diffusion and slip flow models are incorporated to improve the accuracy of the numerical simulation (Freeman 2010; Shabro et al. 2011; Darabi et al. 2012, Fathi et al. 2012). Recently, Sun et al. (2015) developed a comprehensive multimechanistic, multiporosity, and multipermeability model based on experimental data of shale organic and inorganic material properties to predict shale reservoir performance. Their model takes into account gas transport due to both convection and concentration diffusion, desorption of multicomponent gas from the organics' surface, mass transfer in three domains (organic material, inorganic material, and fracture network), and production from hydraulically fractured well. These studies may help us improve our understanding of flow mechanism in shale reservoirs, but none of these models may be completely valid to describe physics of shale flow. Most of these studies were developed by modifying techniques used for conventional reservoirs — only a few of these studies consider the fundamental effects of pore size on hydrocarbon PVT properties and flow behavior (i.e. storage and transport of fluids).

Direct and indirect characterization method, such as Focus Ion Beam combined with Scanning Electron Microscope (FIB/SEM, Chalmers et al. 2009; Sisk et al. 2009; Curtis et al. 2010; Lemmens et al. 2010; Lemmens et al. 2011; Zhang et al. 2012), gas adsorption (Kuila and Prasad 2011), mercury injection (Honarpour et al. 2012), and Nuclear Magnetic Resonance (NMR, Lewis et al. 2013) have exhibited the dominance of nanopores in shales. The common pore size distribution of shale reservoirs is approximately 1-20 nm (Nagarajan et al. 2013). Especially, dominant pore diameters of most shale reservoirs are smaller than 2 nm (Swami et al. 2012). In such a confined space, the interaction between the wall of the container (i.e. shale and kerogen) and the contained fluid (i.e. hydrocarbons) becomes significant to the fluid's behavior. As a result, equations of state derived for bulk fluid (Peng-Robinson, Redlich-Kwong) may not be valid for PVT calculation in the shale reservoirs. In general, fluids under confinement within nanoscale sized pores exhibit significant deviation from bulk thermo-physical properties (Thommes and Findenegg 1994; Zarragoicoechea and Kuz 2004; Singh et al. 2009; Travalloni et al. 2010; Singh and Singh 2011). **Figure 1-1** illustrates the difference between molecular orientation and arrangement of bulk water and that of confined water calculated from Molecular Dynamics (MD) simulations at room temperature and a density of 0.86 g/cm^3. Molecules in bulk water move randomly without specific orientation and direction. On the other hand, water molecules in the slit graphite pore with 1.9 nm of separation between the two layers – measured from the center of one graphite layer to the center of the other one – have a well-ordered, layered structure in the horizontal direction arranged in planes parallel to the graphite surfaces. Such structural differences can cause the change of fluid phase behavior and thermodynamic properties. It is reported that the water mobility of confined water becomes significantly lower than that of bulk water

(Hirunsit and Balbuena 2006). In addition, Zarragoicoechea and Kuz (2004) have shown that the shifts in the critical temperature are proportional to the size of the mesopore. Normally, as the pore size decreases, the critical temperature and freezing/melting point tend to decrease (Kenda et al. 2004; Moore et al. 2010). Zeigermann et al. 2009 reported experimental results indicating that the critical temperature of a confined fluid was depressed compared with its bulk value.

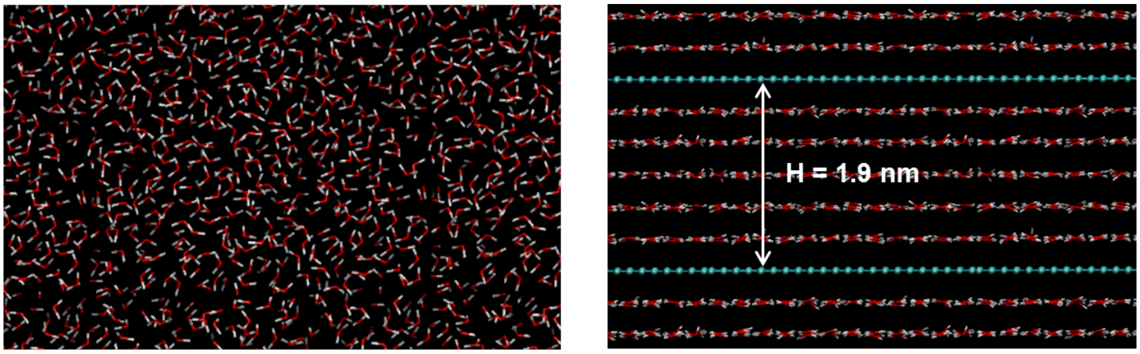

(a) (b)

Figure 1-1 – (a) Snapshot of bulk water molecules and (b) Snapshot of water molecules confined between graphite slabs.

In the oil and gas industry, we currently approximate the critical properties of pure hydrocarbons in shale reservoirs using critical shift models. Zarragoicoechea and Kuz (2004) proposed a critical shift model derived from the Helmholtz free energy for Lennard-Jones fluid confined in nanopores coupled with the van der Waals interactions. Equation (1-1) is the Helmholtz free energy for Lennard-Jones fluid proposed by Zarragoicoechea and Kuz (2002).

$$A = f(T) - N_A k_B T \ln\left(V_p - N_A b \sigma_A^3\right) + 2\frac{N_A^2}{V_p}\varepsilon\sigma_A^3\left(-\frac{a}{2} + \frac{c_1}{\sqrt{A_p}} + \frac{c_2}{A_p}\right) \quad \text{(1-1)}$$

where $b = 2\pi/3$, $a = 16\pi/9$, $c_1 = 4.6571$, $c_2 = -2.1185$, $A_p = \pi(r_p/\sigma_A^3)^2$, $V_p = A_p L_z$ and $\sigma_A = 0.244\sqrt[3]{T_c/p_c}$ (Teklu et al. 2014). The definition of the axial pressure is

$$p_{zz} = -\left(\frac{1}{A_p}\right)\left(\frac{\partial A}{\partial L_z}\right)_{T,A_p} \quad \text{(1-2)}$$

Thus,

$$p_{zz} = -\left(\frac{1}{A_p}\right)\left(\frac{\partial}{\partial L_z}\left(f(T) - N_A k_B T \ln\left(V_p - N_A b \sigma_A^3\right) + 2\frac{N_A^2}{V_p}\varepsilon\sigma_A^3\left(-\frac{a}{2} + \frac{c_1}{\sqrt{A_p}} + \frac{c_2}{A_p}\right)\right)\right)_{T,A_p}$$

$$p_{zz} = -\left(\frac{1}{A_p}\right)\left(0 - \frac{N_A k_B T A_p}{(V_p - N_A b \sigma_A^3)} - 2\frac{N_A^2}{A_p L_z^2}\varepsilon\sigma_A^3\left(-\frac{a}{2} + \frac{c_1}{\sqrt{A_p}} + \frac{c_2}{A_p}\right)\right)$$

$$p_{zz} = \left(\frac{k_B T}{\left(\frac{V_p}{N_A} - b\sigma_A^3\right)} + \frac{N_A^2}{V_p^2}\varepsilon\sigma_A^3\left(-a + \frac{2c_1}{\sqrt{A_p}} + \frac{2c_2}{A_p}\right)\right) \tag{1-3}$$

Multiplying Equation (1-3) by σ_A^3/ε

$$\frac{\sigma_A^3 p_{zz}}{\varepsilon} = \left(\frac{k_B T/\varepsilon}{\left(\left(\frac{V_p}{N_A}\right)\sigma_A^{-3} - b\right)} + \frac{N_A^2}{V_p^2}\sigma_A^6\left(-a + \frac{2c_1}{\sqrt{A_p}} + \frac{2c_2}{A_p}\right)\right) \tag{1-4}$$

Let $p_{zz}^* = \frac{\sigma_A^3 p_{zz}}{\varepsilon}$, $v^* = \left(\frac{V_p}{N_A}\right)\sigma_A^{-3}$ and $T^* = \frac{k_B T}{\varepsilon}$. Equation (1-4) can be rewritten as the following:

$$p_{zz}^* = \left(\frac{T^*}{(v^* - b)} + \frac{\left(-a + \frac{2c_1}{\sqrt{A_p}} + \frac{2c_2}{A_p}\right)}{v^{*2}}\right) \tag{1-5}$$

which is similar to van der Waals equation of state. As it is well known, the bulk van der Waals equation does not predict the critical point unless its parameters were adjusted for each substance. So the corrected confined equation of state is

$$p_{zz}^* = \left(\frac{T^*}{(v^* - b_{adj})} + \frac{\left(\frac{a_{adj}}{a}\right)\left(-a + \frac{2c_1}{\sqrt{A_p}} + \frac{2c_2}{A_p}\right)}{v^{*2}}\right) \tag{1-6}$$

At the critical point,

$$\left(\frac{\partial p_{zz}}{\partial V_p}\right)_T = 0 \text{ and } \left(\frac{\partial^2 p_{zz}}{\partial V_p^2}\right)_T = 0 \tag{1-7}$$

From Equations (1-6) and (1-7), the critical properties of the confined fluid are

$$\begin{aligned}
T_{cp}^* &= \frac{8}{27 b_{adj}}\left(\frac{a_{adj}}{a}\right)\left(a - \frac{2c_1}{\sqrt{A_p}} - \frac{2c_2}{A_p}\right) \\
p_{cp}^* &= \frac{1}{27 b_{adj}^2}\left(\frac{a_{adj}}{a}\right)\left(a - \frac{2c_1}{\sqrt{A_p}} - \frac{2c_2}{A_p}\right) \\
v_{cp}^* &= 3 b_{adj}
\end{aligned} \tag{1-8}$$

The corresponding bulk critical parameters are

$$T_c^* = \frac{8 a_{adj}}{27 b_{adj}}$$

$$p_c^* = \frac{a_{adj}}{27 b_{adj}^2}$$

$$v_c^* = 3b_{adj} \quad \text{(1-9)}$$

Therefore, the shift in the critical temperature is

$$\frac{(T_c^* - T_{cp}^*)}{T_c^*} = \frac{2c_1}{\sqrt{\pi}a}\frac{\sigma_A}{r_p} + \frac{2c_2}{\pi a}\left(\frac{\sigma_A}{r_p}\right)^2 \quad \text{(1-10)}$$

Replacing the parameters by their numerical values yields

$$\frac{(T_c^* - T_{cp}^*)}{T_c^*} = 0.9409\frac{\sigma_A}{r_p} - 0.2415\left(\frac{\sigma_A}{r_p}\right)^2 \quad \text{(1-11)}$$

Figure 1-2 is a comparison of the shift in critical temperatures computed from Equation (1-11) and the experimental data for fluids like Ar, CO_2, N_2, Xe O_2 and C_2H_4 by Morishige et al. (1997), and Morishige and Shikimi (1998).

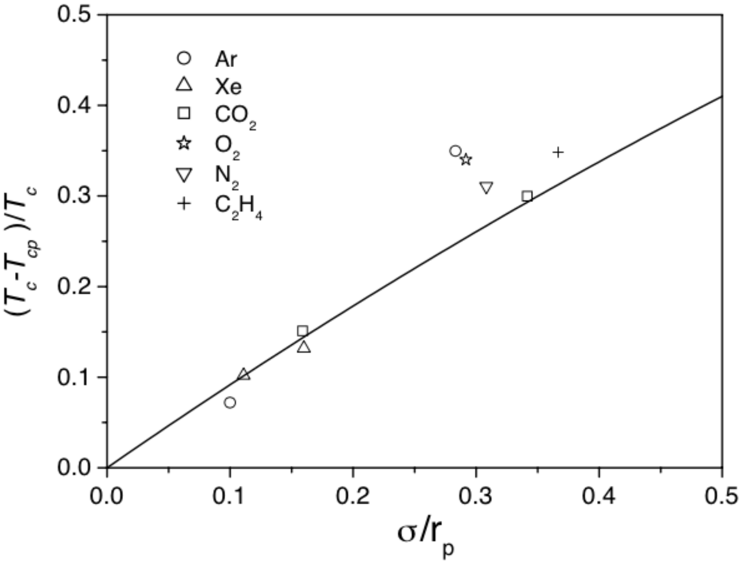

Figure 1-2 – The shift on critical temperatures computed from Equation (1-11) and the experimental data by Morishige et al. (1997) and Morishige and Shikimi (1998). (Zarragoicoechea and Kuz 2004)

Zarragoicoechea and Kuz confirmed that this model gave good estimations of shifts in critical temperatures up to $\sigma_A/r_p = 0.37$ based on their observation. However, according to **Figure 1-2**, the amount of experimental data seems to be too small to validate the model.

Similar to the derivation of the shift of critical temperature, the pressure shift is given by

$$\frac{(p_c^* - p_{cp}^*)}{p_c^*} = 0.9409\frac{\sigma_A}{r_p} - 0.2415\left(\frac{\sigma_A}{r_p}\right)^2 \quad \text{(1-12)}$$

Equation (1-12) has not been yet validated since there are no experimental data of the pressure shift available, and measuring the pressure shift could be a hard task to do.

Singh et al. (2009) investigated vapor-liquid phase coexistence of some species of pure hydrocarbons – methane, butane and octane – in slit graphite pore and mica with widths ranging from 0.8 nm to 5.0 nm by means of the grand-canonical transition-matrix Monte Carlo numerical simulator together with a modified Buckingham exponential intermolecular potential. Later, Devegowda et al (2012) manipulated those results to derive expressions to calculate the deviations of the critical properties of pure hydrocarbons as functions of molecular weight for slit pores with widths of 2.0 nm, 4.0 nm and 5.0 nm as shown in **Figures 1-3** and **1-4.**

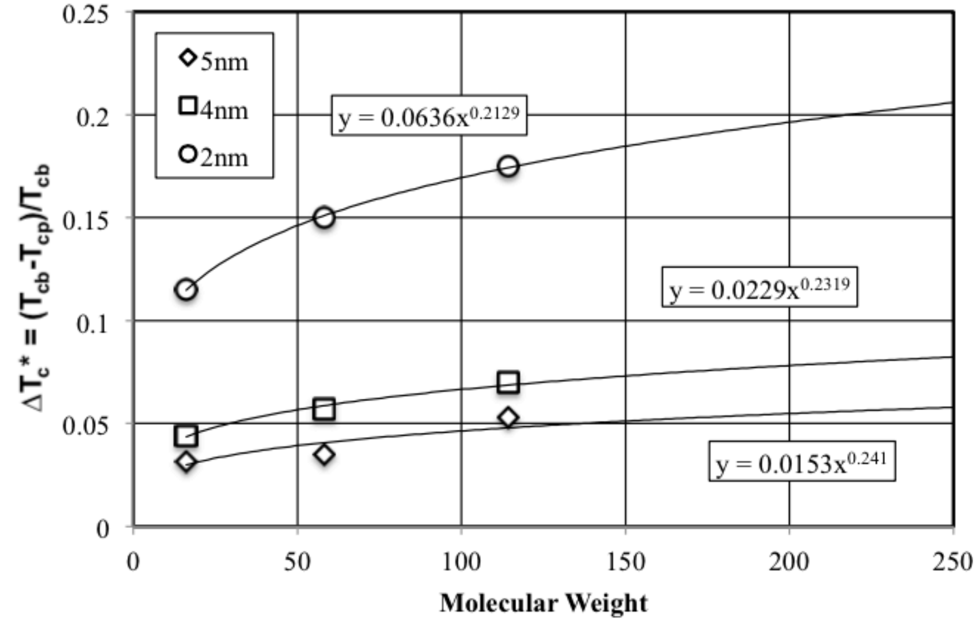

Figure 1-3 – Relative deviations of critical temperatures as functions of molecular weight. (Devegowda et al. 2012)

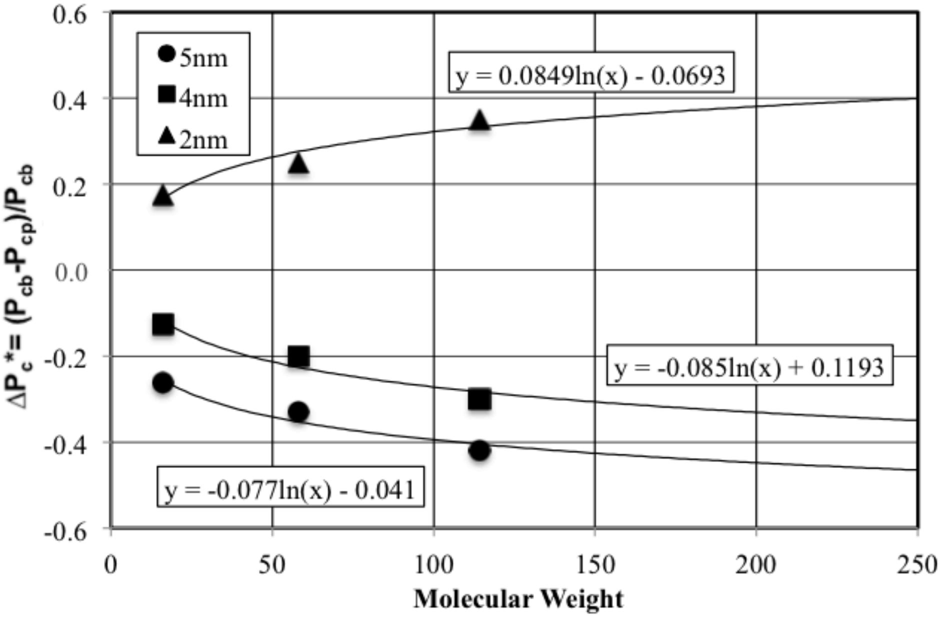

Figure 1-4 – Relative deviations of critical pressures as functions of molecular weight. (Devegowda et al. 2012)

They approximated the shifts in the critical temperature by the power law and the critical pressure by the logarithmic function.

$$\frac{(T_c-T_{cp})}{T_c} = \begin{cases} 0.0636\times MW^{0.2129} & \text{for } H = 2\text{ nm} \\ 0.0229\times MW^{0.2319} & \text{for } H = 4\text{ nm} \\ 0.0153\times MW^{0.2410} & \text{for } H = 5\text{ nm} \end{cases} \quad \text{(1-13)}$$

$$\frac{(p_c-p_{cp})}{p_c} = \begin{cases} 0.0849\ln MW - 0.0693 & \text{for } H = 2\text{ nm} \\ -0.085\ln MW + 0.1193 & \text{for } H = 4\text{ nm} \\ -0.077\ln MW - 0.0410 & \text{for } H = 5\text{ nm} \end{cases} \quad \text{(1-14)}$$

They also implemented their results to generate phase diagrams of confined hydrocarbon mixtures using the Peng-Robinson EOS as shown in **Figure 1-5**.

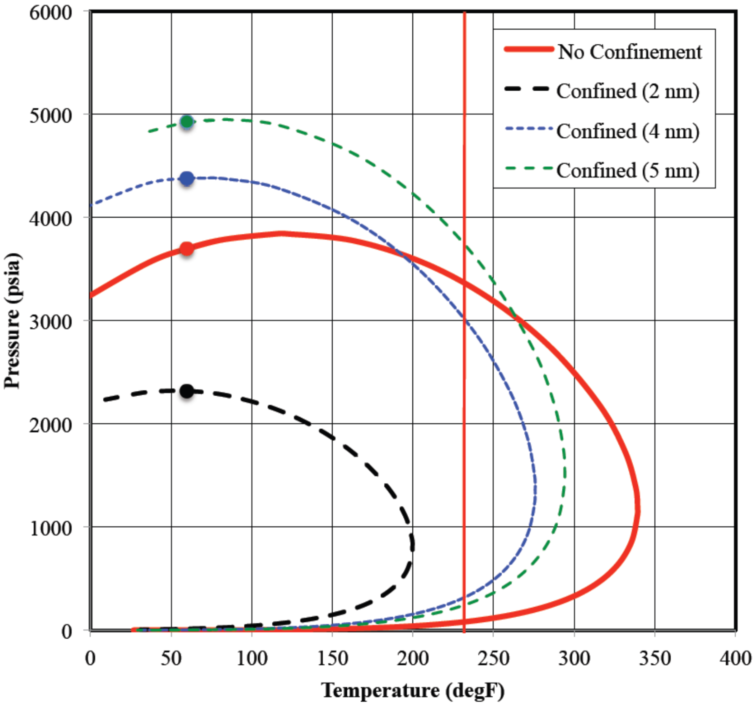

Figure 1-5 – Phase diagrams of confined and unconfined ternary synthetic gas-condensate fluid. The vertical line is the reservoir temperature at 230 °F.
(Deepak et al. 2012)

Ma et al. (2013) and Jin et al. (2013) used the same dataset as Devegowda et al. did with additional experimental data from Vishnyakov et al. (2001) and Singh and Singh (2011) to develop models to approximate the shifts in critical properties of confined hydrocarbons. They plotted the shifts in critical temperature and pressure versus the ratio of pore width (D) and effective molecular size (σ_e), which is the smallest diameter of the molecule, as illustrated in **Figures 1-6** and **1-7**, respectively.

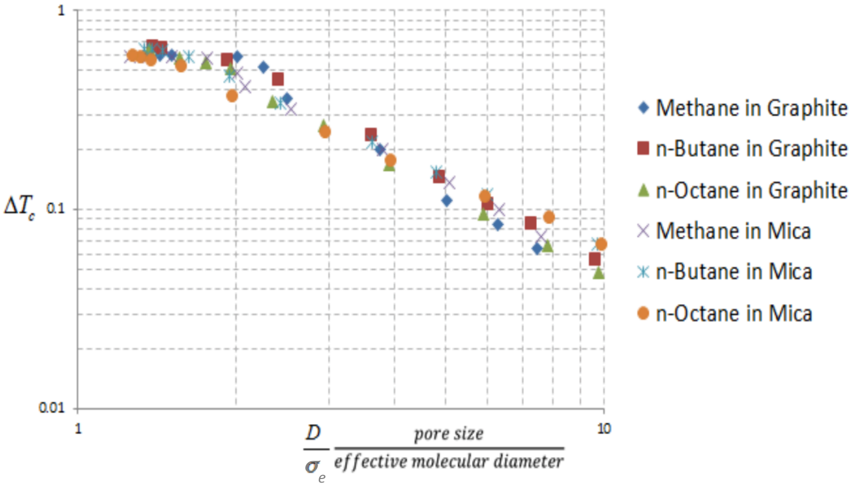

Figure 1-6 – Log-log plot of critical temperature shift vs. dimensionless pore size. (Ma et al. 2013)

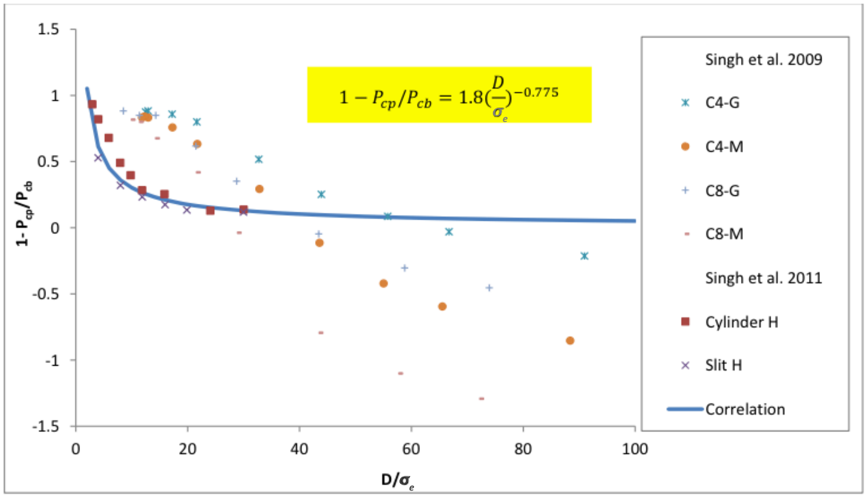

Figure 1-7 – Plot of critical pressure shift vs. dimensionless pore size. (Jin et al. 2013)

Similar to the model from Zarragoicoechea and Kuz, the critical shifts of Ma et al. (2013) and Jin et al. (2013) are functions of pore width and type of contained fluid.

$$\frac{(T_c - T_{cp})}{T_c} = \begin{cases} 1.1775\left(\frac{D}{\sigma_e}\right)^{-1.338} & \text{for } \left(\frac{D}{\sigma_e}\right) \geq 1.5 \\ 0.6 & \text{for } \left(\frac{D}{\sigma_e}\right) < 1.5 \end{cases} \quad \text{...(1-15)}$$

$$\frac{(p_C - p_{cp})}{p_c} = 1.5686\left(\frac{D}{\sigma_e}\right)^{-0.783} \quad \text{...(1-16)}$$

Recently, Sanaei et al. (2014) applied these models to study the effect of pore size distribution and connectivity on phase behavior in unconventional reservoirs. Similar to Devegowda et al. (2012), they directly applied the critical shifts in temperature and pressure computed from Ma et al. (2013) and Jin et al. (2013) to the Peng-Robinson equation of state to obtain phase diagrams of hydrocarbon mixtures for production modeling in shale reservoirs as shown in **Figure 1-8**.

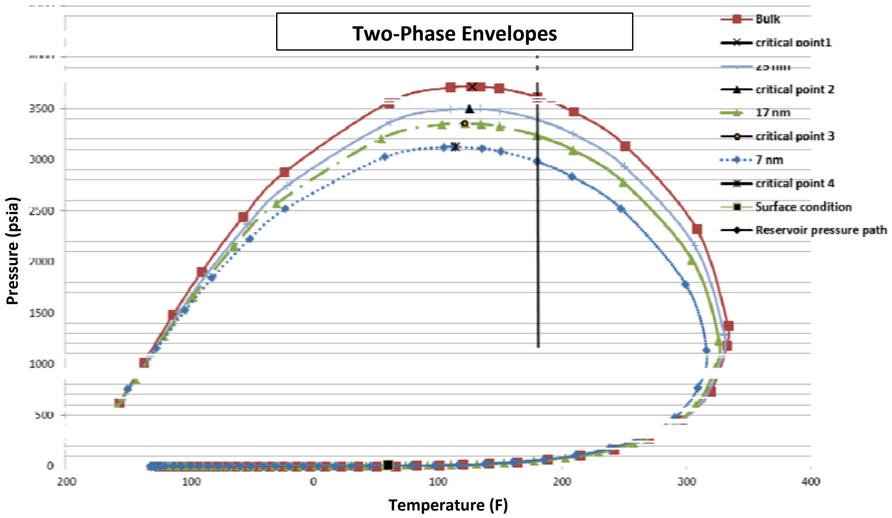

Figure 1-8 – Phase diagrams of confined and unconfined ternary synthetic gas-condensate fluid. (Sanaei et al. 2014)

Figures 1-5 and **1-8** illustrate the variation of mixture phase diagrams in different pore sizes compared to that of bulk mixture at the same fluid composition. Although both plots agree with our presumption that the pore proximity (confinement) affects fluid properties, more work is required to acquire more accurate phase diagrams. The phase diagrams obtained in **Figures 1-5** and **1-8** are derived based on the following assumptions:

- Mixture critical properties are derived from those of confined pure components where those properties were calculated from fitted correlations. These correlations are simply approximations without physical meanings and do not capture the interaction between rock and fluid molecules in the confined system.
- Peng-Robinson EOS for mixtures, which is valid only for bulk fluid, is utilized for confined fluid to estimate the critical properties.

- Surface (confinement) effects, known to significantly change phase behavior, are ignored.

Hydrocarbons in shale reservoirs are always present as mixtures. Brusllovsky (1992) and Ping et al. (1996) studied the effect of capillary pressure and adsorption on phase equilibrium of multicomponent systems and found that capillary forces and pressure change bubble point and dew point pressure. This change may alter many fluid parameters. As a result, phase diagrams of hydrocarbon mixtures in confined systems are necessary to predict fluid flow in the reservoirs and PVT properties of confined hydrocarbon mixtures in shale reservoirs have gained the attention of researchers in the oil and gas industry.

Didar and Akkutlu (2013) applied the NPT-Gibbs ensemble to find the equilibrium adsorption of gas into organic slit pores. They reported fluid density of binary mixtures across the pores width and found that the fluid density is not uniform. In particular, fluid density in adsorption layers is higher than fluid density in central layers. Methane tends to occupy more of the central layers rather than the adsorption layers whereas ethane tends to occupy more of the adsorption layers. This is because the pore walls have different levels of interaction with different fluid molecules. This phenomenon may cause a shift of the phase diagram of hydrocarbon mixtures in a confined system.

Nojabaei et al. (2013) studied the effect of capillary pressure on phase behavior of various binary hydrocarbon mixtures in tight and shale reservoirs. In this study, phase equilibrium was obtained by making the fugacity of each component across a liquid/vapor interface equivalent. The phase pressures differ by the capillary pressure, which is calculated from the Young-Laplace equation. The Macleod and Sugden correlation is used to compute the change in interfacial tension (IFT). Thus the IFT becomes zero at the critical point. The Peng-Robinson equation of state was used to acquire P-T diagrams of binary mixtures. They observed that the small pores decrease bubble point pressure and either decrease or increase dew point pressure. However, since the IFT becomes zero at the critical point, the critical points in this study remain constant for all the cases. This restriction may cause inaccurate results.

Recently, Wang et al. (2014) performed an experimental study of the effect of nanoconfinement on hydrocarbon phase behavior in unconventional reservoirs. A nanofluidic device was applied to visualize phase change of pure alkane and an alkane mixture under confinement. They found that the vaporization of the liquid phase in nano-channels was suppressed. In addition, they observed a shift in the two-phase region of the confined ternary hydrocarbon mixture. Also, Li, Mezzatesta et al. (2014a) proposed an iterative algorithm to solve the phase equilibrium equation system for the confined fluid and observed the difference of liquid molar composition of the confined fluid at the dew point pressure. In addition, Li, Jin et al. (2014b) applied a density functional theory (DFT) combined with the Peng-Robinson equation of state (EOS) to investigate the adsorption and phase behavior of mixtures in nanopores and found that the selectivity became more pronounced as the molar weight of a hydrocarbon component increases even though the mole fractions in bulk were equal. All of these studies imply that the derivation of the mixture phase diagram is not straightforward since the interaction between pore walls and fluid molecules is important to phase equilibrium in confined space.

Teklu et al. (2014) modified the conventional vapor/liquid equilibrium (VLE) calculations to account for both the capillary pressure and the critical shifts in nanopores. In particular, they applied the critical properties obtained from Zarragoicoechea and Kuz's model to an iterative algorithm including the capillary condensation effect (Kelvin equation). In this case, the bubble and dew points of the confined mixture changes due to a combination of both capillary pressure and critical shift effects. However, there are no experimental data of a confined mixture to validate this model. We note that many simulation results for mixture phase behavior including those for mixtures in confined environments have been reported mostly based on the Gibbs ensemble method (Panagiotopoulos 1988). However, to the best of our knowledge, analyses related to mixtures in shale gas environments are not available.

1.2 Study Objectives

This research provides a fundamental understanding of elements and factors which control PVT behavior in nano-volumes such as kerogen pores in shale reservoirs through molecular simulations. To fulfill our objectives, the following tasks need to be achieved:

- Develop PVT models for pure components of small molecule hydrocarbons (CH_4 and C_2H_6) in nano-volumes.
- Determine phase diagrams for binary mixtures of small molecule hydrocarbons (CH_4 and C_2H_6) in nano -volumes.
- Develop PVT models for pure components of long-chain alkanes (C_3H_8 – C_6H_{14}) in nano-volumes.
- Determine phase diagrams for binary mixtures of long-chain alkanes (C_3H_8 – C_6H_{14}) in nano-volumes.
- Determine phase diagrams for ternary mixtures of hydrocarbons in nano-volumes.
- Illustrate a study of the effects of the surrounding inorganic fluid environment (i.e. water) on phase diagrams.

1.3 Significance

We are at a crossroads — we have been trying to apply ‘conventional’ (i.e. high permeability) reservoir engineering methods to unconventional scenarios, and this is no longer practical and justifiable. We must re-work the problem from the fundamentals — and in particular, we must develop a new breed of solutions and methodologies that are derived directly from the phenomena at nano-volume scales.

This research provides a detailed study of fluid behavior and changes of PVT properties at nano-volume scales. This work will reveal the significance of the effect of the interaction between rock and fluid molecules (or confinement) on these PVT properties in shale reservoirs: phase diagram, critical pressure, critical temperature and fluid density. PVT models of pure hydrocarbons and phase diagrams of their mixtures in different pore sizes were developed. This study will help us better understand how fluids – hydrocarbons, carbon dioxide, and water – behave in shale reservoirs, which in turn will enhance the accuracy of production forecast, EUR prediction, and hydrocarbon available.

CHAPTER II

MOLECULAR SIMULATION PROCEDURES

Fluid mechanics is the branch of physics that involves the study of fluids and the forces on them. It is a branch of continuum mechanics where a subject is modeled without information at the atomic or molecular level. In other words, it models matter from a macroscopic point of view. In the petroleum industry, we develop our fundamental flow equations based on fluid dynamics, a branch of fluid mechanics. The application of fluid dynamics relies on the continuum hypothesis: fluid is assumed to be continuous. Properties such as pressure, temperature, velocity, and density are assumed to vary continuously from one point to another and are averaged values for the Representative Elementary Volume (REV), defined as the smallest volume over which a measurement can be made that will yield a value that is representative of a whole. The fact that the fluid is made up of discrete molecules is ignored. Therefore, continuum mechanics result in approximate solutions and may not be valid under some circumstances (e.g. fluid flow in a confined space where interaction between the walls of the container and the contained fluid molecules becomes significant to fluid properties.) These properties must be derived from forced acting on each fluid molecule.

Levels of modeling in physics and chemistry for the calculation of a material's properties or a system's behavior are usually divided into four categories as follows (from macroscopic to macroscopic, see **Figure 2-1**):

- Level of quantum mechanical models: Information about electrons is included. Electron exchange is allowed in the simulation. It can be used to investigate chemical phenomena by predicting protein folding at different temperatures or to study the ground state of individual atoms and molecules, the excited states, and the transition states that occur during chemical reactions.
- Level of molecular dynamics models: Information about individual atoms and molecules is included. The atoms and molecules are allowed to interact with each other for a period of time. This method does not allow electron exchange between atoms or molecules. Therefore, it cannot be used to predict chemical phenomena or reaction. One of the applications of this level of modeling is to examine the physical properties of fluids in a confined system.
- Mesoscale level: Information about groups of atoms and molecules is included. It is used to describe mechanical behavior between an atomic description and an unstructured continuum (intermediate scale length).

- Level of continuum models: At this level, modeling objects contain a large number of atoms and molecules and follow the continuum hypothesis. Physical properties of substances in the system are averaged and are independent of coordinate system or location. Conventional reservoir simulators are developed based on the level of modeling.

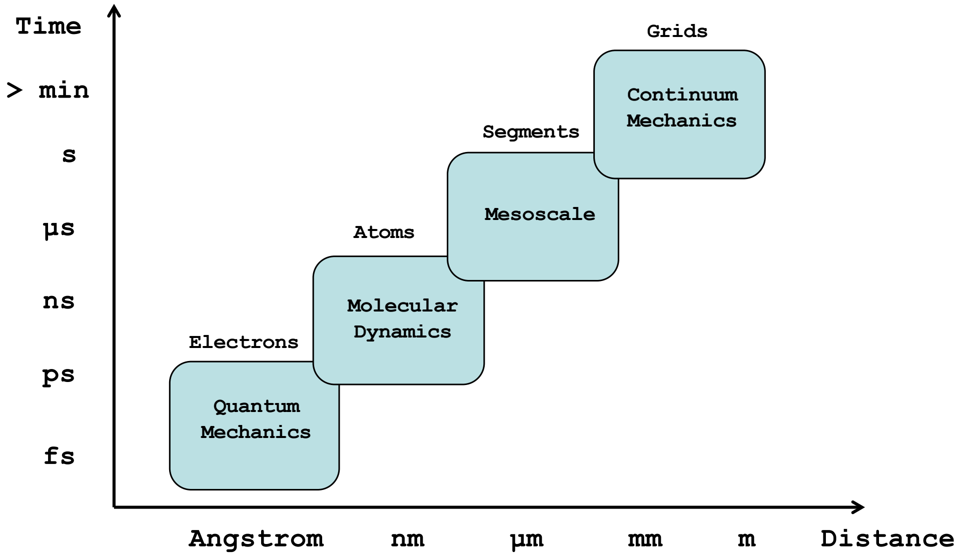

Adapted from: Texas A&M University - Laboratory of Molecular Simulation (LMS)

Figure 2-1 – Level of modeling (from microscopic to macroscopic).

For our problems, we are solving for PVT properties of fluids in a confined system where interaction between the walls of the container and the contained fluid molecules affects the fluid properties. Under such a circumstance, fluids must be treated as if it is made up of discrete molecules. In other words, the continuum is inapplicable to these problems. In addition, electron exchanges between atoms and molecules in the system are ignored (the chemical reaction is not considered in our system). That is, quantum mechanical modeling is not necessary to solve our problems.

In this work, we implement molecular dynamics modeling to observe motion and structures of fluid molecules that (1) yields to physical properties of fluids, (2) investigates the shifts of phase equilibriums, and (3) investigates the changes of PVT properties of pure components and mixtures in the confined space. In the following section, the fundamental concept of statistical molecular thermodynamics is introduced to help us understand the definitions and derivations of physical properties (i.e. pressure, temperature, internal energy, and free energies) in terms of molecular energies or partition functions.

2.1 Molecular Simulations

Owing to the advances in computing power, methodological efficiency, and the development of accurate force fields, molecular simulations have become a breakthrough technology that is widely accepted in the chemical industry. They have been used to investigate fluid behavior at the molecular level and to calculate fluid properties in confined spaces where it is nearly impossible to conduct laboratory experiments to measure such values. The simulations are also utilized to design nanomaterials and nano-devices (i.e. medical devices).

Describing fluid flow in shale reservoirs is a new challenge for petroleum engineers and researchers in the petroleum industry. Molecular simulation can be a breakthrough technology for the industry as a tool for understanding fluid behavior in shale reservoirs with nanoscale pore sizes. Molecular Dynamics (MD) simulation can be used to compute the equilibrium and transport properties such as the diffusion coefficient and investigate the movements of fluid molecules in reservoirs. Grand Canonical Monte Carlo (GCMC) simulation can be used to describe adsorptions in shale reservoirs and to determine the shifts of thermodynamics properties of fluids in the reservoirs.

2.1.1 Molecular Dynamics Simulation

Molecular Dynamics simulation is a technique used to compute the equilibrium and transport properties of fluids by solving equations of motion for a system of *N* particles interacting via potential energy (U). The nuclear motion of the constituent particles obey the laws of classical mechanics.

The potential energy can be expressed as the following:

$$U = \sum_i u_1(r_i) + \sum_i \sum_{j>i} u_2(r_i, r_j) + \sum_i \sum_{j>i} \sum_{k>j>i} u_3(r_i, r_j, r_k) + \cdots \text{ ....(2-1).}$$

The $\Sigma_i\Sigma_{j>i}$ notation indicates a summation of all different pairs, i and j, without counting any pairs twice. The same care must be taken for triplets. $u_1(r_i)$ represents the effect of an external field on the system. The remaining terms represents interaction between particles in the system. For instance, $u_2(r_i, r_j)$ is a pair interaction and $u_3(r_i, r_j, r_k)$ involves triplets of particles. Four-body (and higher) terms in equation (2-1) are expected to be small in comparison with u_2 and u_3. Largely, the pairwise approximation, u_2, gives a remarkably precise description of fluid properties because the average three-body effects can be partially included by defining an effective pair potential (Allen and Tildesley 1987). Thus, without any external field on the system, equation (2-1) can be rewritten as

$$U \approx \sum_i \sum_{j>i} u_2^{eff}(r_i, r_j) \qquad \text{(2-2).}$$

The most fundamental form of the classical equations of motion is the Lagrangian equation

$$\frac{d}{dt}(\partial\mathcal{L}/\partial\dot{q_k}) - \partial\mathcal{L}/\partial q_k = 0 \qquad \text{(2-3)}$$

where the Lagrangian function $\mathcal{L}(\boldsymbol{q}, \dot{\boldsymbol{q}})$ is defined as the difference between the kinetic and potential energy of the system

$$\mathcal{L} = K - U \qquad \text{(2-4)}$$

and is considered to be a function of the generalized coordinates, q_k, and their time derivatives, $\dot{q_k}$. U is potential energy as expressed as Equation (2-1). K is kinetic energy which usually takes the form

$$K \approx \sum_{i=1}^{N} \sum_\alpha p_{i\alpha}^2/2m_i \qquad \text{(2-5)}$$

where m_i is the mass of particle i and the index α runs over the different (x, y, z) components of the momentum of particle i (p_i).

If we consider the system of atoms with Cartesian coordinates, $\boldsymbol{r_i}$, then equation (2-3) becomes

$$m_i\ddot{r_i} = f_i \qquad \text{(2-6)}$$

The total force acting on particle i can be computed by

$$f_i = -\nabla_{r_i}\mathcal{L} = -\nabla_{r_i}U \qquad \text{(2-7).}$$

These equations apply to the center of mass of a molecule. With given potential energy correlation, the trajectories, velocities, and accelerations of particles can be determined using equations (2-6) and (2-7). This method is used to handle only the translational motion of the center of mass of molecules.

In our current work, we study the effects of confinement on the fluid behavior of methane and ethane. Methane is treated as a rigid spherical molecule where only the equations of translational motion are adequate. However, the molecular structure of ethane is linear (non-spherical), and the equations for rotational motion must be considered to capture all the possible ways for the molecules to move. The rotational motion is governed by the torque, $\boldsymbol{\tau_i}$, about the center of mass. When the interactions have the form of forces, $\boldsymbol{f_{ia}}$, acting on sites in the molecule, $\boldsymbol{r_{ia}}$, the torque is simply defined as

$$\boldsymbol{\tau_i} = \textstyle\sum_a (\boldsymbol{r_{ia}} - \boldsymbol{r_i}) \times \boldsymbol{f_{ia}} = \sum_a \boldsymbol{d_{ia}} \times \boldsymbol{f_{ia}} \quad \text{(2-8)}$$

where $\boldsymbol{d_{ia}}$ is the position of atoms relative to the center of mass of the molecule. For instance, when we consider an ethane molecule consisting of spherical methyl groups, $\boldsymbol{d_{ia}}$ equals the distance from the center of the single bond between two carbon atoms to the center of each methyl group as shown in **Figure 2-2**. In this work, we treat ethane as a rigid linear molecule where the bond length between two carbon atoms is constant. This is commonly true at reservoir conditions where the amplitude of vibration is small compared to molecular dimensions. The change in C-C bond length of ethane molecule is approximately 0.0092 Å at 2.56 GPa (Meléndez-Pagán and Ben-Amotz 2000).

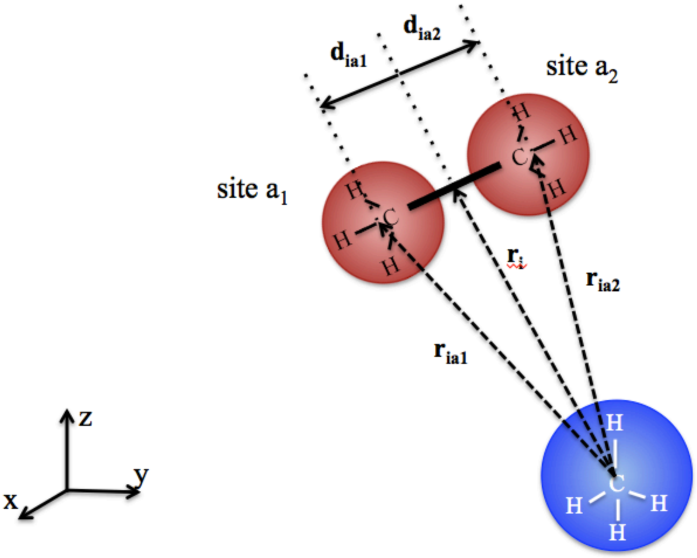

Figure 2-2 – A model describing forces acting on ethane molecule due to methane molecule.

For a rigid linear molecule, the angular velocity and the torque must be perpendicular to the molecular axis at all times. If $\boldsymbol{e^s}$ is the unit vector along the axis, this means that the torque on a molecule can be written as

$$\boldsymbol{\tau} = \boldsymbol{e^s} \times \boldsymbol{g^s} \quad \text{(2-9)}$$

where $\boldsymbol{g^s}$ can be computed from the intermolecular forces. In the particular case of an interaction site model, the location of each site relative to the center of mass of the molecule can be written as

$$\boldsymbol{d_{ia}^s} = d_{ia}\boldsymbol{e^s} \quad \text{(2-10).}$$

So we can write $\boldsymbol{g^s}$ as

$$\boldsymbol{g}^{\boldsymbol{s}} = \sum_{ia} d_{ia}\boldsymbol{f}_{\boldsymbol{ia}} \qquad \text{(2-11).}$$

The vector $\boldsymbol{g}^{\boldsymbol{s}}$ can be written as a combination of two components, which are the component perpendicular, $\boldsymbol{g}^{\perp}$**,** and parallel, $\boldsymbol{g}^{\parallel}$**,** to the molecular axis:

$$\boldsymbol{g}^{\boldsymbol{s}} = \boldsymbol{g}^{\perp} + \boldsymbol{g}^{\parallel} \qquad \text{(2-12).}$$

Thus, Equation (2-9) can be rewritten as

$$\boldsymbol{\tau} = \boldsymbol{e}^{\boldsymbol{s}} \times (\boldsymbol{g}^{\perp} + \boldsymbol{g}^{\parallel}) \qquad \text{(2-13)}$$

which is reduced to

$$\boldsymbol{\tau} = \boldsymbol{e}^{\boldsymbol{s}} \times \boldsymbol{g}^{\perp} \qquad \text{(2-14)}$$

with

$$\boldsymbol{g}^{\perp} = \boldsymbol{g} - \boldsymbol{g}^{\parallel} = \boldsymbol{g}^{\boldsymbol{s}} - (\boldsymbol{g}^{\boldsymbol{s}} - \boldsymbol{e}^{\boldsymbol{s}})\boldsymbol{e}^{\boldsymbol{s}} \qquad \text{(2-15).}$$

The equations of rotational motion can now be written as two-first-order differential equations.

$$\dot{\boldsymbol{e}}^{\boldsymbol{s}} = \boldsymbol{v}^{\boldsymbol{s}} \qquad \text{(2-16)}$$

$$\dot{\boldsymbol{v}}^{\boldsymbol{s}} = \frac{g^{\perp}}{I} + \lambda \boldsymbol{e}^{\boldsymbol{s}} \qquad \text{(2-17)}$$

where I is the moment of inertia. The equation (2-16) is simply a definition of $\boldsymbol{v}^{\boldsymbol{s}}$, which is the time derivative of $\boldsymbol{e}^{\boldsymbol{s}}$, the angular velocity vector. Physically, the first term of the equation (2-17) corresponds to the moment of force $\boldsymbol{g}^{\perp}$ responsible for rotation of the molecule, and the second term corresponds to the force $\lambda\boldsymbol{e}^{\boldsymbol{s}}$ along the bond, which constrains the bond length to be a constant of the motion, where λ can be thought of as a Lagrange multiplier.

In this work, we also consider a system with long chain alkanes (i.e. propane, butane, pentane, and hexane). Although it is reasonable to assume that the C-C bond length is constant in our case study conditions, the bending motions – which change the angle between bonds –, and twisting motions – which alter the torsional angles –, must be considered. These bending and twisting motions are of much lower frequency than bond vibrations. Therefore, it would be unrealistic to assume total rigidity of long chain alkane molecules.

Let us consider a propane molecule consisting of three united atoms, which are two methyl groups and one methylene group. The bond lengths between carbon atoms are fixed whereas the angle between the bonds is allowed to vary under the influence of intramolecular potential. Numbering the central (methylene) united atom as 2, and the two outer (methyl) united atoms as 1 and 3, we can write the equations of motion in the following form:

$$m_1\ddot{\boldsymbol{r}}_{\boldsymbol{1}} = \boldsymbol{f}_{\boldsymbol{1}} + \boldsymbol{g}_{\boldsymbol{1}} \tag{2-18a}$$

$$m_2\ddot{\boldsymbol{r}}_{\boldsymbol{2}} = \boldsymbol{f}_{\boldsymbol{2}} + \boldsymbol{g}_{\boldsymbol{2}} \tag{2-18b}$$

$$m_3\ddot{\boldsymbol{r}}_{\boldsymbol{3}} = \boldsymbol{f}_{\boldsymbol{3}} + \boldsymbol{g}_{\boldsymbol{3}} \tag{2-18c}$$

where $\boldsymbol{f}_{\boldsymbol{1}}$, $\boldsymbol{f}_{\boldsymbol{2}}$, and $\boldsymbol{f}_{\boldsymbol{3}}$ are the forces due to intermolecular interactions and those intramolecular effects that are explicitly included in the potential. The terms $\boldsymbol{g}_{\boldsymbol{1}}$, $\boldsymbol{g}_{\boldsymbol{2}}$, and $\boldsymbol{g}_{\boldsymbol{3}}$ are the constraint forces. Their role is to keep the desired bond lengths constant and to ensure that the following equations:

$$\chi_{12} = r_{12}^2(t) - d_{12}^2 = 0 \tag{2-19a}$$

$$\chi_{23} = r_{23}^2(t) - d_{23}^2 = 0 \tag{2-19b}$$

(where d_{12} and d_{23} are the bond lengths, $r_{12} = |\boldsymbol{r}_{\boldsymbol{1}} - \boldsymbol{r}_{\boldsymbol{2}}|$, and $r_{23} = |\boldsymbol{r}_{\boldsymbol{2}} - \boldsymbol{r}_{\boldsymbol{3}}|$) are satisfied at all times. Thus, the Lagrangian equations of motion are the equations (2-18) with

$$\boldsymbol{g}_{\boldsymbol{a}} = \frac{1}{2}\lambda_{12}\boldsymbol{\nabla}_{\boldsymbol{r}_{\boldsymbol{a}}}\chi_{12} + \frac{1}{2}\lambda_{23}\boldsymbol{\nabla}_{\boldsymbol{r}_{\boldsymbol{a}}}\chi_{23} \tag{2-20}$$

and λ_{12} and λ_{23} are the undetermined (Lagrangian) multipliers. So far, we have no approximation and could solve for the constraint forces. However, using finite difference methods to solve these equations of motion may lead to bond lengths that steadily diverge from the desired values.

Instead of using the true forces of constraint, $\boldsymbol{g}_{\boldsymbol{a}}$, Ryckaert et al. (1977) suggested an approach in which the constraint forces are calculated so as to guarantee that the constraints are satisfied at each time step. Thus, we write

$$m_a\ddot{\boldsymbol{r}}_{\boldsymbol{a}} = \boldsymbol{f}_{\boldsymbol{a}} + \boldsymbol{g}_{\boldsymbol{a}} \approx \boldsymbol{f}_{\boldsymbol{a}} + \boldsymbol{g}_{\boldsymbol{a}}^{(r)} \tag{2-21}$$

where $\boldsymbol{g}_{\boldsymbol{a}}^{(r)}$ is an approximation of $\boldsymbol{g}_{\boldsymbol{a}}$. The equation for advancing the positions is

$$\boldsymbol{r}(t + \delta t) = 2\boldsymbol{r}(t) - \boldsymbol{r}(t - \delta t) + \delta t^2\ddot{\boldsymbol{r}}(t) \tag{2-22}$$

Combining equations (2-21) and (2-22), we obtain

$$\boldsymbol{r}_{\boldsymbol{a}}(t + \delta t) = 2\boldsymbol{r}_{\boldsymbol{a}}(t) - \boldsymbol{r}_{\boldsymbol{a}}(t - \delta t) + \left(\frac{\delta t^2}{m_a}\right)\left(\boldsymbol{f}_{\boldsymbol{a}}(t) + \boldsymbol{g}_{\boldsymbol{a}}^{(r)}(t)\right) \tag{2-23a}$$

$$\boldsymbol{r}_{\boldsymbol{a}}(t + \delta t) = 2\boldsymbol{r}_{\boldsymbol{a}}(t) - \boldsymbol{r}_{\boldsymbol{a}}(t - \delta t) + \left(\frac{\delta t^2}{m_a}\right)\boldsymbol{f}_{\boldsymbol{a}}(t) + \left(\frac{\delta t^2}{m_a}\right)\boldsymbol{g}_{\boldsymbol{a}}^{(r)}(t) \tag{2-23b}$$

Let $\boldsymbol{r'}_{\boldsymbol{a}}(t+\delta t)$ be the position which would have been reached in the absence of any constraints. Thus, we can write

$$\boldsymbol{r}_{\boldsymbol{a}}(t+\delta t)=\boldsymbol{r'}_{\boldsymbol{a}}(t+\delta t)+\left(\frac{\delta t^2}{m_a}\right)\boldsymbol{g}_{\boldsymbol{a}}^{(r)}(t) \tag{2-24}$$

Returning to our example of propane, and recognizing that the constraint forces must be along the bonds and must follow Newton's third law, we see that

$$\boldsymbol{g}_{\boldsymbol{1}}^{(r)}=\lambda_{12}\boldsymbol{r}_{\boldsymbol{12}} \tag{2-25a}$$

$$\boldsymbol{g}_{\boldsymbol{2}}^{(r)}=\lambda_{23}\boldsymbol{r}_{\boldsymbol{23}}-\lambda_{12}\boldsymbol{r}_{\boldsymbol{12}} \tag{2-25b}$$

$$\boldsymbol{g}_{\boldsymbol{3}}^{(r)}=-\lambda_{23}\boldsymbol{r}_{\boldsymbol{23}} \tag{2-25c}$$

where λ_{12} and λ_{23} are the undetermined multipliers. Combining equations (2-24) and (2-25), we obtain

$$\boldsymbol{r}_{\boldsymbol{1}}(t+\delta t)=\boldsymbol{r'}_{\boldsymbol{1}}(t+\delta t)+\left(\frac{\delta t^2}{m_1}\right)\lambda_{12}\boldsymbol{r}_{\boldsymbol{12}}(t) \tag{2-26a}$$

$$\boldsymbol{r}_{\boldsymbol{2}}(t+\delta t)=\boldsymbol{r'}_{\boldsymbol{2}}(t+\delta t)+\left(\frac{\delta t^2}{m_2}\right)\lambda_{23}\boldsymbol{r}_{\boldsymbol{23}}(t)-\left(\frac{\delta t^2}{m_2}\right)\lambda_{12}\boldsymbol{r}_{\boldsymbol{12}}(t) \tag{2-26b}$$

$$\boldsymbol{r}_{\boldsymbol{3}}(t+\delta t)=\boldsymbol{r'}_{\boldsymbol{3}}(t+\delta t)-\left(\frac{\delta t^2}{m_3}\right)\lambda_{23}\boldsymbol{r}_{\boldsymbol{23}}(t) \tag{2-26c}$$

Therefore,

$$\boldsymbol{r}_{\boldsymbol{12}}(t+\delta t)=\boldsymbol{r'}_{\boldsymbol{12}}(t+\delta t)+\delta t^2(m_1^{-1}+m_2^{-1})\lambda_{12}\boldsymbol{r}_{\boldsymbol{12}}(t)-\delta t^2 m_2^{-1}\lambda_{23}\boldsymbol{r}_{\boldsymbol{23}}(t) \tag{2-27a}$$

$$\boldsymbol{r}_{\boldsymbol{23}}(t+\delta t)=\boldsymbol{r'}_{\boldsymbol{23}}(t+\delta t)-\delta t^2 m_2^{-1}\lambda_{12}\boldsymbol{r}_{\boldsymbol{12}}(t)+\delta t^2(m_2^{-1}+m_3^{-1})\lambda_{23}\boldsymbol{r}_{\boldsymbol{23}}(t) \tag*{(2-27a)}$$

Now we can take the square modulus of both sides, and apply our desired constraints:

$$|\boldsymbol{r}_{\boldsymbol{12}}(t+\delta t)|^{\boldsymbol{2}}=|r_{12}(t)^2|=d_{12}^2 \tag{2-28}$$

and similarly for $\boldsymbol{r}_{\boldsymbol{23}}$. The result is a pair of quadratic equations in λ_{12} and λ_{23}. Then, we can solve for the undetermined multipliers. This process can be straightforwardly applied to the more complex molecules such as butane, pentane, and hexane.

Molecular Dynamics (MD) simulations are in many respects very similar to real experiments. In the MD simulation, we first prepare a sample by selecting or generating a model system containing *N* particles that represent the scheme we wish to study; we the find the equilibrium state by solving the equations of motion for this system until the properties of the system no longer change with time. After equilibrium is reached, the measurement of the properties can be performed. To measure an observable quantity in the MD simulation, we must first be able to express this parameter as a function of the position and momenta of the particles (direct output from the simulation) in the system. For example, a definition of the kinetic temperature in a classical, many-body system utilizes the equipartition of energy over all degrees of freedom that enter quadratically into the Hamiltonian system. In other words, the theorem of equipartition of energy states that molecules in thermal equilibrium have the same average energy associated with each degree of freedom of their motion and that the energy is $\frac{1}{2}k_BT$ per molecule per degree of freedom. In particular for the average kinetic energy per degree of freedom, we have

$$\langle \frac{1}{2}mv_\alpha^2 \rangle = \frac{1}{2}k_BT \text{ ....} (2\text{-}29).$$

In a simulation, we use the above equation as an operational definition of the temperature. In practice, the total kinetic energy of the system is measured and divided by the number of degrees of freedom, N_f, to obtain the instantaneous temperature:

$$T(t) = \sum_{i=1}^{N} \frac{m_i v_i^2(t)}{k_B N_f} \text{ ....} (2\text{-}30).$$

As mentioned previously, to obtain accurate properties of the system, the values at the equilibrium state must be measured. Another indicator of the equilibrium state is when the total energy of the system reaches the minimum. This concept is a useful application of statistical thermodynamics to Molecular Dynamics simulation.

2.1.2 Molecular Dynamics Simulation with the Monte Carlo Method

The Monte Carlo method is used to describe a technique that relies on repeated statistical sampling to approximate solutions to quantitative problems. Monte Carlo simulations choose random numbers from given probabilistic distributions of input, and these numbers can be manipulated in statistical processes to yield the desired output. Instead of random sampling, importance sampling is an appropriate technique that picks random numbers from a distribution which allows the function evaluation to be concentrated in the important regions of space that actually contribute to the integral of interest. In other words, this sampling technique would help minimize time spent on calculations where the Boltzmann factor is negligible by sampling many points in the region where the Boltzmann factor is significant. Since the scheme of the system changes during the simulation, the Markov chain is implemented to maintain the appropriate probability. This process is called the Metropolis method (Metropolis et al. 1953).

To help understand the concept of implementation of the Monte Carlo method to the NVT ensemble, **Figure 2-3** illustrates a diagram of two neighboring states of a system containing 6 particles.

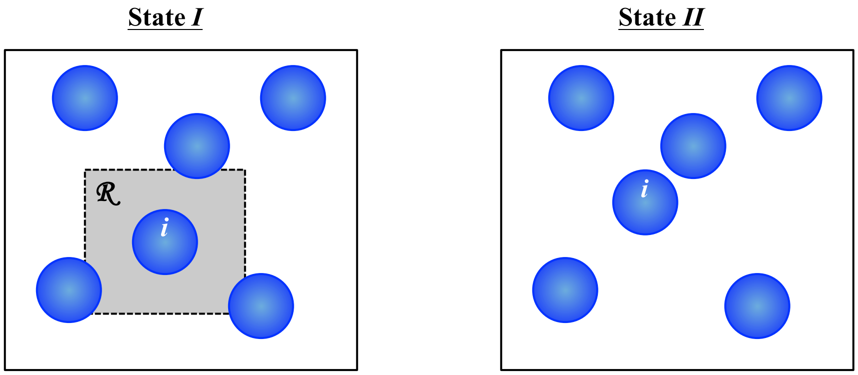

Figure 2-3 – State *I* is an initial configuration. State *II* is obtained from State *I* by moving particle *i* with a uniform probability to any point in region $\mathcal{R}$.

State *I* is an initial state. To construct a neighboring state *II* (new state), one particle (*i*) is chosen at random and displaced from its position, r_i^I, with equal probability to any point, r_i^{II}, inside the square. This square is of side $2\delta r_{max}$ and is centered at r_i^I. This square would be a small cube for the three-dimensional problem. At the beginning of the simulation, an atom is picked at random and given a uniform random displacement along each of coordinate directions to yield the state *II*. In the next step, the simulation calculates the difference of potential energy between state *I*, U_I and state *II*, U_{II}.

$$\delta U_{I\rightarrow II} = U_{II} - U_I \quad \text{........(2-31).}$$

The probability density of finding a configuration in coordinates $\boldsymbol{q}^N$, $P(\boldsymbol{q}^N)$ can be computed from the configurational part of the partition function or the configuration integral, Z. In the canonical ensemble, the number of particles, temperature, and volume are constant. The partition function for this ensemble is

$$Q_{NVT} = \frac{1}{\Lambda^{3N}N!}\int \exp[-\beta U(\boldsymbol{q}^N)]\, \boldsymbol{dq}^N \quad \text{........(2-32)}$$

where Λ is the thermal de Broglie wavelength,

$$\Lambda = \sqrt{h^2/(2\pi m_i k_B T)} \quad \text{........(2-33)}$$

where k_B is the Boltzmann constant and h is Planck's constant. Thus, the classical configuration integral for the canonical ensemble is simply

$$\mathbb{Z}_{NVT} = \int \exp[-\beta U(\boldsymbol{q}^N)]\, \boldsymbol{dq}^N \quad \text{........(2-34).}$$

From the partition function, it follows that the probability density of finding configuration in coordinates $\boldsymbol{q}^N$ for this ensemble is

$$\mathcal{P}_{NVT}(\boldsymbol{q}^N) = \frac{\exp[-\beta U(\boldsymbol{q}^N)]}{Z_{NVT}} \text{ ......(2-35).}$$

From the correlation, it can be observed that the probability density of the lower energy system is greater than the higher energy system. For instance, if $\delta U_{I\to II} \leq 0$, the potential energy of state *II* is lower than that of state *I*. Thus, the probability density of state *II* is greater and the new configuration is accepted. If $\delta U_{I\to II} > 0$, the potential energy of state *II* is higher than that of state *I* and the probability density of state *II* is lower. However, the configuration will be considered for acceptance with a probability

$$\alpha_{I\to II}(\boldsymbol{q}^N) = \frac{\mathcal{P}_{II}(\boldsymbol{q}^N)}{\mathcal{P}_{I}(\boldsymbol{q}^N)} \text{ ......(2-36)}$$

The ratio can be expressed as the Boltzmann factor of the energy difference,

$$\alpha_{I\to II}(\boldsymbol{q}^N) = \frac{\mathbb{Z}_{NVT}{}^{-1}\exp[-\beta U_{II}(\boldsymbol{q}^N)]}{\mathbb{Z}_{NVT}{}^{-1}\exp[-\beta U_{I}(\boldsymbol{q}^N)]} = \exp\left[-\left(\beta U_{II}(\boldsymbol{q}^N) - \beta U_{I}(\boldsymbol{q}^N)\right)\right] = \exp[-\beta\delta U_{I\to II}] \text{ ......(2-37)}$$

For the case of $\delta U_{I\to II} > 0$, the simulation generates a random number, ξ, from uniform distribution on (0,1). The new configuration will be accepted when the random number is lower than $\exp[-\beta\delta U_{I\to II}]$. This procedure can be explained as shown in **Figure 2-4**.

During the simulation, supposing a particular move in the direction from a lower energy to a higher energy system, where $\delta U_{I\to II} > 0$, $\delta U_{I\to II}$ is considered. Different from $\delta U_{I\to II} \leq 0$, where the new configuration is always accepted, the configuration can be either rejected (blank area in **Figure 2-4**) or accepted (blue area in **Figure 2-4**) with a probability of $\exp[-\beta\delta U_{I\to II}]$ when $\delta U_{I\to II} > 0$. If at that point a random number, ξ_1, is selected, the move is accepted. If ξ_2 is selected, the move is rejected. The more the potential energy difference between the two stages is, the lower the chance that the new configuration will be accepted. If the move is rejected, particles in the system retain their old positions, and the old configuration is recounted as a new state that is used for the next step. In summary, the acceptance rule of any moves ($\delta U_{I\to II} \leq 0$ and $\delta U_{I\to II} > 0$) is Min $(1, \exp[-\beta\delta U_{I\to II}])$. This probability changes over a simulation where the Markov chain is necessary for the calculation. A flow chart of the application of Monte Carlo simulation to Molecular Dynamics simulation is illustrated in **Figure 2-5**.

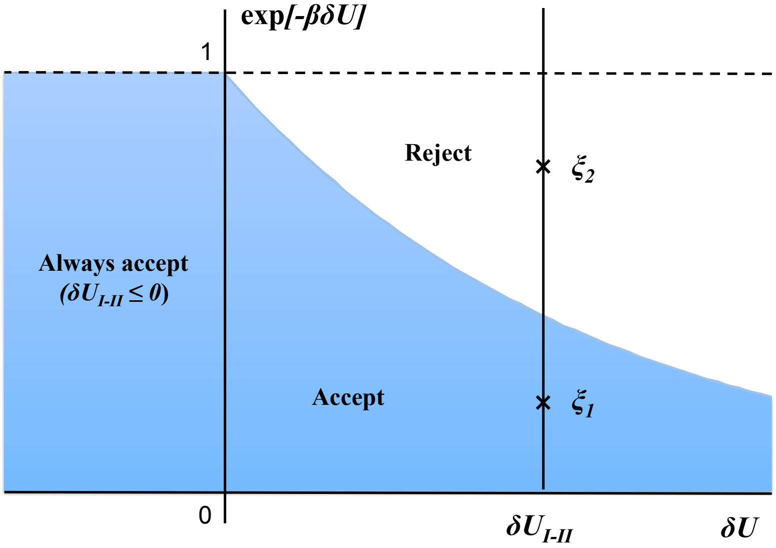

Figure 2-4 – Acceptance probability diagram in the Monte Carlo simulation.

As mentioned earlier, if the probability of the lower energy system is greater than the higher energy system, the simulation seeks for locations of particles in the system giving the lowest energy. In other words, assuming that the number of Monte Carlo simulation runs is large enough, the final configuration must be at equilibrium. This technique is very useful for studies of fluid adsorption in confined systems (i.e. observation of fluid storage in kerogen pores). This method is appropriate for studies where the number of molecules is known and fixed. In the next section, the Grand Canonical Monte Carlo simulation is introduced to solve problems where the number of molecules in the system is variable based upon its chemical potential.

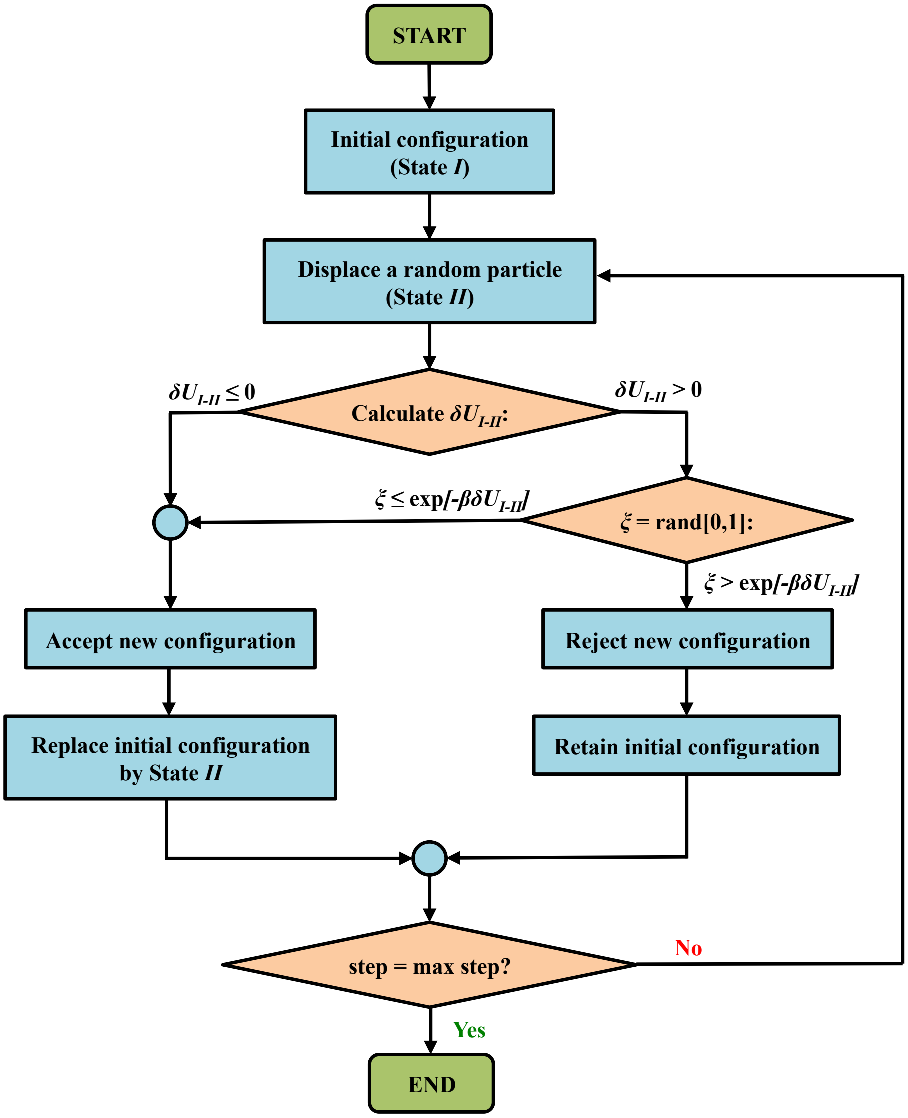

Figure 2-5 – Procedures of the MC simulation.

2.1.3 Grand Canonical Monte Carlo Simulation

Classical Molecular Dynamics and Molecular Dynamics Monte Carlo (GCMC) simulations are proper techniques for statistical ensembles in which the number of particles in the system is imposed (i.e. canonical ensemble, microcanonical ensemble, and isobaric-isothermal ensemble). However, for some systems, we need to obtain the average number of particles in the system as a function of external conditions. For example, in adsorption studies, we need to determine the amount of material adsorbed as a function of the pressure and temperature of the reservoir with which the material is in contact. Moreover, in studies of shifts of phase diagrams of confined fluid, it is necessary to record the number of molecules occupying the confined system at varying pressures and temperatures within the reservoir. Those results yield the phase transition and other PVT properties of the confined fluid. For these kinds of studies, the most appropriate ensemble to use is the grand-canonical ensemble (μVT ensemble). In this ensemble, the temperature, volume, and chemical potential are fixed while the number of molecules fluctuates. This ensemble is used to represent the possible state of the mechanical system of molecules that is being maintained in thermodynamic equilibrium (thermal and chemical) with a reservoir. The system is open and allowed to exchange energy and molecules with a reservoir. Several possible states of the system can differ in both their total energy and total number of molecules. The system's volume, shape, and other external coordinates are retained for all possible states of the system.

In the experiment setup, to represent equilibrium, the reservoir is connected to the ensemble (our confined system) as shown in **Figure 2-6**, and various types of motion are allowed by GCMC simulation to emulate the evolution of the system to the equilibrium state. Thus, during simulation, the GCMC algorithm randomly chooses to act on the confined system from the following choices for a molecule in the confined fluid volume:

a. a molecule is created at a random position (insertion)
b. a molecule is displaced (translation)
c. a molecule is removed (deletion)
d. a molecule is rotated (rotation, for non-spherical molecules).

At each step, one of the four events takes place, and the system energy is computed. The simulation proceeds until reaching thermodynamic equilibrium where the chemical potential of the bulk and the confined system are equal:

$$\mu_{Bulk}(T,p) = \mu_{Confined} \qquad (2\text{-}38).$$

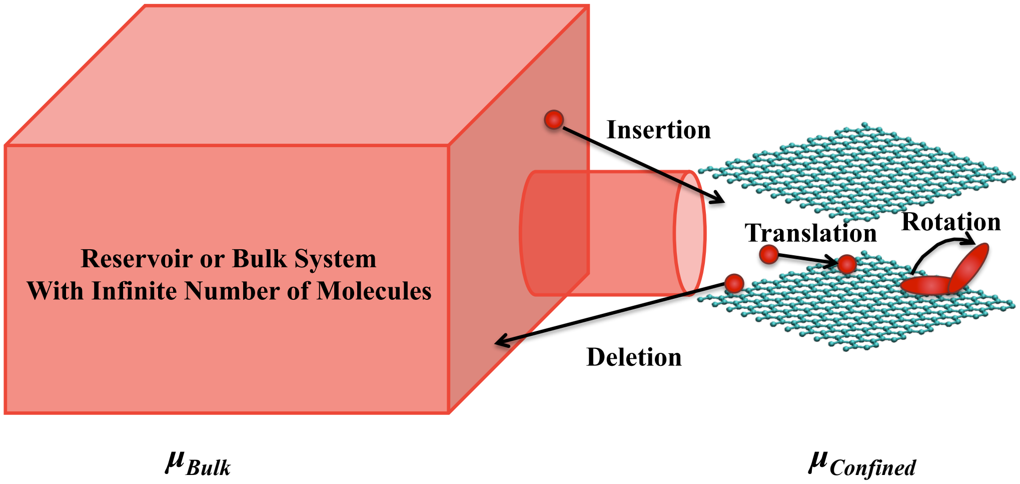

Figure 2-6 – Schematic of the GCMC simulation.

To understand the statistical basis for the Grand Canonical Monte Carlo technique, consider the system restricted in the dashed line where an ideal gas reservoir is in contact as shown in **Figure 2-7**.

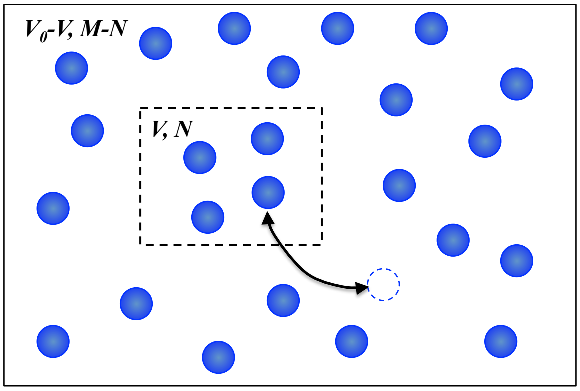

Figure 2-7 – An ideal gas (volume V_0-V, M-N particles) exchanges a particle with an N-particle system with volume V.

The total volume of the restricted system plus the reservoir is fixed at a value of V_0 and the total number of molecules is M. If the volume and the number of molecules in the restricted system equals V and N respectively, the volume accessible to the $M-N$ ideal gas is $V_0 - V$. The partition function of the restricted system is

$$Q(N,V,T)=\frac{1}{\Lambda^{3N}N!}\int_0^L \exp[-\beta U(\boldsymbol{q}^N)]\,\boldsymbol{dq}^N \quad \text{(2-39).}$$

Assuming that the system is contained in a cubic box with length $L=V^{1/3}$, the equation (2-39) can be rewritten in an $\boldsymbol{s}^N$scaled coordinate form

$$Q(N,V,T)=\frac{V^N}{\Lambda^{3N}N!}\int_0^1 \exp[-\beta U(\boldsymbol{s}^N;L)]\,\boldsymbol{ds}^N \quad \text{(2-40)}$$

where $\boldsymbol{q_i}=L\boldsymbol{s_i}$. Similar to the partition function of the system, the partition function of an ideal gas reservoir in a scaled coordinate form is

$$Q(M,N,V,V_0,T)=\frac{(V_0-V)^{M-N}}{\Lambda^{3(M-N)}(M-N)!}\int_0^1 \exp[-\beta U(\boldsymbol{s}^{M-N};L)]\,\boldsymbol{ds}^{M-N} \quad \text{(2-41).}$$

Note that for an ideal gas,

$$U^{id}(\boldsymbol{s}^{M-N};L)=0 \quad \text{(2-42).}$$

Equation (2-41) is reduced to

$$Q(M,N,V,V_0,T)=\frac{(V_0-V)^{M-N}}{\Lambda^{3(M-N)}(M-N)!}\int_0^1 \boldsymbol{ds}^{M-N} \quad \text{(2-43).}$$

The partition function of the total system (the restricted system plus the reservoir) is simply the product of the partition functions of the constituent subsystems

$$Q(M,N,V,V_0,T)=\frac{V^N}{\Lambda^{3N}N!}\int_0^1 \exp[-\beta U(\boldsymbol{s}^N;L)]\,\boldsymbol{ds}^N \times \frac{(V_0-V)^{M-N}}{\Lambda^{3(M-N)}(M-N)!}\int_0^1 \boldsymbol{ds}^{M-N}$$

$$Q(M,N,V,V_0,T)=\frac{V^N(V_0-V)^{M-N}}{\Lambda^{3M}N!(M-N)!}\int_0^1 \boldsymbol{ds}^{M-N}\int_0^1 \exp[-\beta U(\boldsymbol{s}^N;L)]\,\boldsymbol{ds}^N \quad \text{(2-44).}$$

Note that the integral over the $\boldsymbol{s}^{M-N}$ scaled coordinate of the ideal gas yields a value of 1.

Assuming that the molecules in the two subsystems are identical molecules, the only difference is that when the molecules are in the restricted system they interact, but they do not interact when they are in the reservoir. If a molecule, i, is transferred from a scaled coordinate, $\boldsymbol{s_i}$, in the reservoir to the same scaled coordinate in the restricted system, then the potential function changes from $U(\boldsymbol{s}^N;L)$ to $U(\boldsymbol{s}^{N+1};L)$. The expression for the total partition function of the system, including all possible distribution of M particles over the two subsystems, is

$$Q(M,V,V_0,T)=\sum_{N=0}^{M}\frac{V^N(V_0-V)^{M-N}}{\Lambda^{3M}N!(M-N)!}\int_0^1 \boldsymbol{ds}^{M-N}\int_0^1 \exp[-\beta U(\boldsymbol{s}^N;L)]\,\boldsymbol{ds}^N \quad \text{(2-45).}$$

Thus, the probability density to find a system with $M-N$ particles at reduced coordinates $\boldsymbol{s}^{M-N}$ in the reservoir and N particles at reduced coordinates $\boldsymbol{s}^N$ in the restricted system is

$$\mathcal{P}(\boldsymbol{s}^M; N) = \frac{V^N (V_0 - V)^{M-N}}{Q(M,V,V_0,T)\Lambda^{3M} N!(M-N)!} \exp[-\beta U(\boldsymbol{s}^N; L)] \tag{2-46}$$

Let us consider a trial move in which a particle is transferred from the reservoir to the same scaled coordinate in the restricted system. The probability of acceptance of the trial move is determined by the ratio of the corresponding probabilities

$$\alpha(N \to N+1) = \frac{\mathcal{P}(\boldsymbol{s}^M; N+1)}{\mathcal{P}(\boldsymbol{s}^M; N)} \tag{2-47a}$$

$$\alpha(N \to N+1) = \frac{\dfrac{V^{N+1}(V_0 - V)^{M-N-1}}{Q(M,V,V_0,T)\Lambda^{3M}(N+1)!(M-N-1)!} \exp[-\beta U(\boldsymbol{s}^{N+1}; L)]}{\dfrac{V^N (V_0 - V)^{M-N}}{Q(M,V,V_0,T)\Lambda^{3M} N!(M-N)!} \exp[-\beta U(\boldsymbol{s}^N; L)]} \tag{2-47b}$$

$$\alpha(N \to N+1) = \frac{V(M-N)}{(V_0 - V)(N+1)} \exp\left[-\beta[U(\boldsymbol{s}^{N+1}; L) - U(\boldsymbol{s}^N; L)]\right] \tag{2-47c}$$

and the probability of acceptance of the reverse move of the previous action is

$$\alpha(N+1 \to N) = \frac{(V_0 - V)(N+1)}{V(M-N)} \exp\left[-\beta[U(\boldsymbol{s}^N; L) - U(\boldsymbol{s}^{N+1}; L)]\right] \tag{2-48}$$

Now, let us assume that the ideal gas system or reservoir is much larger than the interacting system or $M \to \infty$, $(V_0 - V) \to \infty$, and $M/(V_0 - V) \to \rho$. Note that for an ideal gas, the chemical potential is related to the particle density, ρ, by

$$\mu = k_B T \ln \Lambda^3 \rho \tag{2-49}$$

Substituting μ and taking the limit $(M - N) \to \infty$ in equation (2-45), the partition function becomes

$$Q(\mu, V, T) = \sum_{N=0}^{\infty} \frac{\exp(\beta \mu N) V^N}{\Lambda^{3N} N!} \int_0^1 \exp[-\beta U(\boldsymbol{s}^N; L)]\, \boldsymbol{ds}^N \tag{2-50}$$

and the corresponding probability density is

$$\mathcal{P}_{\mu VT}(\boldsymbol{s}^N) \propto \frac{\exp(\beta \mu N) V^N}{\Lambda^{3N} N!} \exp[-\beta U(\boldsymbol{s}^N; L)] \tag{2-51}$$

As mentioned earlier, in this technique, there are four different types of move, which are insertion, translation, deletion, and rotation. Acceptance probability of each type of move can be described as follows.

a. Insertion of particles:

   A particle is inserted at a random position. The created particle is accepted with a probability.

$$\alpha(N \to N+1) = \frac{\mathcal{P}_{\mu VT}(N+1)}{\mathcal{P}_{\mu VT}(N)} \tag{2-52a}$$

$$\alpha(N \to N+1) = \frac{\frac{\exp(\beta\mu(N+1))V^{N+1}}{\Lambda^{3(N+1)}(N+1)!}\exp[-\beta U(N+1)]}{\frac{\exp(\beta\mu N)V^{N}}{\Lambda^{3N}N!}\exp[-\beta U(N)]} \tag{2-52b}$$

$$\alpha(N \to N+1) = \frac{V}{\Lambda^{3}(N+1)}\exp\big[\beta[\mu - U(N+1) + U(N)]\big] \tag{2-52c}$$

b. Displacement of particles:

A particle is selected and displaced at random. This action gives a new configuration, $\boldsymbol{s}'$. The move is accepted with a probability.

$$\alpha(\boldsymbol{s} \to \boldsymbol{s}') = \frac{\mathcal{P}_{\mu VT}(s\prime)}{\mathcal{P}_{\mu VT}(\boldsymbol{s})} \tag{2-53a}$$

$$\alpha(\boldsymbol{s} \to \boldsymbol{s}') = \frac{\frac{\exp(\beta\mu N)V^{N}}{\Lambda^{3N}N!}\exp[-\beta U(\boldsymbol{s}'^{N})]}{\frac{\exp(\beta\mu N)V^{N}}{\Lambda^{3N}N!}\exp[-\beta U(\boldsymbol{s}^{N})]} \tag{2-53b}$$

$$\alpha(\boldsymbol{s} \to \boldsymbol{s}') = \exp\big[-\beta[U(\boldsymbol{s}'^{N}) - U(\boldsymbol{s}^{N})]\big] \tag{2-53c}$$

c. Removal of particles:

A randomly selected particle is removed. The removal of the particle is accepted with a probability.

$$\alpha(N \to N-1) = \frac{\mathcal{P}_{\mu VT}(N-1)}{\mathcal{P}_{\mu VT}(N)} \tag{2-54a}$$

$$\alpha(N \to N-1) = \frac{\frac{\exp(\beta\mu(N-1))V^{N-1}}{\Lambda^{3(N-1)}(N-1)!}\exp[-\beta U(N-1)]}{\frac{\exp(\beta\mu N)V^{N}}{\Lambda^{3N}N!}\exp[-\beta U(N)]} \tag{2-54b}$$

$$\alpha(N \to N-1) = \frac{\Lambda^{3}N}{V}\exp\big[-\beta[\mu + U(N-1) - U(N)]\big] \tag{2-54c}$$

d. Rotation of particles:

A particle is selected and rotated at random. This action gives a new configuration, $\boldsymbol{s}'$. Similar to the displacement of the particles, the move is accepted with a probability.

$$\alpha(\boldsymbol{s} \to \boldsymbol{s}') = \exp\big[-\beta[U(\boldsymbol{s}'^{N}) - U(\boldsymbol{s}^{N})]\big] \tag{2-53c}$$

The procedures of the Grand Canonical Monte Carlo simulations can be summarized as illustrated in **Figure 2-8**.

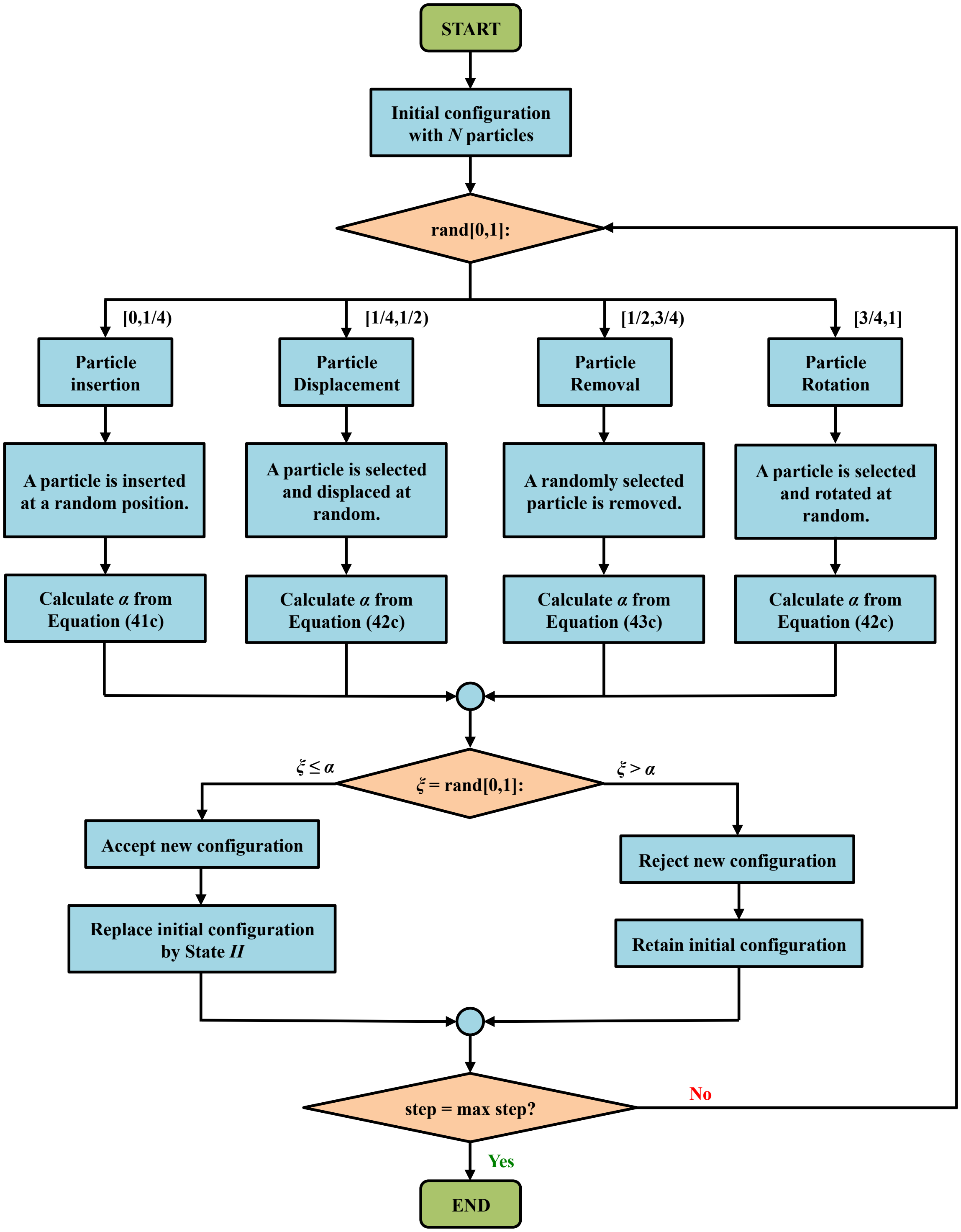

Figure 2-8 – Procedures of the GCMC simulation.

Note that in the experiment setup, the pressure, rather than the chemical potential of the reservoir is usually fixed. Similarly, in the Grand Canonical Monte Carlo simulation, the pressure of the reservoir is an input instead of the chemical potential. Recall that

$$\mu = k_B T \ln \Lambda^3 \rho \qquad \text{(2-49).}$$

Therefore,

$$\exp(\beta\mu) = \Lambda^3 \rho = \Lambda^3 \frac{M}{(V_0 - V)} \qquad \text{(2-55).}$$

From ideal gas law,

$$p_{id,gas}(V_0 - V) = \frac{M}{N_A} RT = M k_B T \qquad \text{(2-56).}$$

Equation (2-55) can be rewritten as

$$\exp(\beta\mu) = \frac{\Lambda^3 p_{id,gas}}{k_B T} = \Lambda^3 \beta p_{id,gas} \qquad \text{(2-57).}$$

Substituting this into equations (2-52) and (2-54), the acceptance probability of the creation in terms of the pressure in the reservoir, is

$$\alpha(N \to N+1) = \frac{V\beta p_{id,gas}}{(N+1)} \exp\left[-\beta[U(N+1) - U(N)]\right] \qquad \text{(2-58)}$$

and the probability of acceptance of the removal in term of the pressure in the reservoir is

$$\alpha(N \to N-1) = \frac{N}{V\beta p_{id,gas}} \exp\left[-\beta[U(N-1) - U(N)]\right] \qquad \text{(2-59).}$$

If the pressure in the reservoir is too high for the ideal gas law to hold, the $p_{id,gas}$ in the acceptance rule should be replaced by fugacity as shown:

$$fug = p/\phi_f \qquad \text{(2-60)}$$

where ϕ_f is the fugacity coefficient of the fluid in the reservoir, which can be computed directly from the equation of the state of vapor in the reservoir.

2.2 Fugacity Calculation

In the previous section, we introduced the GCMC simulation technique to determine fluid density in a confined system. The probabilities of acceptance for the insertion and deletion moves of the simulation are a function of the chemical potential (see equations (2.52c) and (2.54c)) that is directly related to fugacity. The pressure and the fugacity are only the same at very minimal pressure when the gas behaves like an ideal gas. However, for real gases, the fugacity can deviate considerably from the pressure. Especially at reservoir condition, the pressure is normally too high to treat the reservoir fluid as an ideal gas. Therefore, the fugacity calculation is necessary for this research.

From equation (2-60), the gas pressure and fugacity are related through the dimensionless fugacity coefficient, ϕ. In this section, we will show a derivation of the fugacity coefficient for the Peng-Robinson equation.

Fugacity is a measure of the nonideality of a gas. The molar Gibbs energy of an ideal gas is given by

$$\bar{G}(T,p) = G^{\circ}(T) + RT\ln\frac{p}{p^{\circ}} \quad \text{.........(2-61)}$$

where p° is equal to 1 bar, and $G^{\circ}(T)$ is called the standard molar Gibbs energy. Similar to an ideal gas, we can write the molar Gibbs energy of a real gas in terms of fugacity as the following:

$$\bar{G}(T,p) = G^{\circ}(T) + RT\ln\frac{fug(T,p)}{fug^{\circ}} \quad \text{.........(2-62).}$$

The nonideality is buried in $fug(T,p)$. Because all gases behave ideally as $p \to 0$, fugacity must have the property that $fug(T,p) \to p$ as $p \to 0$ so that equation (2-62) reduces to equation (2-61).

Note that the standard molar Gibbs energy, $G^{\circ}(T)$, is taken to be the same quantity in equations (2-61) and (2-62). The standard state in equation (2-61) is the ideal gas at 1 bar, so this must be the standard state in equation (2-62) as well. Thus, the standard state of the real gas in equation (2-62) is taken to be the corresponding ideal gas at 1 bar. This choice of standard state leads to a procedure to calculate $fug(T,p)$ at any pressure and temperature.

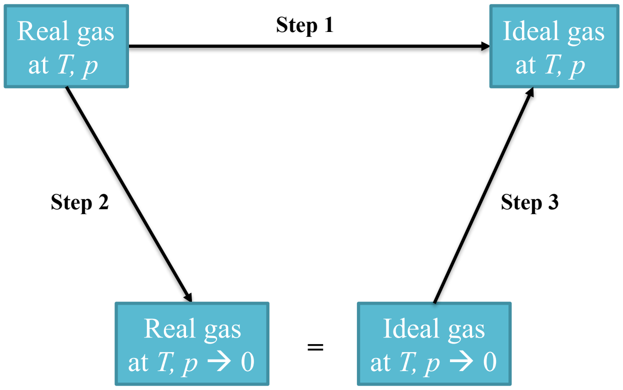

Figure 2-9 – The scheme used to relate the fugacity of a gas to its standard state (ideal gas) at *p* = 1 bar and the *T* of interest.

Figure 2-9 illustrates the difference in molar Gibbs energy between a real gas at p and T and an ideal gas at p and T. We can calculate this difference by starting with the real gas at p and T and then calculating the change in Gibbs energy when the pressure is reduced to zero (step 2), where the gas behaves ideally. Then we calculate the change in Gibbs energy as we compress the gas back to pressure p, but taking the gas to behave ideally (step3). The sum of step 2 and step 3 will be the difference in Gibbs energy of a real gas at p and T and an ideal gas at p and T (step 1):

$$\Delta\bar{G}_1 = \bar{G}^{id,gas}(T,p) - \bar{G}(T,p) \quad \text{(2-63).}$$

Substituting equations (2-61) and (2-62) in to equation (2-63), we have

$$\Delta\bar{G}_1 = G^{\circ}(T) + RT\ln\frac{p}{p^{\circ}} - G^{\circ}(T) + RT\ln\frac{fug(T,p)}{fug^{\circ}} \quad \text{(2-64a)}$$

$$\Delta\bar{G}_1 = RT\ln\frac{p}{p^{\circ}} - RT\ln\frac{fug(T,p)}{fug^{\circ}} \quad \text{(2-64b).}$$

The standard state of the real gas has been chosen such that $fug^{\circ} = p^{\circ} = 1$ bar, therefore

$$\Delta\bar{G}_1 = RT\ln\frac{p}{fug(T,p)} \quad \text{(2-65).}$$

From the definition of the Gibbs energy and Maxwell relations, we have

$$\left(\frac{\partial\bar{G}}{\partial p}\right)_T = \bar{V} \quad \text{(2-65).}$$

Thus,

$$\Delta\bar{G}_2 = \int_p^{p\to 0} dG = \int_p^{p\to 0} \bar{V}\,dp' \quad \text{(2-66)}$$

and

$$\Delta\bar{G}_3 = \int_{p\to 0}^{p} dG = \int_{p\to 0}^{p} \bar{V}^{id,gas}\ dp' \quad \text{(2-67a)}$$

$$\Delta\bar{G}_3 = \int_{p\to 0}^{p} \frac{RT}{p\prime}\ dp' \quad \text{(2-67b).}$$

Combining Equations (2-66) and (2-67b), we obtain

$$\Delta\bar{G}_1 = \Delta\bar{G}_2 + \Delta\bar{G}_3 = \int_{p\to 0}^{p}\left(\frac{RT}{p'} - \bar{V}\right)dp' \quad \text{(2-68).}$$

Equating this expression for $\Delta\bar{G}_1$ to $\Delta\bar{G}_1$ in equation (2-65), we have

$$RT\ln\frac{p}{fug(T,p)} = \int_{p\to 0}^{p}\left(\frac{RT}{p'} - \bar{V}\right)dp' \quad \text{(2-69a)}$$

$$\ln\frac{fug(T,p)}{p} = \int_0^p\left(\frac{\bar{V}}{RT} - \frac{1}{p'}\right)dp' \quad \text{(2-69b).}$$

Substituting the definition of ϕ from Equation (2-60) into equation (2-69b), we get

$$\ln \phi_f = \int_0^p \left(\frac{\bar{V}}{RT} - \frac{1}{p'}\right) dp' \quad \text{......(2-70).}$$

By introducing the compressibility factor,

$$Z = \frac{p\bar{V}}{RT} \quad \text{......(2-71)}$$

Equation (2-70) can be rewritten as

$$\ln \phi_f = \int_0^p \left(\frac{Z-1}{p'}\right) dp' \quad \text{......(2-72).}$$

In application, ρ is a more convenient variable than $\bar{V}$, and equation (2-71) can be written in an alternative form:

$$p = Z\rho RT \quad \text{......(2-73).}$$

For constant T, differentiation gives:

$$dp = RT(Zd\rho + \rho dZ) \quad \text{......(2-74a)}$$

$$dp = Z\rho RT\,\frac{(Zd\rho + \rho dZ)}{Z\rho} \quad \text{......(2-74b)}$$

$$\frac{dp}{p} = \frac{d\rho}{\rho} + \frac{dZ}{Z} \quad \text{......(2-74c).}$$

Substituting equation (2-74c) into equation (2-72), we have

$$\ln \phi_f = \int_0^\rho \frac{(Z-1)}{\rho} d\rho + \int_1^Z \frac{(Z-1)}{Z} dZ \quad \text{......(2-75a)}$$

$$\ln \phi_f = \int_0^\rho \frac{(Z-1)}{\rho} d\rho + \int_1^Z 1\, dZ - \int_1^Z \frac{1}{Z} dZ \quad \text{......(2-75b)}$$

$$\ln \phi_f = \int_0^\rho \frac{(Z-1)}{\rho} d\rho + Z - 1 - \ln Z \quad \text{......(2-75c)}$$

Recall Peng-Robinson equation of state:

$$p = \frac{RT}{\bar{V}-b} - \frac{a(T)}{\bar{V}^2+2b\bar{V}-b^2} \quad \text{......(2-76)}$$

where $a(T) = 0.45724\,\frac{(RT_c)^2}{p_c} \times \left[1 + m\left(1 - \sqrt{T_r}\right)\right]^2$, $b = 0.07780\,\frac{RT_c}{p_c}$, $T_r = \frac{T}{T_c}$, and $m = 0.37464 + 1.54226\omega - 0.26992\omega^2$. Therefore, the compressibility factor, Z, for the Peng-Robinson equation is

$$Z = \left(\frac{RT}{\bar{V}-b} - \frac{a(T)}{\bar{V}^2+2b\bar{V}-b^2}\right)\frac{\bar{V}}{RT} \quad \text{......(2-77a)}$$

$$Z = \frac{\bar{V}}{\bar{V}-b} - \left(\frac{a(T)\bar{V}}{RT\bar{V}^2}\right)\left(\frac{1}{1+\frac{2b}{\bar{V}}-\left(\frac{b}{\bar{V}}\right)^2}\right) \qquad \text{(2-77b).}$$

Let $\bar{V} = 1/\rho$ into Equation (2.77b), thus

$$Z = \frac{1}{1-b\rho} - \left(\frac{a(T)\rho}{RT}\right)\left(\frac{1}{1+2b\rho-b^2\rho^2}\right) \qquad \text{(2-78a)}$$

$$Z = \frac{1}{1-b\rho} - \left(\frac{a(T)}{bRT}\right)\left(\frac{b\rho}{\left(1+\left(1+\sqrt{2}\right)b\rho\right)\left(1+\left(1-\sqrt{2}\right)b\rho\right)}\right) \qquad \text{(2-78b).}$$

The quantity needed for evaluation of the integrals in equation (2-75c), $Z-1$, is readily found from this equation:

$$Z - 1 = \frac{b\rho}{1-b\rho} - \left(\frac{a(T)}{bRT}\right)\left(\frac{b\rho}{\left(1+\left(1+\sqrt{2}\right)b\rho\right)\left(1+\left(1-\sqrt{2}\right)b\rho\right)}\right) \qquad \text{(2-79).}$$

The integral of equation (2-75c) is evaluated as follows:

$$\int_0^\rho \frac{(Z-1)}{\rho}d\rho = \int_0^\rho \frac{b\rho}{1-b\rho}\frac{d(b\rho)}{b\rho} - \left(\frac{a(T)}{bRT}\right)\int_0^\rho \frac{d(b\rho)}{\left(1+\left(1+\sqrt{2}\right)b\rho\right)\left(1+\left(1-\sqrt{2}\right)b\rho\right)} \qquad \text{(2-80).}$$

Finally, it yields (Smith et al. 2005)

$$\int_0^\rho \frac{(Z-1)}{\rho}d\rho = -\ln(1-b\rho) - \left(\frac{a(T)}{bRT}\right)\frac{1}{2\sqrt{2}}\ln\left(\frac{1+\left(1+\sqrt{2}\right)b\rho}{1+\left(1-\sqrt{2}\right)b\rho}\right) \qquad \text{(2-81).}$$

Thus, equation (2-75) can be rewritten as

$$\ln\phi_f = -\ln(1-b\rho) - \left(\frac{a(T)}{bRT}\right)\frac{1}{2\sqrt{2}}\ln\left(\frac{1+\left(1+\sqrt{2}\right)b\rho}{1+\left(1-\sqrt{2}\right)b\rho}\right) + Z - 1 - \ln Z \qquad \text{(2-82).}$$

Let $A = \frac{a(T)p}{(RT)^2}$, and $B = \frac{bp}{RT}$, an alternative form of equation (2-82) is

$$\ln\phi_f = -\ln\left(1-\frac{BRT\rho}{p}\right) - \frac{A}{B}\frac{1}{2\sqrt{2}}\ln\left(\frac{1+\left(1+\sqrt{2}\right)\frac{BRT\rho}{p}}{1+\left(1-\sqrt{2}\right)\frac{BRT\rho}{p}}\right) + Z - 1 - \ln Z \qquad \text{(2-83a)}$$

$$\ln\phi_f = -\ln\left(1-\frac{B}{Z}\right) - \frac{A}{B}\frac{1}{2\sqrt{2}}\ln\left(\frac{1+\left(1+\sqrt{2}\right)\frac{B}{Z}}{1+\left(1-\sqrt{2}\right)\frac{B}{Z}}\right) + Z - 1 - \ln Z \qquad \text{(2-83b)}$$

$$\ln\phi_f = -\ln(Z-B) - \frac{1}{2\sqrt{2}}\frac{A}{B}\ln\left(\frac{Z+\left(1+\sqrt{2}\right)B}{Z+\left(1-\sqrt{2}\right)B}\right) + Z - 1 \qquad \text{(2-83c).}$$

Finally, the expression to calculate the fugacity coefficient is

$$\phi_f = \exp\left(-\ln(Z-B) - \frac{1}{2\sqrt{2}}\frac{A}{B}\ln\left(\frac{Z+\left(1+\sqrt{2}\right)B}{Z+\left(1-\sqrt{2}\right)B}\right) + Z - 1\right) \qquad \text{(2-84).}$$

Compressibility, Z, in this expression can be determined by solving the following cubic equation:

$$Z^3 + (1-B)Z^2 + (A-3B^2-2B)Z + (-AB+B^2+B^3) = 0 \qquad \text{(2-85).}$$

A procedure for fugacity calculation for a pure component fluid using Peng-Robinson equation of state is illustrated as **Figure 2-10**.

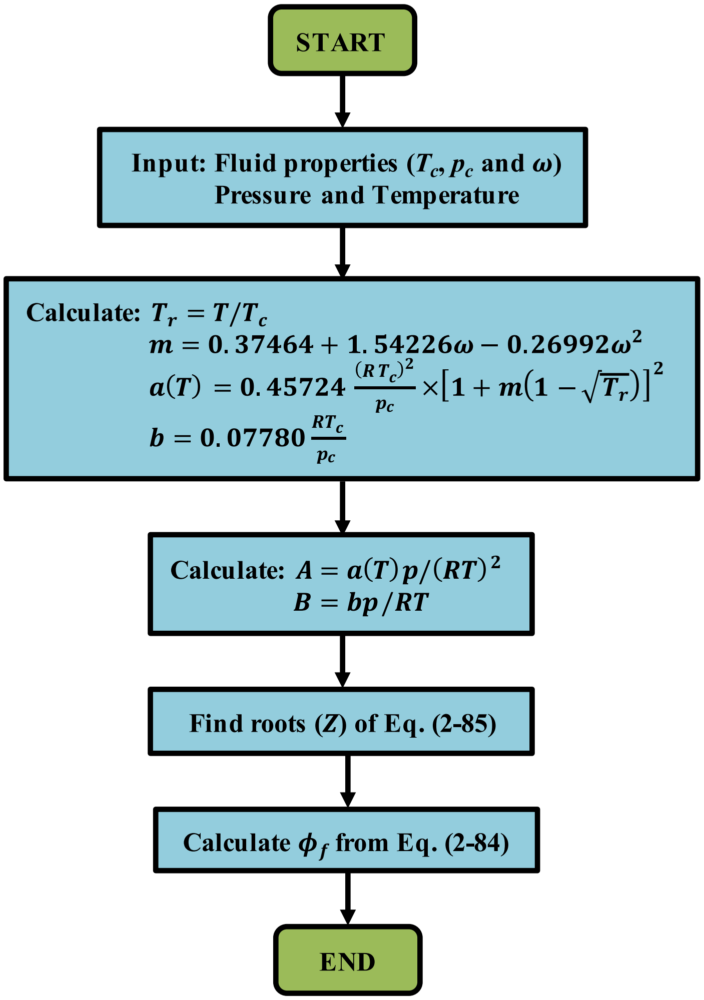

Figure 2-10 – A procedure for fugacity calculation for a pure component fluid using Peng-Robinson equation of state.

For mixture system, we can still use equation (2-85) to determine compressibility of the fluid. However, mixing rules must be applied to compute A and B:

$$A = \sum_{i=1}^{C}\sum_{j=1}^{C} x_i x_j A_{ij} \quad \text{(2-86a)}$$

$$B = \sum_{i=1}^{C} x_i B_i \quad \text{(2-86b)}.$$

where $A_{ij} = (A_i A_j)^{0.5}(1 - k_{ij})$ and k_{ij} is the binary interaction parameter. After the compressibility of the mixture is obtained, we can compute the fugacity of the system using equation (2-84). A procedure for fugacity calculation for a mixture using Peng-Robinson equation of state is illustrated as **Figure 2-11**.

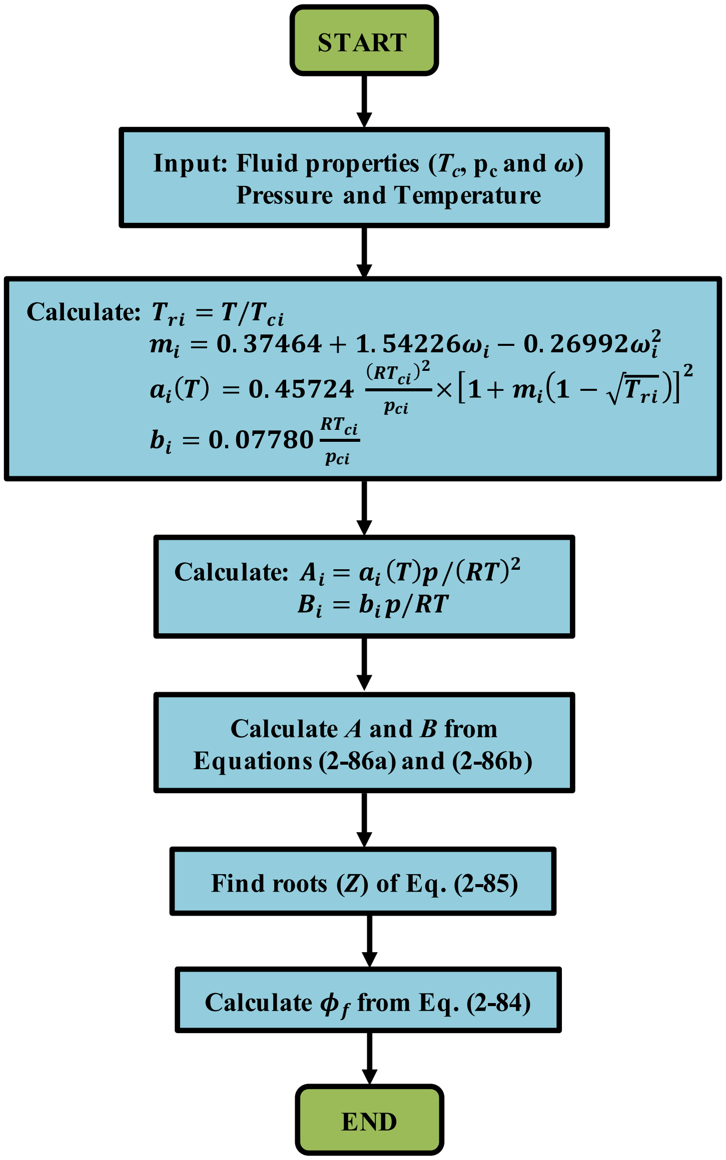

Figure 2-11 – A procedure for fugacity calculation for a mixture using Peng-Robinson equation of state.

In our work, we study fluid behavior and changes of PVT properties of fluid systems comprised of hydrocarbons (i.e. methane, ethane, propane, butane, pentane, and hexane), and water. Fluid property parameters used for fugacity calculation are summarized in **Table 2-1**.

Table 2-1 – Fluid property parameters used for fugacity calculation.

Fluid type	Critical temperature (T_c)	Critical pressure (p_c)	ω
Methane (CH_4)	190.45 K	4600 kPa	0.011
Ethane (C_2H_6)	305.30 K	4884 kPa	0.099
Propane (C_3H_8)	369.80 K	4250 kPa	0.153
Butane (C_4H_{10})	425.20 K	3796 kPa	0.199
Pentane (C_5H_{12})	469.70 K	3369 kPa	0.249
Hexane (C_6H_{12})	507.40 K	3012 kPa	0.305
Water (H_2O)	647.30 K	22120 kPa	0.344

Binary interaction parameters used for the fugacity calculation of a mixture system in our study are summarized in **Table 2-2 (**Li, Jin et al. 2014).

Table 2-2 – Binary interaction parameters used for fugacity calculation for mixture systems.

	CH_4	C_2H_6	C_3H_8	C_4H_{10}	C_5H_{12}	C_6H_{12}
CH_4	–	–	–	–	–	–
C_2H_6	0.005	–	–	–	–	–
C_3H_8	*	*	–	–	–	–
C_4H_{10}	0.0035	*	*	–	–	–
C_5H_{12}	*	*	*	*	–	–
C_6H_{12}	0.0037	*	*	0	*	–
H_2O	0	*	*	*	*	*

** We do not include those components in our mixture system.*

2.3 Intermolecular Forces

Intermolecular forces are forces that describe the interactions between molecules. Based on Coulomb's law, the force between two charged particles z_1e and z_2e separated by a distance is given by

$$f(r) = -\frac{z_1 z_2 e^2}{r^2} \quad \text{(2-87)}$$

and the Coulomb's potential is

$$U(r) = \frac{z_1 z_2 e^2}{r} \quad \text{(2-88).}$$

If the charges of the two particles are alike, positive and positive or negative and negative, the force will be repulsive. On the other hand, if the charges of the two particles are opposite, positive and negative, the force will be attractive. According to Coulomb's law, the electrostatic force between an ion and an uncharged particle (ze = 0) should be zero. However, Coulomb's law assumes that the two particles are point charges having zero radii. In actuality, a real particle such as an atom or a molecule occupies a finite volume of space. It is possible that the spatial distribution of the electron cloud representing the valence electrons might be asymmetrical, giving rise to an electric dipole moment. There are three kinds of dipole moments:

a. Permanent dipole moments can arise when bonding occurs between elements having different electronegativities. For instance, one atom attracts electrons more than another and becomes more negative whereas the other atom becomes more positive. A molecule with a permanent dipole moment is called a polar molecule.

b. Induced dipole moments occur when an external electric field distorts the electron cloud of a neutral molecule.

c. Instantaneous dipole moments occur due to chance when electrons in a neutral molecule happen to be more concentrated in one place than another creating a temporary dipole.

Depending on its strength, intermolecular forces cause a forming of three physical states: solid, liquid and gas. The various types of interactions are classified as follows:

a. Ion – ion interaction

b. Ion – permanent dipole interactions

c. Ion – induced dipole interactions

d. Permanent dipole – permanent dipole interactions

e. Permanent dipole – induced dipole interactions

f. London Dispersion forces

In this study, our system does not contain any ionic molecules. Therefore, we focus on only permanent dipole – permanent dipole interactions, permanent dipole – induced dipole interactions, and dispersion forces.

2.3.1 Permanent Dipole – Permanent Dipole Interactions

In physics, an electric dipole refers to a separation of electric charge. An idealized electric dipole consists of two-point charges of magnitude $+q_e$ and $-q_e$ separated by a distance r. Although the overall molecule is neutral, the charge separation can cause an electrostatic effect. The electric dipole moment, $\boldsymbol{\mu_e}$, of a molecule with two point charges is:

$$\boldsymbol{\mu_e} = q_e\boldsymbol{d_q} \tag{2-89}$$

where $\boldsymbol{d_q}$ is the displacement vector pointing from the negative charge to the positive change. Thus, the electric dipole moment is a vector pointing from the negative charge to the positive change.

The most well-known molecule having a dipole moment is water. The charge imbalance occurs because oxygen pulls the electron cloud that comprises each O-H bond toward itself as shown in **Figure 2-12**. These two bond moments add to produce the permanent dipole moment (a vector pointing from the negative charge to the positive change) denoted by a solid green arrow.

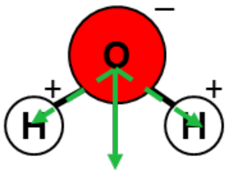

Figure 2-12 – Dipole moment of a water molecule.

When an electric dipole is subjected to an external electric field, it will tend to orient itself so as to minimize the potential energy. Thus, its negative end will point toward the higher electric potential (more positive). An example of water molecule orientations is illustrated in **Figure 2-13**.

For the case that the partially positive area of one molecule interacts only with the partially negative area of the other molecule (see **Figure 2-14a**), the potential energy is given by

$$U(r) = -\frac{2\mu_{e1}\mu_{e2}}{r^3} \quad \text{(2-90).}$$

If the molecular dipoles do not interact in this straight end to end, then we have to account mathematically for the change in potential energy due to the angle between the dipoles (see **Figure 2-14b**). We can add an angular term to equation (2-90) to account for this new parameter of the system:

$$U(r) = -\frac{\mu_{e1}\mu_{e2}}{r^3}\left(\cos\theta_{12} - 3\cos\theta_1\cos\theta_2\right) \quad \text{(2-91).}$$

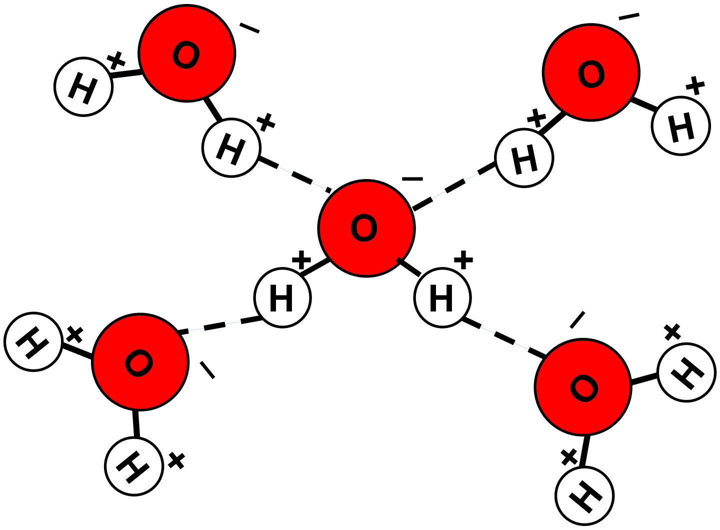

Figure 2-13 – Water molecule orientations (its negative end will point toward the higher electric potential (more positive)).

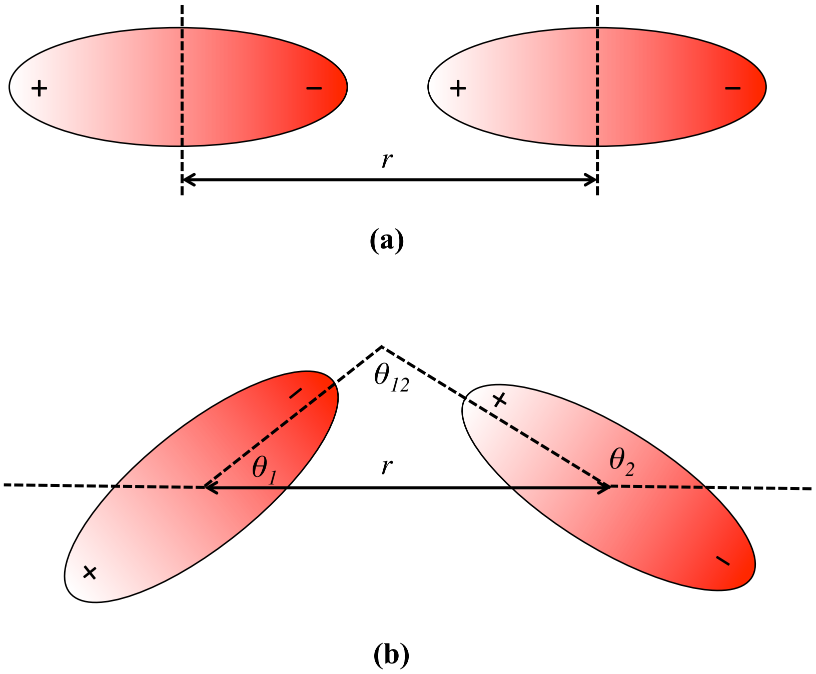

Figure 2-14 – Schematics for permanent dipole – permanent dipole interactions.

Equations (2-90) and (2-91) give the instantaneous interaction energy of two particles. For a large number of particles, there is average interaction energy, $\langle U(r)\rangle$, that is obtained by averaging the interaction potential at a fixed r over all possible orientations of the two interacting particles. At each orientation, the potential must be weighted by the Boltzmann factor given by $\exp(-U(\theta_1,\theta_2;r)/k_BT)$. For instance, the partially positive area of a molecular dipole being held next to the partially positive area of a second molecular dipole is a high potential energy configuration and few molecules in the system will have sufficient energy to adopt it at room temperature. In general, the high potential energy configurations can only be populated at evaluated temperature. Thus, the interactions of dipoles are not random, and instead adopt more probable, lower energy configuration. The following equation takes this into account:

$$\langle U(r)\rangle = -\frac{2}{3}\frac{\mu_{e1}^2\mu_{e2}^2}{k_BTr^6} \quad \text{(2-92).}$$

2.3.2 Permanent Dipole – Induced Dipole Interactions

Even if a molecule is neutral and possesses no permanent dipole moment, it can still be affected by an external electric field. Because all atoms and molecules are composed of charged particles (nuclei, and electrons), the electric field of a nearby particle can cause a shift of the centers of positive and negative charges in opposite directions. Therefore, a separation of charge may be induced in any molecule by another molecule that contains a permanent dipole moment.

Figure 2-15 illustrates a creation of an induced (temporary) dipole moment by an external electric field from a molecule having a permanent dipole moment. In **Figure 2-15a**, the distance between a polar molecule *A*, which contains a permanent dipole moment, and a nonpolar molecule *B* is too far for an electric field from the molecule *A* to cause a change in the molecule *B*. As molecule *A* and molecule *B* are moving toward each other, the electric field from molecule *A* becomes influential to electron movements in the molecule *B*. For instance, the negative end of the molecule *A* pushes the electrons in molecule *B* to the far side. The phenomenon creates an induced (temporary) dipole moment in molecule *B* as shown in **Figure 2-15b**. When molecule *B* moves away from molecule *A* to a point far beyond the effect of the electric field from molecule *A*, molecule *B* will turn back to a nonpolar molecule without a dipole moment as shown in **Figure 2-15c**.

The strength of induced dipole moment, $\mu_{induced}$, depends on the strength of the external electric field, E_f, from the polar molecule and the polarization, α_p, of the atom or molecule in which the dipole is induced.

$$\mu_{induced} = \alpha_p E_f \qquad \text{(2-93).}$$

Although the above discussion used a nonpolar molecule as the molecule without a permanent dipole moment, equation (2-93) implies to other situations as long as the second molecule has non-zero polarizability, an induced dipole moment can be produced in polar molecules. Thus, it is important to note that induced dipoles occur in molecules with or without an existing permanent dipole moment. The potential energy of two particles due to the permanent dipole – induced dipole interaction is given by:

$$U(r) = -\frac{\alpha_{p2}\mu_{e1}^2(3\cos^2\theta+1)}{2r^6} \qquad \text{(2-94)}$$

where θ is the angle between the permanent dipole and the inter-particle axis, α_{p2} is the polarizability of the nonpolar molecule, and μ_{e1} is the permanent dipole.

Equation (2-94) can be generalized to represent the total permanent dipole – induced dipole interaction potential between two polar molecules. Averaging those potential overall orientations of the two dipoles μ_{e1}, and μ_{e2}, and Boltzmann weighting gives:

$$\langle U(r)\rangle = -\frac{(\mu_{e1}^2\alpha_{p2}+\mu_{e2}^2\alpha_{p1})}{r^6} \qquad \text{(2-95).}$$

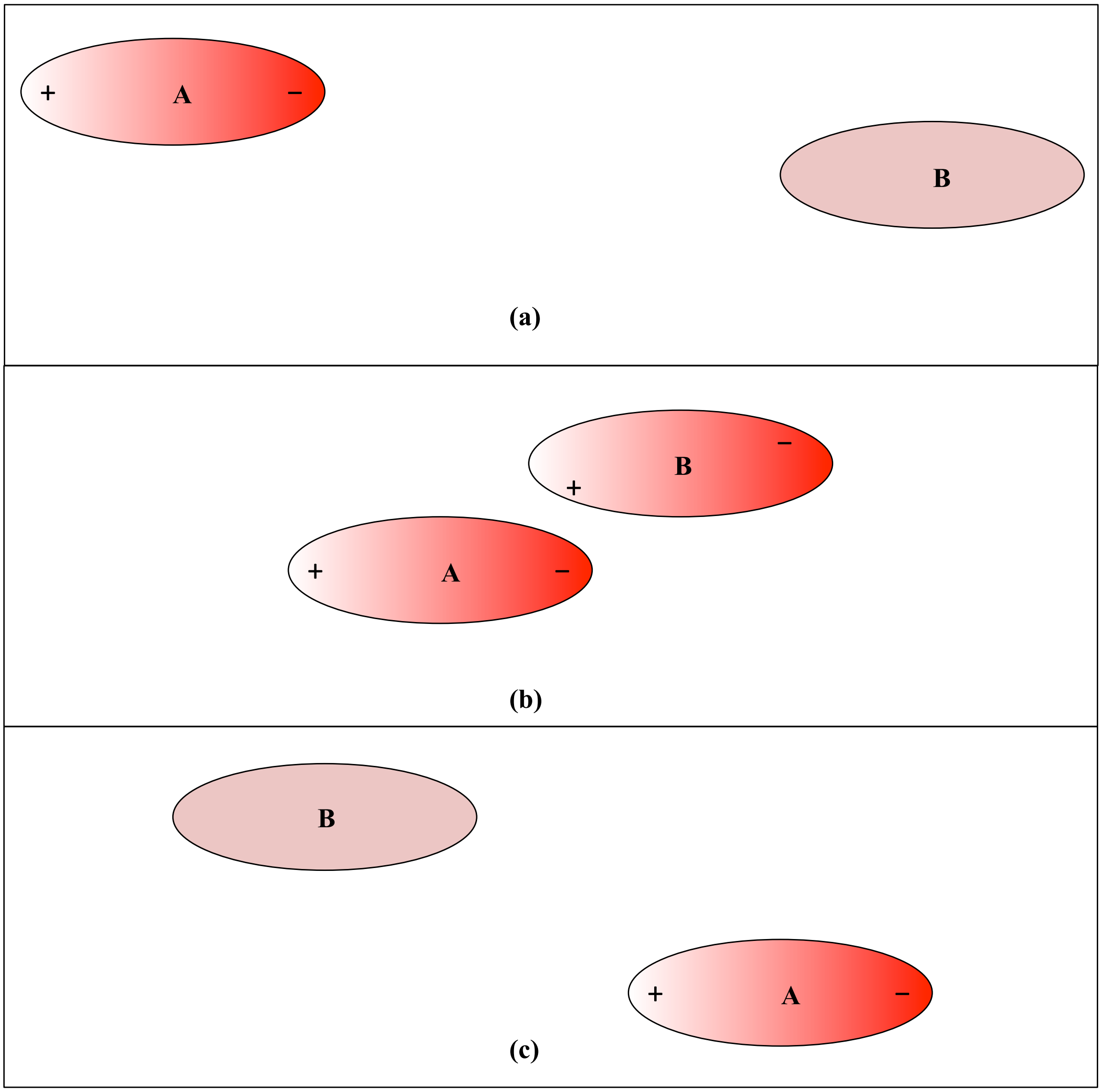

Figure 2-15 – A creation of an induced (temporary) dipole moment by an external electric field from a molecule having a permanent dipole moment.

2.3.3 London Dispersion Forces

Even if the net charge of a permanent dipole moment in a molecule equals zero, there still remains London dispersion forces. In contrast to the above, these forces cannot be explained by classical electrostatics. Although the time-averaged electron distribution of a nonpolar molecule is symmetric, fluctuations in the distribution can lead to a transient dipole moment, which can induce a dipole in a neighboring molecule. Consider what happens when two molecules approach each other, the electron clouds of each molecule tend to repel the other. The distortion of the electron cloud in molecules is proportional to the polarizability of the molecules. Once these transient dipoles are formed, they interact electrostatically with each other. This type of interaction, between atoms and molecules that do not possess a permanent dipole moment, is called a London dispersion force. An approximate expression of interacting energy due to London dispersion forces is:

$$U(r) = -\frac{3I_{p1}I_{p2}}{2(I_{p1}+I_{p2})}\frac{\alpha_{p1}\alpha_{p2}}{r^6} \quad \text{......(2-96)}$$

where I is the first ionization potential.

If the particles are neutral and only dipoles are considered, the total potential is a sum of the average permanent dipole – permanent dipole interaction in equation (2-92), the average permanent dipole – induced dipole interaction in equation (2-95), and the dispersion forces. For most cases, the dispersion contribution is the largest and is the only interaction when the particles are nonpolar (Steinfeld et al. 1989).

In this work, we mainly study the phase behavior and PVT properties of hydrocarbons that are nonpolar molecules. Thus, the London dispersion forces are the main contribution to the potential energy of our system. In the next section, we will introduce a model that we use to estimate the London dispersion interaction between two particles in our confined system.

2.4 Molecular Modeling

2.4.1 Building the Model System

Figure 2-16a illustrates an example of the Scanning Tunneling Microscopy (STM) image of Haynesville shale (Curtis et al. 2010). Shale reservoirs consist of inorganic (i.e. clay) and organic matter known as kerogen. Hydrocarbons are stored in the shale reservoirs in both the rock and kerogen pores. In this work, we focus only on kerogen pores. **Figure 2-16b** illustrates an example of 3D molecular structure of kerogen (Vandenbroucke 2003). It can be observed that the kerogen pore can be modeled in first approximation by a slit graphite pore. Here the slit pore model is constructed so that graphite-like crystallites are semi-infinite and composed of two-layer graphite slabs aligned parallel to one another and separated by a distance, H, as shown in **Figure 2-16c**. The value of the separation is varied from 1 nm to 10 nm. The dimensions of the graphite slabs are 42.53 Å × 41.90 Å.

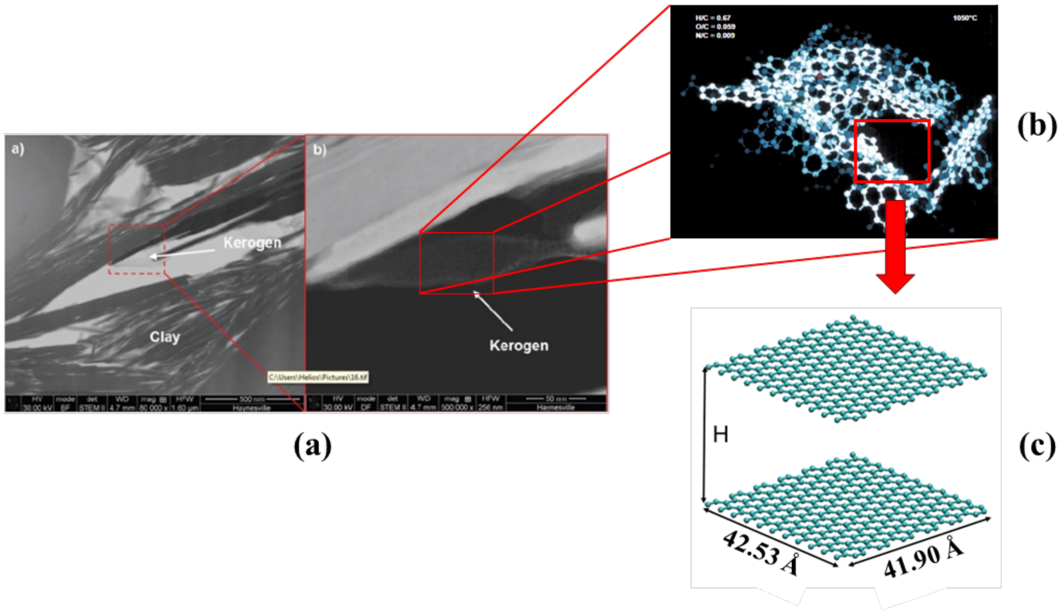

Figure 2-16 – (a) STM image of Haynesville shale (Curtis et al. 2010), (b) 3D molecular structure of kerogen (Vandenbroucke 2003), and (c) molecular model representing kerogen in shale reservoirs.

2.4.2 Periodic Boundary

Periodic boundary conditions are applied to extend the simulated system to a pore network and account for interactions between molecules at the edge of the system and molecules in the next periodic cell (identical to the simulated system) as shown in **Figure 2-17.**

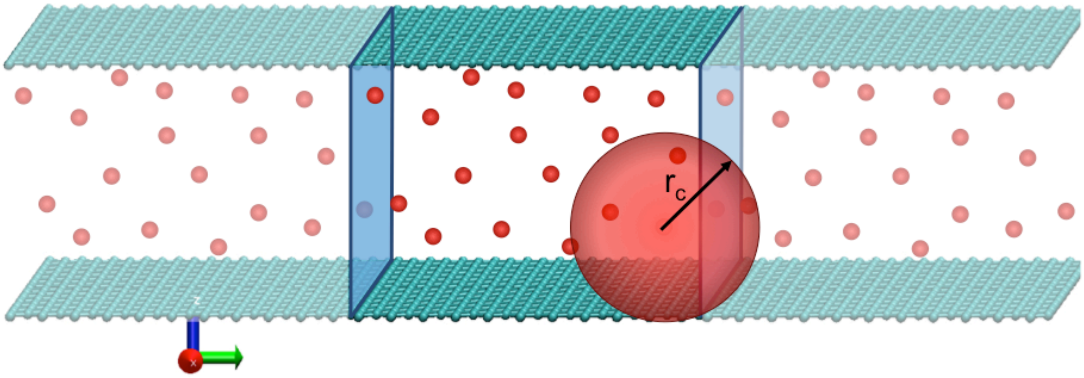

Figure 2-17 – Periodic boundary conditions are used to extend the simulated system to represent the kerogen pore network.

The cubic box is replicated throughout the space to form a pore network. During simulation, as a molecule moves in the original box, its periodic image in each of neighboring boxes moves in the same way. Therefore, as a molecule leaves the original box, one of its images will enter through the opposite side. There are no wall boundaries of the box and no surface molecules. Applying the periodic boundary, the number density in the central box (and hence the entire system) is conserved.

2.4.3 Force Fields

As mentioned in the previous section, both the trajectories of molecule particles in the system for classical Molecular Dynamics simulation and the acceptance probability of configurations in the Monte Carlo simulations are derived from a given force field. In molecular modeling, a force field is used to describe an interaction between two particles. In this study, the united-atom force field model is applied to methane and ethane. Methane is represented as one spherical particle and ethane is treated as one particle comprised of two spheres of methyl groups connected by a single bond of 1.54 Å. Meléndez-Pagán and Ben-Amotz (2000) reported that the change of C-C bond length of ethane molecule is approximately 0.0092 Å (0.5%) at 2.56 GPa (~371,000 psi), which is much higher than normal reservoir pressure. Thus, the bond length of the ethane molecule is kept constant for this study.

In this work, our confined system consists of graphene sheets, methane, and ethane molecules (nonpolar molecules). As a result, the system is dominated by van der Waal interactions that can be described by London Dispersion forces or instantaneous dipole-induced dipole forces. The London Dispersion force is a weak intermolecular force developing from quantum-induced, instantaneous polarization multipoles, or fluctuation of electron clouds in molecules. Therefore, they can act between molecules without permanent multipole moments. Lennard-Jones (LJ) potential is used to pronounce the potential energy of interaction between two non-bonding molecules in the system based on their distance of separation. The potential equation accounts for the difference between attractive forces and repulsive forces.

12-6 Lennard-Jones potential can be expressed as

$$U(r_{ij}) = \begin{cases} 4\epsilon_{ij}\left[\left(\frac{\sigma_{ij}}{r_{ij}}\right)^{12} - \left(\frac{\sigma_{ij}}{r_{ij}}\right)^{6}\right] & ; r_{ij} \leq r_c \\ 0 & ; r_{ij} > r_c \end{cases} \quad \text{.......................................(2-97).}$$

where ϵ_{ij} and σ_{ij} are the LJ potential parameters that characterize the molecular size and strength of the intermolecular interactions; r_{ij} is the distance between the centers of mass of the molecular pair; and r_c is the cut-off distance beyond which the interaction between the i and j molecules – assumed to be negligible. The minimum half-cell distance of the system is used as the r_c value. However, r_c should be equal to or greater than $5\times \max(\sigma_{ij})$, where the potential or interaction between the molecules becomes insignificant. In this study, the Optimized Potential for Liquid Simulations (OPLS) model (Jorgensen et al. 1984) is used for methane and ethane. The Lennard-Jones potential parameters of carbon atoms in graphite are from Kurniawen et al. (2006).

For long chain alkanes, we also used the united-atom force field model for methyl and methylene groups in the molecules. The lengths of the single bond between carbon atoms are kept constant at 1.54 Å because the amplitude of vibration is small compared to molecular dimensions. However, the bending motions, which change the angle between bonds, and the twisting motions, which alter the torsional angles are considered. The intramolecular forces corresponding to bond motions will be discussed in Chapter IV. The UNICEPP force field by Dunfield et al. (1978) is used to calculate interactions between long chain alkane molecules.

The model parameters of the like interaction are given in **Table 2-3**, whereas those for the unlike interaction are determined by the Lorentz-Berthelot combining rules:

$$\sigma_{ij} = \frac{\sigma_{ii}+\sigma_{jj}}{2} \quad \text{(2-98a)}$$

$$\epsilon_{ij} = \sqrt{\epsilon_{ii}\epsilon_{jj}} \quad \text{(2-98b).}$$

Table 2-3 – L-J potential parameters.

Pair interaction	σ_{ii}, Å	ϵ_{ii}/k, K
$CH_4 - CH_4$	3.730	148.0
$CH_3 - CH_3$ (for ethane)	3.775	104.1
$CH_3 - CH_3$ (for n-alkane)	3.790	90.6
$CH_2 - CH_2$ (for n-alkane)	3.960	70.5
C – C	3.400	28.0

An example of the potential map between two methane molecules derived from the 12-6 Lennard-Jones potential equation is shown as **Figure 2-18**. The potential equation consists of repulsive and attractive potential terms. The repulsive potential is in the order of 12 and has a positive sign, whereas the attractive potential is in the order of 6 and has a negative sign. Contributions of both repulsive and attractive potential energies to the total potential are illustrated as a red dashed line and a green dashed line in **Figure 2-18** respectively. The summation of both energies is the total potential energy and is illustrated as a solid brown line. A dashed orange line represents a cut-off radius where the repulsive and attractive forces almost cancel each other out. Observe that the total potential energy is very small, or the interaction between the two molecules is extremely weak beyond the cut-off distance. As a result, it is reasonable to assume that there is no interaction between the molecules beyond the cut-off distance (*I*). As molecules are brought closer to each other, the attractive potential becomes stronger and creates an attractive force between them (*II*). The attractive force brings the molecules even closer together until they reach the equilibrium separation at which their minimum potential is reached (*III*). At this point, the potential trough is used to determine ϵ_{ij}. To further reduce the distance between the two molecules, the repulsive force becomes stronger rapidly. The distance at which the total potential energy equals to zero is σ_{ij}. As the electron clouds of both molecules overlap, the repulsive force acts and pushes both molecules further apart. At this point, the force of repulsion is greater than the force of attraction (*IV*).

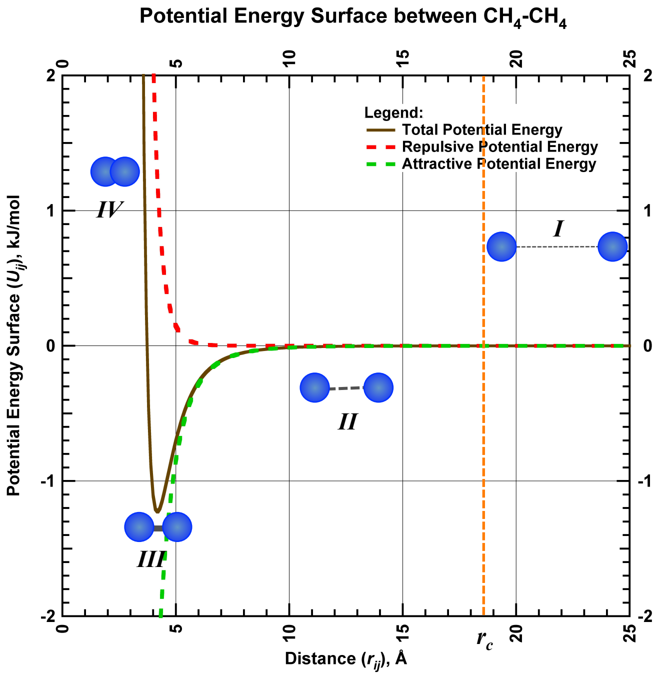

Figure 2-18 – Potential map between two methane molecules.

CHAPTER III

SIMULATION STUDIES OF CONFINED PURE SMALL MOLECULE HYDROCARBONS

In this chapter, we show the effect of confinement on pure methane and ethane using molecular simulations. The GCMC simulation is implemented to derive new phase diagrams for confined pure methane and ethane in different pore sizes. The critical properties of the confined fluid are obtained from the phase diagrams. Also, the GCMC simulation is used to observe the shifts in the confined fluid properties from the bulk density at the reservoir condition. The results emphasize the importance of this study because the deviation in the densities of the confined pure hydrocarbons in shale reservoirs from the bulk densities is significant. In addition, the classical MD simulation is employed to support our conclusion obtained from the GCMC simulation.

3.1 Analysis of Simulation Data

The GCMC simulation allows us to evaluate the equilibrium density of the confined fluid at given conditions of temperature and pressure. This density yields adsorption isotherms as a function of gas pressure. The adsorption is computed as the amount of molecules present in the unit cell (system) at equilibrium conditions – where the chemical potentials (of all phases for each component) of both the reservoir (bulk fluid) and the confined system are equal under given conditions of temperature and pressure.

$$\mu^{vapor}_{Bulk,CH_4}(T,p) = \mu^{vapor}_{Confined,CH_4} = \mu^{liquid}_{Confined,CH_4} \qquad \text{(3-1a)}$$

and

$$\mu^{vapor}_{Bulk,C_2H_6}(T,p) = \mu^{vapor}_{Confined,C_2H_6} = \mu^{liquid}_{Confined,C_2H_6} \qquad \text{(3-1b)}$$

To clarify the above expressions, let us suppose we have two systems: “bulk” and “pore”, each one at different state conditions (separated from each other). If we put them in contact with each other for example, the pore is exposed to the external bulk environment, the molecules will start moving from one system to the other and vice versa until a dynamic equilibrium is established. At that point, the temperature will be equal in both systems and the chemical potential of each species, i.e. methane and ethane, will be the same in both systems. (See for example in Smith et al. (2005))

Because of the effect of the interaction between fluid molecules and the surface wall, the fluid density in the bulk and the confined space may be different. Once the number of molecules per unit cell (n) is obtained from the GCMC simulations, the density can be computed using the following formula:

$$\rho_{Confined} = \frac{n \times MW}{N_A \times V_{Unit\ Cell}} \quad \text{(3-2)}$$

where MW is the molecular weight of the fluid, n is the number of molecules per unit cell, N_A is Avogadro's number, and $V_{Unit\ Cell}$ is the unit cell volume (excluding the volume occupied by the graphite slab). The calculated fluid density in the confined space is used to determine the critical point of a pure component. At $T < T_c$, a phase transition can be observed when there is an occurrence of a jump of fluid density (from vapor to liquid) while pressure increases. On the other hand, at $T \geq T_c$, the fluid density is a continuous function of pressure, and this phase is called a supercritical fluid. As a result, a tip of a phase envelope that contains a two-phase region may yield a critical point of a pure component.

3.2 Methane Adsorption Model Validation

The validation process involved generating methane adsorption isotherms in a 2.34 nm slit graphite pore. Avgul and Kiselev (1970) experimentally measured methane adsorption isotherms on graphited thermal carbon black were. These authors provided the isotherms at 113 K, 123 K, 133 K, and 143 K. The experimental data were reported in surface excess, Q, (mol/m^2). To be able to compare results from molecular simulations with the experimental data, the isotherms from the molecular simulations need to be converted to surface excess using the following expression:

$$Q\ (mol/m^2) = \frac{\rho_{Confined,CH_4}(mol/m^3) - \rho_{bulk,CH_4}(mol/m^3)}{2 \times Area_{Graphite}(m^2)} \times V_{Unit\ Cell}(m^3) \quad \text{(3-3)}$$

Figure 3-1 illustrates the surface excess versus pressure at 113 K, 123 K, 133 K and 143 K in a log-log plot. The experimental data are presented as square symbols whereas the results from the GCMC simulations are presented as solid lines. As can be seen, the simulation results and the experimental data agree well, thus validating the model used for the interactions between the fluid and the slit walls.

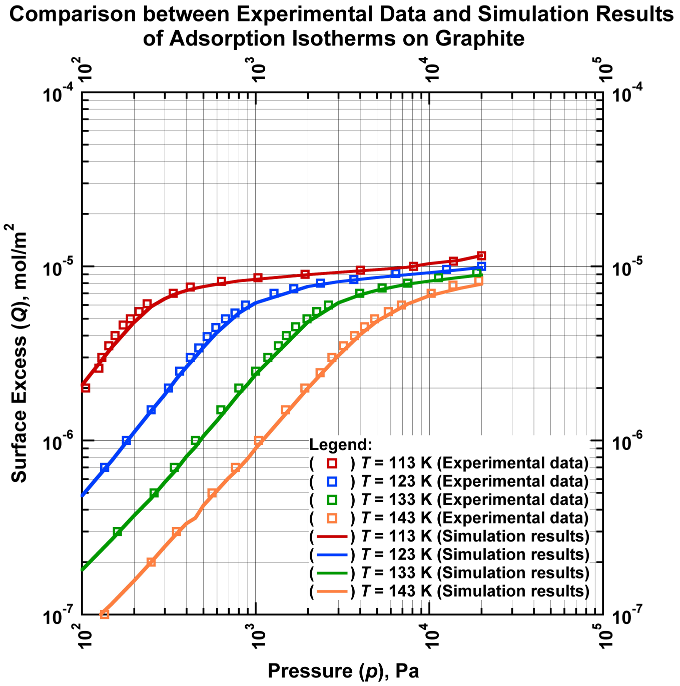

Figure 3-1 – Comparison between experimental data and simulation results of adsorption isotherms on graphite at *T* = 113K, 123K, 133K and 143K.

3.3 Phase Diagram and Critical Properties of Confined Pure Small Molecule Hydrocarbon

3.3.1 Methane

Figure 3-2 illustrates an example of a calculated phase diagram for confined methane in a 5.0 nm separation slit graphite pore, which represents kerogen in shale reservoirs. The GCMC simulations are performed to derive methane isotherms at different temperatures. At higher temperatures, the first-order phase transitions vanish at the critical points as pressure increases and the isotherm becomes a continuous function of pressure at supercritical conditions. On the other hand, at lower temperatures, a jump or discontinuity of the fluid density (from vapor to liquid) occurs while pressure increases. Such a jump is called a first-order phase transition. A phase envelope of the confined methane containing a two-phase region can be drawn by connecting points of vapor and liquid densities at vapor pressures for different temperatures as shown in a black envelope in **Figure 3-2**. The critical properties can be read from the tip of the envelope. In this case, the critical temperature and pressure of the confined methane in a 5.0 nm separation of a slit graphite pore are approximately 175 K or -144.7°F and 2450 kPa or 355 psi, respectively. These procedures are applied to determine the critical properties of confined methane in different pore sizes as summarized in **Table 3-1**. See Appendix A for calculated phase diagrams for confined methane in different pore sizes (1.0 nm – 7.0 nm).

According to the data in **Table 3-1**, it is noticeable that for the nanoscale pore size, the fluid's critical properties change with the pore size and become different from the bulk properties. This is because the interactions between the pore walls and the fluid molecules become significant and impact the behavior of the fluid molecules. The smaller the pore is, the lower both critical temperature and pressure of the confined methane are. At low pressure, with the same temperature, the confined methane is denser than the bulk fluid because the attractive potential of the surface wall allows fluid molecules to adhere to the walls of the confining system and also to interact strongly with each other. Consequently, the confined fluid condenses at a lower pressure than the bulk fluid does. This phenomenon may shift the phase envelope to lower critical temperature and pressure, and different critical density.

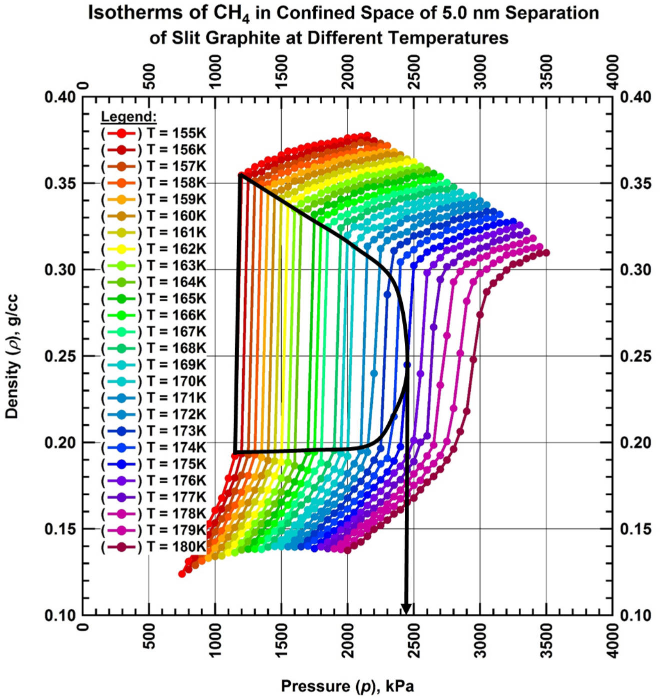

Figure 3-2 – Phase diagram of confined methane in 5.0 nm of separation of a slit graphite pore (representing kerogen in shale reservoir).

Table 3-1 – Critical properties of confined methane in different pore sizes.

Separation (H), nm	Critical temperature (T_c)	Critical pressure (p_c)
1.0	99 K or -281.5°F	4.0×10^{-4} kPa or 5.8×10^{-4} psi
2.0	127 K or -231.1°F	34 kPa or 5 psi
3.0	155 K or -180.7°F	610 kPa or 88 psi
4.0	169 K or -155.5°F	1625 kPa or 236 psi
5.0	175 K or -144.7°F	2450 kPa or 355 psi
6.0	178 K or -139.3°F	2950 kPa or 428 psi
7.0	181.5 K or -133.0°F	3550 kPa or 515 psi
Bulk Fluid	190.45 K or -116.9°F	4600 kPa or 667 psi

Figures 3-3a and **3-3b** are plots of the critical temperature and pressure of the confined methane versus pore size (separation between the two graphite layers representing the kerogen pore). It can be observed that when $H \leq 5.0$ nm, the critical properties decay rapidly due to the strong effect of the confinement. In addition, as the separation increases, those properties of the confined methane approach the bulk critical properties. Based on this indication, the effect of confinement on the fluid's behavior decreases when the pore size increases, as the fluid's properties become closer to the bulk properties.

These observations agree with the hypothesis that interaction between the wall of the container and the contained fluid becomes significant to the fluid's behavior and causes changes in the fluid's properties. However, this effect is negligible when the pore is adequately large. Consequently, for sufficiently large pores, the fluid can be treated as a bulk fluid.

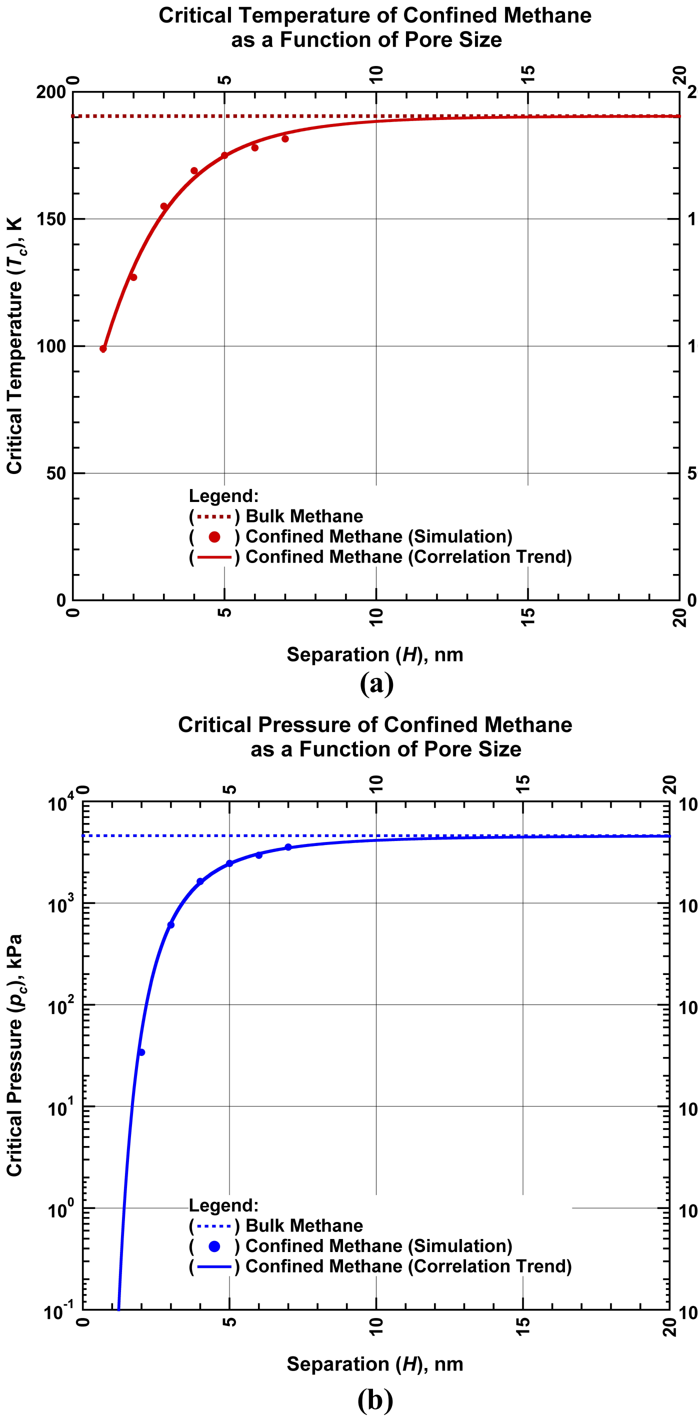

Figure 3-3 – (a) Plot of critical temperature and (b) critical pressure of confined methane versus separation of a slit graphite pore (representing kerogen in shale reservoir).

3.3.2 Ethane

The same method shown in the previous section is applied to obtain critical points of the confined ethane. **Figure 3-4** illustrates an example of the phase diagram of confined ethane in a 5.0 nm separation of a slit graphite pore. The phase envelope (black envelope) contains a two-phase region. The critical temperature and pressure of the confined ethane, read from the tip of the envelope, are approximately 292 K or 66.9°F and 2450 kPa or 355 psi, respectively. The critical properties of the confined ethane in different pore sizes are summarized in **Table 3-2**. See Appendix A for calculated phase diagrams for confined methane in different pore sizes (2.0 nm – 10.0 nm).

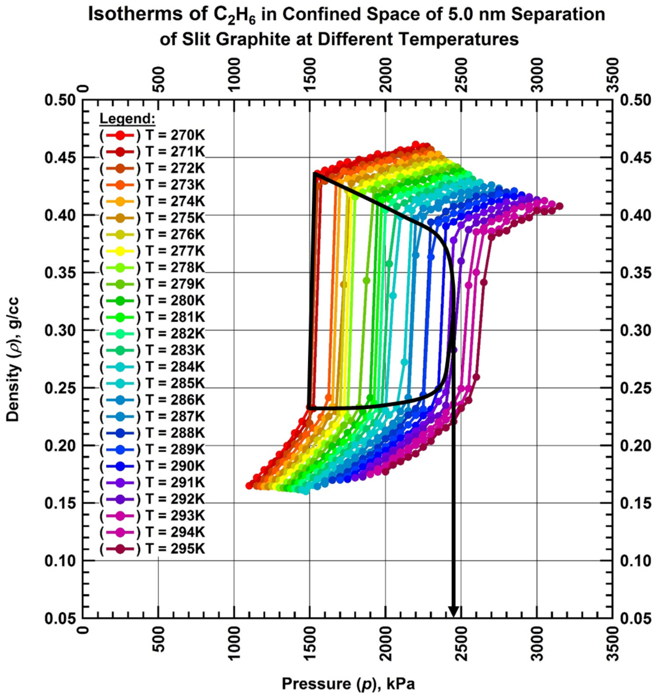

Figure 3-4 – Phase diagram of confined ethane in 5.0 nm of separation of a slit graphite pore (representing kerogen in shale reservoir).

Table 3-2 – Critical properties of confined ethane in different pore sizes.

Separation (H), nm	Critical temperature (T_c)	Critical pressure (p_c)
2.0	215 K or -72.7°F	32 kPa or 5 psi
3.0	258 K or -4.7°F	580 kPa or 84 psi
4.0	281.5 K or 47.0°F	1675 kPa or 243 psi
5.0	292 K or 66.9°F	2450 kPa or 355 psi
6.0	298 K or 76.7°F	3050 kPa or 442 psi
7.0	300 K or 80.3°F	3400 kPa or 493 psi
8.0	302 K or 83.9°F	3650 kPa or 529 psi
9.0	304 K or 87.5°F	3800 kPa or 551 psi
10.0	305 K or 89.3°F	3900 kPa or 566 psi
Bulk Fluid	305.3 K or 89.9°F	4884 kPa or 708 psi

Similar to the case of confined methane, the critical properties of confined ethane are dependent on the pore size. Both the critical temperature and pressure decrease when the pore is smaller. **Figures 3-5a** and **3-5b** are plots of those properties versus pore size. It can be observed that when $H \leq 5.0$ nm, the critical properties decay rapidly. This reduction rate of confined ethane is faster than that of confined methane, especially when $H \leq 2.0$ nm because the separation is almost as long as the effective length of the ethane molecule. The effect of the interaction between the surface wall and the confined fluid becomes less significant when the pore size increases and its critical properties approach the bulk properties.

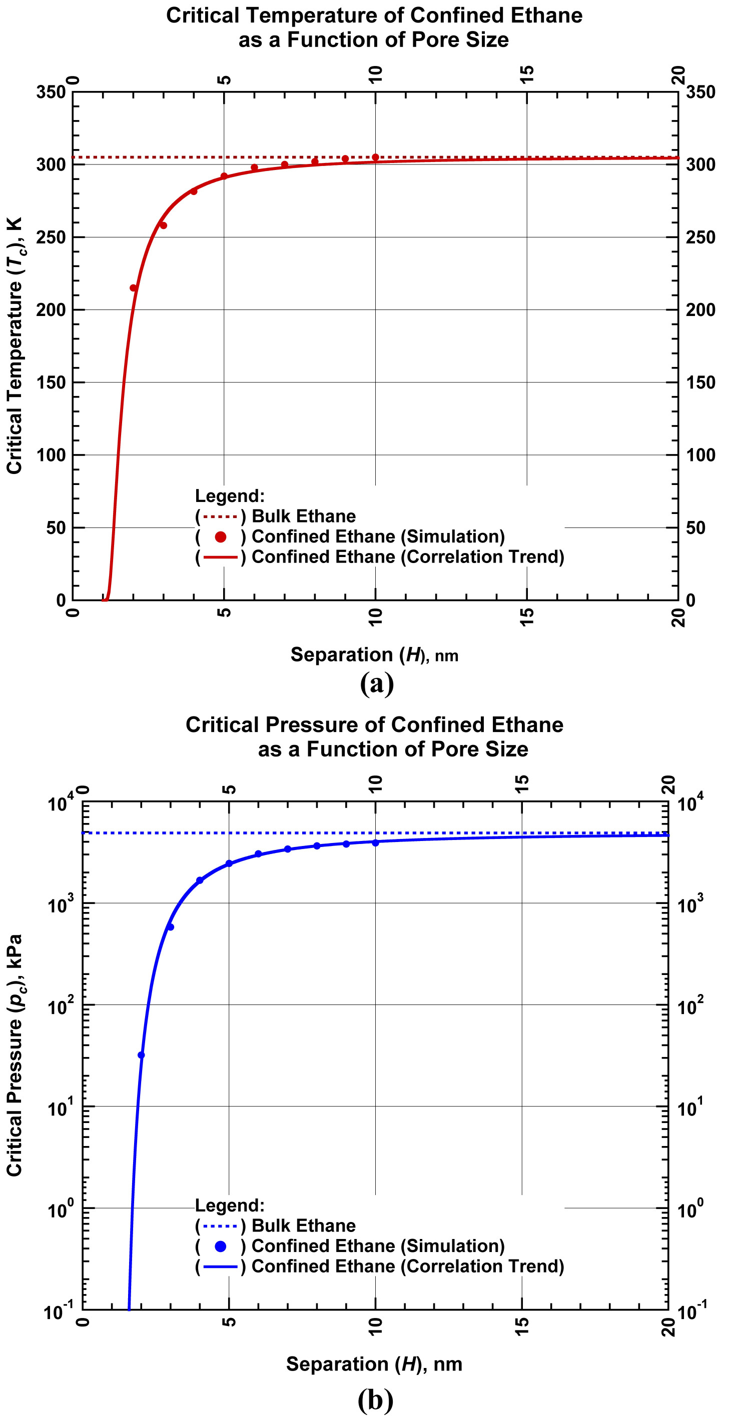

Figure 3-5 – (a) Plot of critical temperature and (b) critical pressure of confined ethane versus separation of a slit graphite pore (representing kerogen in shale reservoir).

For applications in reservoir simulations, we can incorporate these results of new critical properties of confined pure hydrocarbons, along with pore size distribution from core data, to compute critical properties of hydrocarbons in shale reservoirs in a reservoir simulator.

3.3.3 Comparison of Critical Shifts from Our Simulations with the Approximation Models

After we obtained the new critical properties of confined pure hydrocarbons from the previous section, the critical shifts can be computed by their definition, where the critical temperature shift is $(T_c - T_{cp})/T_c$ and the critical pressure shift is $(p_c - p_{cp})/p_c$.

Figures 3-6 and **3-7** illustrate comparisons of the shifts in critical properties of methane and ethane in different pore sizes from our GCMC simulation results and from the approximation models discussed in Chapter I (i.e., Zarragoicoechea and Kuz (2004): equations (1-11) and (1-12), Devegowda et al. (2012): equations (1-13) and (1-14), and Jin et al. (2013), and Ma et al. (2013): equations (1-15) and (1-16)). It can be noticed that the shifts in critical temperatures of both methane and ethane from the simulations are in similar trend to those from the models in **Figure 3-6a** and **3-7a**. Specifically, Jin et al. and Ma et al.'s models give a very good match on the shift in critical temperature of ethane. On the other hand, none of these models provide a good approximation of the shifts in critical pressures of both methane and ethane. We remark that the shifts in the critical properties from Zarragoicoechea and Kuz's model, Jin et al. and Ma et al.'s models, and the GCMC simulations approach zero when the pore size increases. It implies that the confined fluids tend to behave as the bulk when the pore is large. However, there is a large discrepancy for the critical shift in the pressure of the approximated models with the simulation results in small pores.

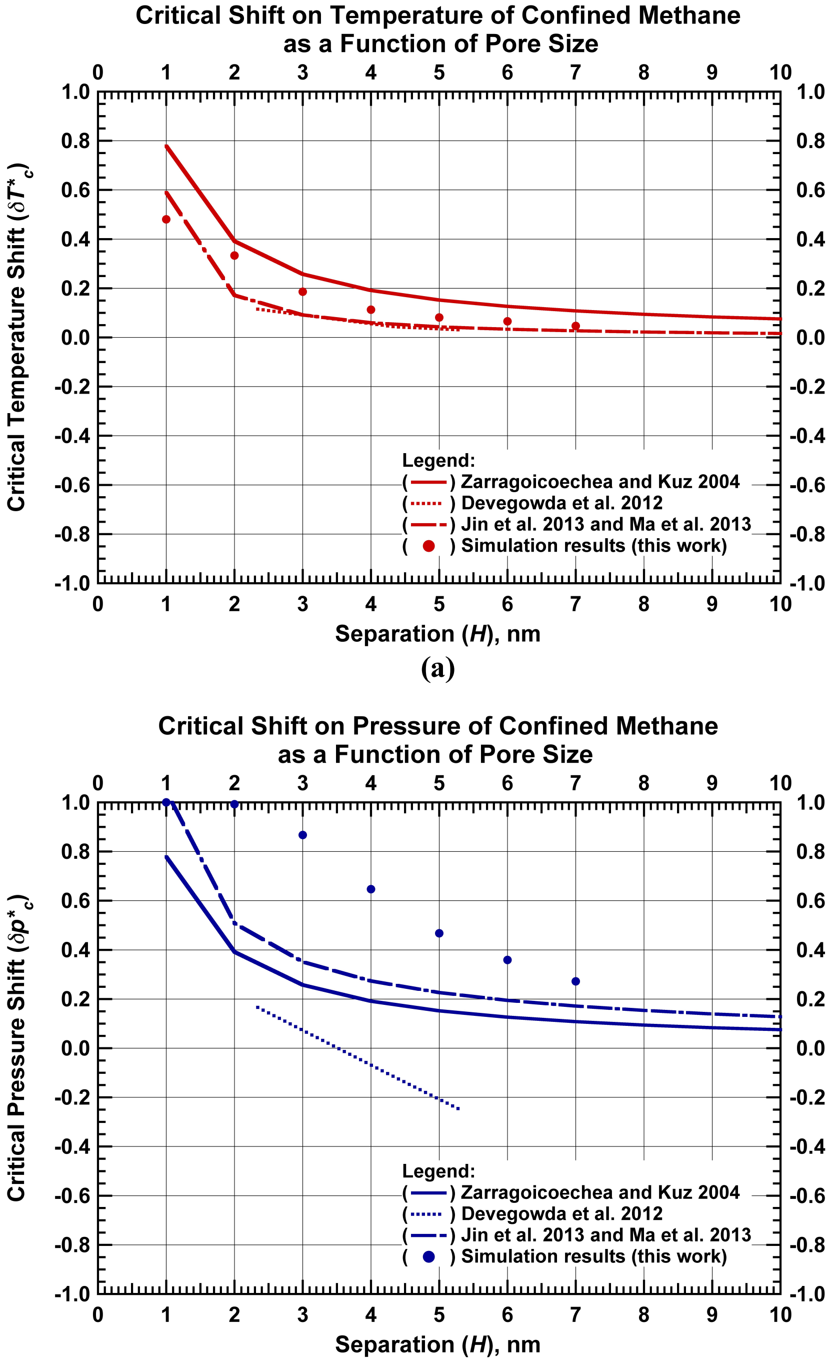

(a)

(b)

Figure 3-6 – Comparison of the critical shifts on temperature (a) and pressure (b) of confined methane from Zarragoicoechea and Kuz's, Devegowda et al.'s, Jin et al. and Ma et al.'s models, and this work GCMC simulation results.

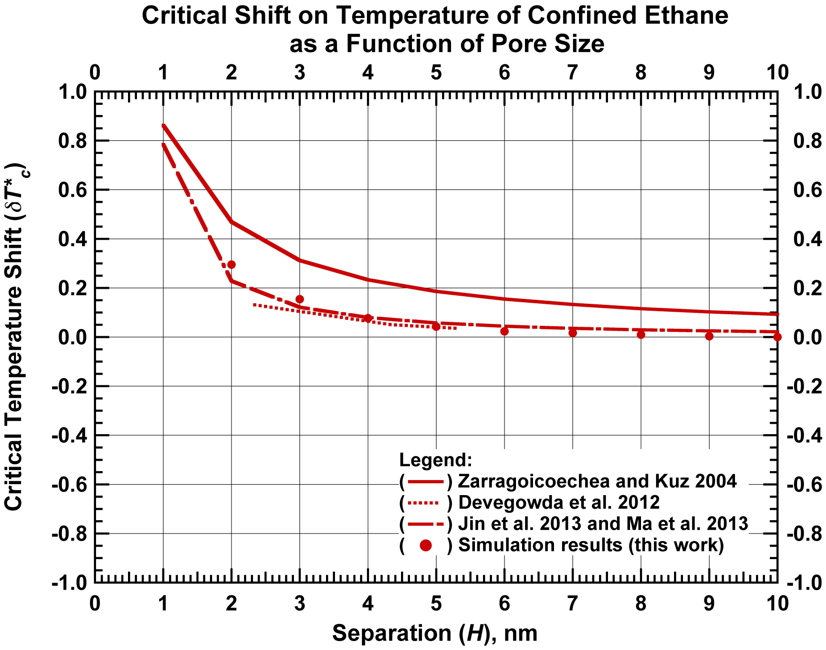

(a)

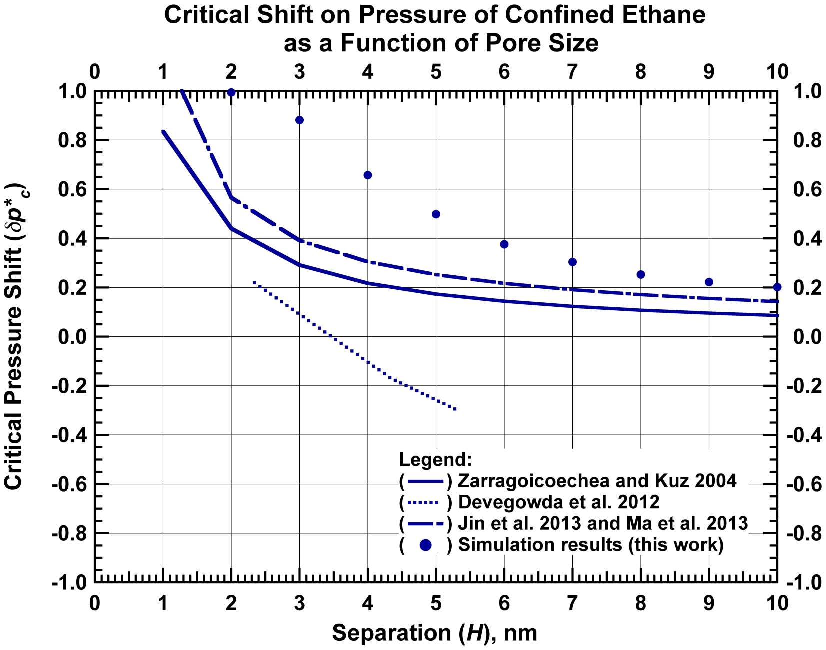

(b)

Figure 3-7 – Comparison of the critical shifts on temperature (a) and pressure (b) of confined ethane from Zarragoicoechea and Kuz's, Devegowda et al.'s, Jin et al. and Ma et al.'s models, and this work GCMC simulation results.

3.4 Density Shift Confined Pure Hydrocarbon at Reservoir Condition

The phase diagrams and critical properties of pure components of methane and ethane, in the nanoscale, differ from those in bulk conditions. As a result, new GCMC simulations were carried out to obtain fluid densities of pure components of methane and ethane at reservoir conditions. **Table 3-3** summarizes the ranges of Eagle Ford reservoir temperatures and pressures obtained from Orangi et al. (2011). In this work, according to the reservoir properties listed in **Table 3-3**, the possible lower and upper limits of the temperatures used in the molecular simulations are T = 385 K and T = 460 K, respectively, and the pressure is varied from 42.5 MPa to 80 MPa for both cases.

Table 3-3 – Eagle Ford reservoir temperature and pressure.

Temperature (T)	Pressure (p)
237°F – 352°F or 387 K – 451 K	6300 psi – 11400 psi or 43 MPa – 79 MPa

The isotherms obtained from the GCMC simulation are converted to the confined fluid densities using equation (3-3) and compared with the bulk densities from the National Institute of Standards and Technology database. The maximum absolute deviation for the confined fluid densities compared with the bulk properties can be calculated using the following formula:

$$\%\ Max.Dev. = \frac{|\rho_{confined} - \rho_{bulk}|}{\rho_{bulk}} \times 100\% \text{ .... } (3\text{-}4).$$

3.4.1 Methane

Figures 3-8a and **3-8b** illustrate densities of the confined methane in different sizes of slit graphite pores at T = 385 K and T = 460 K, respectively. In both cases, it can be observed that the confined density is higher than the bulk density under the same condition. In particular, the fluid density in smaller pores deviates from the bulk density more so than it does in bigger pores. This is because the strength of the attractive potential allows more molecules to populate the system and this effect increases as the pore size decreases.

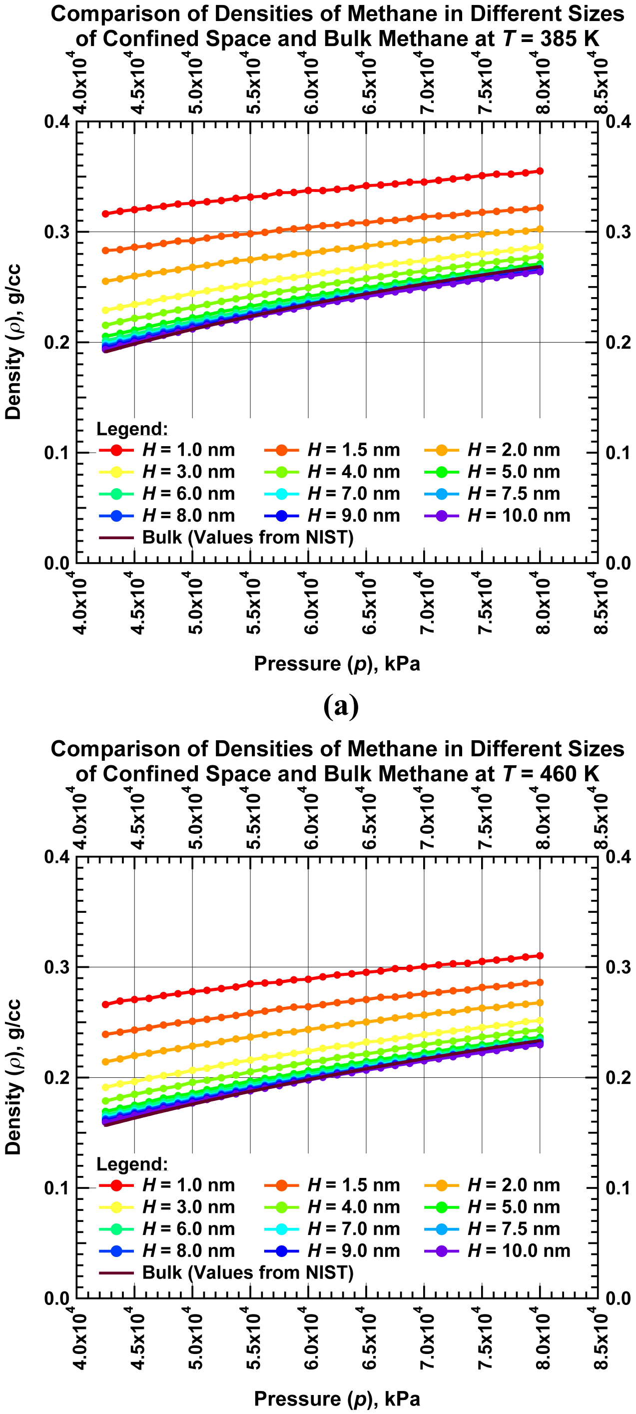

(b)

Figure 3-8 – Comparison of bulk and confined methane densities at the (a) minimum and (b) maximum Eagle Ford shale reservoir temperatures.

The absolute maximum deviations of the confined methane in different pore sizes from the bulk fluid are summarized in **Table 3-4**. At these reservoir conditions, huge deviations of confined methane densities (~70%) occur when H = 1.0 nm due to the strong effect of confinement of kerogen pore in the shale reservoir. However, it becomes less significant when the pore size increases as the deviations reduce to lower than 5% when $H \geq 7.0$ nm.

According to the results, the density of the confined fluid in smaller pores is higher than that in bigger pores. This statement can be proven by the results from the classical MD simulation. A slit graphite pore system with multiple connecting pore sizes is generated. The system contains pure methane with the average fluid density of 0.078 g/cc. The classical MD simulation is implemented to locate methane molecules at equilibrium. The temperature of the system is 385 K and the simulation time is 1500 ps. To ensure that the final configuration is at equilibrium, the total energy must be reached and almost stabilizes at the minimal point as shown in **Figure 3-9**. The final configuration is illustrated in **Figure 3-10**. Based on the final configuration, most of the methane molecules in the system are adsorbed on the graphite surface, and only small amounts of methane molecules are in the free gas phase. The densities of methane in different segments with different pore sizes are varied as summarized in **Table 3-5**. The fluid density in the smaller pore is higher than that of the bigger pore, similar to the conclusion obtained from the GCMC simulation. This is because the fluid in the adsorbed phase is denser than the free gas phase. In the smaller pore, the ratio between the surface area of the pore (for adsorption) and the pore volume is greater than in the bigger pore. Thus, the methane density in the smaller pore is higher than in the bigger pore.

Table 3-4 – Absolute maximum deviation of confined methane densities from bulk methane.

Separation (H), nm	% of Absolute maximum deviation from bulk methane	
	at T = 385 K	at T = 460 K
1.0	65.3 %	69.8 %
1.5	47.9 %	52.6 %
2.0	33.4 %	36.7 %
3.0	19.6 %	22.0 %
4.0	12.5 %	14.1 %
5.0	7.3 %	8.1 %
6.0	5.3 %	6.1 %
7.0	3.7 %	4.7 %
7.5	3.0 %	3.9 %
8.0	2.6 %	3.5 %
9.0	1.7 %	2.6 %
10.0	1.7 %	2.0 %

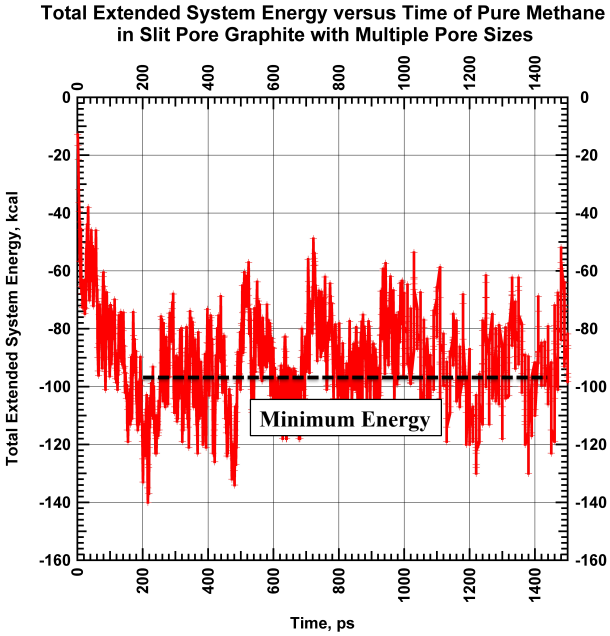

Figure 3-9 – Total energy system over simulation time of pure methane in slit graphite pore with multiple pore sizes at T = 385K.

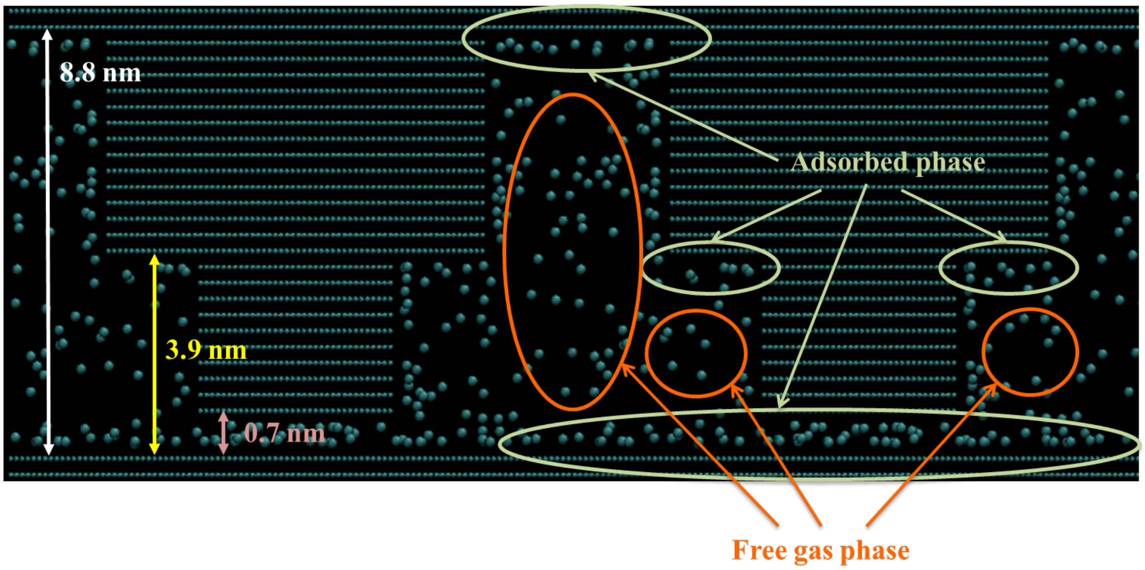

Figure 3-10 – Configuration at t_s = 1500 ps from classical MD simulation of pure methane in slit graphite pore with multiple pore sizes at T = 385K.

Table 3-5 – Densities of confined methane in slit graphite pore with multiple pore sizes from classical MD simulation at T = 385K.

Separation (H), nm	Density (ρ), g/cc
0.7	0.23
3.9	0.088
8.8	0.061

3.4.2 Ethane

Figures 3-11a and **3-11b** illustrate densities of confined ethane in different sizes of slit graphite pores at T = 385 K and T = 460 K, respectively. Similar to the previous case, the confined density is higher than the bulk density. In particular, when $H \geq 1.5$ nm, the fluid density in smaller pores deviates from the bulk density more so than it does in bigger pores. However, it is noticed that the fluid density in the slit pore with $H = 1.0$ nm is lower than that in the pore with $H = 1.5$ nm. This is because when $H = 1.0$ nm, the distance between the two layers of the graphite is too short to offer flexibility in terms of molecular orientation and arrangement to the confined ethane. In other words, the separation is less than twice the effective length of the ethane molecule (one adsorbed layer on each side).

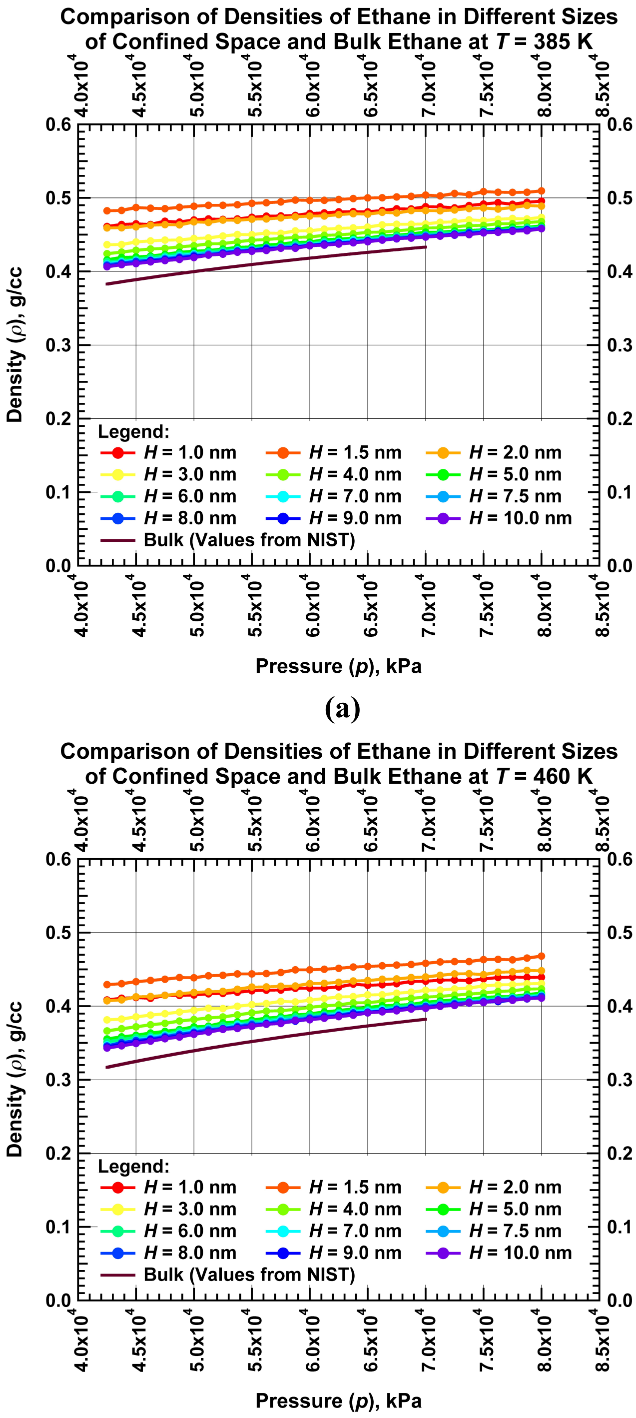

(a)

(b)

Figure 3-11 – Comparison of bulk and confined ethane densities at the (a) minimum and (b) maximum Eagle Ford shale reservoir temperatures.

The maximum absolute deviations of the confined ethane in different pore sizes from the bulk are summarized in **Table 3-6**. At the reservoir conditions, huge deviations of confined ethane densities (~36%) occur when H = 1.5 nm due to a strong effect of confinement of the kerogen pore in the shale reservoir. However, it becomes less significant when the pore size increases. The difference between the confined ethane density in the largest pore in this work (H = 10.0 nm) and the bulk density may be caused by a combination of the effect of confinement and the error from force field used to represent a methyl group in the ethane molecule.

Table 3-6 – Absolute maximum deviation of confined ethane densities from bulk ethane.

Separation (H), nm	% of Absolute maximum deviation from bulk ethane	
	at T = 385 K	at T = 460 K
1.0	20.4 %	28.9 %
1.5	26.0 %	35.5 %
2.0	19.9 %	28.6 %
3.0	14.0 %	20.4 %
4.0	10.8 %	15.6 %
5.0	8.6 %	12.2 %
6.0	8.0 %	10.9 %
7.0	7.2 %	9.7 %
7.5	7.0 %	9.2 %
8.0	6.7 %	9.2 %
9.0	6.3 %	8.7 %
10.0	6.1 %	8.3 %

3.5 Conclusion

In this study, we limited our work to pure methane and pure ethane components. As we observed from the GCMC simulation results, interactions between the surface walls and the fluid molecules will cause changes in the thermodynamic behavior of the hydrocarbon phases. We observed from our simulations that the critical temperature and pressure of pure component methane and ethane reduces as the pore size decreases. In short, the larger the pore size, the less significant the effect of confinement, and the more their critical properties approach the bulk properties (as expected).

Moreover, according to the deviations of the confined methane and ethane densities from the bulk densities at the reservoir conditions, they may cause intolerable errors in reserves estimations and production forecast calculations if the bulk densities are used instead of the proper densities. The confined pure component of methane and ethane densities can deviate from their bulk properties by up to 69.8%

and 35.5%, respectively. We note that the pore actually has a distribution of pore sizes, and other restrictions such as pore interconnections may occur, which will make the phenomena even more complex. These will be incorporated in future work. However, the present results provide a first approximation of the confinement effect on the phase behavior of fluids in kerogen pores.

CHAPTER IV

SIMULATION STUDIES OF CONFINED PURE COMPONENT LONG CHAIN ALKANES

In this chapter, we derive new phase diagrams of confined pure long chain alkanes to determine the new critical properties of the confined fluid in different pore sizes as well as compute densities of the confined fluid at the reservoir conditions. The Configurational-biased Grand Canonical Monte Carlo (CB-GCMC) simulations are implemented instead of using the conventional GCMC simulations because for dense or confined phases of long chain alkanes, standard particle insertion and transfer moves in the conventional GCMC simulations become impractical due to steric overlap. To help understand this problem, **Figure 4-1** illustrates a diagram of two neighboring states of the grand canonical ensemble of the system containing a dense butane system after a standard particle insertion move.

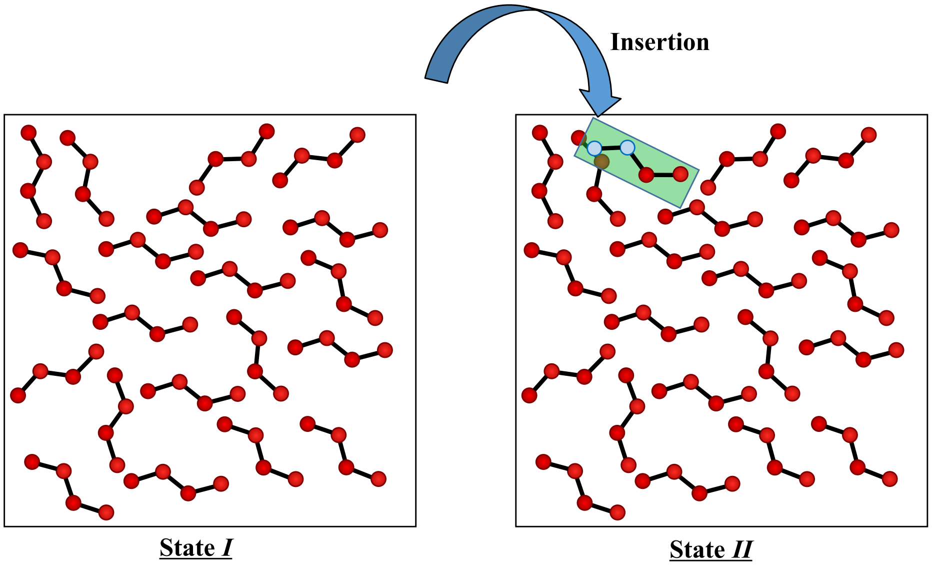

Figure 4-1 – State *I* is an initial configuration. State *II* is obtained from State *I* by adding a rigid butane molecule in a green box using standard particle insertion technique.

State *I* is the initial state. Implementing standard particle insertion – the rigid butane molecule in the green box – may result in steric overlap (see the bond between the blue particles in the molecule) as shown in State *II*. This occurrence causes a very high potential energy in the system, and it is almost impossible for State *II* to be accepted. Since the space available for a new molecule to be added is very restricted, if we use the standard particle insertion, we will waste many moves in the simulations by the moves similar to

State *II* in **Figure 4-1**. To overcome this problem, the Configurational-biased Monte Carlo (CBMC) technique has been developed, and the implementation of the CBMC technique to the GCMC simulation is called CB-GCMC simulation. The CB-GCMC simulation applies a chain growth technique and allows the internal bond bending angle and bond torsion (dihedral) angle to change during the creation of a molecule in the system. **Figure 4-2** illustrates a diagram of two neighboring states of grand canonical ensemble of the system containing a dense butane system after a particle insertion move using the CBMC technique.

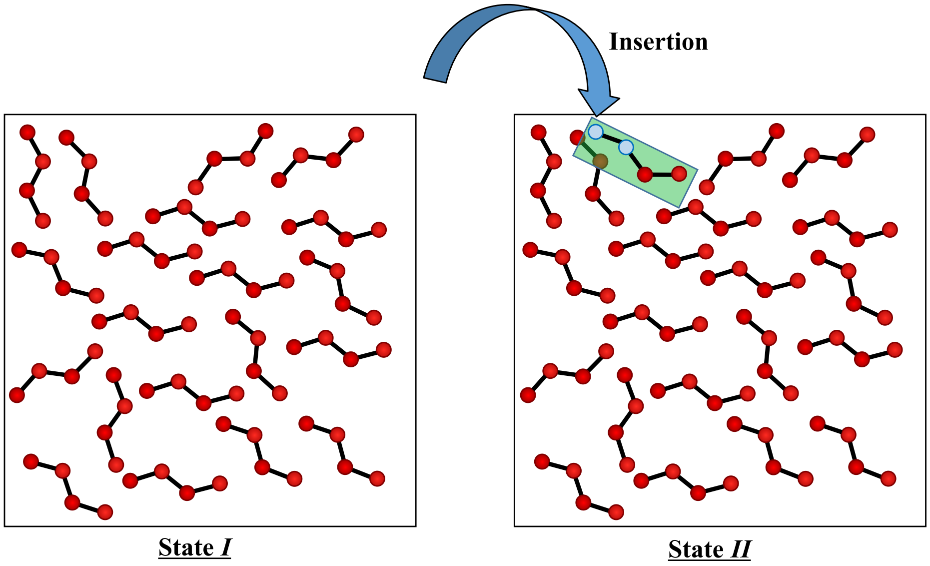

Figure 4-2 – State *I* is an initial configuration. State *II* is obtained from State *I* by adding a butane molecule in a green box using CBMC technique.

The CB-GCMC simulation offers more flexibility for a molecule to change its internal structure to fit in the system more properly. As a result, it allows the bond bending angle between the blue particles of the butane molecule in the green box of State *II* to change to avoid the steric overlap as seen in **Figure 4-2**. State *II* in **Figure 4-2** definitely has lower potential energy than State *II* in **Figure 4-1**, thus the probability for the State *II* to be accepted is higher and its chemical potential may be closer to the bulk system under the given pressure and temperature. In short, the CBMC technique helps us save some MC moves, which is impossible to occur in reality as shown in State *II* of **Figure 4-1**.

In addition, as mentioned in Chapter II, real gas bond bending and bond torsion angles may alter at high pressure. Therefore, it is more reasonable to allow the internal molecular structure to change during the simulations (CB-GCMC simulation) than to insert or transfer a rigid molecule (conventional GCMC simulation).

Since we allowed the internal molecular structure – bond bending angle and bond torsion angle – to change and since the potential energy of the different structures are varied, the intramolecular interactions must be taken into account for the probability calculation.

4.1 Intramolecular Potential

This section concludes all possible bond motions for long chain alkanes and the potential energy corresponding to those moves. The bond motions include:

a. Bond stretching

b. Bond bending

c. Bond twisting

4.1.1 Bond Stretching

Figure 4.3 illustrates propane's (united-atom model) normal mode of vibration due to bond stretching. The motions can be either symmetric stretch or asymmetric stretch. This motion causes the change in bond length between two particles in a molecule.

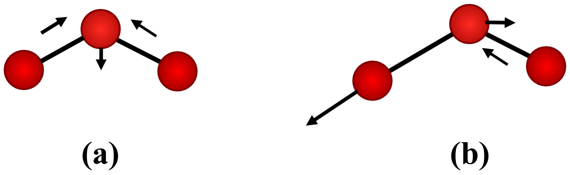

Figure 4-3 – Propane's (united atom model) normal modes of vibration due to bond stretching: (a) symmetric stretch, and (b) asymmetric stretch.

The simplest representation of the stretching potential as a function of distance, r, is that of the harmonic oscillator model:

$$U(r) = U(r_e) + \frac{1}{2}k_r(r - r_e)^2 \qquad (4\text{-}1)$$

where r_e is the equilibrium bond length, k_r is the force constant, and $U(r_e)$ is the potential energy at the equilibrium bond length. Let $U(r_e)$ become a reference potential energy ($U(r_e) = 0$), thus equation (4-1) can be rewritten as

$$U(r) = \frac{1}{2}k_r(r - r_e)^2 \quad \text{.......(4-2).}$$

The blue line in **Figure 4-4** represents the calculated bond stretching potential of a long chain alkane using the harmonic oscillator model. The harmonic oscillator model is an accurate representation of the stretching potential for only small displacements from the equilibrium bond length. Differences between the true potential and the harmonic potential are called "anharmonic effects". These differences are amplified at large r's where the tail tends to be flatted and approaches the classical dissociation energy, D_e.

One of the most common models used to approximate a bond stretching potential is the Morse function:

$$U(r) = D_e\left(1 - \exp\left(-\beta_e(r - r_e)\right)\right)^2 \quad \text{.......(4-3).}$$

In the three parameters equation (4-3), D_e, β_e, and r_e, all have positive values and are usually chosen to fit the bond dissociation energy, the harmonic vibrational frequency (ν_e) and the equilibrium bond length. The green line in **Figure 4-4** represents the calculated bond stretching potential of a long chain alkane using the Morse function. The shape of the Morse function is the same as the true potential. At $r = r_e$, the potential energy equals zero. For $r \ll r_e$, the potential energy is large and positive according to short-range repulsion. As $r \to \infty$, the potential energy approaches the Morse function dissociation energy as shown in a red dashed line in **Figure 4-4**.

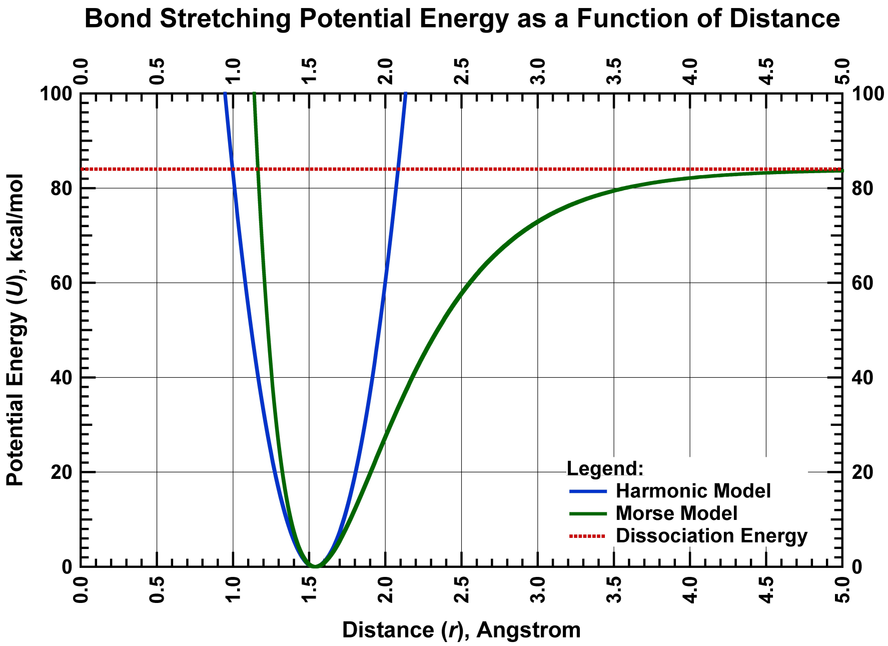

Figure 4-4 – Calculated bond stretching potential energy as a function of distance using harmonic oscillator model (a blue line), and the Morse function (a green line).

By taking the second derivative of equations (4-2) and (4-3) with respect to r at r_e, it is found that the relationship between k_r in the harmonic oscillator model, and D_e, and β_e in the Morse function is:

$$k_r = 2D_e\beta_e^2 \qquad (4\text{-}4).$$

In the CB-GCMC simulation, we assume that the bond lengths between carbon atoms in the hydrocarbon molecules are constant. As a result, the bond stretching potential is not taken into account for the calculation in the CB-GCMC simulation. However, since the classical MD simulation is employed to support our conclusion obtained from the CB-GCMC simulation, the Morse function will be used to take into account the intramolecular forces due to bond stretching in the MD simulation.

Parameters for the Morse function to calculate the bond stretching potential energy of long chain alkanes are summarized in **Table 4-1**.

Table 4-1 – Morse function parameters for bond stretching potential energy calculation of a long chain alkane.

D_e, kcal/mol	β_e	r_e, nm
83.94	1.841	1.54

4.1.2 Bond Bending

Figure 4.5 illustrates propane's (united-atom model) normal mode of vibration due to bond bending. This motion causes the change in bond angle, θ, between two particles in a molecule.

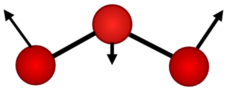

Figure 4-5 – Propane's (united atom model) normal mode of vibration due to bond bending.

In this work, the harmonic oscillator model:

$$U(\theta) = U(\theta_e) + \frac{1}{2}k_\theta(\theta - \theta_e)^2 \quad \text{(4-5)}$$

is used to calculate the internal potential energy associated with the bond bending motion. θ_e is the equilibrium bond angle, k_θ is the force constant, and $U(\theta_e)$ is the potential energy at the equilibrium bond angle. Similar to the bond stretching potential calculation using the harmonic oscillator model, let $U(\theta_e)$ become a reference potential energy ($U(\theta_e) = 0$), thus equation (4-5) can be rewritten as

$$U(\theta) = \frac{1}{2}k_\theta(\theta - \theta_e)^2 \quad \text{(4-6).}$$

Figure 4-6 illustrates the calculated bond bending potential of a long chain alkane using the harmonic oscillator model. Parameters for the bond bending potential energy calculation are summarized in **Table 4-2**.

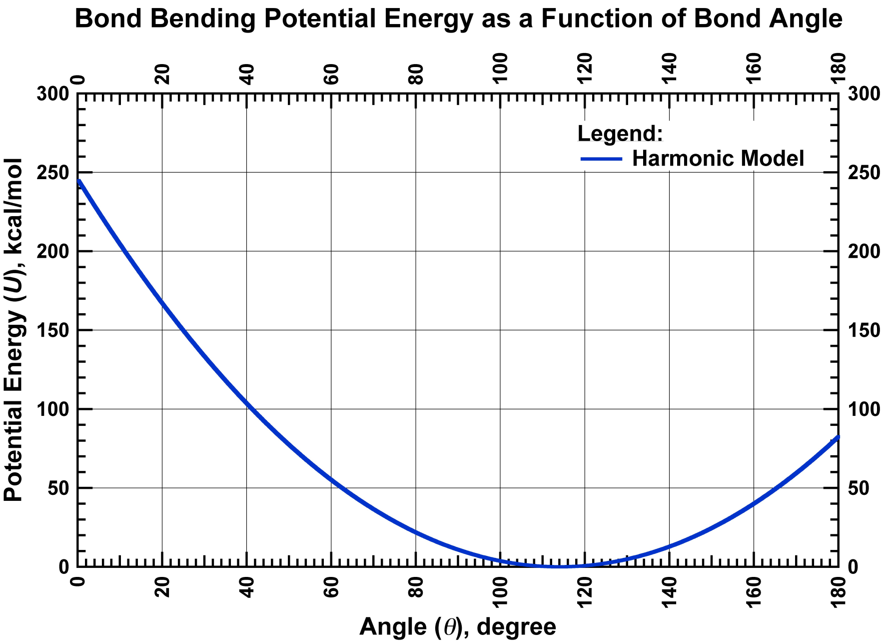

Figure 4-6 – Calculated bond bending potential energy as a function of bond angle using harmonic oscillator model.

Table 4-2 – Harmonic oscillator model parameters for bond bending potential energy calculation of a long chain alkane.

k_θ, kcal/rad^2/mol	θ_e, degree
124.2	114

Since a long chain molecule is symmetric, the range of the possible bond bending angle in the molecule is from 0° to 180°. It can be noticed that at θ equals to the equilibrium bond angle ($\theta_e = 114^\circ$), the potential energy is zero, and it rises when the bond angle deviates from the equilibrium bond angle.

4.1.3 Bond Twisting

Figure 4.7 illustrates the bond twisting of a butane molecule that alters the torsion or dihedral angle, ϕ, of two planes in the molecule.

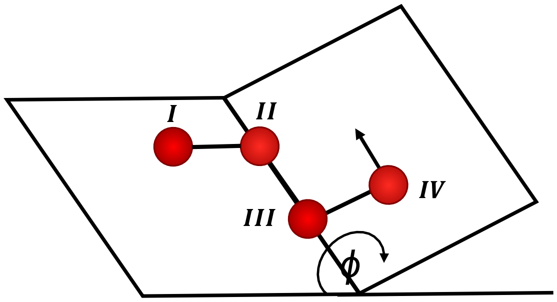

Figure 4-7 – Bond twisting in butane (united atom model) alters bond dihedral angle.

In this work, the triple cosine model:

$$U(\phi) = \frac{1}{2}\left(A_1(1 + \cos\phi) + A_2(1 - \cos 2\phi)\,) + A_3(1 + \cos 3\phi)\right) \quad \text{...(4-5)}$$

is used to calculate the internal potential energy associated with the bond twisting motion. **Figure 4-8** illustrates the calculated bond potential of a long chain alkane associated with bond twisting using the triple cosine model. Parameters used for the potential energy calculation are summarized in **Table 4-3**.

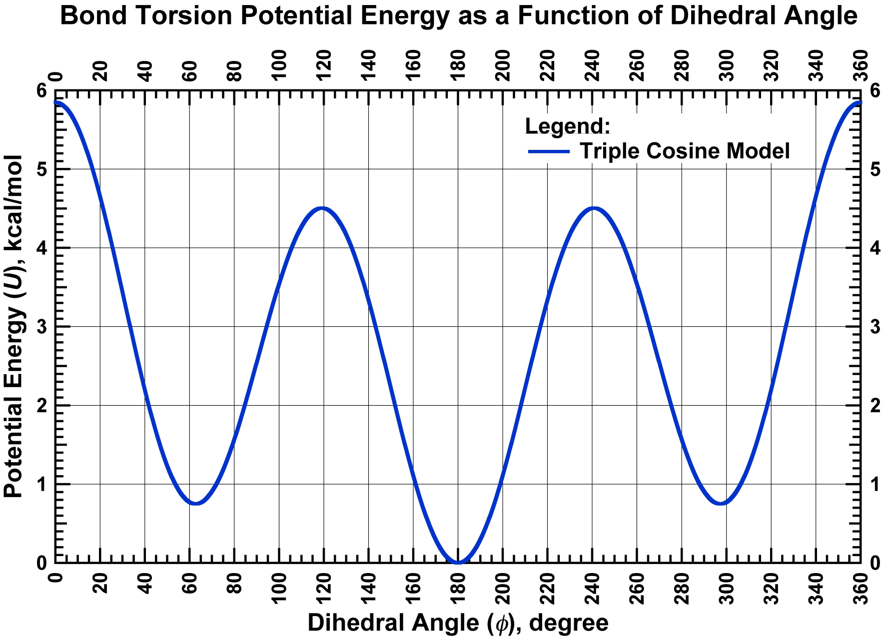

Figure 4-8 – Calculated bond torsion potential energy as a function of dihedral angle using triple cosine model.

Table 4-3 – Triple cosine model parameters for bond torsion potential energy calculation of a long chain alkane.

A_1, kcal/mol	A_2, kcal/mol$_e$	A_3, kcal/mol
1.411	-0.271	-3.145

The range of possible dihedral angles in a long chain alkane is from 0° to 360°. It can be observed that the minimum potential occurs at $\phi = 180^{\circ}$. It implies that the equilibrium dihedral angle of a long chain alkane is 180°.

4.2 Configurational-Biased Monte Carlo Simulation

A sequential chain growth with biased sampling technique is implemented and can be explained as shown in **Figure 4.9**. For the molecule creation of a long chain alkane in a united-atom model, the CB-GCMC starts with inserting the first fragment (united-atom *I*) of the molecule in a slit graphite pore using the first-atom sampling (FAS) technique. Then, the simulation will insert the second fragment (united-atom *II*) using the sphere sampling (SS) technique. Finally, it will complete the chain (united-atoms *III* and *IV*) with the disc sampling (DS) technique.

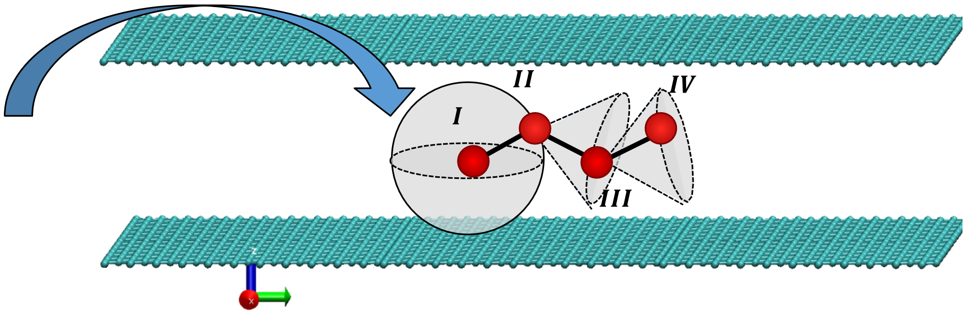

Figure 4-9 – Sequential chain growth: particle *I* is created using the FAS method, particle *II* is added using the SS method, and particles *III* and *IV* are added using the DS method.

Let $\Pi_{I \to II}$ be the one-step transition probability of going from State *I* to State *II* in a Monte Carlo simulation, $\alpha_{I \to II}$ be the probability of attempting move (FAS, SS, and DS), and $\mathcal{P}_I$ and $\mathcal{P}_{II}$ be the grand canonical ensemble probability distribution function of state *I* and state *II*. For instance, $\mathcal{P}_I$ is $\mathcal{P}_{\mu VT}(N)$ and $\mathcal{P}_{II}$ is $\mathcal{P}_{\mu VT}(N+1)$ in equation (2-52) for the insertion of particles. The acceptance rule for moves will be

$$\Pi_{I\to II} = \min\left(1, \frac{\alpha_{I\to II}\mathcal{P}_{II}}{\alpha_{II\to I}\mathcal{P}_{I}}\right) \tag{4-6}$$

For insertion of particles,

$$\Pi_{I\to II} = \min\left(1, \frac{\alpha_{I\to II}}{\alpha_{II\to I}}\frac{V\beta p_{id,gas}}{(N+1)}\exp\left[-\beta\left[U(N+1)-U(N)\right]\right]\right) \tag{4-7}$$

and for the reverse move,

$$\Pi_{II\to I} = \min\left(1, \frac{\alpha_{II\to I}}{\alpha_{I\to II}}\frac{N}{V\beta p_{id,gas}}\exp\left[-\beta\left[U(N-1)-U(N)\right]\right]\right) \tag{4-8}$$

Equations (4-7) and (4-8) do not include intramolecular potential energy for the calculation. After incorporating the intramolecular potential energy, the insertion acceptance rule becomes (Macedonia and Maginn 1998)

$$\Pi_{I\to II} = \min\left(1, \frac{\alpha_{I\to II}}{\alpha_{II\to I}}\frac{\Omega}{\mathbb{Z}_{IG}}\frac{V\beta p_{id,gas}}{(N+1)}\exp\left[-\beta\left[U(N+1)-U(N)\right]\right]\right) \tag{4-9}$$

and the deletion acceptance rule becomes

$$\Pi_{II\to I} = \min\left(1, \frac{\alpha_{II\to I}}{\alpha_{I\to II}}\frac{\mathbb{Z}_{IG}}{\Omega}\frac{N}{V\beta p_{id,gas}}\exp\left[-\beta\left[U(N-1)-U(N)\right]\right]\right) \tag{4-10}$$

4.2.1 Configuration Integral and Phase Space Volume

The additional term after including the intramolecular potential energy in the acceptance rule (equations (4-9) and (4-10)) is $\mathbb{Z}_{IG}/\Omega$ where $\mathbb{Z}_{IG}$ is the ideal gas configuration integral of a single molecule:

$$\mathbb{Z}_{IG} = \int \exp(-\beta U_{intra})\, d\boldsymbol{q}^{\boldsymbol{N}} \tag{4-11}$$

and Ω is the phase space volume of the molecule:

$$\Omega = \int d\boldsymbol{q}^{\boldsymbol{N}} \tag{4-12}$$

$\boldsymbol{q}^{\boldsymbol{N}}$ is the vector generalized coordinates for molecule *i*. Let us consider a butane molecule as shown in **Figure 4-7**. The molecule is associated with 2 bond bending angles and 1 bond torsion angle. Let θ_1 be the bond angle between particles *I*, *II*, and *III* and θ_2 be the bond angle between particles *II*, *III*, and *IV*. Thus,

$$\frac{\mathbb{Z}_{IG}}{\Omega} = \frac{\int \exp(-\beta U_{\theta_1})d\boldsymbol{q}^{\boldsymbol{\theta_1}} \int \exp(-\beta U_{\theta_2})d\boldsymbol{q}^{\boldsymbol{\theta_2}} \int \exp(-\beta U_{\phi})d\boldsymbol{q}^{\boldsymbol{\phi}}}{\int d\boldsymbol{q}^{\boldsymbol{\theta_1}} \int d\boldsymbol{q}^{\boldsymbol{\theta_2}} \int d\boldsymbol{q}^{\boldsymbol{\phi}}} \tag{4-13a}$$

$$\frac{\mathbb{Z}_{IG}}{\Omega} = \frac{\int_0^{\pi} \exp(-\beta U(\theta_1)) \sin\theta_1 d\theta_1 \int_0^{\pi} \exp(-\beta U(\theta_2)) \sin\theta_1 d\theta_2 \int_0^{2\pi} \exp(-\beta U(\phi)) d\boldsymbol{\phi}}{\int_0^{\pi} \sin\theta_1 d\theta_1 \int_0^{\pi} \sin\theta_2 d\theta_2 \int_0^{2\pi} d\boldsymbol{\phi}} \tag{4-13b}$$

The bond lengths between carbon atoms in the molecule are assumed to be constant for this case. We may substitute the intramolecular potential functions as mentioned in the previous section for $U(\theta_1)$, $U(\theta_2)$, and $U(\phi)$ in equation (4-13b). For example, if we use the harmonic oscillator model for $U(\theta_1)$ and $U(\theta_2)$ and the triple cosine model for $U(\phi)$ with their parameters from **Tables 4-2** and **4-3**, the $\mathbb{Z}_{IG}/\Omega$ of a butane molecule at T = 300K will equal 8.169×10^{-4}. $\mathbb{Z}_{IG}/\Omega$ is an additional input for the CB-GCMC simulation. It is proportional to the temperature of a confined system. As temperature increases, the value of $\mathbb{Z}_{IG}/\Omega$ increases.

4.2.2 Sequential Chain Growth Procedures

For a long chain alkane with n_{UA} fragments,

$$\frac{\alpha_{II\to I}}{\alpha_{I\to II}} = \prod_{i=1}^{n_{UA}} \frac{\alpha_{II\to I}(i)}{\alpha_{I\to II}(i)} \qquad (4\text{-}14)$$

where $\frac{\alpha_{II\to I}(i)}{\alpha_{I\to II}(i)}$ is the ratio of attempt probabilities for each fragment i of the molecule.

First Atom Sampling

For the first-atom sampling technique, the simulation will place the first atom of a sorbate molecule based on the accessibility to a location in the confined system. There are two different sampling methods for low and high sorbate loading. Since we are interested on a phase transition of fluid in a confined system, it is certain that the loading of sorbate molecules in our confined system is high. Therefore, we implemented the high loading first atom sampling (HL-FAS) in our simulations. The probability of this attempting move is given by

$$\alpha_{I\to II}(1) = \frac{\exp[-\beta U(r_1)]dV_1}{\int dV_1 \exp[-\beta U(r_1')]} \qquad (4\text{-}15)$$

and the probability of its reverse move is

$$\alpha_{II\to I}(1) = \frac{dV_1}{V} \qquad (4\text{-}16).$$

$U(r_1)$ is the total potential energy due to the placement of atom 1, which includes interactions with both the sorbent, which is graphene layer, and sorbate molecules at the selected location, whereas $U(r_1')$ is the total potential energy at trial locations. In practice, the simulation divides our confined system into n_{FAS} regions. Then, it will insert the first atoms at trial locations in all regions and calculate the total potential corresponding to those locations for every Monte Carlo simulation. The probability of inserting the first atom at the selected location is

$$\alpha_{I\to II}(1) = \frac{\exp[-\beta U(r_1)]\Delta V_1}{\sum_{i=1}^{n_{FAS}} \exp[-\beta U(r_1')]\Delta V_1} \qquad (4\text{-}17).$$

Since the system volume is divided equally, equation (4-17) can be rewritten as

$$\alpha_{I\rightarrow II}(1) = \frac{\exp[-\beta U(r_1)]\Delta V_1}{\frac{V}{n_{FAS}}\sum_{i=1}^{n_{FAS}}\exp[-\beta U(r_1')]} \quad \text{(4-18).}$$

Finally, the ratio of attempt probabilities for HL-FAS is

$$\left(\frac{\alpha_{II\rightarrow I}(1)}{\alpha_{I\rightarrow II}(1)}\right)^{HL-FAS} = \frac{\sum_{i=1}^{n_{FAS}}\exp[-\beta U(r_1')]}{n_{FAS}\exp[-\beta U(r_1)]} \quad \text{(4-19).}$$

Sphere Sampling

After the first particle is placed in the system, the second particle of a long chain alkane is inserted using the sphere sampling method. A random location, r_2, will be selected on the surface of the sphere centered at r_1 with a radius equal to the fixed bond length. The location of r_2 on the sphere is defined by Eulerian angles ψ_1 and ψ_2. The probability of this attempting move is given by

$$\alpha_{I\rightarrow II}(2) = \frac{\exp[-\beta U(\psi_1,\psi_2;\boldsymbol{q_p})]dV_2}{\int(\sin\psi_1')d\psi_1'd\psi_2'\exp[-\beta U(\psi_1',\psi_2';\boldsymbol{q_p})]} \quad \text{(4-20)}$$

and the probability of its reverse move is

$$\alpha_{II\rightarrow I}(2) = \frac{dV_2}{4\pi} \quad \text{(4-21).}$$

$U(\psi_1,\psi_2;\boldsymbol{q_p})$ is the total potential energy due to the placement of atom 2 with Eulerian angles ψ_1 and ψ_2, given that the position of atom 1 is described by the generalized coordinates $\boldsymbol{q_p}$. $U(\psi_1',\psi_2';\boldsymbol{q_p})$ is the total potential energy of the atom 2 at trial positions. In practice, the simulation equally divides the surface of the sphere into n_{SS} regions. Then, it randomly selects trial points in those regions and evaluates the total potential energies. Therefore a discrete form of equation (4-20) is

$$\alpha_{I\rightarrow II}(2) = \frac{\exp[-\beta U(\psi_1,\psi_2;\boldsymbol{q_p})]\Delta V_2}{\int d\cos(\psi_1')d\psi_2'\exp[-\beta U(\psi_1',\psi_2';\boldsymbol{q_p})]} \quad \text{(4-22a)}$$

$$\alpha_{I\rightarrow II}(2) = \frac{\exp[-\beta U(\psi_1,\psi_2;\boldsymbol{q_p})]\Delta V_2}{\frac{4\pi}{n_{SS}}\sum_{i=1}^{n_{SS}}\exp[-\beta U(\psi_1',\psi_2';\boldsymbol{q_p})]} \quad \text{(4-22b).}$$

Finally, the ratio of attempt probabilities for sphere sampling is

$$\left(\frac{\alpha_{II\rightarrow I}(2)}{\alpha_{I\rightarrow II}(2)}\right)^{SS} = \frac{\sum_{i=1}^{n_{SS}}\exp[-\beta U(\psi_1',\psi_2';\boldsymbol{q_p})]}{n_{ss}\exp[-\beta U(\psi_1,\psi_2;\boldsymbol{q_p})]} \quad \text{(4-23).}$$

Disc Sampling

In this section, we will consider the potential energy associated with both bond bending and bond torsion angles. According to **Figures 4-6** and **4-8**, the amplitude of the potential energy of a long chain alkane associated with the bond bending angle (~ 240 kcal/mol) is more than the bond torsion angle (~ 5.9 kcal/mol). It means that the bond angle is a hard contributor whereas the dihedral angle is a soft contributor. The disc sampling method involves selections of both a hard contributor (i.e. bond angle), and a soft contributor (i.e. dihedral angle). However, for a propane molecule, the method involves only the potential associated with the bond angle. **Figure 4-10** illustrates an example of the disc sampling method of particle *IV* in a butane molecule. When particle *IV* is added, the hard degree of freedom (bond angle) is always selected first.

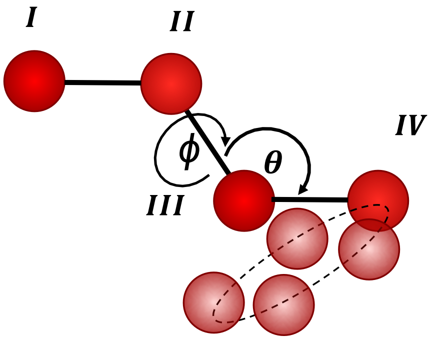

Figure 4-10 – Schematic of the disc sampling method for a butane molecule.

Consider the probability distribution of a bond angle selection:

$$\mathcal{P}(\theta) = \frac{\exp(-\beta U(\theta)) \sin\theta d\theta}{\int_0^{\pi} \exp(-\beta U(\theta')) \sin\theta' d\theta'} \text{ ......(4-24).}$$

If we apply the harmonic oscillator model for $U(\theta)$ in the above equation, the probability distribution of the bond angle in a long chain can be obtained as shown in **Figure 4-11**. The highest probability is at the equilibrium bond angle ($\theta_e = 114^{\circ}$), where the potential energy is zero (see **Figure 4-6**). In addition, we found that the probability distribution is a function of temperature. For instance, as temperature increases, the shape of the distribution widens (higher standard deviation) and its peak decreases. It implies that the deviation of the bond angles from the equilibrium bond angle is smaller in a lower temperature system; however, high-energy molecular configuration can be developed at an elevated temperature.

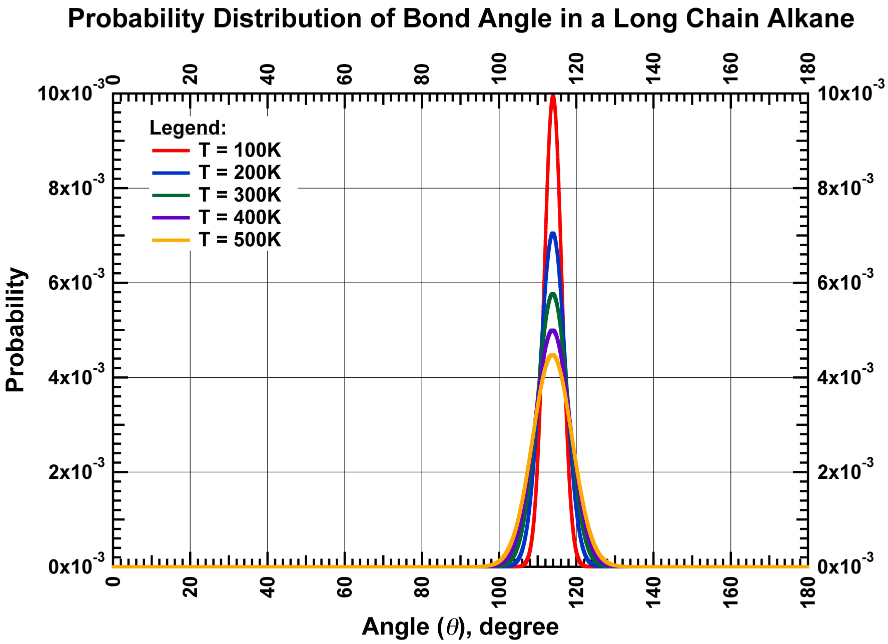

Figure 4-11 – Probability distribution of bond angle in a long chain alkane at different temperatures.

In practice, a method using discrete points is employed to take a sample point from the distribution in **Figure 4-11**. A bond angle is selected by choosing a region θ_i from a series of discretized regions from 0 to π. An equivalent discrete form of equation (4-24) is

$$\mathcal{P}(\theta) = \frac{\exp\left(-\beta U(\theta_i)\right)\sin\theta\Delta\theta}{\sum_{i=1}^{N_\theta}\exp\left(-\beta U(\theta_i{}')\right)\sin\theta\Delta\theta} \quad \text{(4-25).}$$

where N_θ is the number of discretized regions, $U(\theta_i)$ is the potential energy associated with the selected region, and $U(\theta_i')$ is the potential energy at the centers of the trial regions. Since $\sum_{i=1}^{N_\theta}(\sin\theta\,\Delta\theta) = 2$,

$$\mathcal{P}(\theta) = \frac{\exp\left(-\beta U(\theta_i)\right)\sin\theta\Delta\theta}{\frac{2}{N_\theta}\sum_{i=1}^{N_\theta}\exp\left(-\beta U(\theta_i{}')\right)} \quad \text{(4-26).}$$

After a bond angle is selected, the dihedral angle, ϕ, is selected by choosing a random position on the edge of the disc (see **Figure 4-10**). The probability distribution of a dihedral angle selection is

$$\mathcal{P}(\phi) = \frac{\exp\left(-\beta U(\phi)\right)d\phi}{\int_0^{2\pi}\exp\left(-\beta U(\phi')\right)d\phi'} \quad \text{(4-27).}$$

If we apply the triple cosine function for $U(\phi)$ in the above equation, the probability distribution of the dihedral angle in a long chain can be obtained as shown in **Figure 4-12**.

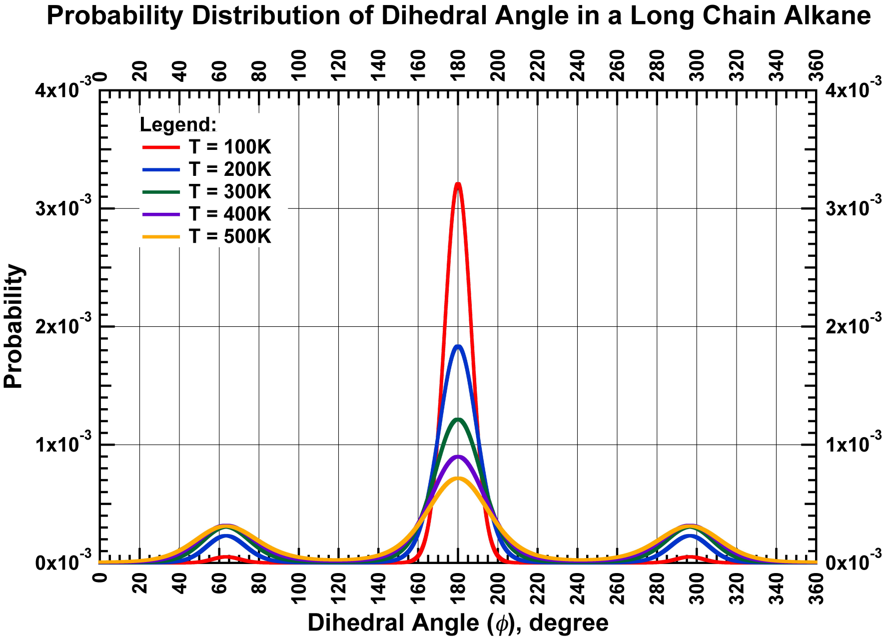

Figure 4-12 – Probability distribution of dihedral angle in a long chain alkane at different temperatures.

The highest probability occurs at $\phi = 180^{\circ}$, where the potential energy is zero (see **Figure 4-8**). Similar to the bond angle probability distribution, the probability distribution is a function of the temperature. When the temperature increases, the shape of the distribution widens, and its peak becomes lower. Moreover, the probabilities of $\phi = 60^{\circ}$ and 180° are almost equal to the probability of $\phi = 180^{\circ}$ at T = 500K. According to the distributions of the bond and dihedral angles, the dihedral angle is more flexible than the bond angle.

Similar to the bond angle selection, a dihedral angle is selected by choosing a region ϕ_i from a series of discretized regions from 0 to 2π of the disc. An equivalent discrete form of equation (4-27) is

$$\mathcal{P}(\phi) = \frac{\exp\left(-\beta U(\phi_i)\right)\Delta\phi}{\sum_{i=1}^{N_\phi} \exp\left(-\beta U(\phi_i{}')\right)\Delta\phi} \quad \text{...(4-28).}$$

where N_ϕ is the number of discretized regions, $U(\phi_i)$ is the potential energy associated with the selected region, and $U(\phi_i')$ is the potential energy at the centers of the trial regions. These potential energies include torsion and non-bond (intermolecular) energy. Since $\sum_{i=1}^{N_\phi}(\Delta\phi) = 2\pi$,

$$\mathcal{P}(\phi) = \frac{\exp\left(-\beta U(\phi_i)\right)\Delta\phi}{\frac{2\pi}{N_\phi}\sum_{i=1}^{N_\phi}\exp\left(-\beta U(\phi_i{}')\right)} \cdots\cdots\cdots (4\text{-}29).$$

Finally, the forward attempt probability (inserting particle *IV* in **Figure 4-10**) is

$$\alpha_{I\rightarrow II}(IV) = \mathcal{P}(\theta)\mathcal{P}(\phi) = \left(\frac{\exp\left(-\beta U(\theta_i)\right)\sin\theta\Delta\theta}{\frac{2}{N_\theta}\sum_{i=1}^{N_\theta}\exp\left(-\beta U(\theta_i{}')\right)}\right)\left(\frac{\exp\left(-\beta U(\phi_i)\right)\Delta\phi}{\frac{2\pi}{N_\phi}\sum_{i=1}^{N_\phi}\exp\left(-\beta U(\phi_i{}')\right)}\right) \cdots\cdots\cdots (4\text{-}30\text{a})$$

$$\alpha_{I\rightarrow II}(IV) = \frac{N_\theta N_\phi}{4\pi}\left(\frac{\exp\left(-\beta U(\theta_i)\right)\sin\theta\Delta\theta}{\sum_{i=1}^{N_\theta}\exp\left(-\beta U(\theta_i{}')\right)}\right)\left(\frac{\exp\left(-\beta U(\phi_i)\right)\Delta\phi}{\sum_{i=1}^{N_\phi}\exp\left(-\beta U(\phi_i{}')\right)}\right) \cdots\cdots\cdots (4\text{-}30\text{b}).$$

For the reverse move, particle *IV* could occupy any position on the sphere surrounding particle *III*, such that

$$\alpha_{II\rightarrow I}(IV) = \frac{\sin\theta\, d\theta d\phi}{\int\sin\theta\, d\theta d\phi} = \frac{\sin\theta\, d\theta d\phi}{4\pi} \cdots\cdots\cdots (4\text{-}31).$$

Finally, the ratio of the attempt probabilities for disc sampling is

$$\left(\frac{\alpha_{II\rightarrow I}(IV)}{\alpha_{I\rightarrow II}(IV)}\right)^{DS} = \frac{1}{N_\theta N_\phi}\left(\frac{\sum_{i=1}^{N_\theta}\exp\left(-\beta U(\theta_i{}')\right)}{\exp\left(-\beta U(\theta_i)\right)}\right)\left(\frac{\sum_{i=1}^{N_\phi}\exp\left(-\beta U(\phi_i{}')\right)}{\exp\left(-\beta U(\phi_i)\right)}\right) \cdots\cdots\cdots (4\text{-}32).$$

4.3 Analysis of Simulation Data

The CB-GCMC simulation is implemented to evaluate the equilibrium density of the confined fluid under the given conditions of temperature and pressure. Similar to the method used in the previous chapter, the adsorption is computed as the amount of molecules present in the unit cell (system) at equilibrium conditions where equations (3-1a) and (3-1b) are satisfied. Once the number of molecules per unit cell (*n*) is obtained from the GCMC simulations, the density can be computed using equation (3-2).

The calculated fluid density in the confined space is used to determine the critical point of a pure component. At $T < T_c$, a phase transition can be observed when there is an occurrence of a jump of fluid density (from vapor to liquid) while pressure increases. On the other hand, at $T \geq T_c$, the fluid density is a continuous function of pressure, and this phase is called a supercritical fluid. As a result, the tip of a phase envelope that contains a two-phase region may yield a critical point of a pure component.

4.4 Phase Diagram and Critical Properties of Confined Long Chain Alkanes

This section shows examples of calculated phase diagrams and derivations of critical properties of confined propane, butane, pentane, and hexane. **Figures 4-11**, **4-12**, **4-13**, and **4-14** illustrate examples of calculated phase diagrams for confined propane, butane, pentane, and hexane in a 3.0 nm separation slit graphite pore representing the kerogen in shale reservoirs. Similar to the confined molecule hydrocarbons, a jump or discontinuity of the fluid density (from vapor to liquid) occurs while pressure increases at low temperatures. Such a jump is called a first-order phase transition, and the pressure at which the phase transition occurs is called the vapor pressure. On the other hand, at higher temperatures, the first-order phase transition vanishes at the critical points as pressure increases and the isotherm becomes a continuous function of pressure at supercritical conditions. A phase envelope of the confined long chain alkanes containing a two-phase region can be drawn by connecting points of vapor and liquid densities at the vapor pressures of different temperatures as shown by the black envelope in **Figures 4-11**, **4-12**, **4-13**, and **4-14**. The critical properties can be read from the tip of the envelope. These procedures are applied to determine the critical properties of confined long chain alkanes in different pore sizes. The new critical temperatures and critical pressures of the confined propane, butane, pentane, and hexane in different pore sizes are summarized in **Tables 4-4**, **4-5**, **4-6** and **4-7**, respectively. See Appendix A for calculated phase diagrams for confined propane, butane, pentane, and hexane in different pore sizes (2.0 nm – 10.0 nm).

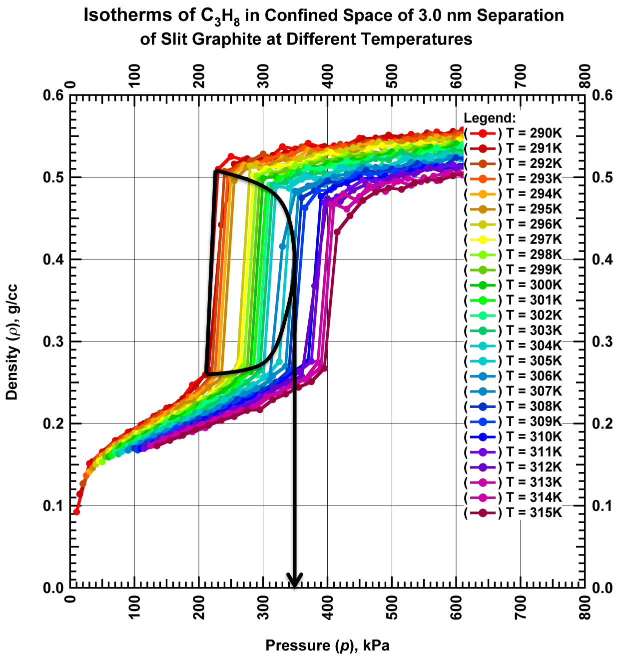

Figure 4-13 – Phase diagram of confined propane in 3.0 nm of separation of a slit graphite pore (representing kerogen in shale reservoir).

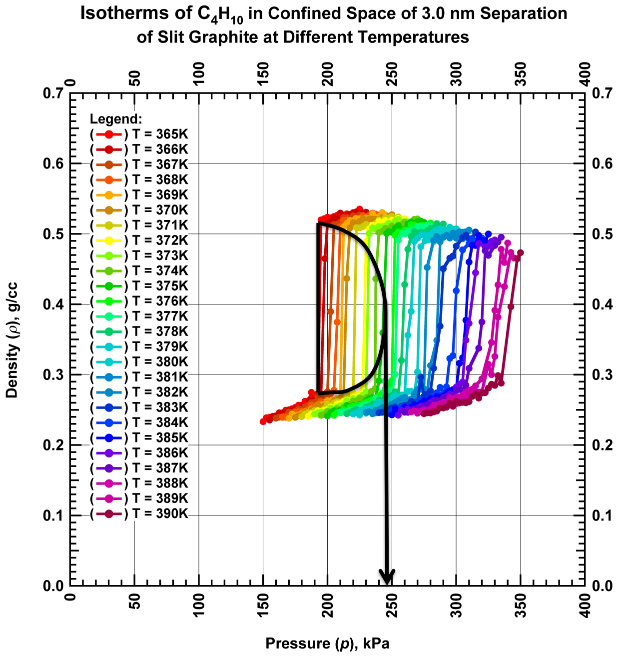

Figure 4-14 – Phase diagram of confined butane in 3.0 nm of separation of a slit graphite pore (representing kerogen in shale reservoir).

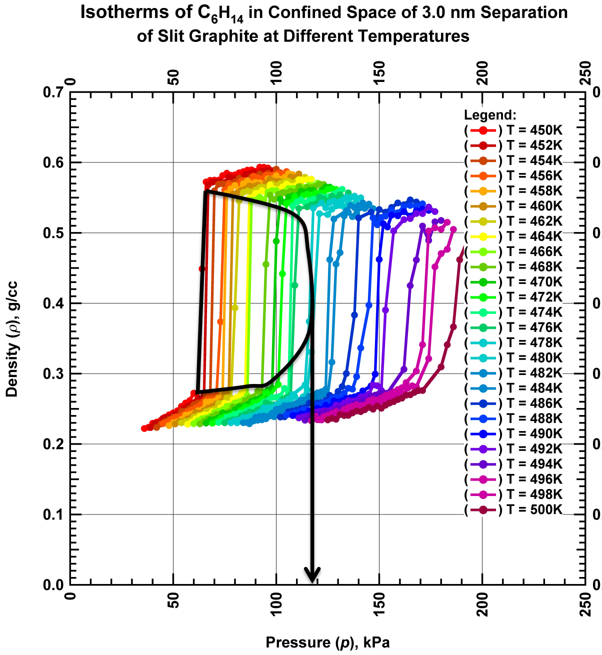

Figure 4-15 – Phase diagram of confined pentane in 3.0 nm of separation of a slit graphite pore (representing kerogen in shale reservoir).

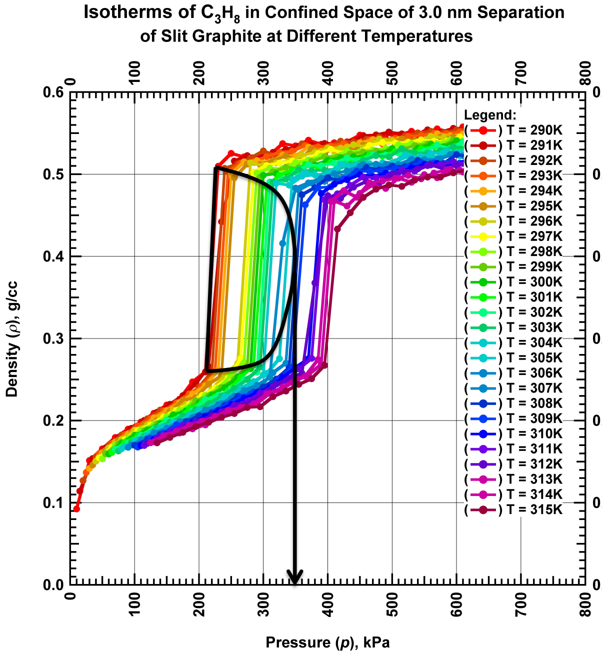

Figure 4-16 – Phase diagram of confined hexane in 3.0 nm of separation of a slit graphite pore (representing kerogen in shale reservoir).

Table 4-4 – Critical properties of confined propane in different pore sizes.

Separation (H), nm	Critical temperature (T_c)	Critical pressure (p_c)
2.0	244 K or -20.5˚ F	7 kPa or 1.0 psi
3.0	307 K or 92.93˚ F	345 kPa or 50 psi
4.0	333 K or 139.7˚ F	1010 kPa or 146 psi
5.0	348 K or 166.7˚ F	1675 kPa or 243 psi
6.0	358 K or 184.7˚ F	2300 kPa or 334 psi
7.0	364 K or 195.5˚ F	2675 kPa or 388 psi
8.0	366 K or 199.1˚ F	2875 kPa or 417 psi
9.0	367 K or 200.9˚ F	3000 kPa or 435 psi
10.0	368 K or 202.7˚ F	3075 kPa or 446 psi
Bulk Fluid	369.8 K or 206˚ F	4250 kPa or 616 psi

Table 4-5 – Critical properties of confined butane in different pore sizes.

Separation (H), nm	Critical temperature (T_c)	Critical pressure (p_c)
2.0	279 K or 42.5˚ F	1.5 kPa or 0.2 psi
3.0	375 K or 215.3˚ F	245 kPa or 35 psi
4.0	402 K or 263.9˚ F	710 kPa or 103 psi
5.0	414 K or 285.5˚ F	1120 kPa or 162 psi
6.0	422 K or 299.9˚ F	1400 kPa or 203 psi
7.0	423 K or 301.7˚ F	1540 kPa or 223 psi
8.0	424 K or 303.5˚ F	1645 kPa or 239 psi
9.0	425 K or 305.3˚ F	1725 kPa or 250 psi
10.0	425 K or 305.3˚ F	1750 kPa or 254 psi
Bulk Fluid	425.1 K or 305.5˚ F	3796 kPa or 551 psi

Table 4-6 – Critical properties of confined pentane in different pore sizes.

Separation (H), nm	Critical temperature (T_c)	Critical pressure (p_c)
2.0	333 K or 139.7˚ F	1.1 kPa or 0.2 psi
3.0	432 K or 317.9˚ F	180 kPa or 26 psi
4.0	456 K or 361.1˚ F	487 kPa or 71 psi
5.0	460 K or 368.3˚ F	700 kPa or 102 psi
6.0	464 K or 375.5˚ F	840 kPa or 122 psi
7.0	465 K or 377.3˚ F	925 kPa or 134 psi
8.0	466 K or 379.1˚ F	980 kPa or 142 psi
9.0	467 K or 380.9˚ F	1020 kPa or 145 psi
10.0	468 K or 382.7˚ F	1050 kPa or 152 psi
Bulk Fluid	469.7 K or 385.8˚ F	3369 kPa or 489 psi

Table 4-7 – Critical properties of confined hexane in different pore sizes.

Separation (H), nm	Critical temperature (T_c)	Critical pressure (p_c)
2.0	370 K or 206.3˚ F	0.5 kPa or 0.1 psi
3.0	480 K or 404.3˚ F	118 kPa or 17 psi
4.0	489 K or 420.5˚ F	280 kPa or 41 psi
5.0	494 K or 429.5˚ F	410 kPa or 59 psi
6.0	499 K or 438.5˚ F	515 kPa or 75 psi
7.0	502 K or 443.9˚ F	580 kPa or 84 psi
8.0	504 K or 447.5˚ F	635 kPa or 92 psi
9.0	506 K or 451.1˚ F	670 kPa or 97 psi
10.0	507 K or 452.9˚ F	700 kPa or 102 psi
Bulk Fluid	507.4 K or 453.7˚ F	3012 kPa or 437 psi

According to the data in **Tables 4-4**, **4-5**, **4-6** and **4-7**, it is noticeable that for the nanoscale pore size, the fluid's critical properties change with the pore size and become different from the bulk properties. This is because the interactions between the pore walls and the fluid molecules become significant and impact the behavior of the fluid molecules. Both the critical temperature and pressure of the confined propane, butane, pentane, and hexane decrease when the pore is smaller. At low pressure, with the same temperature, the confined hydrocarbons are denser than the bulk fluid because the attractive potential of the surface wall allows fluid molecules to adhere to the walls of the confining system and also to interact strongly with each other. Consequently, the confined fluid condenses at lower pressure than the bulk fluid does. This phenomenon may shift the phase envelope to a lower critical temperature and pressure, and a different critical density.

Figures 4-17a and **4-17b** are plots of those properties versus pore size of the confined propane. It can be observed that when $H \leq 4.0$ nm, the critical properties decay rapidly. The effect of the interaction between the surface wall and the confined fluid becomes less significant when the pore size increases and its critical properties approach the bulk properties which is similar to what we observed in the previous chapter. This observation agrees with the hypothesis that interaction between the wall of the container and the contained fluid becomes significant to the fluid's behavior and causes changes in the fluid properties. However, this effect is negligible when the pore is adequately large. Consequently, for sufficiently large pores, the confined fluid can be treated as a bulk fluid.

In addition, we notice that the critical temperature of the confined fluid becomes equal to the bulk critical temperature when $H > 10.0$ nm, whereas the critical pressure of the confined fluid becomes equal to the bulk critical pressure when $H > 30.0$ nm. It implies that the effect of confinement on both of the critical properties is not the same. For instance, the confinement effects a greater change in the critical pressure than in the critical temperature.

Figures 4-18, **4-19,** and **4-20** are plots of those properties versus pore size of the confined butane, pentane, and hexane, respectively. Similar to the confined propane, it can be observed that when $H \leq 4.0$ nm, the critical properties decay rapidly and the effect of the interaction between the surface wall and the confined fluid becomes less significant when the pore size increases. For these confined fluids, the critical temperatures become equal to the bulk critical temperatures when $H > 10.0$ nm, whereas the critical pressures of the confined fluids are still less than the bulk critical pressures when $H = 40.0$ nm. This shows that there is a greater effect of confinement on critical pressures than on critical temperatures.

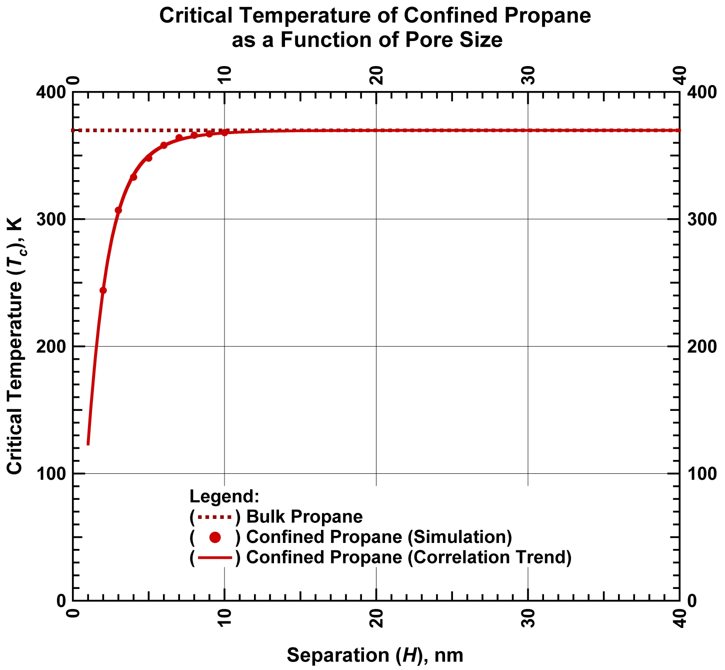

(a)

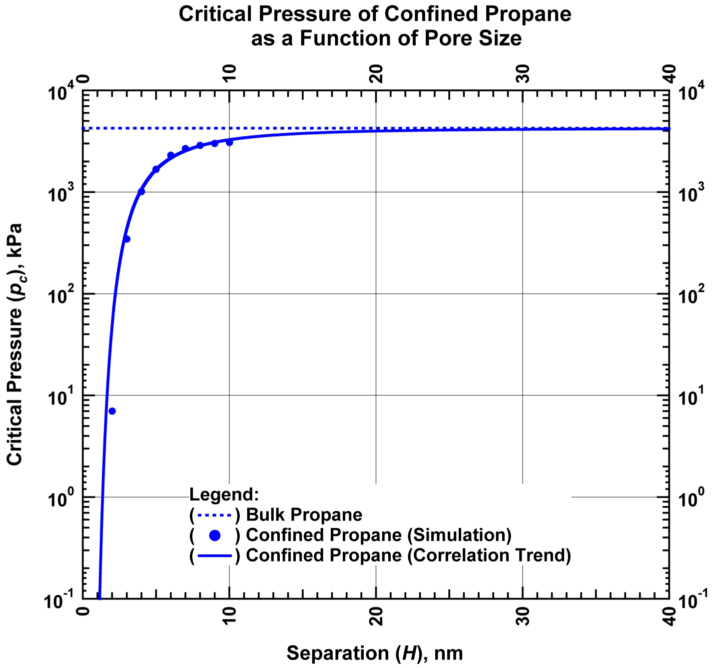

(b)

Figure 4-17 – (a) Plot of critical temperature and (b) critical pressure of confined propane versus separation of a slit graphite pore (representing kerogen in shale reservoir).

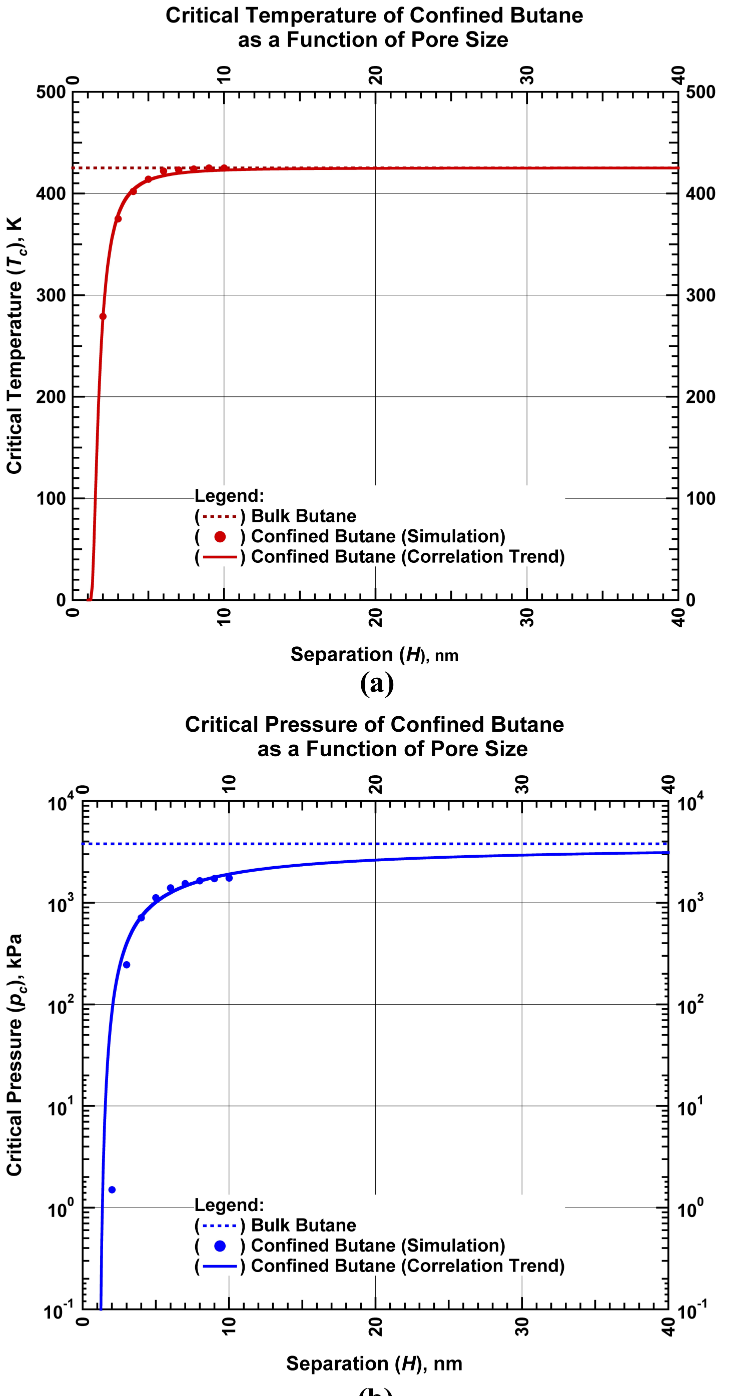

(a)

(b)

Figure 4-18 – (a) Plot of critical temperature and (b) critical pressure of confined butane versus separation of a slit graphite pore (representing kerogen in shale reservoir).

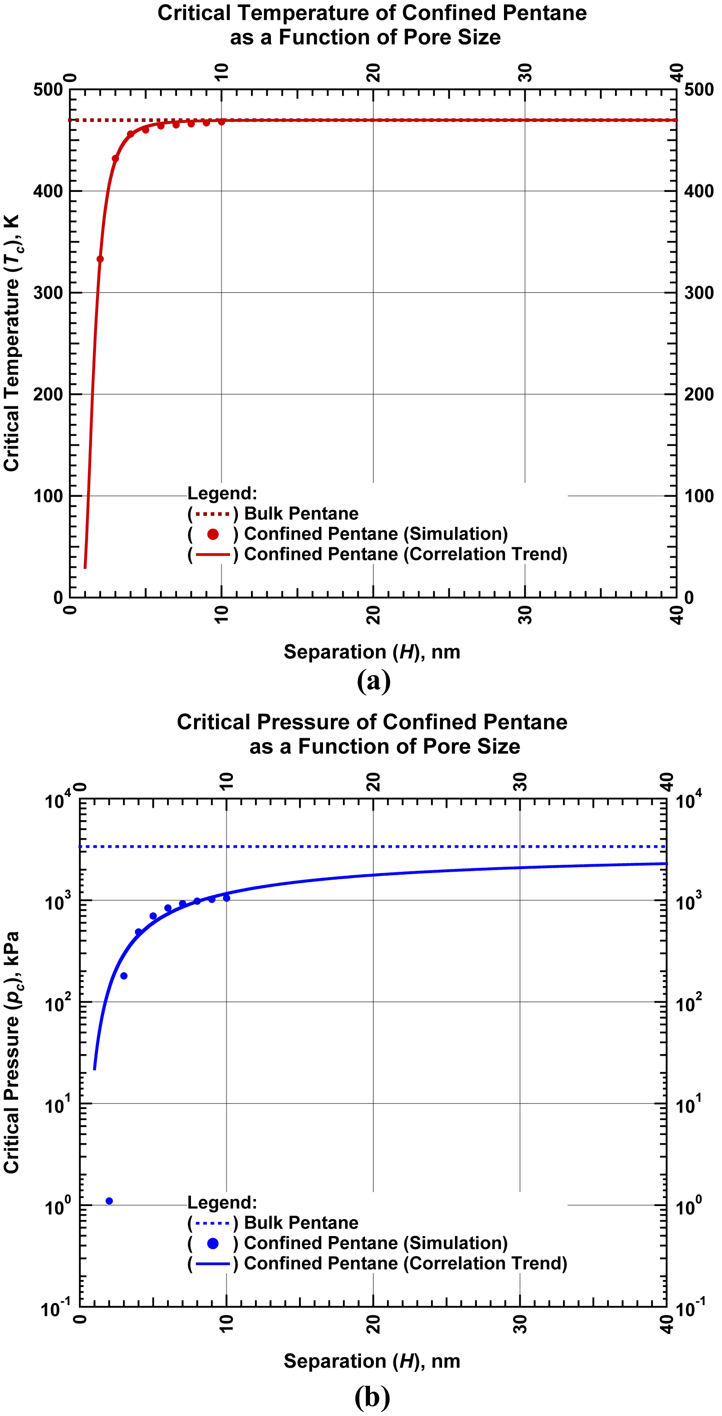

Figure 4-19 – (a) Plot of critical temperature and (b) critical pressure of confined pentane versus separation of a slit graphite pore (representing kerogen in shale reservoir).

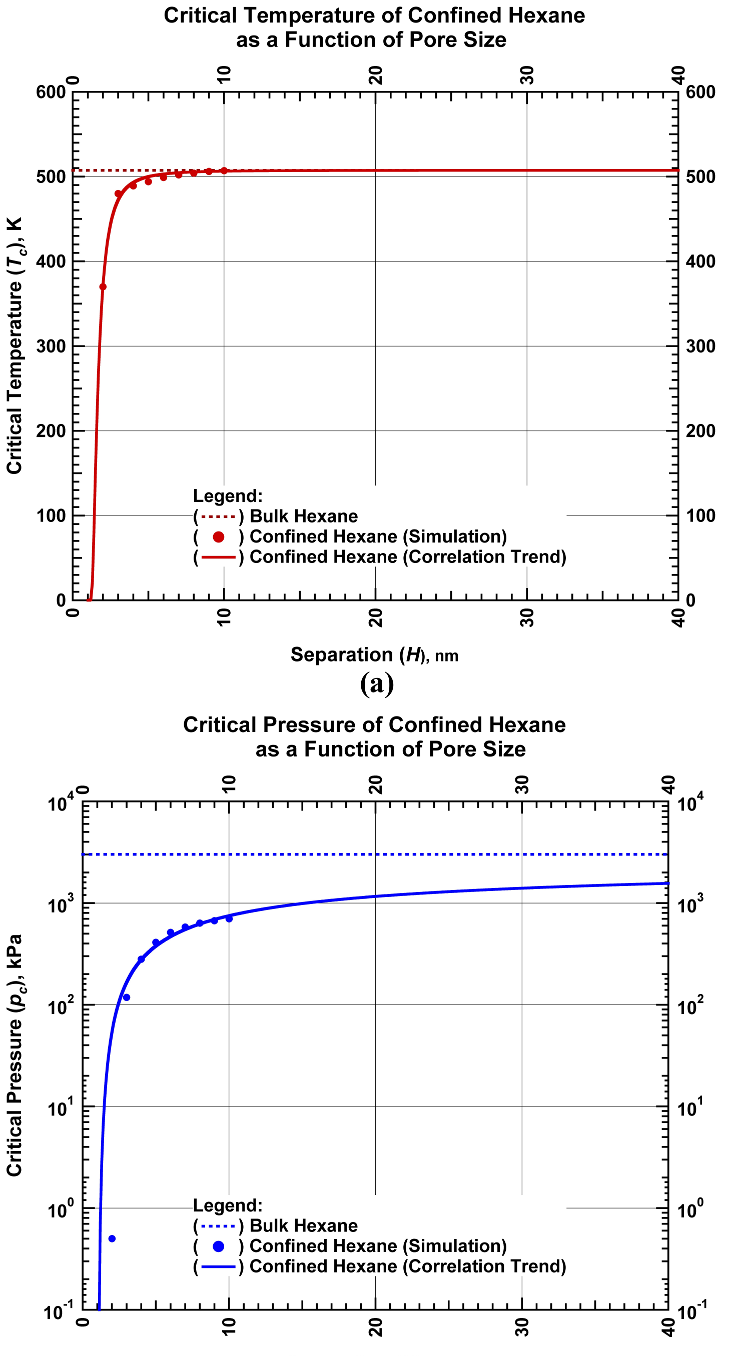

(a)

(b)

Figure 4-20 – (a) Plot of critical temperature and (b) critical pressure of confined hexane versus separation of a slit graphite pore (representing kerogen in shale reservoir).

4.5 Comparison of Critical Shifts from Our Simulations with the Approximation Models

Once we obtained the new critical properties of confined pure hydrocarbons in the previous section, the critical shifts were able to be computed by their definition, where the critical temperature shift is $\left(T_c - T_{cp}\right)/T_c$ and the critical pressure shift is $\left(p_c - p_{cp}\right)/p_c$.

Figures 4-21, **4-22**, **4-23,** and **4-24** illustrate comparisons of the shifts in critical properties of propane, butane, pentane, and hexane in different pore sizes from our GCMC simulation results and from the approximation models discussed in Chapter I (i.e. Zarragoicoechea and Kuz (2004): equations (1-11) and (1-12), Devegowda et al. (2012): equations (1-13) and (1-14), and Jin et al. (2013) and Ma et al. (2013): equations (1-15) and (1-16)). It can be noticed that the shifts in critical temperatures of long chain alkanes from the simulations have a similar trend to those from the models (**Figures 4-21a**, **4-22a**, **4-23a,** and **4-24a**). Specifically, Jin et al. and Ma et al.'s models which give a very good match on the shift in the critical temperature of ethane. On the other hand, none of these models provide a good approximation of the shifts in critical pressures of propane, butane, pentane, and hexane. We remark that the shifts in the critical properties from Zarragoicoechea and Kuz's model, Jin et al. and Ma et al.'s models, and the GCMC simulations approach zero when the pore size increases. This implies that the confined fluids tend to behave as the bulk when the pore is large. However, there is a large disagreement in the critical shifts of the pressure from the approximation models with our simulation results, especially for heavier hydrocarbon components.

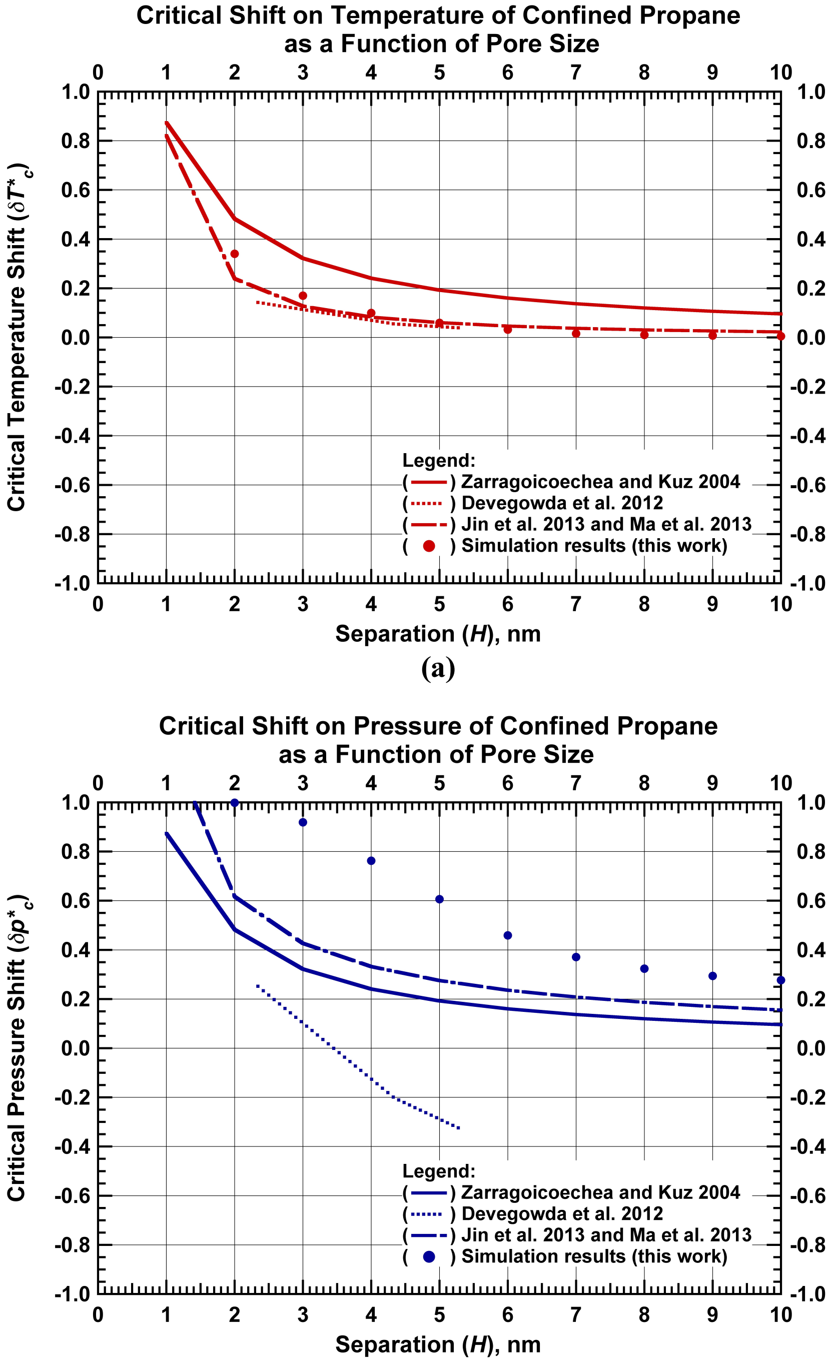

(a)

(b)

Figure 4-21 – Comparison of the critical shifts on temperature (a) and pressure (b) of confined propane from Zarragoicoechea and Kuz's, Devegowda et al.'s, Jin et al. and Ma et al.'s models, and this work GCMC simulation results.

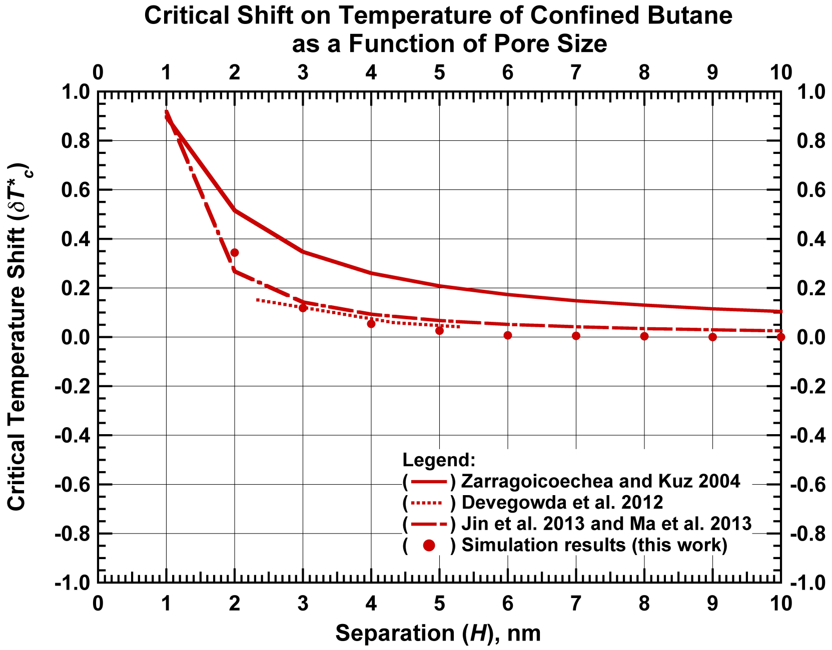

(a)

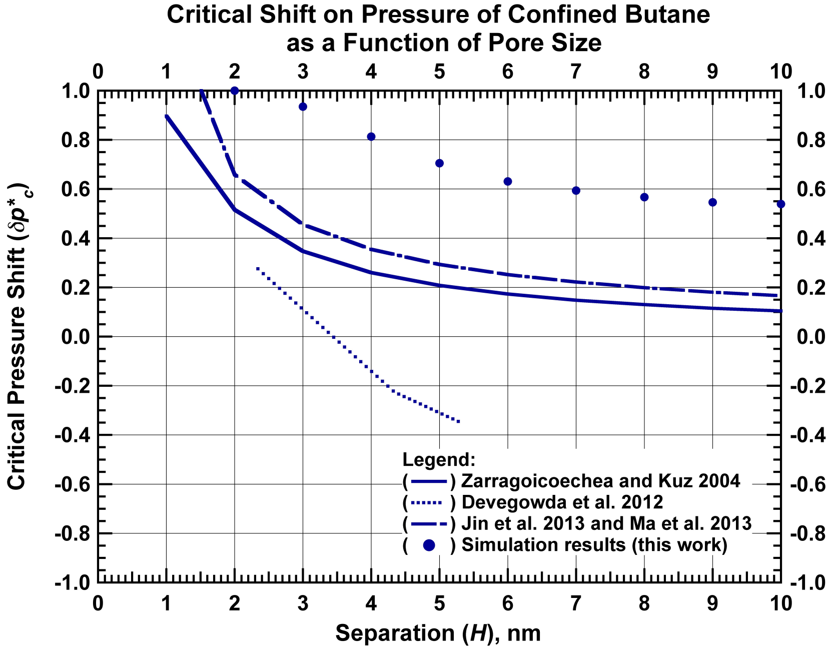

(b)

Figure 4-22 – Comparison of the critical shifts on temperature (a) and pressure (b) of confined butane from Zarragoicoechea and Kuz's, Devegowda et al.'s, Jin et al. and Ma et al.'s models, and this work GCMC simulation results.

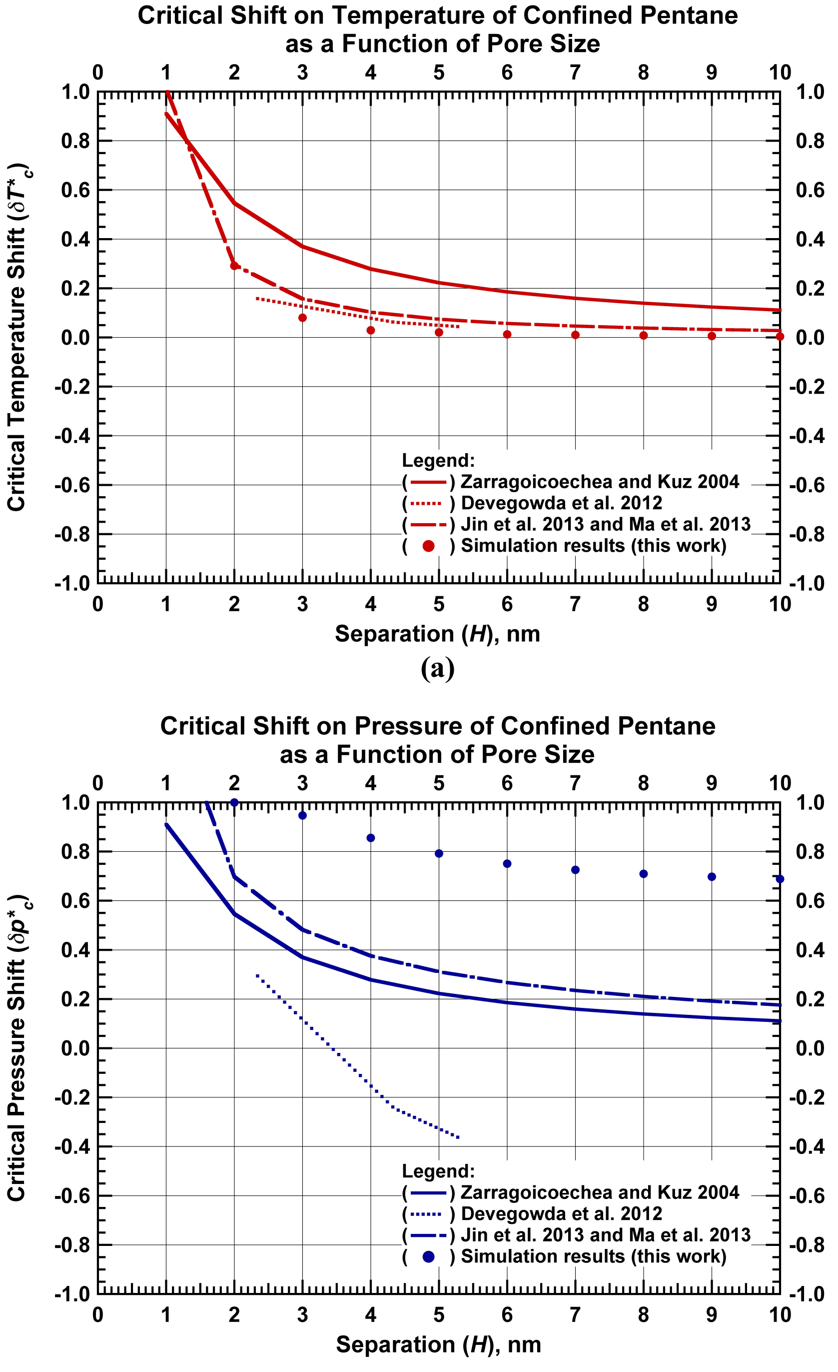

(a)

(b)

Figure 4-23 – Comparison of the critical shifts on temperature (a) and pressure (b) of confined pentane from Zarragoicoechea and Kuz's, Devegowda et al.'s, Jin et al. and Ma et al.'s models, and this work GCMC simulation results.

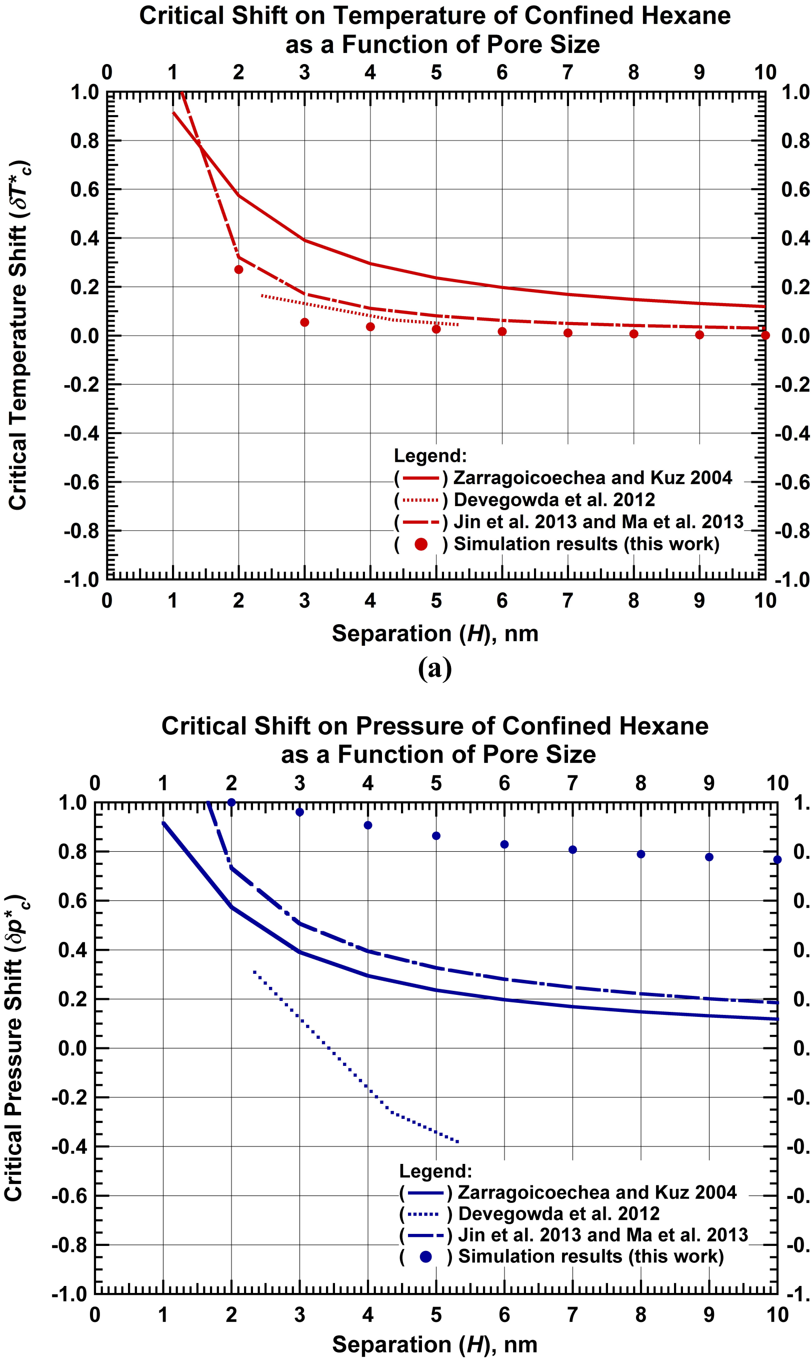

(a)

(b)

Figure 4-24 – Comparison of the critical shifts on temperature (a) and pressure (b) of confined hexane from Zarragoicoechea and Kuz's, Devegowda et al.'s, Jin et al. and Ma et al.'s models, and this work GCMC simulation results.

4.6 Density Shift Confined Pure Hydrocarbon at Reservoir Condition

The phase diagrams and critical properties of the confined pure components of propane, butane, pentane, and hexane, in the nanoscale, differ from those in bulk conditions. As a result, CB-GCMC simulations were employed to obtain fluid densities of pure components of those long chain alkanes at reservoir conditions. Eagle Ford reservoir temperatures and pressures listed in **Table 3-3** were used in this work. According to the reservoir properties, the possible lower and upper limits of the temperatures used in the molecular simulations are T = 385 K and T = 460 K, respectively, and the pressure is varied from 42.5 MPa to 80 MPa for all the cases.

The isotherms obtained from the CB-GCMC simulation are converted to the confined fluid densities using equation (3-3) and compared with the bulk densities from the National Institute of Standards and Technology database. The absolute maximum deviation for the confined fluid densities compared with the bulk properties can be calculated using equation (3-4).

Figures 4-25a and **4-25b** illustrate densities of confined propane in different sizes of slit graphite pores at T = 385 K and T = 460 K, respectively. In both cases, the confined density is higher than the bulk density. In particular, when $H \geq 1.5$ nm, the fluid density in smaller pores deviates from the bulk density more so than it does in bigger pores. This is because the strength of the attractive potential allows more molecules to populate the system and this effect increases as the pore size decreases. However, it is noticed that the fluid density in the slit pore with $H = 1.0$ nm is lower than that in the slit pore with $H = 1.5$ nm. This is because when $H = 1.0$ nm, the distance between the two layers of the graphite is too short to offer flexibility in terms of molecular orientation and arrangement for the confined propane. In other words, the separation is less than twice the smallest effective length of the propane molecule (one adsorbed layer on each side).

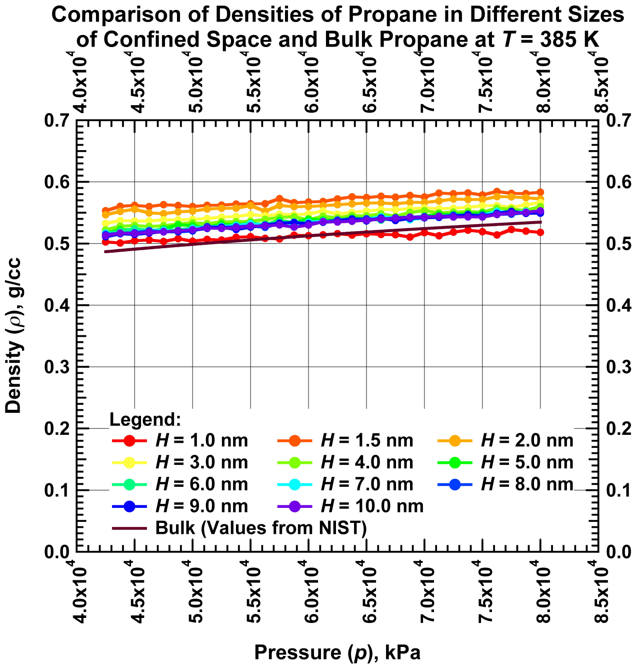

(a)

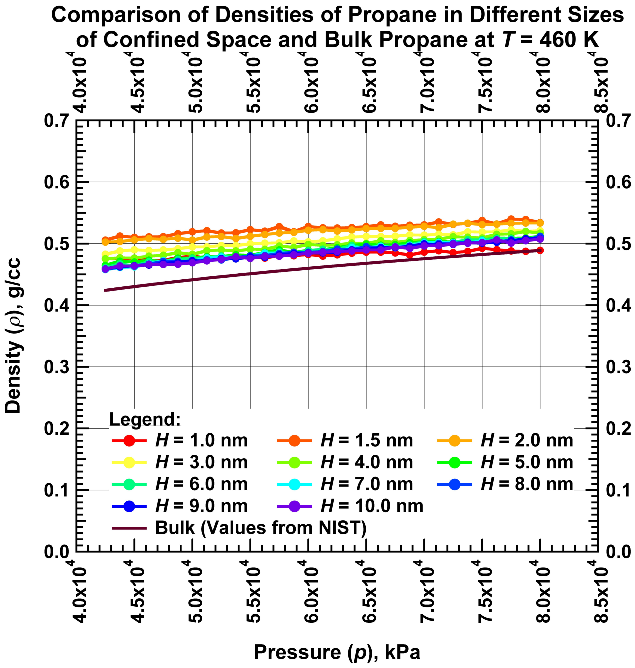

(b)

Figure 4-25 – Comparison of bulk and confined propane densities at the (a) minimum and (b) maximum Eagle Ford shale reservoir temperatures.

The maximum absolute deviations of the confined propane in different pore sizes from the bulk are summarized in **Table 4-8**. At the reservoir conditions, huge deviations of confined propane densities (~19.9%) occur when H = 1.5 nm due to the strong effect of confinement of the kerogen pore in the shale reservoir. However, it becomes less significant when the pore size increases. The difference between the confined fluid density in the largest pore in this work (H = 10.0 nm) and the bulk density may be caused by a combination of the effect of confinement and the error from force fields used to represent methyl and methylene groups in the propane molecule.

Figures 4-26a and **4-26b** illustrate densities of confined butane in different sizes of slit graphite pores at T = 385 K and T = 460 K, respectively. Similar to the propane case, the confined density is higher than the bulk density. In particular, when $H \geq 1.5$ nm, the fluid density in smaller pores deviates from the bulk density more so than it does in bigger pores because the strength of the attractive potential allows more molecules to populate the system and this effect increases as the pore size decreases. In addition, it is noticed that the fluid density in the slit pore with $H = 1.0$ nm is lower than that in the pore with $H = 1.5$ nm. This is because when $H = 1.0$ nm, the distance between the two layers of the graphite is too short to offer flexibility in terms of molecular orientation and arrangement for the confined butane.

Table 4-8 – Absolute maximum deviation of confined propane densities from bulk propane.

Separation (H), nm	% of Absolute maximum deviation from bulk propane	
	at T = 385 K	at T = 460 K
1.0	3.3%	12.1%
1.5	14.7%	19.9%
2.0	13.2%	18.5%
3.0	9.9%	14.2%
4.0	8.6%	12.1%
5.0	7.2%	10.4%
6.0	6.9%	9.3%
7.0	7.1%	8.3%
8.0	6.9%	8.2%
9.0	7.1%	8.3%
10.0	7.3%	8.6%

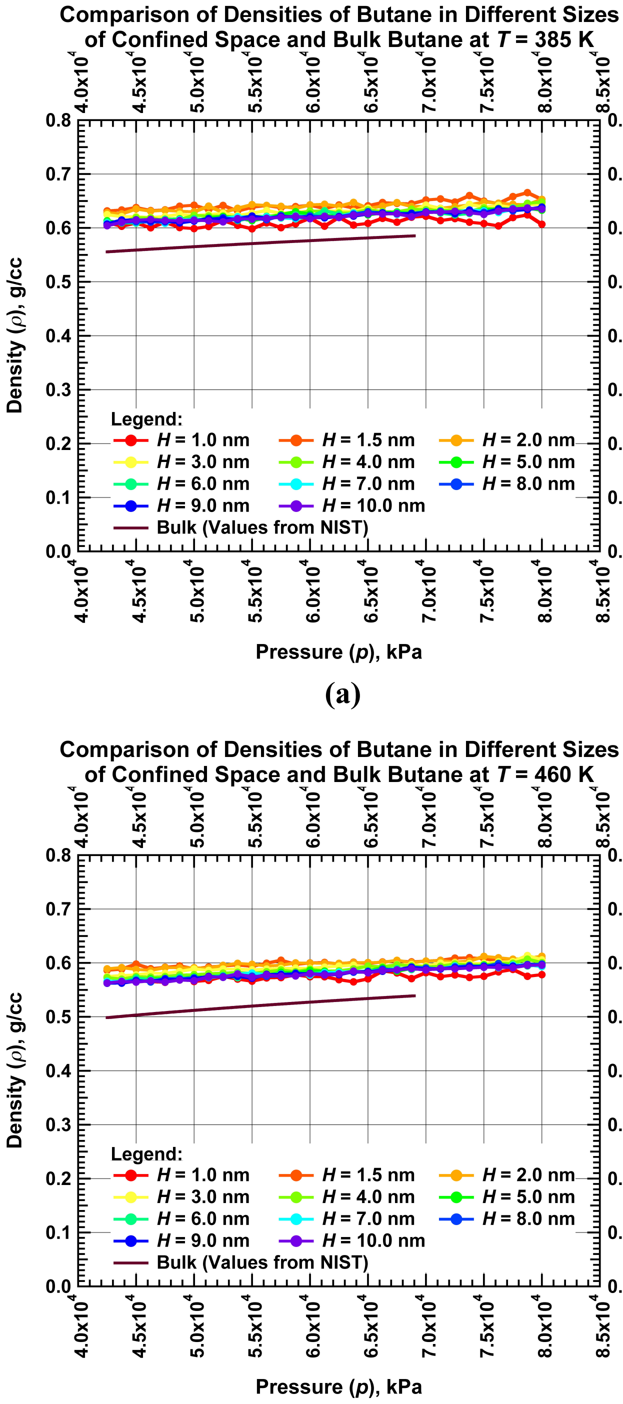
Comparison of Densities of Butane in Different Sizes of Confined Space and Bulk Butane at T = 385 K

(a)

Comparison of Densities of Butane in Different Sizes of Confined Space and Bulk Butane at T = 460 K

(b)

Figure 4-26 – Comparison of bulk and confined butane densities at the (a) minimum and (b) maximum Eagle Ford shale reservoir temperatures.

The maximum absolute deviations of the confined butane in different pore sizes from the bulk are summarized in **Table 4-9**. At the reservoir conditions, huge deviations of confined butane densities (~18.8%) occur when H = 1.5 nm due to a strong effect of confinement of the kerogen pore in the shale reservoir. However, it becomes less significant when the pore size increases. The range of the confined butane densities in different pore sizes at the same temperature and pressure is narrower than that of the propane case. This is because at the reservoir conditions, the butane density is already high. Consequently, it is harder to insert additional larger molecules (butane) than smaller molecules (propane) into the confined system. Moreover, the difference between the confined fluid density in the largest pore in this work (H = 10.0 nm) and the bulk density may be caused by a combination of the effect of confinement and the error from force fields used to represent methyl and methylene groups in the butane molecule.

Table 4-9 – Absolute maximum deviation of confined butane densities from bulk butane.

Separation (H), nm	% of Absolute maximum deviation from bulk butane	
	at T = 385 K	at T = 460 K
1.0	9.8%	13.1%
1.5	15.0%	18.8%
2.0	13.6%	18.1%
3.0	12.4%	15.6%
4.0	11.9%	14.9%
5.0	10.4%	13.5%
6.0	10.3%	13.7%
7.0	10.3%	13.5%
8.0	10.1%	13.0%
9.0	10.3%	12.8%
10.0	10.0%	13.0%

Figures 4-27a and **4-27b** illustrate densities of confined pentane in different sizes of slit graphite pores at T = 385 K and T = 460 K, respectively. Similar to the previous cases, the confined density is higher than the bulk density. In particular, when $H \geq 1.5$ nm, the fluid density in smaller pores deviates from the bulk density more so than it does in bigger pores because the strength of the attractive potential allows more molecules to populate the system and this effect increases as the pore size decreases. In addition, it is noticed that the fluid density in the slit pore with $H = 1.0$ nm is lower than that in the pore with $H = 1.5$

nm. This is because when $H = 1.0$ nm, the distance between the two layers of the graphite is too short to offer flexibility in terms of molecular orientation and arrangement for the confined pentane.

The maximum absolute deviations of the confined pentane in different pore sizes from the bulk are summarized in **Table 4-10**. At the reservoir conditions, huge deviations of confined pentane densities (~19.6%) occur when H = 1.5 nm due to the strong effect of confinement of the kerogen pore in the shale reservoir. However, it becomes less significant when the pore size increases. The range of the confined pentane densities in different pore sizes at the same temperature and pressure is narrower than that of the previous cases. This is because at the reservoir conditions, the pentane density is already high. Consequently, it is harder to insert additional larger molecules (pentane) than smaller molecules (propane and butane) into the confined system. Moreover, the difference between the confined fluid density in the largest pore in this work (H = 10.0 nm) and the bulk density may be caused by a combination of the effect of confinement and the error from force fields used to represent methyl and methylene groups in the pentane molecule.

Figures 4-28a and **4-28b** illustrate densities of confined hexane in different sizes of slit graphite pores at T = 385 K and T = 460 K, respectively. Similar to the previous cases, the confined density is higher than the bulk density. In particular, when $H \geq 1.5$ nm, the fluid density in smaller pores deviates from the bulk density more so than it does in bigger pores because the strength of the attractive potential allows more molecules to populate the system and this effect increases as the pore size decreases. In addition, it is noticed that the fluid density in the slit pore with $H = 1.0$ nm is lower than that in the pore with $H = 1.5$ nm. This is because when $H = 1.0$ nm, the distance between the two layers of the graphite is too short to offer flexibility in terms of molecular orientation and arrangement for the confined hexane.

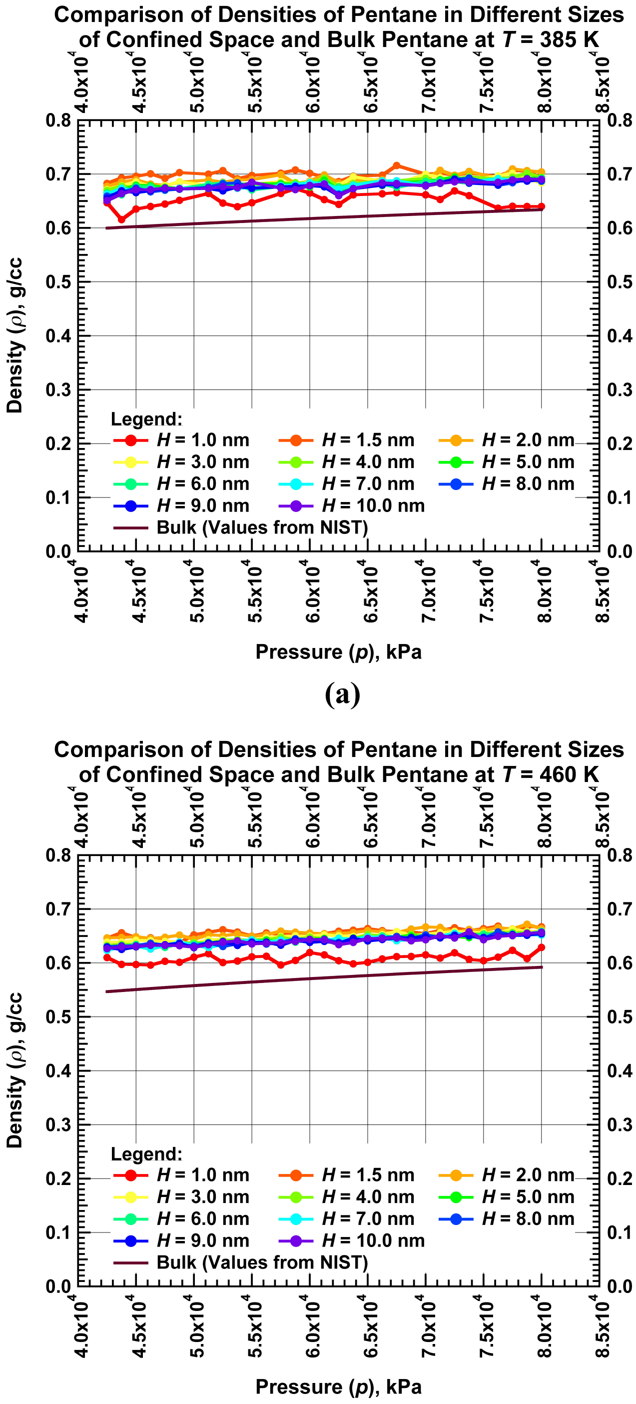
Comparison of Densities of Pentane in Different Sizes of Confined Space and Bulk Pentane at T = 385 K

(a)

Comparison of Densities of Pentane in Different Sizes of Confined Space and Bulk Pentane at T = 460 K

(b)

Figure 4-27 – Comparison of bulk and confined pentane densities at the (a) minimum and (b) maximum Eagle Ford shale reservoir temperatures.

Table 4-10 – Absolute maximum deviation of confined pentane densities from bulk pentane.

Separation (H), nm	% of Absolute maximum deviation from bulk pentane	
	at T = 385 K	at T = 460 K
1.0	9.2%	11.6%
1.5	16.0%	19.6%
2.0	14.5%	18.3%
3.0	13.7%	16.8%
4.0	13.3%	15.7%
5.0	12.8%	15.3%
6.0	12.3%	15.2%
7.0	12.1%	14.9%
8.0	11.8%	15.2%
9.0	11.4%	15.0%
10.0	11.8%	14.8%

The maximum absolute deviations of the confined hexane in different pore sizes from the bulk are summarized in **Table 4-11**. At the reservoir conditions, huge deviations of confined hexane densities (~18.8%) occur when H = 1.5 nm due to the strong effect of confinement of the kerogen pore in the shale reservoir. However, it becomes less significant when the pore size increases. The range of the confined hexane densities in different pore sizes at the same temperature and pressure is narrower than that of the previous cases. This is because at the reservoir conditions, the hexane density is already high. Consequently, it is harder to insert additional larger molecules (hexane) than smaller molecules (propane, butane, and pentane) into the confined system. Moreover, the difference between the confined fluid density in the largest pore in this work (H = 10.0 nm) and the bulk density may be caused by a combination of the effect of confinement and the error from force fields used to represent methyl and methylene groups in the hexane molecule.

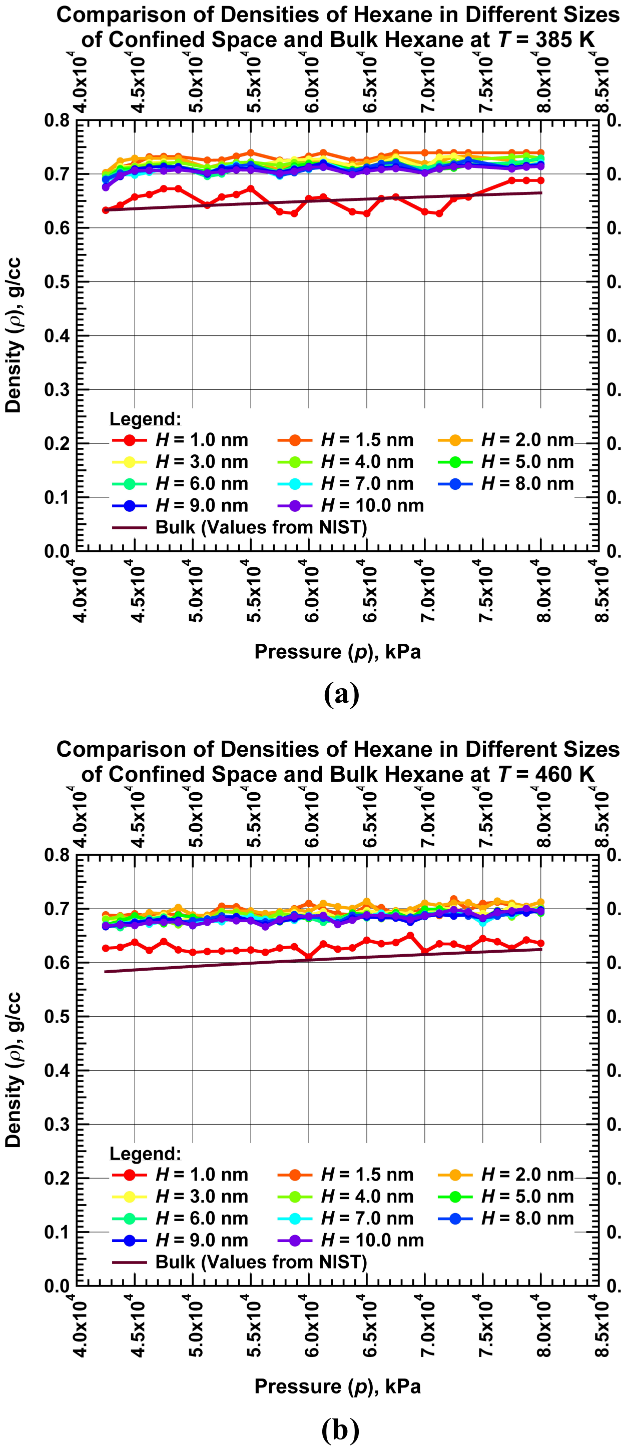

Comparison of Densities of Hexane in Different Sizes of Confined Space and Bulk Hexane at T = 385 K

(a)

Comparison of Densities of Hexane in Different Sizes of Confined Space and Bulk Hexane at T = 460 K

(b)

Figure 4-28 – Comparison of bulk and confined hexane densities at the (a) minimum and (b) maximum Eagle Ford shale reservoir temperatures.

Table 4-11 – Absolute maximum deviation of confined hexane densities from bulk hexane.

Separation (H), nm	% of Absolute maximum deviation from bulk hexane	
	at T = 385 K	at T = 460 K
1.0	5.6%	8.8%
1.5	14.9%	18.3%
2.0	14.7%	18.8%
3.0	13.2%	17.0%
4.0	12.9%	17.1%
5.0	12.2%	17.1%
6.0	11.9%	16.1%
7.0	11.6%	15.3%
8.0	11.4%	15.4%
9.0	11.9%	15.5%
10.0	11.2%	15.3%

4.7 Conclusion

For long chain alkanes, bond bending and bond torsion angles in the molecules may alter at high pressures and temperatures. The probability distribution of molecular configuration is dependent on the temperature and internal potential energy of the molecule. Therefore, intramolecular forces are necessary for the computation to obtain reasonable results. The CB-GCMC simulation is an appropriate technique to derive PVT properties of long chain alkanes. For this technique, bond lengths between carbon atoms are fixed while bond angles and dihedral angles are allowed to change.

We observed from our simulations that the critical temperature and pressure of pure component methane and ethane reduces as the pore size decreases. In short, the larger the pore size, the less significant the effect of confinement, and the more their critical properties approach the bulk properties (as expected).

The approximation models give good estimations of the shifts in critical pressures of propane, butane, pentane, and hexane. However, there is a large disagreement for the critical shifts of the pressure from the approximation models with our simulation results especially for heavier hydrocarbon components.

Moreover, according to the deviations of the confined propane, butane, pentane, and hexane densities from the bulk densities at the reservoir conditions, they may cause intolerable errors in reserves estimations and production forecast calculations if the bulk densities are used instead of the proper densities. The confined pure component of methane and ethane densities can deviate from their bulk properties by up to 19.9%, 18.8%, 19.6%, and 18.8%, respectively. We also noticed that the range of the confined fluid densities of the heavier hydrocarbon in different pore sizes at the same temperature and pressure is narrower than that of the lighter hydrocarbon.

We note that the pore actually has a distribution of pore sizes, and other restrictions such as pore interconnections may occur, which will make the phenomena even more complex. These will be incorporated in future work. However, the present results provide a first approximation of the confinement effect on the phase behavior of fluids in kerogen pores.

CHAPTER V

SIMULATION STUDIES OF CONFINED HYDROCARBON BINARY MIXTURES

In this chapter, the GCMC and CB-GCMC simulations are implemented to study the effect of interactions between the pore walls and the different types of fluid molecules in the system on the fluid's properties. The effect of confinement can cause the difference in fluid composition in the confined system from the bulk composition as the force field for different types of fluid molecules are varied. This creates a selective environment in the pore. The selectivity may change over pressure, temperature, and bulk fluid composition. The classical MD simulation helps us endorse the conclusion about the selectivity of the system obtained from the GCMC and CB-GCMC simulations. Furthermore, phase diagrams of confined binary methane-ethane mixtures in different pore sizes are derived using the GCMC and CB-GCMC simulations.

5.1 Analysis of Simulation Data

For a binary mixture system, the GCMC is used to determine not only the equilibrium density of the confined fluid at the given pressure and temperature, but also the fluid's composition in the confined system at equilibrium. Again, the isotherm of the confined system obtained from the GCMC simulation must satisfy equations (3-1a) and (3-1b) for each of the components of the mixture. The amounts of each type of fluid molecules in the confined system is dependent on the interaction between the sorbent (slit graphite pore) and sorbate (methane and ethane). Since the force fields of methane and ethane are different, the interactions between the pore wall and those fluid molecules are varied. This event causes a selective environment in the pore, and the system tends to adsorb one fluid more than the other. Thus, the fluid composition of the mixture in the confined system may disagree with the given bulk fluid composition.

To understand the selective environment in the confined space, consider the pore system with a separation of 5.0 nm connecting to a reservoir containing a binary mixture of methane and ethane as shown in **Figure 5-1**. The reservoir temperature and pressure are varied to study their effects on the isotherms of the confined mixture.

Figure 5-1 – Schematic of GCMC simulation of a methane-ethane mixture system.

Figures 5-2a, **5-2b**, **5-2c**, **5-2d**, and **5-2e** illustrate isotherms of methane and ethane in the confined space with 5.0 nm of separation at temperatures of 300 K, 325 K, 350 K, 375 K, and 400 K, respectively. The reservoir (bulk) pressure is varied from 200 kPa to 6.2 MPa for all cases. The *y*-axis of each plot is the density of each fluid type occupying the system in the unit of molecules per unit cell. The red line represents the isotherm of ethane, and the blue line represents the isotherm of methane in the mixture. If the confined system contained a mixture of 50% methane molecules and 50% ethane molecules as specified in the reservoir, the red line and the blue line must have been on top of each other. However, none of our cases gave results that suggested that the fluid composition in the confined system is the same as that in the reservoir. Again, this is because the interactions of both components with the pore walls create a selective environment in the slit graphite pore, and therefore result in changes in fluid behavior and properties in the confined system, including the fluid composition. From **Figures 5-2a**, **5-2b**, **5-2c**, **5-2d**, and **5-2e**, it can be concluded that our confined system adsorbs ethane (heavier component) more readily than methane, as the isotherms of ethane are higher than isotherms of methane for all the cases. However, the differences between isotherms of both components are different and dependent on temperature. For instance, the selective environment becomes weaker at a higher temperature. It is necessary to study further which parameters influence the selective environment in the confined system because this phenomenon may consequently effect the changes of phase diagrams of the mixture in confined space.

In the next section, we will introduce a parameter called selectivity, which is used to describe the selective environment in the confined system and study trends of this parameter as a function of a reservoir (bulk) pressure, temperature, pore size, and fluid composition.

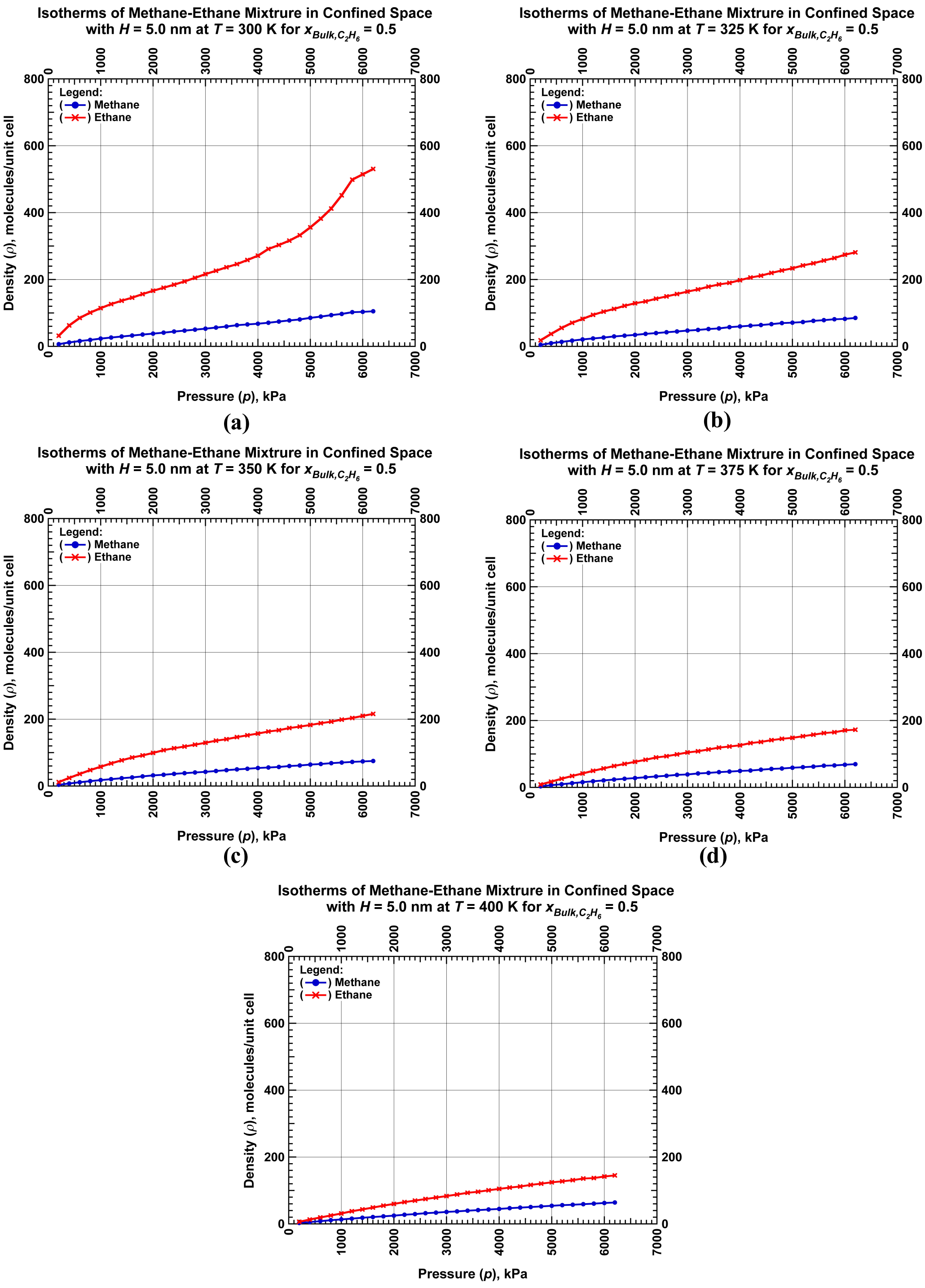

(a)

(b)

(c)

(d)

(e)

Figure 5-2 – Isotherms of methane and ethane in confined space with H = 5.0 nm and x_{Bulk,C_2H_6} = 0.5 at (a) T = 300 K, (b) T = 325 K, (c) T = 350 K, (d) T = 375 K, and (e) T = 400 K.

5.2 Selectivity of Confined System

5.2.1 Methane-Ethane Mixture

In the previous section, the GCMC simulation is used to demonstrate the effect of confinement on the fluid composition of a mixture in a slit graphite pore. We discover that the interactions between both components in the mixture and the pore walls generate a selective environment in the confined space. We also conclude that our confined system likes to adsorb ethane rather than methane as the isotherms of ethane are higher than the isotherms of methane for all the cases. The classical MD simulation is implemented to prove this statement.

We initiate a configuration with a fluid composed of 50% methane molecules and 50% ethane molecules as shown in **Figure 5-3a**. Graphene layers are put in the middle of the system to create a restricted space, representing a pore, while the rest of the system represents a bulk segment. The separation between the graphene layers is varied from 1.0 nm to 7.0 nm to study the effect of confinement. The temperature of the system is 300 K and the simulation time is 35 ns. An example of the final configuration for the case of $H =$ 5.0 nm is illustrated as **Figure 5-3b**. After the simulations have finished, the total energy must be reached and allowed to stabilize at the minimal point to ensure that the final configuration is at equilibrium. An example of a plot of the total energy versus simulation time in this study is shown by **Figure 5-3c**. Mole fraction of ethane, $x_{C_2H_6}$, in each interval is computed over the y-direction. The plots of ethane mole fraction versus location in the y-direction for all the cases are shown in **Figure 5-3d**. From the plot, it can be observed that although the initial ethane mole fraction of fluid in all intervals of the system (including both the pore and the bulk segments) is equal to 0.5, the ethane mole fraction at equilibrium of each interval changes and varies throughout the system. For instance, at equilibrium, the ethane mole fraction in the slit pore segment (the area between the two red dashed line in **Figure 5-3d**) for all the cases is greater than 0.5 and consequently the ethane mole fraction in the bulk segment is lower than 0.5. Especially, the mole fraction of ethane of the confined mixture in a smaller pore is significantly higher than that in a bigger pore. This confirms our conclusion obtained from the previous section that ethane is preferable to methane for our system. Moreover, the ethane mole fraction in the smaller pore is greater than that in the larger pore even though the starting condition of each case is the same. According to the ethane mole fraction profiles in the y-direction (see **Figure 5-3d**), the difference of the ethane mole fraction between the slit pore segment and the bulk segment is larger for a smaller pore, and the profile turns out to be less fluctuated as the ethane mole fraction approaches 0.5, the average value of the total system as the pore is bigger. This implies that as the pore size increases, the influence of the interactions between the fluid molecules and the pore walls becomes less significant upon fluid behavior and properties so that fluid composition in the slit pore segment and the bulk segment are similar. Thus, it can be concluded that the selective environment is also dependent on pore size.

To further study the effect of confinement on fluid properties of binary mixtures, one of the parameters that should be explored is selectivity. Selectivity is defined as the ratio of mole fractions in the adsorbed pore divided by the ratio of mole fractions in the bulk mixture (Cracknell et al., 1993). The selectivity of ethane over methane is computed as follows:

$$S_{C2/C1} = \frac{x_{Confined,C_2H_6}/x_{Confined,CH_4}}{x_{Bulk,C_2H_6}/x_{Bulk,CH_4}} \quad \text{..(5-1).}$$

The GCMC simulation is implemented to study trends of selectivity as a function of reservoir (bulk) pressure, temperature, pore size, and fluid composition.

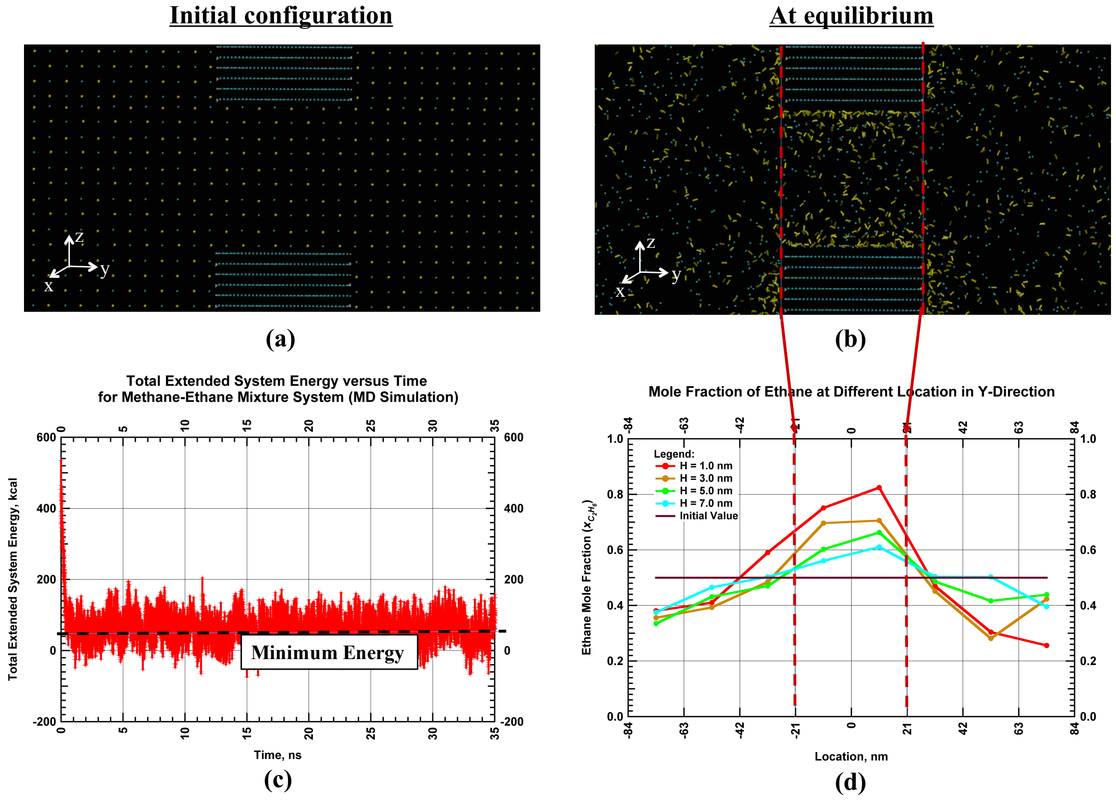

Figure 5-3 – (a) Initial and (b) final configuration at t_s = 35 ns from classical MD simulation of methane-ethane mixture in slit graphite pore with H = 5.0 nm at T = 300K, (c) total extended system energy over simulation time, and (d) ethane mole fraction profile in the *y*- direction of the mixture in different pore sizes.

The GCMC simulation was set up (see **Figure 5-1**) to study the trends of selectivity as a function of temperature. The reservoir pressure and bulk ethane mole fraction are fixed at 5 MPa and 0.5, respectively. The reservoir temperature was varied from 300 K to 400 K. The selectivity as a function of temperature in different pore sizes is plotted (see **Figure 5-4**). It can be observed that the selectivity of ethane over methane are greater than unity for all the cases, meaning that ethane is preferable to methane in our confined system. As temperature increases, the selectivity tends to decrease. This implies that our confined system becomes less selective at higher temperatures. Furthermore, as pore size increases, the selectivity decreases and approaches unity. Here, the fluid composition of the bulk and confined mixtures are identical, as expected, since the effect of the interaction between the fluid molecules and the pore walls becomes less significant.

Figure 5-5 illustrates the selectivity as a function of the reservoir (bulk) pressure at a temperature of 400K and an ethane mole fraction of 0.5 in the bulk. The reservoir pressure is varied from 200 kPa to 6.2 MPa. It can be observed that the selectivity tends to decrease as the reservoir pressure increases at H = 3.0 nm, but it is almost constant over the pressure range for H = 5.0 nm to 7.0 nm. However, this statement is not always valid. For instance, at different temperatures, the selectivity may not remain constant when the reservoir pressure changes, especially during the phase transition. The selectivity may increase when the mixture changes from the vapor phase to the liquid phase. We can apply this concept to derive the *P-x* diagram of the binary mixture in a confined space. We will discuss the variation of selectivity at the phase transition later in this chapter. Similar to the previous study, as pore size increases, the selectivity decreases and approaches unity.

Figure 5-6 illustrates the selectivity as a function of the bulk fluid composition at a temperature of 400K and a reservoir pressure of 5 MPa. The ethane mole fraction in the bulk fluid is varied from 0.1 to 0.9. It is noticeable that the selectivity decreases as the ethane mole fraction in bulk increases at H = 3.0 nm, but it almost remains the same over the ethane mole fraction for H = 5.0 nm and 7.0 nm. Again, this statement is not always true. For instance, at different temperatures and pressures, the selectivity may vary when the bulk fluid composition changes, especially at the phase transition. In addition, the selectivity decreases and approaches unity when the pore size increases.

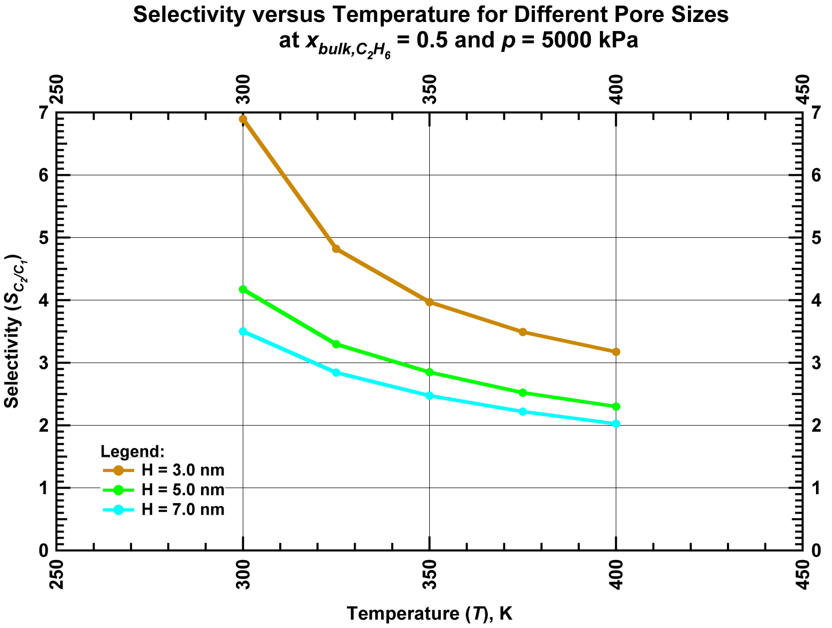

Figure 5-4 – Selectivity as a function of temperature in different pore sizes at p = 5.0 MPa and x_{Bulk,C_2H_6} = 0.5.

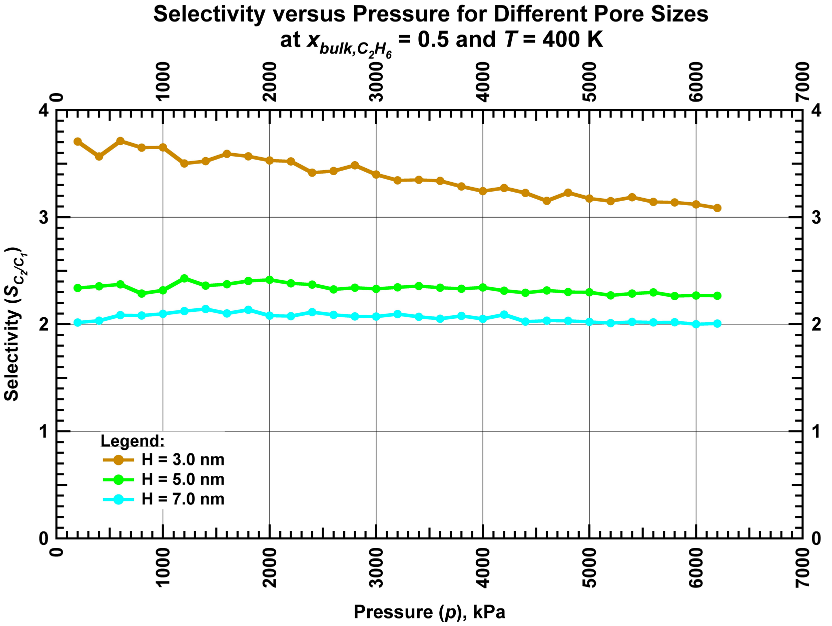

Figure 5-5 – Selectivity as a function of pressure in different pore sizes at T = 400 K and x_{Bulk,C_2H_6} = 0.5.

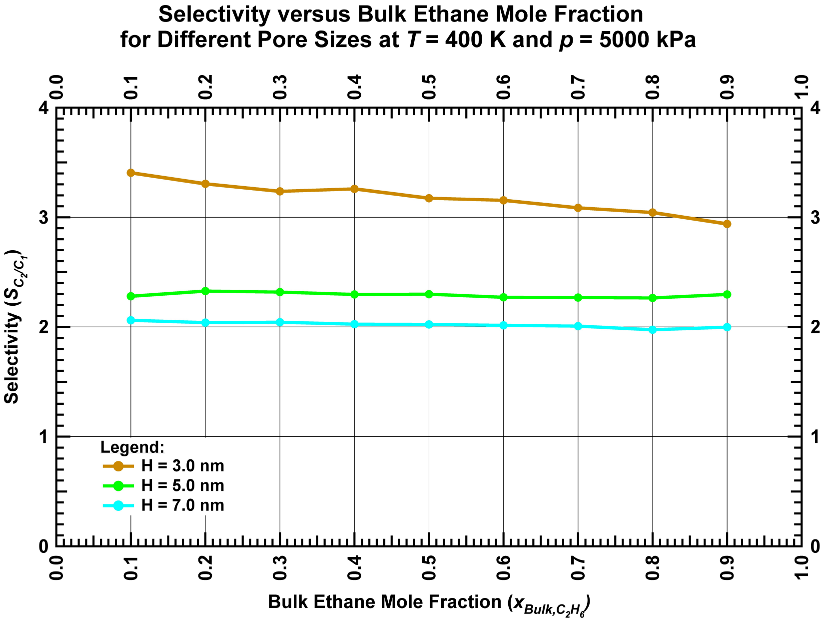

Figure 5-6 – Selectivity as a function of bulk fluid composition in different pore sizes at T = 400 K and p = 5.0 MPa.

From this study, it can be concluded that our confined system likes to adsorb ethane rather than methane and that the selectivity of ethane over methane is a function of the reservoir (bulk) temperature, pressure, bulk fluid composition, and pore size. As the temperature increases, the selectivity tends to decrease. In some cases, the selectivity tends to decrease as pressure and bulk ethane mole fraction increase. In addition, as the pore size increases, the selectivity trend decreases and approaches unity because the effect of confinement becomes ineffective upon the confined fluid properties and behavior. In other words, the confined fluid behaves more like the bulk fluid when the pore size increases.

5.2.2 Methane-Butane Mixture

In this section, the CB-GCMC simulation is employed to observe the selectivity of methane-butane mixture in our confined system. **Figures 5-7a**, **5-7b**, **5-7c**, **5-7d**, and **5-7e** illustrate isotherms of methane-butane mixtures in the confined space with 5.0 nm of separation at temperatures of 300 K, 325 K, 350 K, 375 K, and 400 K, respectively. The reservoir (bulk) pressure is varied from 200 kPa to 6.2 MPa for all cases. The red line represents the isotherm of butane in the mixture, and the blue line represents the isotherm of methane in the mixture. We found that the fluid composition in the confined space differed from the bulk fluid composition because of the effect of confinement. From **Figures 5-7a**, **5-7b**, **5-7c**, **5-**

7d, and **5-7e**, it can be concluded that our confined system adsorbs butane (heavier component) more readily than methane, considering the isotherms of butane are higher than the isotherms of methane in all cases. The differences between the isotherms of both components are different and dependent on temperature. For instance, the selective environment becomes weaker at higher a temperature.

Similar to the previous case, we initiated a configuration with a fluid composed of 50% methane molecules and 50% butane molecules as shown in **Figure 5-8a**. In this case, the separation between the graphene layers is fixed at 5.0 nm. Temperature of the system is 300 K and the simulation time is 35 ns. The final configuration is illustrated in **Figure 5-8b**. After the simulation is done, the total energy must be reached and almost stabilize at the minimal point to ensure that the final configuration is at equilibrium. The total energy versus simulation time in this study is shown by **Figure 5-8c**. The mole fraction of butane, $x_{C_4H_{10}}$, in each interval is computed over the *y*-direction. The plot of the butane mole fraction versus location in the *y*-direction, as compared with the ethane mole fraction at the same condition from the previous case, is shown in **Figure 5-8d**. From the plot, it can be observed that although the initial butane mole fraction of fluid in all intervals in the system – including both of the pore and the bulk segments – is equal to 0.5, the butane mole fraction at equilibrium of each interval changes and varies throughout the system. For instance, at equilibrium, the butane mole fraction in the slit pore segment – the area between the two red dashed lines in **Figure 5-8d** – is greater than 0.5, and consequently the butane mole fraction in the bulk segment is lower than 0.5. It can be concluded that butane is preferable to methane for our system. According to **Figure 5-8d**, although the condition of methane-ethane and methane-butane mixtures are in the same condition, the butane mole fraction (solid line) in the pore segment is higher than the ethane mole fraction (dashed line). This implies that the selectivity of butane over methane in our confined system must be higher than the selectivity of ethane over methane at the same condition.

Similar to equation (5-1), the selectivity of butane over methane is computed as follows:

$$S_{C4/C1} = \frac{x_{C4,Confined}/x_{C1,Confined}}{x_{C4,Bulk}/x_{C1,Bulk}} \quad \text{..........} (5\text{-}2).$$

The CB-GCMC simulation is implemented to study trends of selectivity as a function of the reservoir (bulk) pressure, temperature, pore size, and fluid composition.

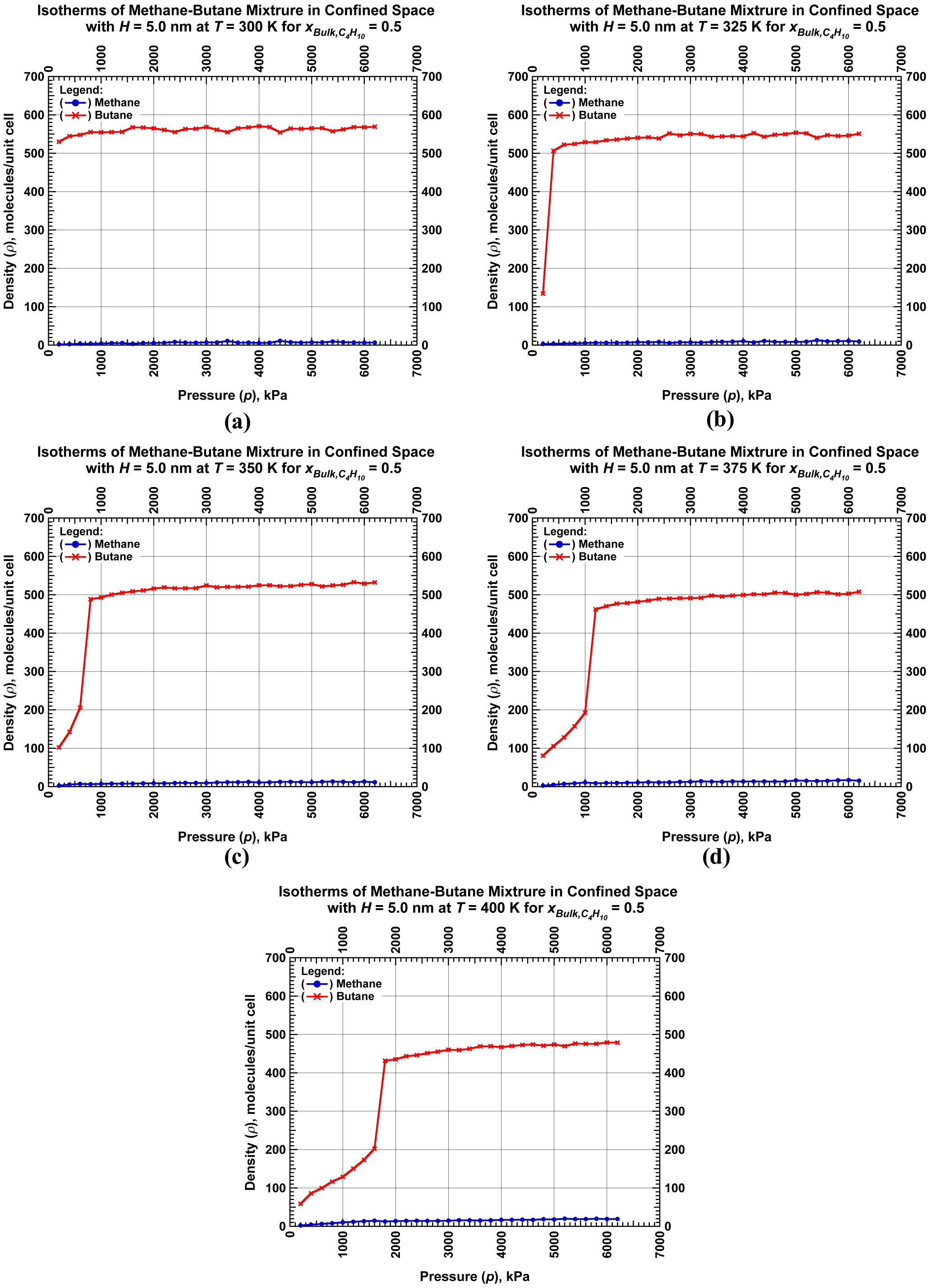

(a) (b) (c) (d) (e)

Figure 5-7 – Isotherms of methane and butane in confined space with H = 5.0 nm and $x_{Bulk,C_4H_{10}}$ = 0.5 at (a) T = 300 K, (b) T = 325 K, (c) T = 350 K, (d) T = 375 K, and (e) T = 400 K.

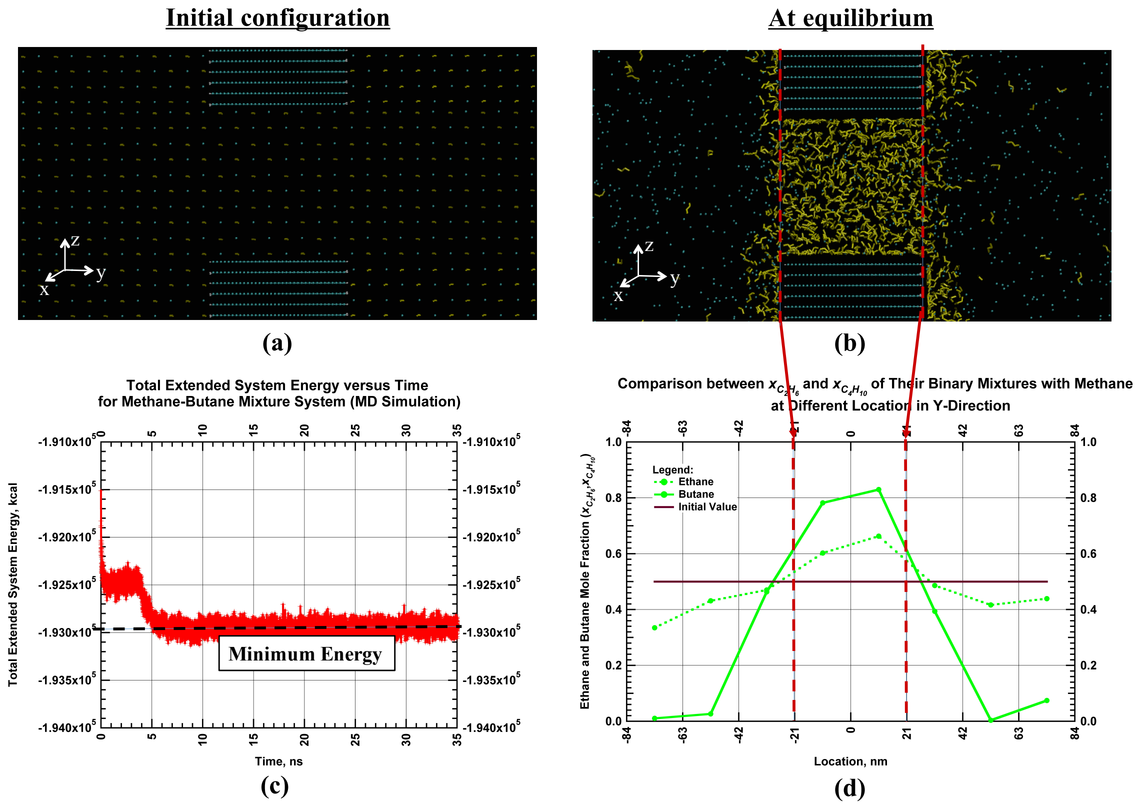

Figure 5-8 – (a) Initial and (b) final configuration at t_s = 35 ns from classical MD simulation of methane-butane mixture in slit graphite pore with H = 5.0 nm at T = 300K, (c) total extended system energy over simulation time, and (d) comparison of butane and ethane mole fraction profile in the y- direction of the mixture in 5.0 nm slit graphite pore.

The CB-GCMC simulation was set up (see **Figure 5-1**) to study the trends of selectivity as a function of temperature. The reservoir pressure and bulk ethane mole fraction are fixed at 5 MPa and 0.5, respectively. The reservoir temperature is varied from 300 K to 400 K. The selectivity, as a function of temperature, is plotted as a solid line in **Figure 5-9**. It can be observed that the selectivity of butane over methane is much higher than unity, meaning that butane is preferable to methane in our confined system. As temperature increases, the selectivity tends to decrease. This implies that our confined system becomes less selective at higher temperatures. In addition, the selectivity of butane over methane is higher than the selectivity of ethane over methane in all cases of temperature. We may conclude that our confined system adsorbs butane more readily than ethane.

Figure 5-10 illustrates selectivity as a function of the reservoir (bulk) pressure at a temperature of 400K and an ethane mole fraction of 0.5 in the bulk. The reservoir pressure is varied from 200 kPa to 6.2 MPa. It can be observed that the selectivity of butane over methane (solid line) tends to decrease as the reservoir pressure increases; however, at the phase transition, the jump of selectivity occurs. Then, the selectivity decreases as the pressure increases again. Similar to the previous study, the selectivity of butane over methane is always higher than the selectivity of ethane over methane (dashed line).

Figure 5-11 illustrates the selectivity as a function of the bulk fluid composition at a temperature of 400K and a reservoir pressure of 5 MPa. The butane mole fraction in the bulk is varied from 0.1 to 0.9. It is noticeable that the selectivity of butane over methane (solid line) is varied throughout different fluid compositions. There is a discontinuity in the selectivity between $x_{Bulk,C_4H_{10}}$ = 0.1 and $x_{Bulk,C_4H_{10}}$ = 0.2, because the confined mixture is in a vapor phase when $x_{Bulk,C_4H_{10}}$ = 0.1 and a liquid phase when $x_{Bulk,C_4H_{10}}$ = 0.2. Similar to the previous studies, the selectivity of butane over methane is always higher than the selectivity of ethane over methane (dashed line).

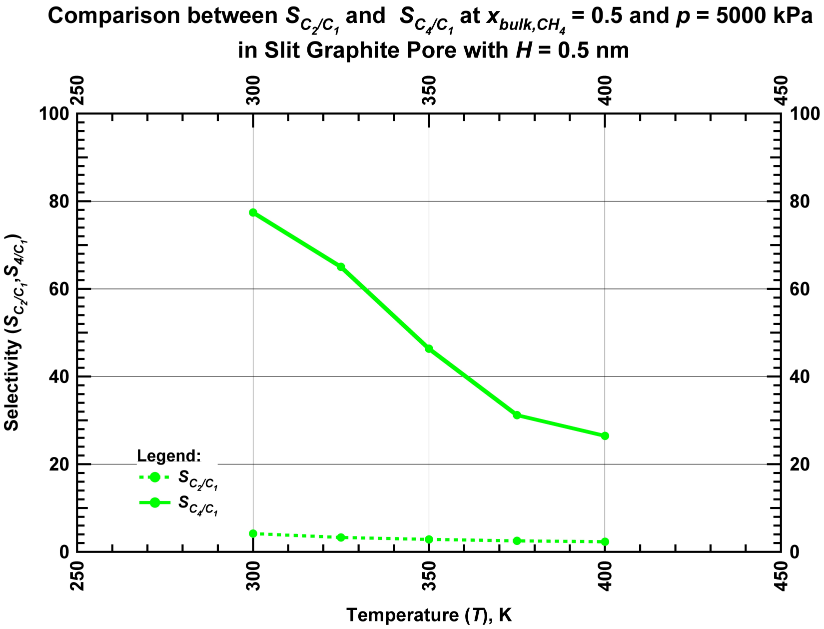

Figure 5-9 – Comparisons between selectivity of butane and ethane over methane as a function of temperature in 5.0 slit graphite pore at p = 5.0 MPa and $x_{Bulk,C_4H_{10}}$ = 0.5.

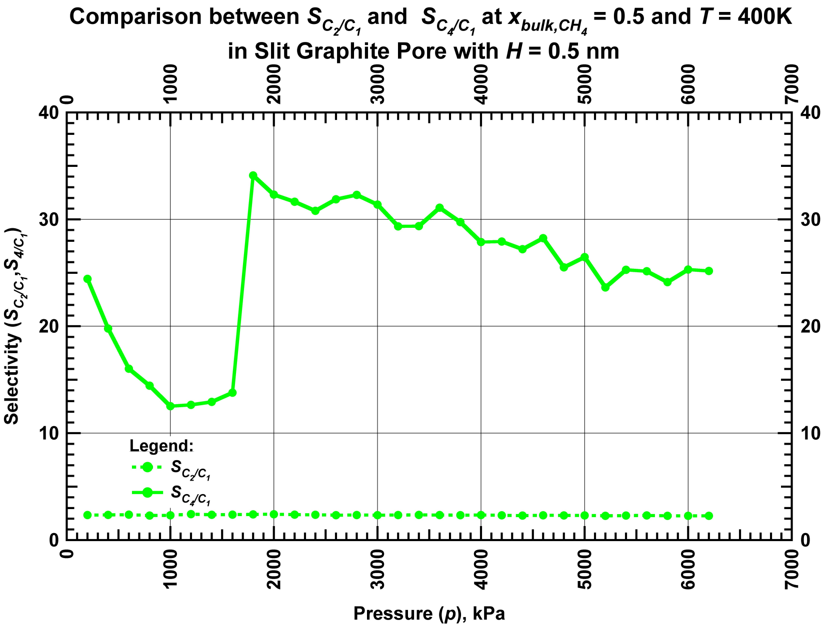

Figure 5-10 – Comparisons between selectivity of butane and ethane over methane as a function of pressure in 5.0 slit graphite pore at T = 400 K and $x_{Bulk,C_4H_{10}}$ = 0.5.

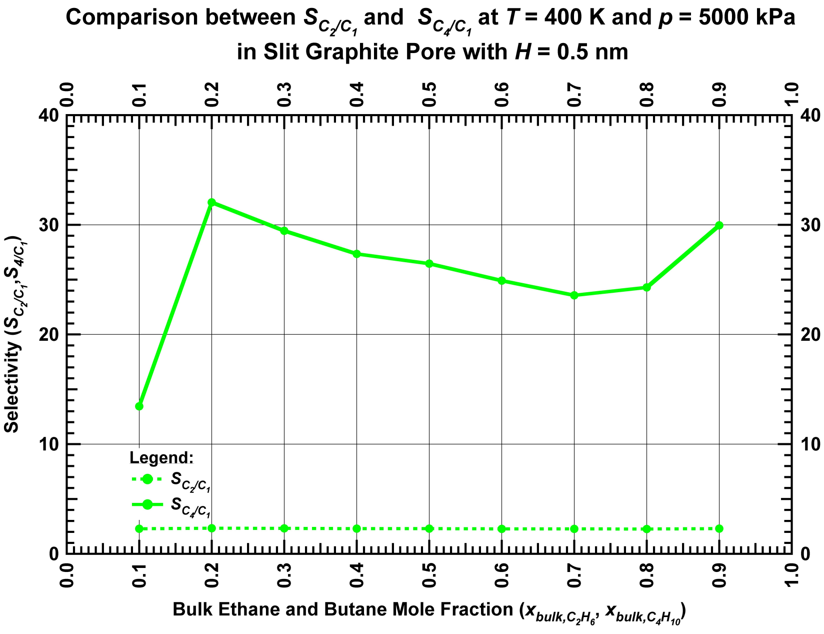

Figure 5-11 – Comparisons between selectivity of butane and ethane over methane as a function of bulk fluid composition in 5.0 slit graphite pore at T = 400 K and p = 5.0 MPa.

From this study, it can be concluded that our confined system likes to adsorb butane rather than ethane or methane and that the selectivity of butane over methane is a function of the reservoir (bulk) temperature, pressure, bulk fluid composition, and pore size. As the temperature increases, the selectivity tends to decrease. We also observe a jump or discontinuity of selectivity at the phase transition. The molar composition of the confined fluid at its vapor pressure can be used to generate a *P*-x diagram of the confined mixture.

5.3 Phase Diagram of Confined Hydrocarbon Binary Mixtures

5.3.1 Methane-Ethane Mixture

In the preceding section, the interactions between the fluid molecules and the pore walls caused deviations of fluid composition in the confined space. For our pore system, ethane was preferable to methane. Selectivity was introduced to describe the selective environment in our system and the deviation from bulk. The higher the selectivity was, the more our system deviated from the bulk. This selective environment may cause shifts of the phase diagrams in the confined space. The selectivity is a function of the reservoir (bulk) temperature, pressure, bulk fluid composition, and pore size.

In the previous section, we also observed a constant value of selectivity over the pressure range and ethane mole fraction when the pore size was equal to 5.0 nm and 7.0 nm. However, this is not always true, especially when the condition is close to the phase transition and critical point. To prove this statement, the GCMC simulation is implemented to determine the isotherms of methane and ethane in the slit graphite pore with H = 5.0 nm, T = 250 K, and x_{Bulk,C_2H_6} = 0.35 (see **Figure 5-12a**). The bulk pressure is varied from 4.2 MPa to 5.7 MPa by increments of 50 kPa. Similar to the confined pure component, as the pressure increased, the presence of both methane and ethane isotherms increased, causing an increase in the fluid density. At low pressure, the mixture fluid is in the vapor phase. At $p \approx$ 2350 kPa – 2400 kPa, the jump of isotherms occurred. This jump represents the phase transition, the shift from vapor density to liquid density of the mixture. The mole fraction of ethane in the confined mixture over the pressure range is computed and plotted in **Figure 5-12b**. From the plot, the ethane mole fraction of the confined mixture in the vapor phase is almost constant around 0.78. Similarly, the ethane mole fraction of the confined mixture in the liquid phase is almost constant around 0.85. At the vapor pressure, the jump of the ethane mole fraction can be detected. It implies that at the phase transition, the equilibrium ethane mole fractions of the vapor and liquid phases are different, and the discontinuity of the trend of selectivity or ethane mole fraction of the confined mixture occurs. This concept is applied to derive *P*-x diagrams of confined binary mixtures later in this chapter. The selectivity of the mixture in the vapor phase and liquid phase are approximately 7.0 and 10.9. Thus, at this condition, the selectivity jumps from 7.0 to 10.9 at the phase transition. This proves that the selectivity of slit graphite pore with H = 5.0 nm varies based on the bulk pressure.

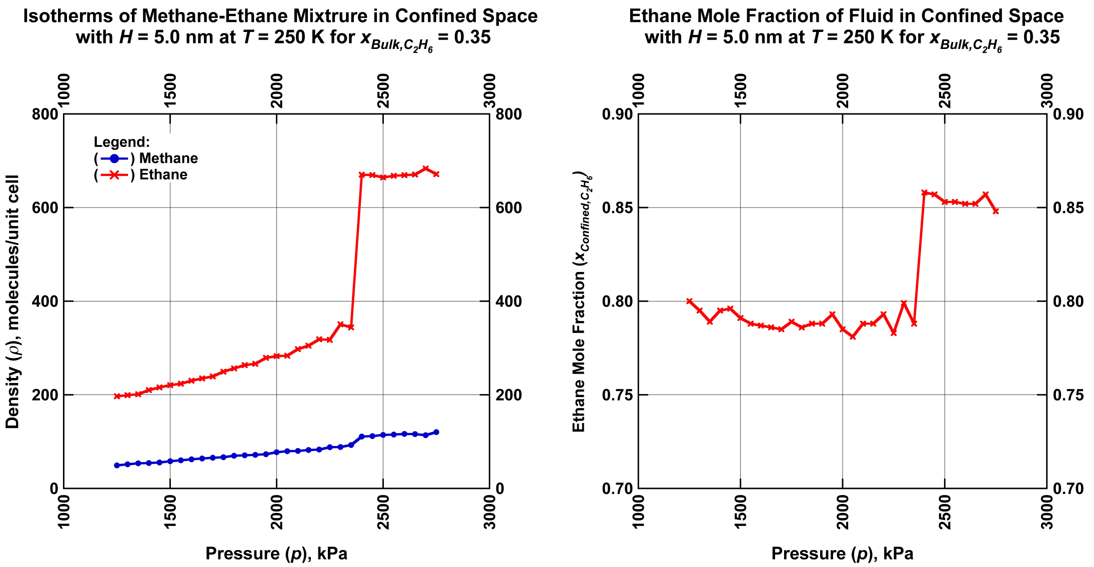

(a) **(b)**

Figure 5-12 – (a) Isotherms of methane and ethane, and (b) ethane mole fraction of confined mixture in slit graphite pore with H = 5.0 nm at T = 250 K and x_{Bulk,C_2H_6} = 0.35.

Figure 5-13a illustrates isotherms of methane and ethane in the slit graphite pore with H = 5.0 nm at T = 250 K and x_{Bulk,C_2H_6} = 0.15. At this condition, the mixture is a supercritical fluid near its critical point. Again, the bulk pressure is varied from 4.2 MPa to 5.7 MPa by increments of 50 kPa. At low pressures, similar to the previous case, the presence of methane and ethane isotherms increased, causing increased fluid density with increased pressure. However, the jump of isotherms cannot be noticed in this case. In other words, there is no phase transition since the fluid is in its supercritical condition. The mole fraction of ethane in the confined mixture over the pressure range is computed and plotted in **Figure 5-13b**. From the plot, the trend of the ethane mole fraction is continuous and increasing over the pressure range. This differs from the previous case where the trend is discontinuous at the phase transition. The selectivity continuously increases from 6.8 at p = 4.2 MPa to 8.8 at p = 5.7 MPa. Again, this proves that the selectivity of a slit graphite pore with H = 5.0 nm varies based on the bulk pressure. At the same bulk pressure, the selectivity of this case is lower than that of the previous case (x_{Bulk,C_2H_6} = 0.35). For example, at p = 4.2 MPa, the selectivity of the previous case is equal to 7.4 which is higher than the selectivity of 6.8 from this case. Thus, we can conclude that the selectivity is dependent on bulk fluid composition.

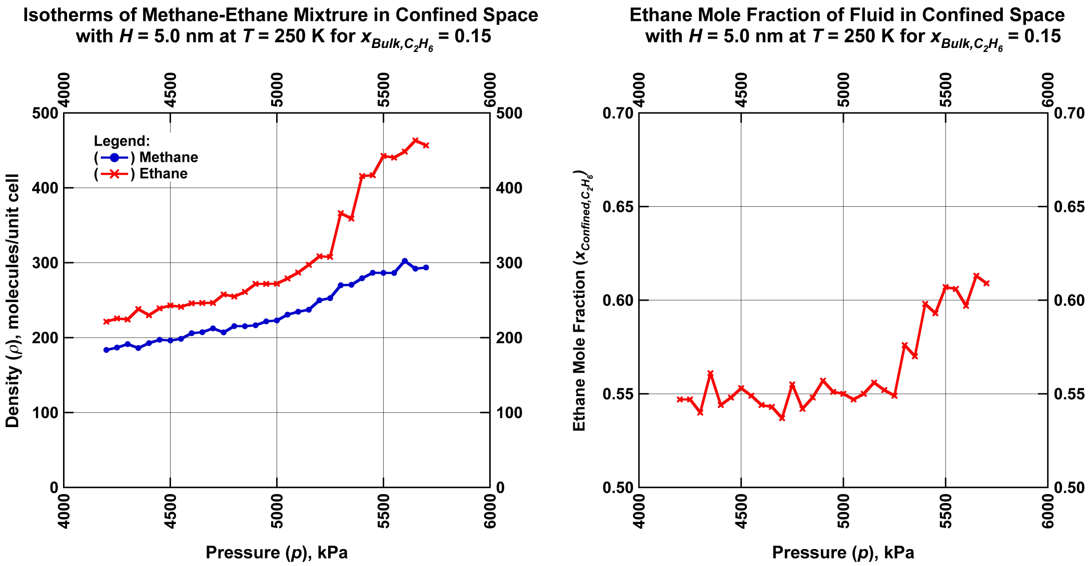

(a) **(b)**

Figure 5-13 – (a) Isotherms of methane and ethane, and (b) ethane mole fraction of confined mixture in slit graphite pore with H = 5.0 nm at T = 250 K and x_{Bulk,C_2H_6} = 0.15.

To draw a phase diagram and find critical properties of a hydrocarbon mixture, phase transitions of the mixture with different compositions must be determined. According to the isotherms of the confined mixture shown in **Figure 5-12**, the equilibrium composition of the confined pore is a two-phase mixture having ethane in vapor ($y_{Confined,C_2H_6}$) (78.8%) and liquid ($x_{Confined,C_2H_6}$) phases (85.8%). These results indicate that the original gas mixture splits into two phases that are rich in ethane. Multiple scenarios of this type of simulation with different fluid compositions are needed to generate a phase diagram, or *P-x* diagram (pressure-composition), for a mixture. Once isotherms for each component are acquired, the fluid composition in the vapor and liquid phases, at the saturation pressure of the mixture, can be computed. Consequently, these data are used to create a phase diagram and obtain a critical point of the mixture. **Figure 5-14a** illustrates isotherms of a methane-ethane mixture indicating phase transition in a slit graphite pore with 5.0 nm of separation for different fluid compositions at T = 250K. **Figure 5-14b** is a corresponding *P-x* diagram at the constant temperature of 250 K. The critical point, shown as the purple circle (no. 9), can be seen in **Figures 5-14a** and **5-14b**. The line connecting critical points of the mixture with different fluid compositions is called the critical locus curve. This curve can be obtained by drawing a line that passes through the critical points of *P*-*x* diagrams at different temperatures. It is used to approximate critical properties of a mixture as a function of its fluid composition.

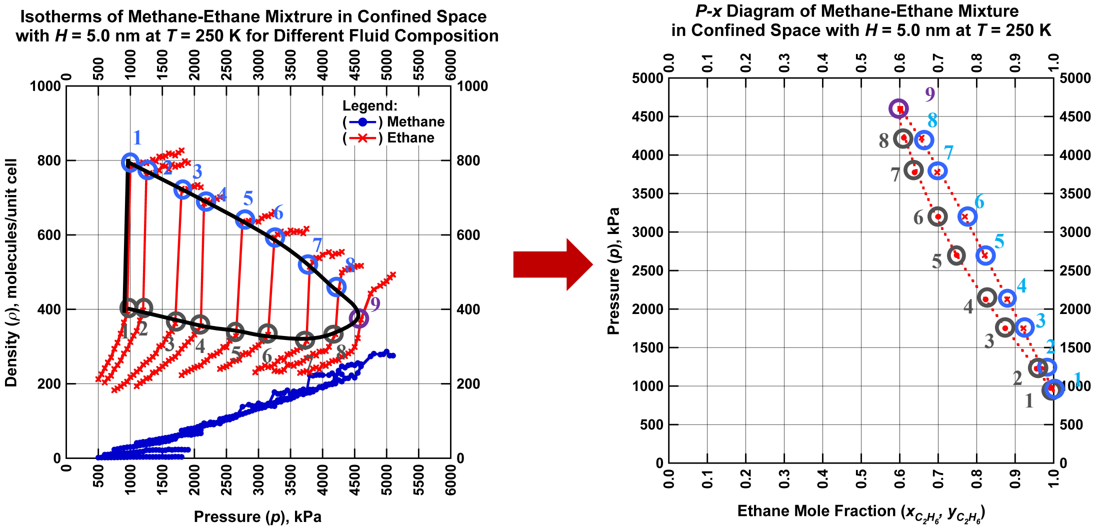

(a) **(b)**

Figure 5-14 – (a) Isotherms of the methane-ethane mixture in a slit graphite pore with 5.0 nm of separation at *T* = 250 K and (b) the *P*-*x* diagram of the mixture corresponding to the isotherms.

In the previous chapter, it was shown that the effect of confinement caused the reduction in critical temperature and pressure of pure components of confined methane and ethane in slit graphite pores. For confined methane-ethane mixtures, interactions between the pore walls and the fluid molecules also affects the shape of the mixture phase envelope and critical properties such as the critical locus curve. **Figure 5-15a** illustrates a bulk phase diagram of a methane-ethane mixture derived from experimental data from Bloomer et al. (1953). The diagram contains a collection of the mixture phase envelopes (*P*-*x* diagram) at different temperatures. Connecting the critical points of each envelope yields a critical locus curve as shown by the maroon line in the plot. The area above the curve is the supercritical region. The intersections between the curve and the y-axis at $x_{Bulk,C_2H_6} = 0$ and $x_{Bulk,C_2H_6} = 1$ are the critical pressures of bulk methane and ethane respectively. Critical properties of the mixture at a specified composition can be estimated from this plot.

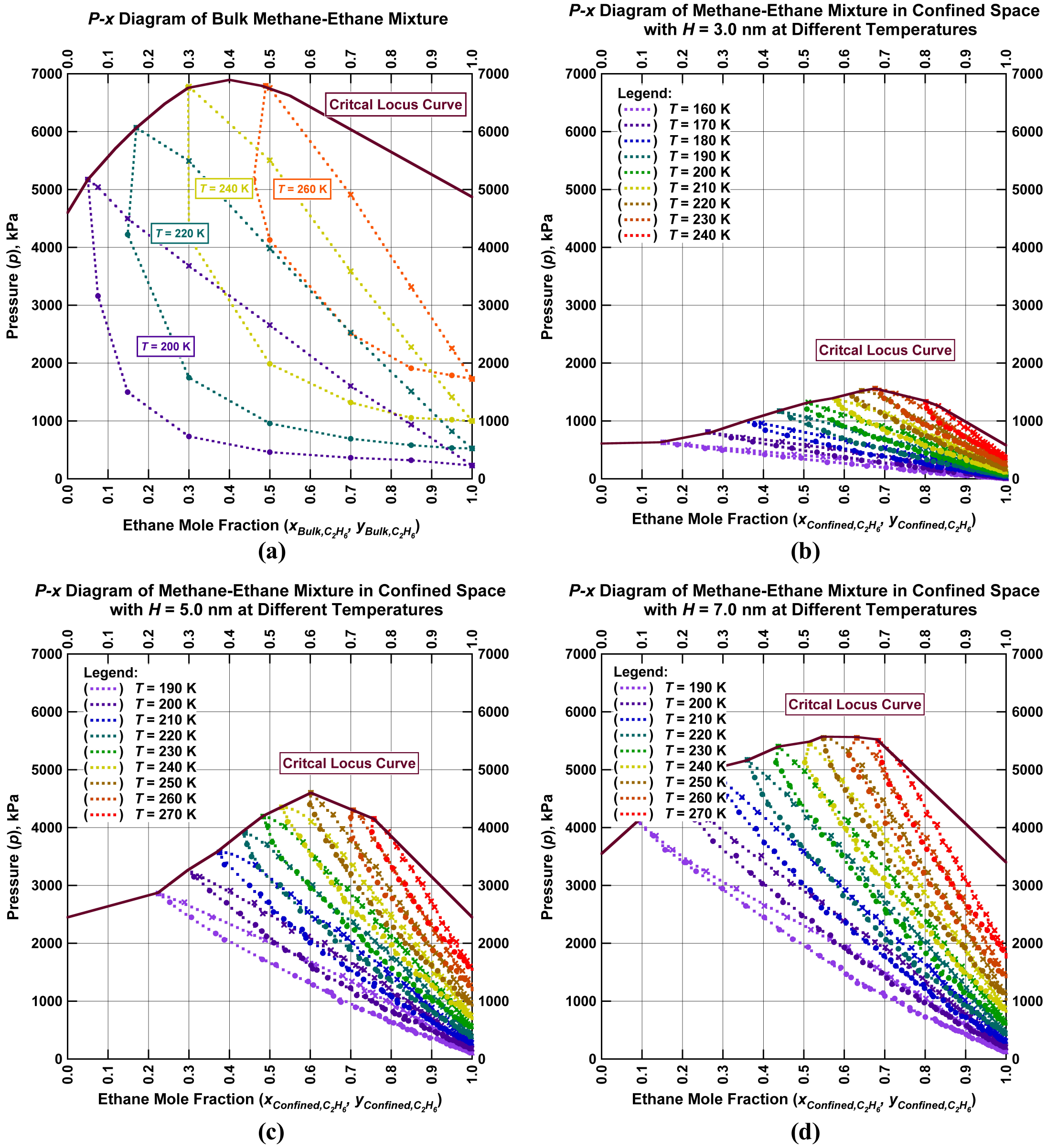

Figure 5-15 – Comparison of (a) bulk methane-ethane mixture phase diagram and (b) that of the confined mixture in the slit pore with *H* = 3.0 nm, (c) *H* = 5.0 nm, and (d) *H* = 7.0 nm.

As explained earlier, a phase diagram of the confined mixture in a slit graphite pore with 3.0 nm, 5.0 nm, and 7.0 nm of separation can be generated as illustrated in **Figures 5-15b**, **5-15c**, and **5-15d**, respectively. A series of phase envelopes of the confined mixture is obtained from the GCMC simulations using the described procedures. For *H* = 3.0 nm, the phase envelopes are generated from *T* = 160 K to *T* = 240 K, which fall between the critical temperatures of the confined methane (155 K) and ethane (258 K). For *H* =

5.0 nm, the phase envelopes are generated from T = 190 K to T = 270 K, which is between the critical temperatures of the confined methane (175 K) and ethane (292 K). For H = 7.0 nm, the phase envelopes are generated from T = 190 K to T = 270 K, which is between the critical temperatures of the confined methane (181.5 K) and ethane (300 K). Again, the intersections between the critical locus curve and the y-axis at $x_{confined,C_2H_6}$ = 0 and $x_{confined,C_2H_6}$ = 1 are the critical pressures of confined methane and ethane respectively.

It can be observed that at the same temperature, the shapes and magnitudes of the bulk and the confined phase envelopes change dramatically because of the restricted environment existent in kerogen pores of shale reservoirs. Furthermore, the subsequent shift of the critical locus curve of the mixture is in the direction of lower critical temperature and pressure, as similarly observed with the pure components.

In addition, the critical locus curve of the confined mixture in the smaller pore is lower than that in the bigger pore. This means that for the same fluid composition, the critical pressure of the confined mixture in the smaller pore is lower than that in the larger pore. The *P-x* diagram also shows that the critical temperature decreases as the pore size decreases. The magnitude of critical properties of the confined mixture decreases rapidly when the pore size reduces from 5.0 nm to 3.0 nm. As the pore size increases, the critical locus curve of the confined mixture becomes closer to that of the bulk mixture as expected. This is because the effect of confinement becomes less meaningful to the confined fluid properties.

Figures 5-16 illustrates a comparison of P-T diagrams for a binary methane-ethane mixture with a methane mole fraction of 30.02% and ethane mole fraction of 69.98% in bulk phase – from experimental data from Bloomer et al. (1953) – and that in a slit graphite pore with a 3.0 nm, 5.0 nm and 7.0 nm of separation. It can be noticed that the shape and area of the confined mixture phase enveloped are different from those of the bulk mixture, and that the critical point of the confined mixture shifts from the bulk critical point. Both critical pressure and temperature are reduced in the small pore. The confined mixture has a higher dew point pressure than the bulk mixture with the same fluid composition while the bubble point pressure of the confined mixture may be either lower or higher than that of the bulk mixture, depending on the temperature.

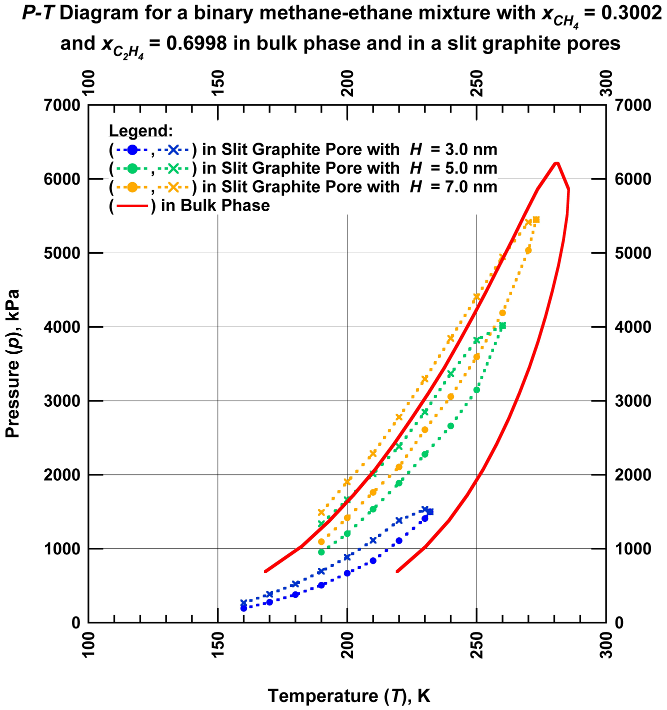

Figure 5-16 – Comparison of *P-T* diagrams for a binary methane-ethane mixture with a methane mole fraction of 30.02% and ethane mole fraction of 69.98% in bulk phase and in a slit graphite pore with 5.0 nm of separation.

5.3.2 Methane-Butane Mixture

Figure 5-17a illustrates a bulk phase diagram of a methane-butane mixture derived from the Peng-Robinson Equation of State (See for example in Stanley (1984) and Orbey and Sandler (1998)). With the same methodology as shown in the previous section, we can obtain a phase diagram of the confined mixture in a slit graphite pore with 5.0 nm of separation (see **Figure 5-17b**). Owing to a lack of data close to the critical points, the phase envelopes and the critical points in **Figure 5-17b** are approximations. However, we can observe that at the same temperature, the shapes and magnitudes of the bulk and confined phase envelopes change dramatically because of the restricted environment existent in kerogen pores of shale reservoirs, which is similar to the previous case. In addition, the critical point of the confined mixture may differ from the bulk critical point at the same temperature.

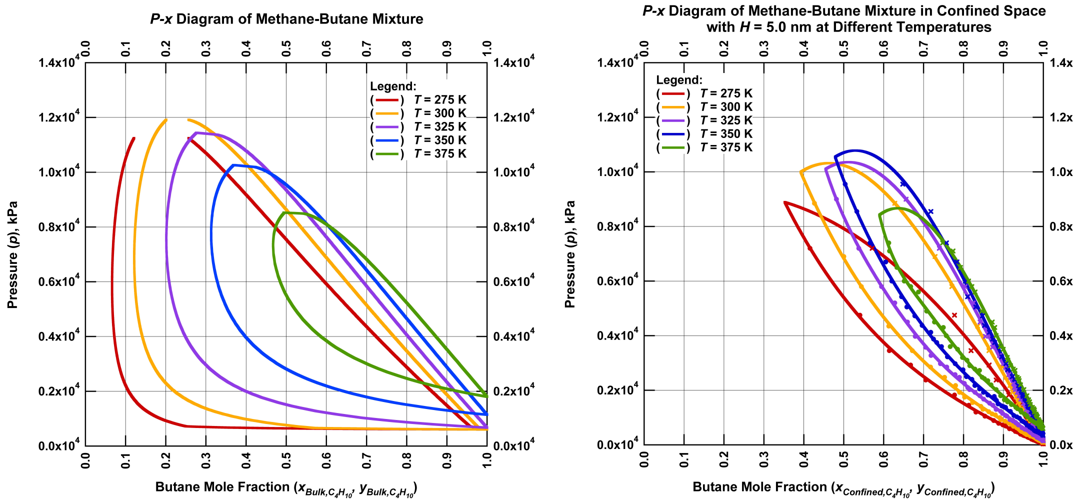

(a) **(b)**

Figure 5-17 – Comparison of (a) bulk methane-butane mixture phase diagram and (b) that of the confined mixture in the slit pore with *H* = 5.0 nm.

5.4 Conclusion

In conclusion, the interactions between fluid molecules and the pore walls create a selective environment in the confined space. As we observed from the GCMC, CB-GCMC, and classical MD simulation results, the slit graphite pore representing a kerogen pore in a shale reservoir prefers to adsorb a heavier component more than a lighter component as the butane and ethane mole fractions of the confined mixtures are always greater than that of the bulk mixture. Selectivity was introduced to describe the selective situation in the pore. Selectivity tends to decrease when the temperature increases. Furthermore, selectivity is varied when the reservoir (bulk) pressure and the bulk fluid composition change. As the pore size increases, the trend of selectivity decreases and approaches unity, where the fluid composition of the confined mixture and bulk mixture are identical.

In addition, we found a jump or discontinuity in the trend of the ethane mole fraction of the confined fluid at the phase transition while the trend is continuous for the supercritical fluid. This concept was used to generate *P-x* diagrams. A phase envelope was created from a collection of *P-x* diagrams. The effect of confinement causes deviations of the shapes and magnitudes of phase diagrams from the bulk. The critical properties and the phase envelope shapes are substantially different from those of the bulk mixture. As the pore size decreases, both critical pressure and temperature tend to decrease, as similarly observed with the pure component. As the pore size increases, the critical locus curve of the confined mixture rises and approaches the bulk curve since there is less influence from the effect of confinement.

According to the *P-T* diagrams, both critical pressure and temperature of the confined mixture are lower than those of the bulk fluid. The confined mixture has higher dew point pressure than the bulk mixture with the same fluid composition. The bubble point pressure of the confined mixture may be either lower or higher than that of the bulk mixture, depending on the temperature.

Based on the observations obtained in this chapter, the fluid composition of the produced hydrocarbon mixture may not be a good representation of original fluid in the reservoir. The mole fraction of the heavy component of the contained mixture is higher than that of the produced fluid. At the beginning of production, shale reservoirs tend to release lighter components (i.e. methane) and the heavier components are left behind. Once the lighter components are almost completely drained from the shale reservoirs, the reservoirs will start releasing the heavier components. This phenomenon may cause changes in the produced fluid composition over the production time.

CHAPTER VI

SIMULATION STUDIES OF CONFINED HYDROCARBON TERNARY MIXTURES

Previously, we showed how interactions between pore walls and different fluid molecules could cause a selective environment in a confined space. For a binary hydrocarbon mixture system, our confined system tends to adsorb a heavier component rather than a lighter one. As a result, phase diagrams and critical properties of the confined binary mixture differ from those of the bulk mixture.

In this chapter, we used CB-GCMC simulation to study selectivity and derive phase diagrams of ternary hydrocarbon mixture. A ternary phase diagram can be represented by a triangle where each side represents mole fraction of each component. One triangle is used to describe a phase of the ternary mixture at a particular pressure and temperature. It may contain only one region; single phase – either vapor or liquid phase –, or three regions; single vapor phase, single liquid phase, and coexistence between two phases, as shown in **Figure 6-1**. The number of regions in a phase diagram is dependent on the pressure and temperature at which the diagram is determined. To help understand a ternary phase diagram, let us consider the red point in the phase diagram. At that point, the mixture comprises of 40% propane, 40% R227ea, and 20% R32 as it can be read from the read arrows. At T = 293K and p = 8500 kPa, the mixture is in equilibrium between both vapor and liquid phases.

In this chapter, we use CB-GCMC simulation to study selectivity and derive phase diagrams of ternary hydrocarbon mixtures in a confined space and the classical MD simulation is employed to help us endorse the conclusion about selectivity of the system obtained from the CB-GCMC simulations.

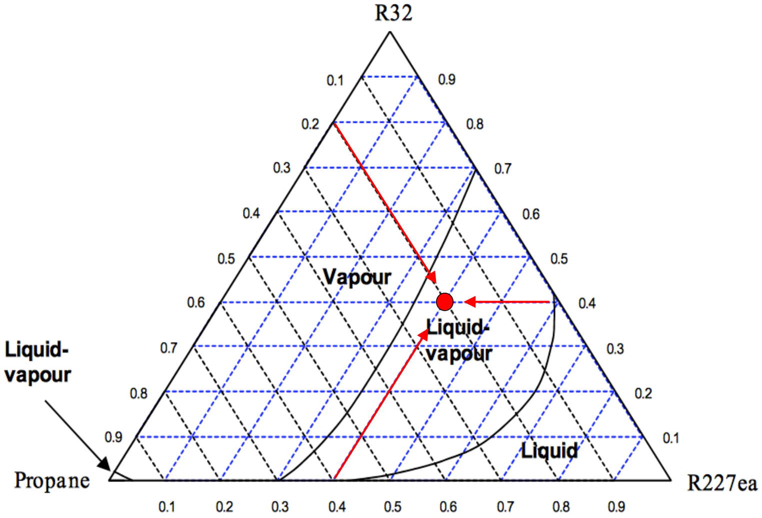

Figure 6-1 – Phase diagram of the ternary system R32-R290-R227ea at *T* = 293 K and *p* = 8500 kPa (Coquelet et al., 2004).

6.1 Selective Environment of Confined System

For a ternary mixture system, the CB-GCMC is used to determine not only the equilibrium density of the confined fluid at the given pressure and temperature, but also the fluid composition in the confined system at equilibrium. The isotherm of the confined system obtained from the GCMC simulation must satisfy equations (6-1a), (6-1b), and (6-1c) for each component of the mixture.

$$\mu^{vapor}_{Bulk,CH_4}(T,p) = \mu^{vapor}_{Confined,CH_4} = \mu^{liquid}_{Confined,CH_4} \cdots\cdots \text{(6-1a),}$$

$$\mu^{vapor}_{Bulk,C_4H_{10}}(T,p) = \mu^{vapor}_{Confined,C_4H_{10}} = \mu^{liquid}_{Confined,C_4H_{10}} \cdots\cdots \text{(6-1b),}$$

and

$$\mu^{vapor}_{Bulk,C_6H_{14}}(T,p) = \mu^{vapor}_{Confined,C_6H_{14}} = \mu^{liquid}_{Confined,C_6H_{14}} \cdots\cdots \text{(6-1c).}$$

The amounts of each type of fluid molecules in the confined system is dependent on the interaction between the sorbent (slit graphite pore) and sorbate (methane, butane, and hexane). Since the force fields of different fluid molecules are different, the interactions between the pore wall and those fluid molecules are varied. This event causes selective environment in the pore. Thus, the fluid composition of the mixture in the confined system may disagree with the given bulk fluid composition.

Figures 6-2a, **6-2b**, **6-2c**, **6-2d**, and **6-2e** illustrate mole fraction of methane, butane, and hexane in the confined space with 5.0 nm of separation at temperatures 300 K, 325 K, 350 K, 375 K, and 400 K, respectively. The reservoir (bulk) pressure is varied from 200 kPa to 6.2 MPa in all cases. The y-axis of each plot is the density of each fluid type occupying the system in unit of molecules per unit cell. The red line represents the mole fraction of hexane, the green line represents the mole fraction of butane, and the blue line represents the mole fraction of methane in the mixture. If the confined system contained a mixture of 1/3 methane molecules, 1/3 butane molecules, and 1/3 hexane molecules as specified in the reservoir, the red line, green line and the blue line must overlay on each other. However, none of our cases gave results that suggested the fluid composition in the confined system is the same as that in the reservoir. This is because the interactions of the mixture's components with the pore walls created a selective environment in the slit graphite pore, and therefore resulted in changes in fluid behavior and properties in the confined system, including the fluid composition. According to **Figures 6-2a**, **6-2b**, **6-2c**, **6-2d**, and **6-2e**, it is noticeable that our confined system adsorbs a heavier component more readily than a lighter component, as the hexane mole fraction of the confined fluid is greater than the butane mole fraction and the methane mole fraction is the lowest in all the cases. The classical MD simulation is implemented to prove this statement.

We initiate a configuration with a fluid composed of 1/3 methane molecules, 1/3 butane molecules, and 1/3 hexane molecules as shown in **Figure 6-3a**. Graphene layers are put in the middle of the system to create a restricted space representing a pore while the rest of the system represents a bulk segment. The graphene layers are arranged at a distance of 5.0 nm to study the effect of confinement. Temperature of the system is 300 K and the simulation time is 35 ns. The final configuration is illustrated as **Figure 6-3b**. After the simulation is completed, the total energy must be reached and almost stabilize at the minimal point to ensure that the final configuration is at equilibrium. The total energy versus simulation time in this study is shown by **Figure 6-3c**. Snapshots of the MD simulation are illustrated as **Figure 6-4**. At t_s = 0 ns or initial state, the total potential energy is high, thus the molecules in the system move to reduce the energy. At t_s = 2 ns, butane and hexane molecules form a liquid phase outside the slit graphite pore. At this state, the total potential energy is lower than at the initial state; however, the energy is still high, and the system is still not in equilibrium. From t_s = 2 ns to t_s = 20 ns, the liquid phase migrates from the bulk to the confined space and the total energy declines, meaning that the system is approaching the equilibrium. From t_s = 20 ns to t_s = 35 ns, the total energy stabilizes at the minimal point, which means the system has reached the equilibrium. According to the final configuration, the liquid phase completely migrates and resides in/nearby the confined space. Mole fraction of each component in each interval is computed over the y-direction. The plot of the mole fractions versus location in the y-direction is shown in **Figure 6-3d**. From the plot, it can be observed that although the initial mole fraction of each component in all intervals in the system – including both of the pore and the bulk segments – equals 1/3, the mole fractions at equilibrium of each interval changes and varies throughout the system. For instance, at equilibrium, the hexane mole fraction in the slit pore segment – the area between two red dashed lines in **Figure 6-3d** – is the highest and higher 1/3, while the methane mole fraction is the lowest and almost equals 0. On the other hand, in the bulk segment, the methane mole fraction is the highest and the hexane mole fraction is the lowest because most hexane molecules already reside in the confined space. Similar to hexane molecules, butane molecules are adsorbed near the graphene layers but with smaller amounts because the interactions of the graphene layers with hexane molecules are stronger than the interactions with butane molecules. This result confirms our conclusion obtained from the results of the CB-GCMC simulations that a heavier component is preferable to a lighter component for our confined system.

6.2 Phase Diagram of Confined Hydrocarbon Ternary Mixtures

The ternary phase diagrams can be derived from isotherms of confined ternary mixtures obtained from the CB-GCMC simulations. Apart from pressure and temperature, the CB-GCMC simulation requires the molar composition of the bulk mixture to calculate the chemical potential of the mixture surrounding the confined system. In this study, we varied the molar composition of the bulk mixture (see **Figure 6-5**). As known from the previous section, fluid properties, including the fluid composition in a confined space, differ from the bulk properties because of the effect of confinement. Therefore, for each sampling point, we need to compute the mole fraction of each component of the confined fluid and the average confined fluid density from isotherms obtained from the CB-GCMC simulation. Mole fraction of each component and the average density of the confined fluid can be calculated by the following formula:

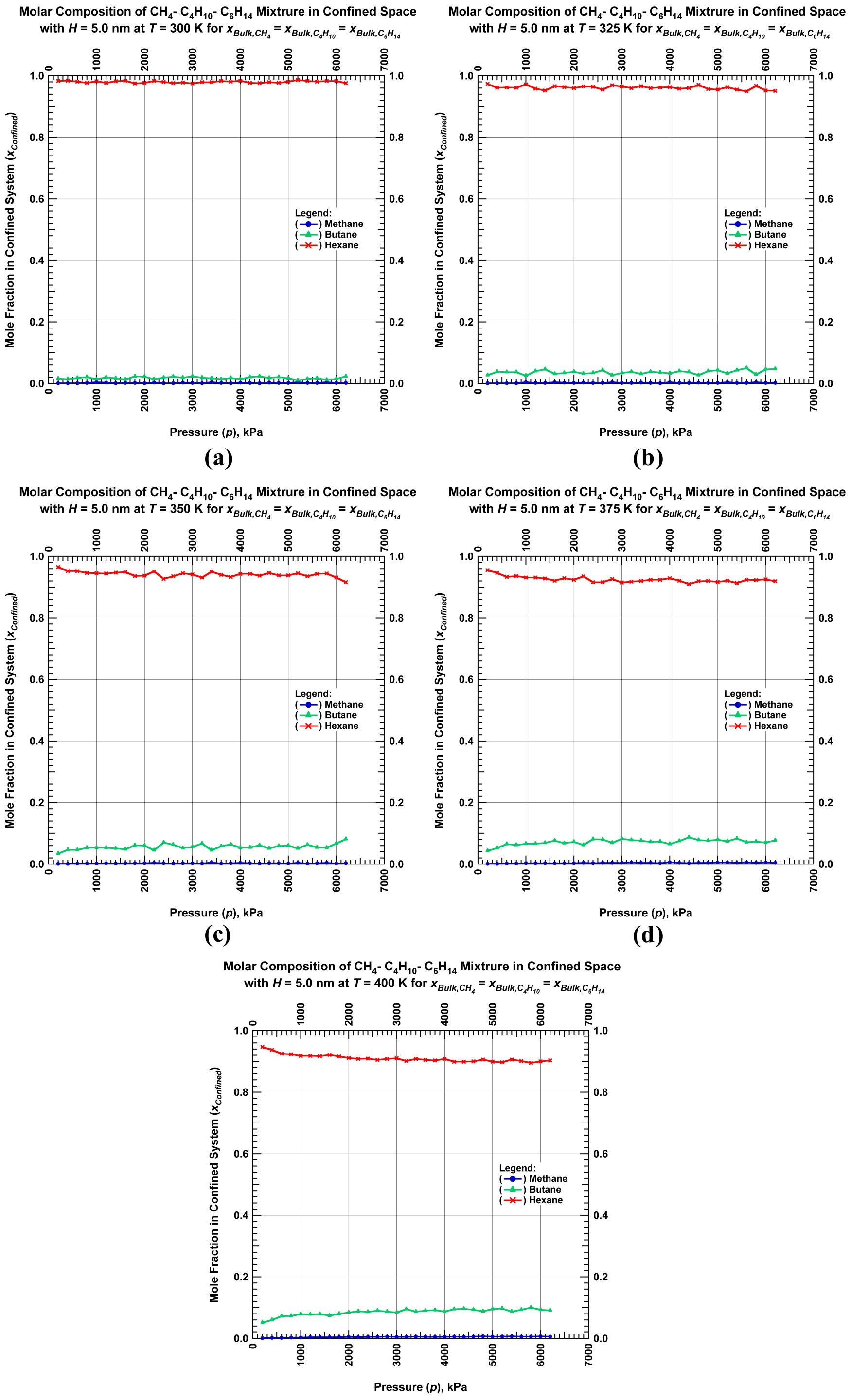

(a)

(b)

(c)

(d)

(e)

Figure 6-2 – Mole fraction of methane, butane and hexane in confined space with $H = 5.0$ nm and $x_{Bulk,CH_4} = x_{Bulk,C_4H_{10}} = x_{Bulk,C_6H_{14}} = 1/3$ at (a) $T = 300$ K, (b) $T = 325$ K, (c) $T = 350$ K, (d) $T = 375$ K, and (e) $T = 400$ K.

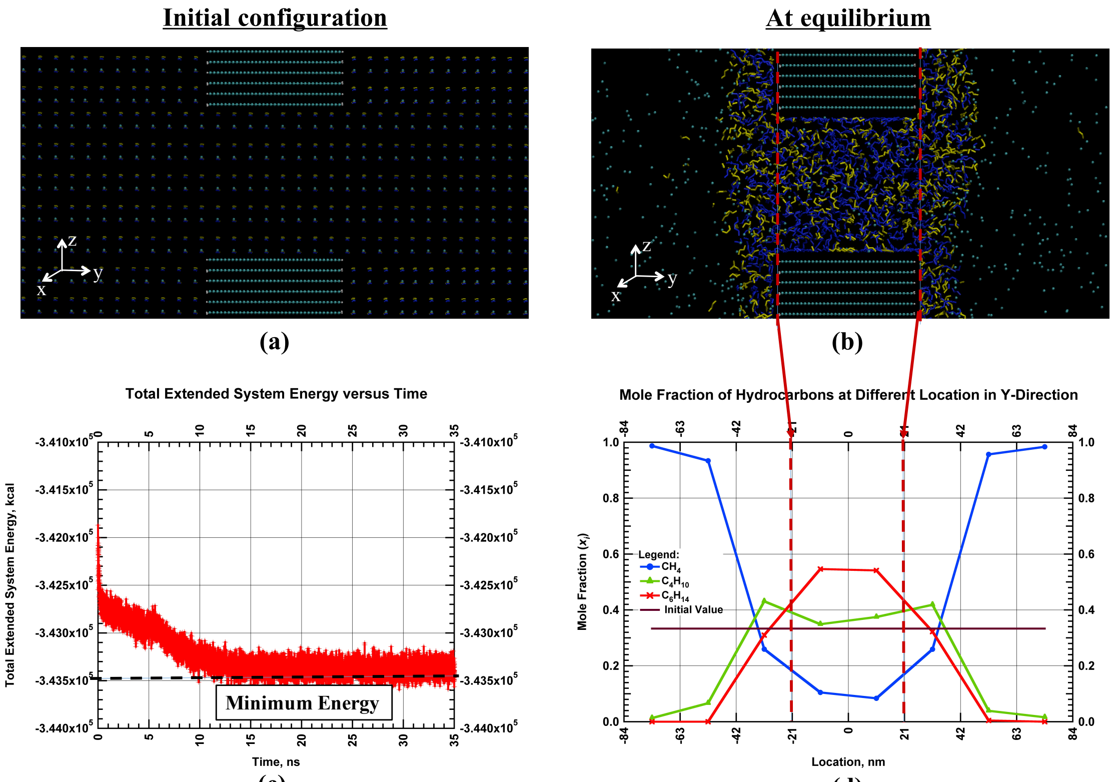

(a) (b)

(c) (d)

Figure 6-3 – (a) Initial and (b) final configuration at t_s = 35 ns from classical MD simulation of methane-butane-hexane mixture in slit graphite pore with H = 5.0 nm at T = 300K, (c) total extended system energy over simulation time, and (d) mole fraction profiles in the y- direction of the mixture.

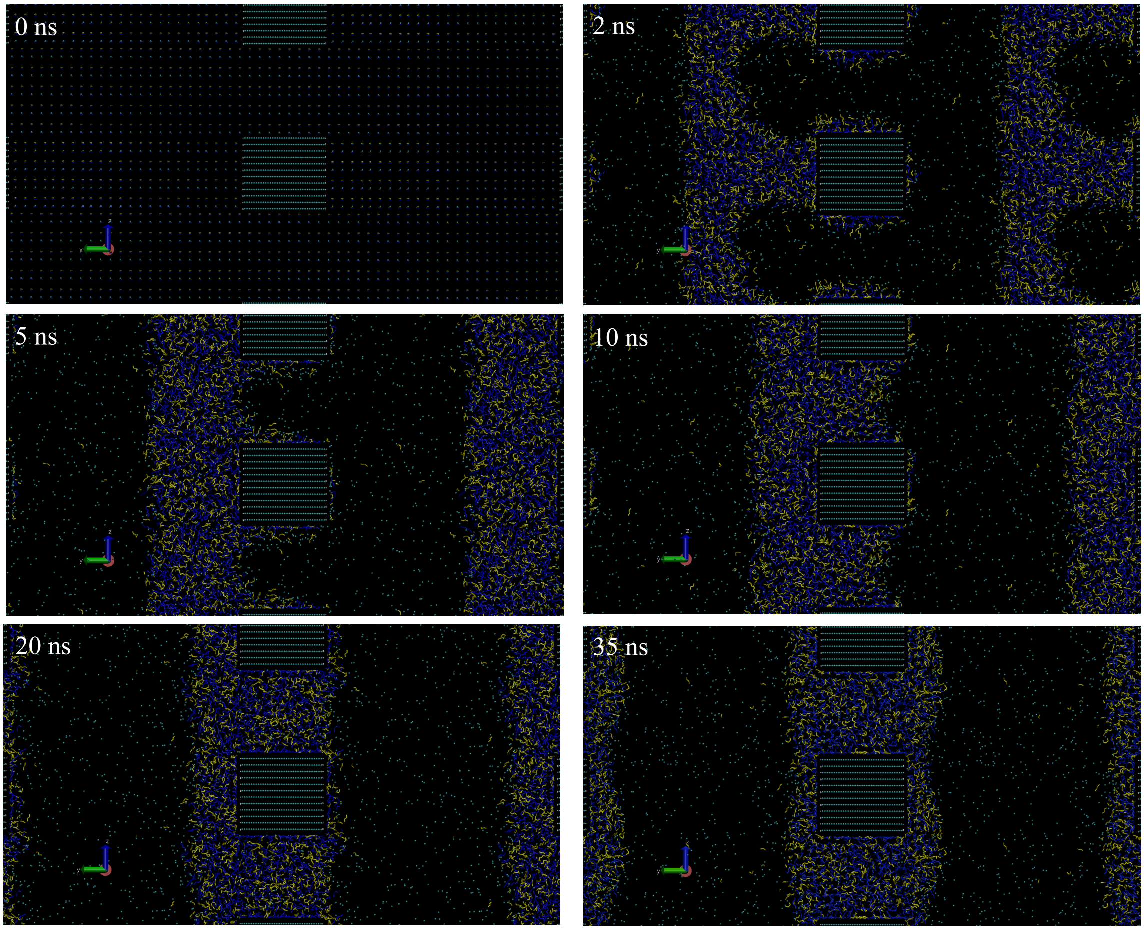

Figure 6-4 – Snapshots of MD simulations of methane-butane-hexane mixture in slit graphite pore with H = 5.0 nm at T = 300K.

$$x_{Confined,CH_4} = \frac{n_{CH_4}}{n_{CH_4}+n_{C_4H_{10}}+n_{C_6H_{14}}} \qquad (6\text{-}2a),$$

$$x_{Confined,C_4H_{10}} = \frac{n_{C_4H_{10}}}{n_{CH_4}+n_{C_4H_{10}}+n_{C_6H_{14}}} \qquad (6\text{-}2b),$$

$$x_{Confined,C_6H_{14}} = \frac{n_{C_6H_{14}}}{n_{CH_4}+n_{C_4H_{10}}+n_{C_6H_{14}}} \qquad (6\text{-}2c),$$

and

$$\rho_{Confined} = \frac{(n_{CH_4} \times MW_{CH_4})+(n_{C_4H_{10}} \times MW_{C_4H_{10}})+(n_{C_6H_{14}} \times MW_{C_6H_{14}})}{N_A \times V_{Unit\ Cell}} \qquad (6\text{-}3).$$

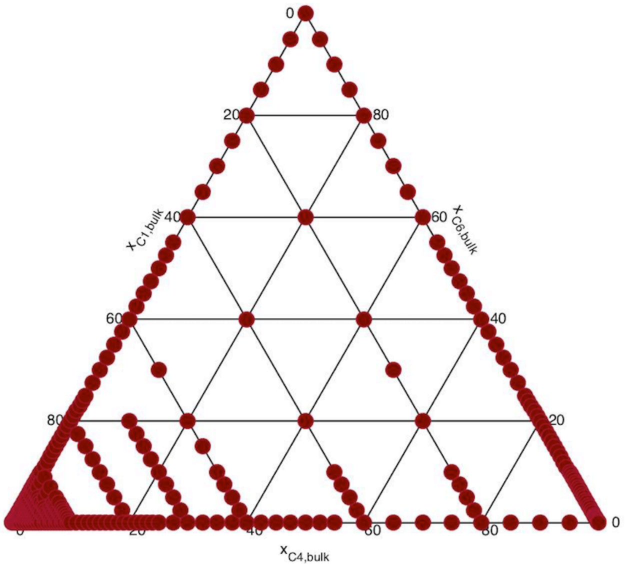

Figure 6-5 – Bulk molar fluid composition of ternary mixture used in our study.

An example of a derivation of ternary phase diagrams is illustrated in **Figure 6-6**. This example for a phase diagram at T = 400 K and p = 300 kPa. **Figure 6-6a** illustrates isotherms of a confined ternary mixture with $x_{Bulk,CH_4} = 0.8$ and $x_{Bulk,C_4H_{10}} = x_{Bulk,C_6H_{14}} = 0.1$ and **Figure 6-6b** illustrates isotherms of a confined ternary mixture with $x_{Bulk,CH_4} = x_{Bulk,C_4H_{10}} = 0.2$ and $x_{Bulk,C_6H_{14}} = 0.6$. For the first case, the mixture is in vapor phase at T = 400 K and p = 300 kPa with $x_{Confined,CH_4} \approx 0.04$, $x_{Confined,C_4H_{10}} \approx 0.07$, and $x_{Confined,C_6H_{14}} = 0.89$. This confined fluid composition is different from the bulk fluid composition. The average density of the confined mixture is computed using equation (6-3), which is equal to 0.18 g/cc. Then, we can plot this point (a blue dot) in a 3D- and 2D-phase diagram as shown in **Figure 6-6c** and **Figure 6-6d**, respectively. As seen in the color bar, the blue color represents low density, meaning that the mixture is in the vapor phase. The level of the point in a 3D-phase diagram also represents the mixture density. For the second case, the mixture is in the liquid phase with $x_{Confined,CH_4} \approx 0.001$, $x_{Confined,C_4H_{10}} \approx 0.023$, and $x_{Confined,C_6H_{14}} = 0.976$. The average density of the confined mixture is 0.66 g/cc. Again, we can plot this point (a red dot) in a 3D- and 2D-phase diagrams. The red color represents high density, meaning that the mixture is in the liquid phase. We can repeat this procedure to determine the mixture phase at each point to obtain complete phase diagrams.

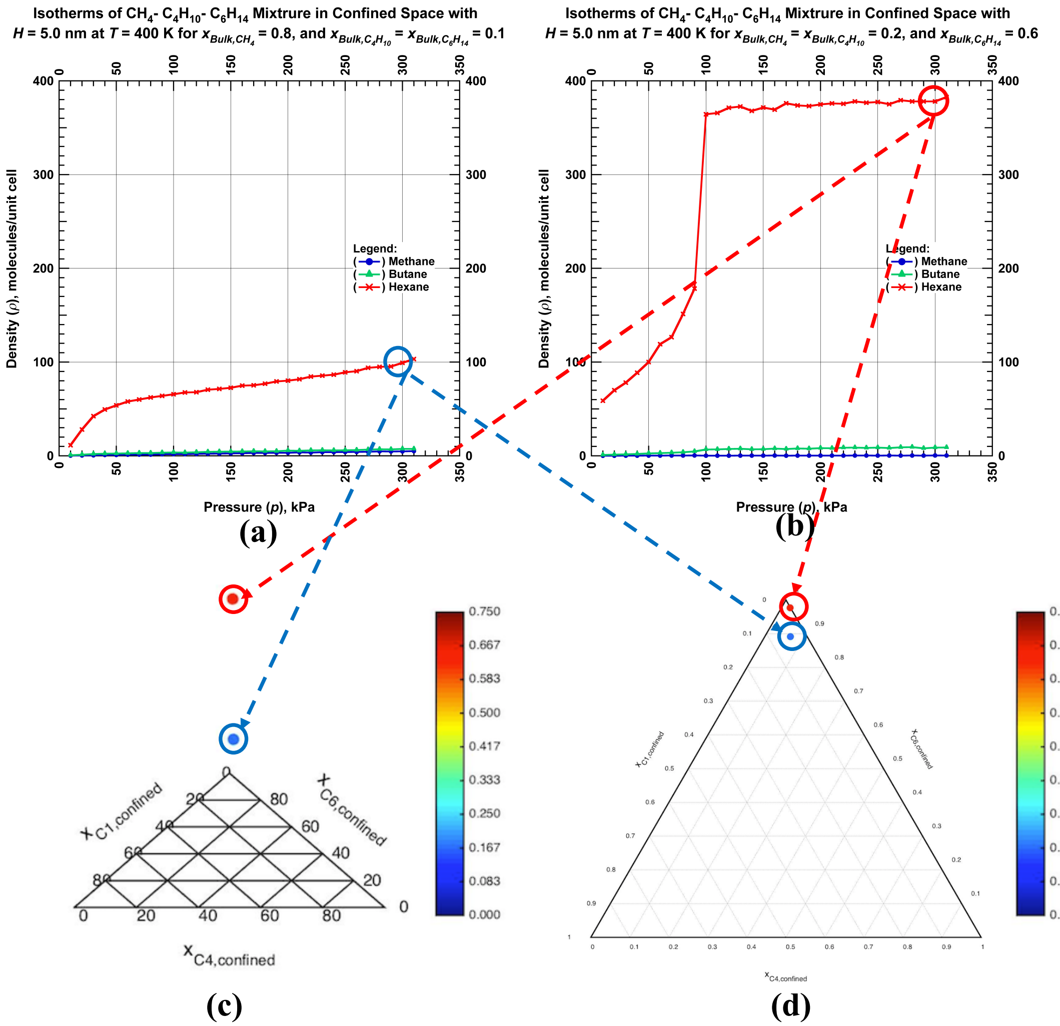

Figure 6-6 – Isotherms of a confined ternary mixture with (a) x_{Bulk,CH_4} = 0.8 and $x_{Bulk,C_4H_{10}}$ = $x_{Bulk,C_6H_{14}}$ = 0.1, and (b) x_{Bulk,CH_4} = $x_{Bulk,C_4H_{10}}$ = 0.2 and $x_{Bulk,C_6H_{14}}$ = 0.6, (c) example of density plots on 3D – and (d) 2D – phase diagrams of the confined mixture at T = 400 K and p = 300 kPa.

Figure 6-7 illustrates phase diagrams of the confined ternary mixture at T = 400 K and p = 10 kPa. According to the phase diagrams, the mixture is always in vapor phase since the average mixture density is low. From the 3D-phase diagram as shown in **Figure 6-7a**, the mixture density is rising when it approaches the corner where the hexane mole fraction equals 1. Here is an example of a phase diagram that contains only one vapor region.

Figure 6-8 illustrates phase diagrams of the confined ternary mixture at T = 400 K and p = 300 kPa. According to the phase diagrams, the mixture can be either vapor or liquid phase depending on the confined fluid composition. For instance, the red dots close to the corner, where the hexane mole fraction equals unity represent the liquid mixture, whereas the other points in the phase diagrams away from that corner represent the vapor mixture. From the 3D-phase diagram as shown in **Figure 6-8b**, we observe a jump or discontinuity of density from vapor density to liquid density when phase changes occur. It implies that the fluid has not yet reached the supercritical condition. In other words, for T = 400 K, p = 300 kPa is still lower than the critical pressure.

Figure 6-9 illustrates phase diagrams of the confined ternary mixture at T = 400 K and p = 3000 kPa. According to the phase diagrams, the mixture can be either vapor or liquid phase depending on the confined fluid composition. A two-phase region in these phase diagrams, as highlighted in the green color in **Figure 6-9b,** is bigger than the two-phase region of the previous case. **Figure 6-9c** depicts an approximation of the complete phase diagram at this condition. The red area represents a single liquid phase region; the blue area represents a single vapor phase region; and the area between those regions represents a two-phase region. We can notice that the two-phase region in **Figure 6-9c** is bigger than that in **Figure 6-9b**. This is because our data points are not enough to generate an accurate approximation of a complete phase diagram. See Appendix B for phase diagrams of confined methane-butane-hexane ternary mixture in 5.0 nm slit graphite pore for T = 350 – 400 K and p = 10 – 3000 kPa.

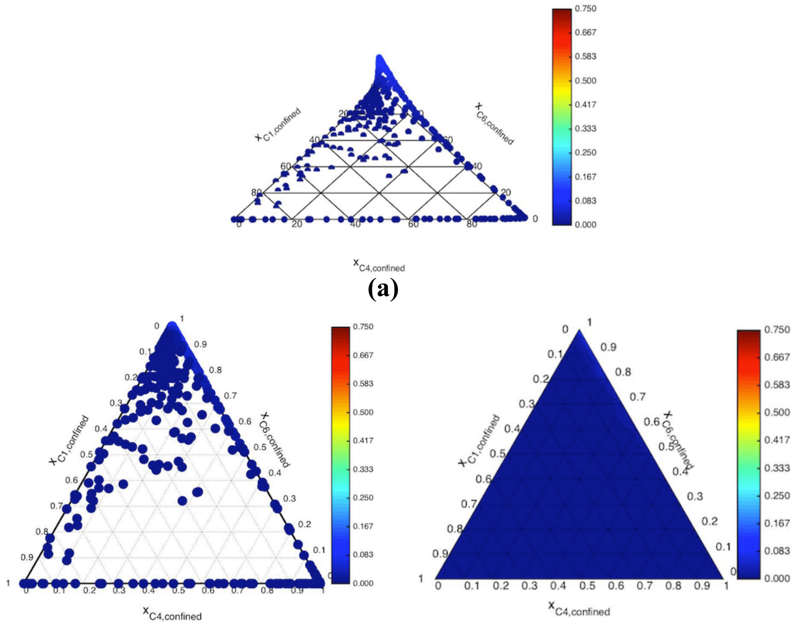

(a)

(b)

(c)

Figure 6-7 – Density plots on (a) 3D – and (b) 2D – phase diagrams, and approximation of complete 2D – phase diagram of the confined mixture at T = 400 K and p = 10 kPa.

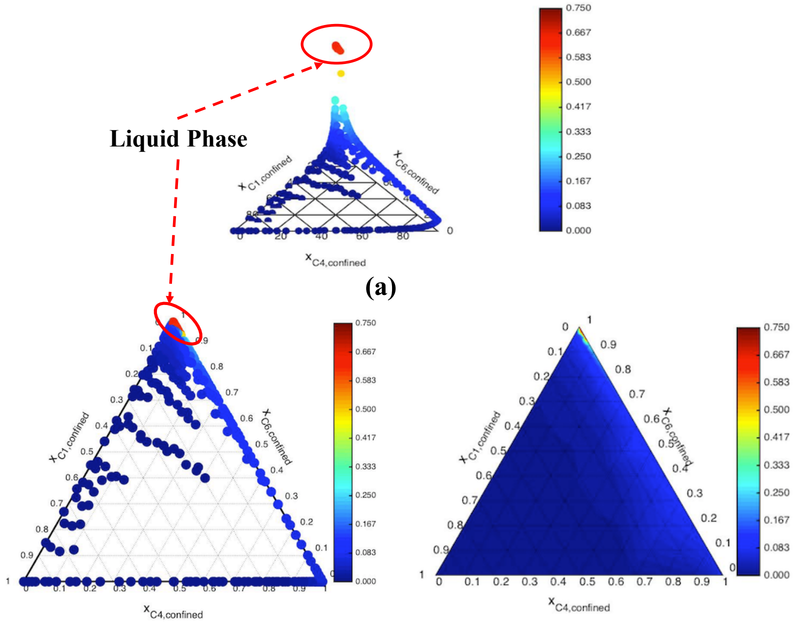

(a)

(b)

(c)

Figure 6-8 – Density plots on (a) 3D – and (b) 2D – phase diagrams, and approximation of complete 2D – phase diagram of the confined mixture at T = 400 K and p = 300 kPa.

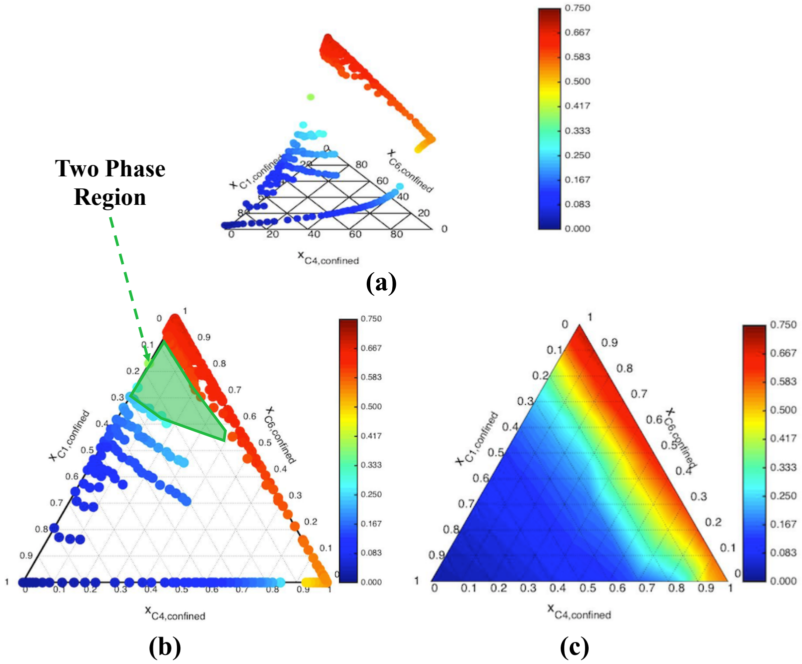

(a)

(b)

(c)

Figure 6-9 – Density plots on (a) 3D – and (b) 2D – phase diagrams, and approximation of complete 2D – phase diagram of the confined mixture at *T* = 400 K and *p* = 3000 kPa.

6.3 Conclusion

Results from both the CB-GCMC simulation and the classical MD simulation for a methane-butane-hexane ternary mixture system verified our conclusion from the previous chapter that our confined system or shale reservoirs adsorbs heavier components more readily than lighter components because the interactions of the pore wall with heavier hydrocarbon molecules is stronger than the interactions with lighter hydrocarbon molecules. This creates a selective environment in our confined system and consequently causes changes of phase diagrams and fluid properties in the confined system. Especially, confined fluid composition and density differ from bulk fluid composition and density. From the confined fluid composition and density derived from the isotherms of a confined mixture, a ternary phase diagram of the confined mixture can be generated. Phase diagrams may contain one region (single phase) or three regions (two single phases and one two-phase) depending on pressure and temperature. A discontinuity of the mixture density can be observed in the phase diagram when the mixture changes from a vapor phase to a liquid phase. The procedure we implemented in this chapter to derive a ternary phase diagram can be coupled with a pseudo binary phase diagram to obtain critical properties of a confined ternary mixture.

CHAPTER VII

SIMULATION STUDIES OF CONFINED FLUID WITH INORGANIC FLUID SURROUNDING

As known, petroleum fluid systems do not contain only hydrocarbons but also inorganic fluids such as water. Water is involved in petroleum reservoirs in many ways. For example, we injected water to create fractures in tight/unconventional reservoirs. This water may be in contact with kerogen pores in the reservoir. Moreover, water may already exist in source rocks or shales with hydrocarbons because water is part of the organic matter deposition environment that is the origin of hydrocarbons. Therefore, it is important to include water in this work to study the fluid behavior of petroleum fluid systems in shale reservoirs.

First of all, the classical MD simulation is employed to observe the difference in fluid behavior between bulk water and water in our confined system, which is a slit graphite pore representing a kerogen pore in shale reservoirs. The GCMC simulation is used to derive a shift in fluid property such as the vapor pressure of water due to the effect of confinement.

Then, we consider a confined binary mixture system of water and methane. A *T-x* diagram is generated using isotherms obtained from the GCMC simulations. The final configurations at equilibriums are analyzed to help us understand solubility of the binary mixture in our confined system under different conditions.

7.1 Fluid Behavior of Confined Pure Water

In all of the preceding chapters, we have considered a system comprising of only hydrocarbons and graphene layers, which represent a kerogen in shale reservoir. Those molecules are non-polar molecules and the only intermolecular forces in the system are dispersion forces. The dispersion force is defined as a short-range interaction that decreases with distance quicker than r^{-3} for a three-dimensional system. For short-range interaction, we can assume that interactions beyond a cut-off radius, r_c, are negligible. Normally, r_c should be equal to or greater than $5\times \max(\sigma_{ij})$ to ensure that the interactions are definitely insignificant. As a result, Lennard-Jones potential is just to describe interactions of molecules in the system. However, water is usually found in petroleum fluid systems. As known, a water molecule is a polar molecule. Interactions between molecules in a system containing polar molecules must include Coulombic interactions as shown in Chapter II. Coulombic interaction is defined as a long-range interaction, which is too strong to be neglected beyond the cut-off radius. The simple model to compute a potential energy due to interactions between two water molecules (*a* and *b*) is

$$U(r) = \sum_{i}^{on\ a} \sum_{j}^{on\ b} \frac{k_C z_{ei} z_{ej}}{r_{ij}} + 4\epsilon_{OO}\left[\left(\frac{\sigma_{OO}}{r_{OO}}\right)^{12} - \left(\frac{\sigma_{OO}}{r_{OO}}\right)^{6}\right] \ldots\ldots (7\text{-}1)$$

where k_C is the electric constant whose value is 1389.5 Å·kJ/mol; q_{ei} and q_{ej} are the partial charges relative to the charge of the electron; r_{ij} is the distance between two charged sites or atoms; r_{OO} is the distance between two oxygen atoms in the molecules; and ϵ_{OO} and σ_{OO} are Lennard-Jones parameters of the oxygen atom in a water molecule. The first term of equation (7-1) takes account of the Coulombic interactions or long-range potential and the second term is the Lennard-Jones potential to describe a short-range potential. To help understand a potential calculation of two water molecules, let us consider a system as shown in **Figure 7-1**. In this study, we use the SPC/E model to represent a water molecule. The partial charges of oxygen, q_{eO}, and hydrogen, q_{eH}, atoms relative to the charge of the electron are -0.82 and +0.41 respectively. The bond lengths between the oxygen atom and hydrogen atoms equal 95.84 pm, and the bond angle is 104.45°. ϵ_{OO} and σ_{OO} are equal to 0.65 kJ/mol and 3.166 Å, respectively. Parameters of the SPC/E model for a water molecule are summarized in **Table 7-1**.

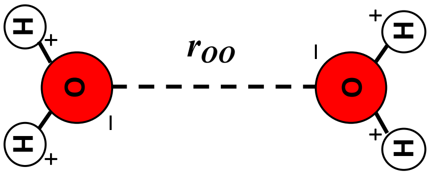

Figure 7-1 – Interactions between two water molecules.

Table 7-1 – SPC/E model of water molecule.

z_{eO}	-0.82
z_{eH}	+0.41
$r(OH)$, Å	0.9584
HOH, deg	104.45°
ϵ_{OO}, kJ/mol	0.65
σ_{OO}, Å	3.1660

The potential map between the two water molecules, which is derived from equation (7-1), is shown in **Figure 7-2**. The contribution of both Coulombic (long-range) and Lennard-Jones (short-range) potential energies to the total potential are illustrated as a red dashed line and a green dashed line in **Figure 7-2**, respectively. The summation of both energies is the total potential energy, and it is illustrated as a solid brown line. The dashed orange line represents a cut-off radius where $r_c = 5\times\sigma_{OO}$. Observe that the Lennard-Jones potential energy is very small which means that the dispersion force between two molecules is extremely weak beyond the cut-off distance. As a result, it is reasonable to assume that there is no dispersion force between the molecules beyond the cut-off distance (the yellow dashed line in **Figure 7-2**). However, a contribution of the Coulombic potential energy is much greater than the Lennard-Jones potential, meaning that electrostatic forces dominate the total potential energy of the system. At the cut-off radius, the Lennard-Jones potential energy equals -1.664×10^{-4} kJ, whereas the Coulombic potential energy equals -0.1060 kJ. This is why we define the Coulombic interaction as a long-range interaction. The total potential energy at the cut-off radius is -0.1061 kJ. It is noticeable that the main contribution to the total potential energy at the cut-off radius is the Coulombic potential energy. The value of the total potential energy is still too high to be neglected.

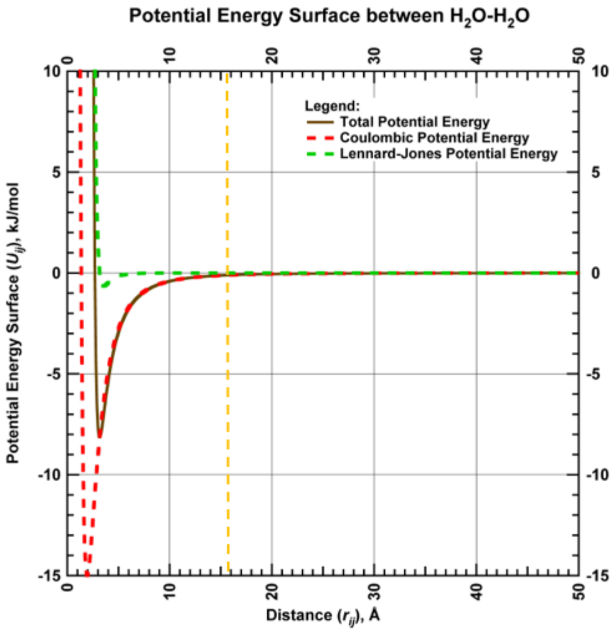

Figure 7-2 – Potential map between two water molecules.

As Coulombic interactions are infinitely ranged, the simulation cell and all its periodic images must be considered. In principle, a large enough system screening by neighboring molecules would diminish the effect of the potential. However, this would occur over a range of several tens or hundreds of nanometers while the half-cell length of our simulation box is ~ 2 nm. Therefore, to account for electrostatic interaction in the systems, we must consider the effect of the periodic images. The Coulombic interaction for a set of point charges, N, can be written as

$$U_{Coul} = \frac{1}{2}\sum_{\boldsymbol{n}}\left(\sum_{i=1}^{N}\sum_{j=1}^{N}\frac{z_{ei}z_{ej}}{|\boldsymbol{r_{ij}}+\boldsymbol{n}|}\right) \quad \text{(7-2).}$$

where $\boldsymbol{n}$ is the lattice vectors, $\boldsymbol{n} = \left(L_x n_x, L_y n_y, L_z n_z\right)$. In this work, we implement the Ewald summation method for computing long-range interactions in our periodic confined system. Ewald summation is a special case of the Poisson summation formula that replaces the summation of the interactions in equation (7-2), which is in real space with an equivalent summation in the Fourier space. The final potential energy is

$$U_{Coul} = \frac{1}{2}\sum_{\boldsymbol{n}}\left(\sum_{i=1}^{N}\sum_{j=1}^{N} q_{ei}q_{ej}\frac{\operatorname{erfc}\left(\alpha|\boldsymbol{r_{ij}}+\boldsymbol{n}|\right)}{|\boldsymbol{r_{ij}}+\boldsymbol{n}|}\right) + \frac{1}{\pi L^3}\sum_{k\neq 0} q_{ei}q_{ej}\frac{4\pi^2}{k^2}\exp\left(-\frac{k^2}{4\alpha^2}\right)\cos\left(\boldsymbol{k}\cdot\boldsymbol{r_{ij}}\right) - \frac{\alpha}{\pi^{0.5}}\sum_{i=1}^{N} q_{ei} + \frac{2\pi}{3L^3}\left|\sum_{i=1}^{N} q_{ei}\,\boldsymbol{r_i}\right|^2 \quad \text{(7-3)}$$

where $\boldsymbol{k} = 2\pi\boldsymbol{n}/L^2$, and α is an Ewald convergence parameter (see Allen and Tildesley 1987 for a derivation of the Ewald summation).

The methods above are applied in our molecular simulations to study the fluid behavior of water in our confined system. **Figure 7-3** depicts a comparison of the water structure of synthetic bulk water and confined water with a 0.85 g/cc density in a slit graphite pore with 2.1 nm of separation at T = 300K obtained from the Molecular Dynamics simulations. It can be seen that the water molecules are well aligned and different from the bulk water structure, which is more random. **Figure 7-4** is a plot of the densities of oxygen atoms in the water molecules at any locations in the *z*-direction of the bulk water and the confined water regarding **Figure 7-3**. The red line represents the density of the bulk water, and the blue line represents the density of the confined water. We confirm that the water molecule arrangement in the confined space differs from the bulk water. The confined water molecules form roughly seven layers in the slit graphite pore since we can observe seven peaks in the oxygen density of the confined fluid in **Figure 7-4**. On the other hand, there is no specific formation of water molecules in the bulk phase. The change of the water molecule arrangement in the confined space is caused by the effect of confinement. Consequently, fluid properties of confined water may differ from bulk properties.

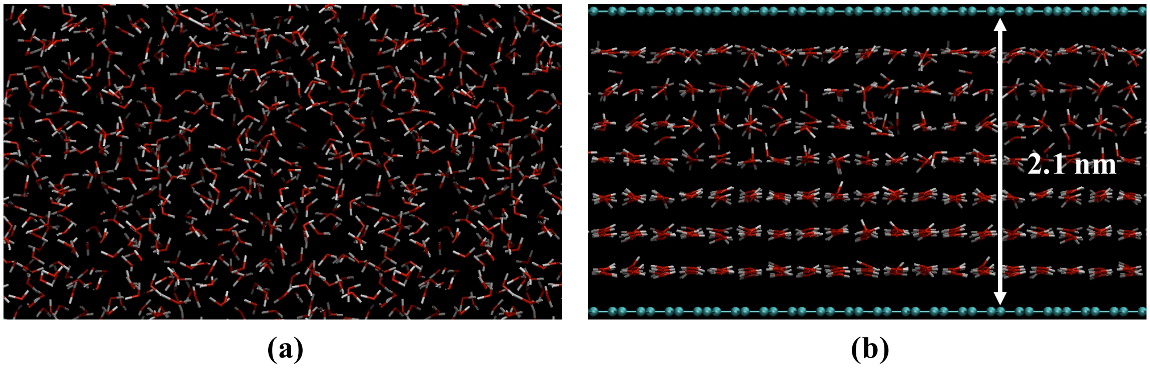

Figure 7-3 – Molecule structure of (a) bulk water and (b) confined water.

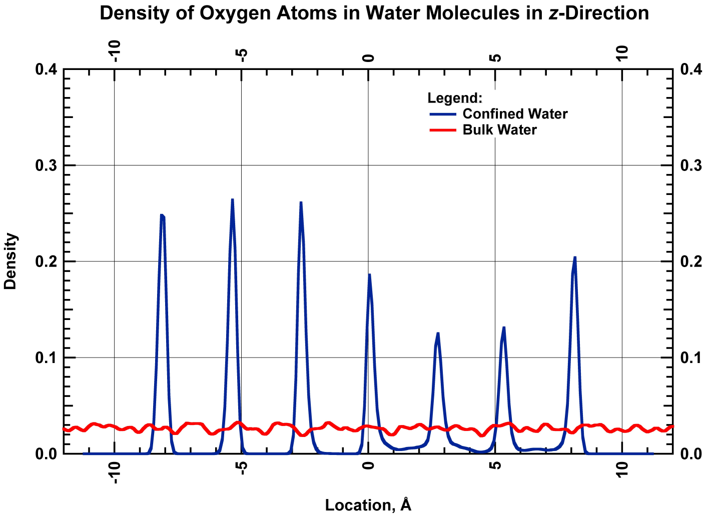

Figure 7-4 – Z-density of oxygen atoms in water molecules of bulk water (red line) and confined water (blue line) in the slit graphite pore with *H* = 2.1 nm at *T* = 300 K.

The conventional GCMC simulation is employed to obtain an isotherm of water in our confined system. Water density can be computed from the isotherm. A comparison of water density as a function of pressure between the bulk water and the confined water in a graphite pore with 3.0 nm of separation at T = 400K is depicted in **Figure 7-5**. Again, the red line represents the density of the bulk water, and the blue line represents the density of the confined water. The bulk water density is obtained from National Institute of Standards and Technology database. From **Figure 7-5**, we can observe that both the vapor and liquid water densities of the confined water are higher than the bulk densities. In addition, the interactions between the pore walls and water molecules cause a shift in vapor pressure. The jumps or discontinuities of the water densities in the plot define the vapor pressures of the bulk water and the confined water. As a result, the vapor pressure of the confined water in the slit graphite pores with 3.0 nm of separation at *T* = 400K is approximately 210 kPa, which is lower than the vapor pressure of the bulk water (245.77 kPa).

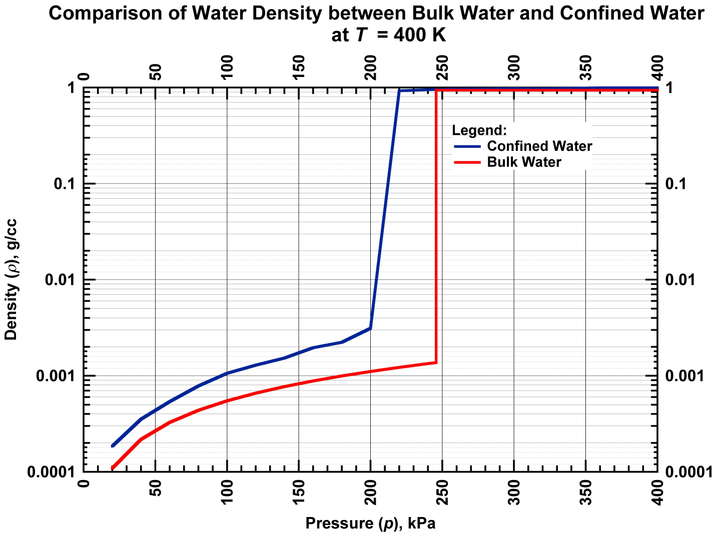

Figure 7-5 – Water density as a function of pressure of bulk water (red line) and confined water (blue line) in the slit graphite pore with *H* = 3.0 nm at *T* = 400 K.

We can conclude that the effect of confinement may cause changes in water structure, which consequently alter fluid properties of water, including water density, and vapor pressure.

7.2 Phase Diagram of Confined Methane-Water Binary Mixture

In this section, we use the GCMC simulation to study the effect of confinement on the phase diagrams of a methane-water binary mixture. The prevailing knowledge is that methane and water are not miscible. Therefore, it is not practical to determine critical properties of the methane-water binary mixture. However, we may need to find out if there are any conditions under which methane and water are miscible and how the mixture behaves in our confined system. Let us first consider isotherms of a confined methane-water binary mixture as shown in **Figure 7-6**. The isotherms are for the confined binary mixture in a slit graphite pore with 3.0 nm of separation at *T* =350 K. The bulk fluid composition is 50% methane and 50% water and the bulk pressure is varied from 80 kPa to 460 kPa by increments of 20 kPa.

According to the results, the confined fluid composition differs from the given bulk fluid composition considering the isotherms of both components do not overlay each other. At low pressure, when both components are in the vapor phase, the methane isotherm is higher than the water isotherm. However, as pressure increases, water condenses, forms a liquid phase, and dominates the confined system as the methane isotherm declines to lower than 0.02 molecules per unit cell at high pressure.

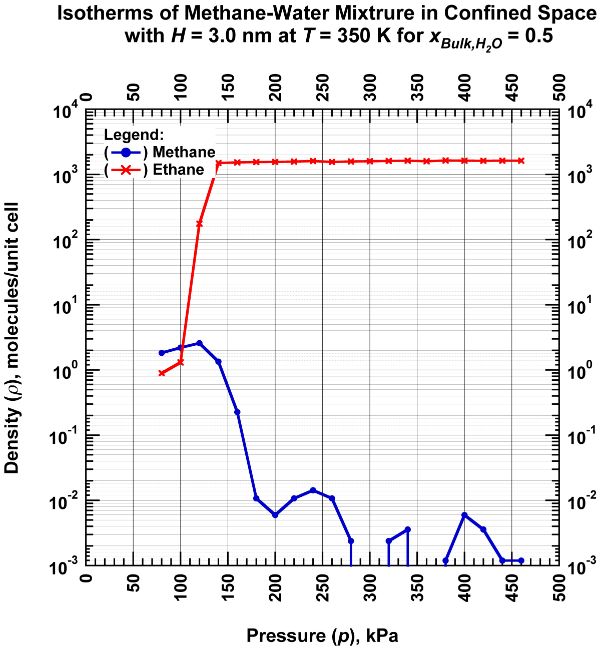

Figure 7-6 – Isotherms of methane and water in confined space with H = 3.0 nm and $x_{Bulk,\ H_2O}$ = 0.5 at T = 350 K.

7.2.1 *P-x* Phase Diagram

To derive a *P-x* phase diagram of a confined methane-water binary mixture in a slit graphite pore with 3.0 nm of separation at T =350 K, we varied the molar composition of the bulk mixture as shown in **Figure 7-7**. The bulk pressure is varied depending on the molar composition of the bulk mixture. When the methane mole fraction is small, the fluid mixture may be in a liquid phase at low pressure. For this case, the bulk pressure should be low in order to obtain the phase transition from the isotherm. On the other hand, when the methane mole fraction is high, the fluid mixture will be in a liquid phase at high pressure. As a result, the bulk pressure should be high for this case in order to obtain the phase transition from the isotherm. As mentioned earlier, fluid properties, including the fluid composition in a confined space, differ from the bulk properties because of the effect of confinement. Therefore, for each sampling point, we need to compute the mole fraction of each component of the confined fluid, and the average confined fluid density from isotherms obtained from the GCMC simulation. Mole fraction of each component and average density of the confined fluid can be calculated by the following formulas:

$$x_{Confined,CH_4} = \frac{n_{CH_4}}{n_{CH_4}+n_{H_2O}} \quad \text{(7-4a)},$$

$$x_{Confined,H_2O} = \frac{n_{H_2O}}{n_{CH_4}+n_{H_2O}} \quad \text{(7-4b)},$$

and

$$\rho_{Confined} = \frac{(n_{CH_4} \times MW_{CH_4})+(n_{H_2O} \times MW_{H_2O})}{N_A \times V_{Unit\ Cell}} \quad \text{(7-4c)}.$$

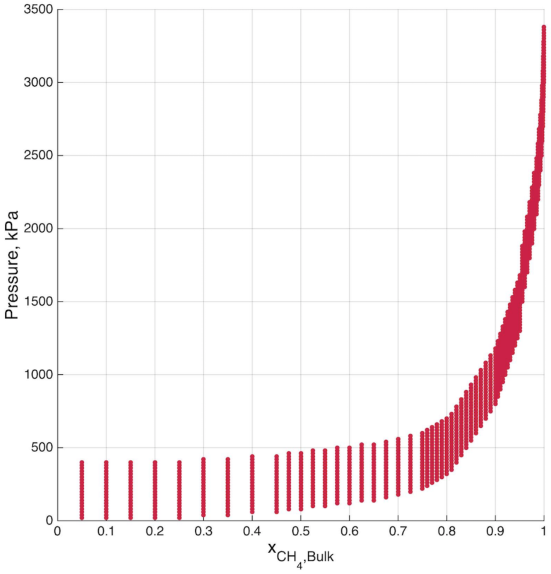

Figure 7-7 – Bulk molar fluid composition of methane-water binary mixture used in our study.

Figures 7-8a and **7-8b** are 2D- and 3D-*P*-*x* phase diagrams of a methane-water binary mixture in a slit graphite pore with 3.0 nm of separation at *T* = 350 K. As seen in the color bar, the blue color represents low density, meaning that the mixture is in vapor phase; and the red color represents high density. The level of the point in the 3D-phase diagram also represents the mixture density. There are five interesting regions in the 2D-*P*-*x* phase diagram as shown in **Figure 7-8a**.

- Region 1: At low pressure, the confined fluid is in the vapor phase for any fluid compositions. An example of a final configuration for this case is illustrated in **Figure 7-9a**. The configuration is in equilibrium at *p* = 80 kPa. The bulk methane mole fraction is 0.35.

According to the configuration, the confined fluid contains a few of both methane and water molecules scattered in the system.

- Region 2: As the bulk pressure increases, water may form a liquid phase in the confined system as shown in **Figure 7-9b**. In this region, the confined fluid consists of two different phases of two different components, which are pure liquid water and pure methane vapor. According to the configuration, water molecules and methane molecules accumulate separately in the confined system, meaning that water and methane are immiscible under this condition. Moreover, it can be seen that methane molecules tend to reside near the graphite wall. The configuration as shown in **Figure 7-9b** is in equilibrium at p = 280 kPa with the bulk methane mole fraction of 0.78.
- Region 3: **Figure 7-9c** depicts an example of the equilibrium state in this region. As seen in region 3 of **Figure 7-8a**, the methane mole fraction of the confined fluid is almost zero, although the bulk mixture contains a methane component. This is because the liquid water dominates our confined system as shown in the final configuration, meaning that only water molecules accumulate in the confined space. The configuration as shown in **Figure 7-9c** is in equilibrium at p = 1000 kPa with the bulk methane mole fraction of 0.92.
- Region 4: As the chemical potential of methane in the bulk mixture increases (bulk methane mole fraction increases), methane molecules may begin sharing some space in the confined system (see **Figure 7-9d**). The configuration is in equilibrium at p = 1920 kPa and the bulk methane mole fraction is 0.965. Again, water molecules and methane molecules accumulate separately in the confined system. In addition, most of the methane molecules in the confined space are adsorbed near the pore walls.
- Region 5: When the chemical potential of methane in the bulk mixture or the methane mole fraction of methane is very high compared with those of the water component, we mostly observe only methane molecules in our confined system (see **Figure 7-9e**). The configuration is in equilibrium at p = 2100 kPa. The bulk methane mole fraction is 0.985. Similar to previous cases, when methane molecules occupy the system, they tend to be adsorbed near the pore walls.

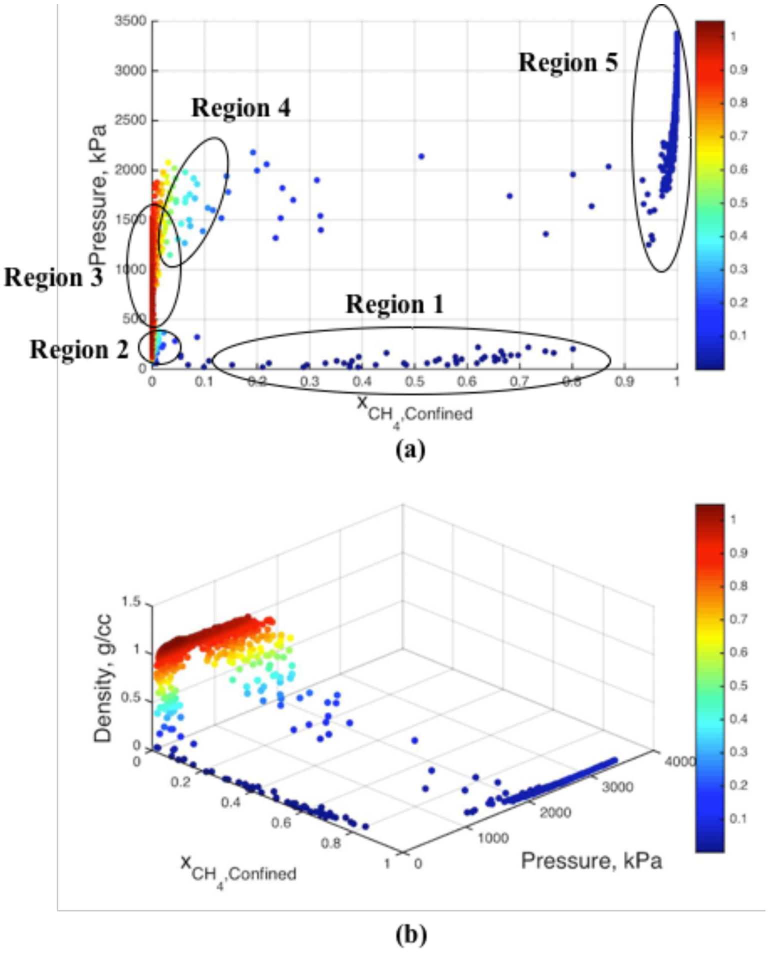

Figure 7-8 – Density plots on (a) 3D – and (b) 2D – *P-x* phase diagrams of the confined methane-water binary mixture at *T* = 350 K.

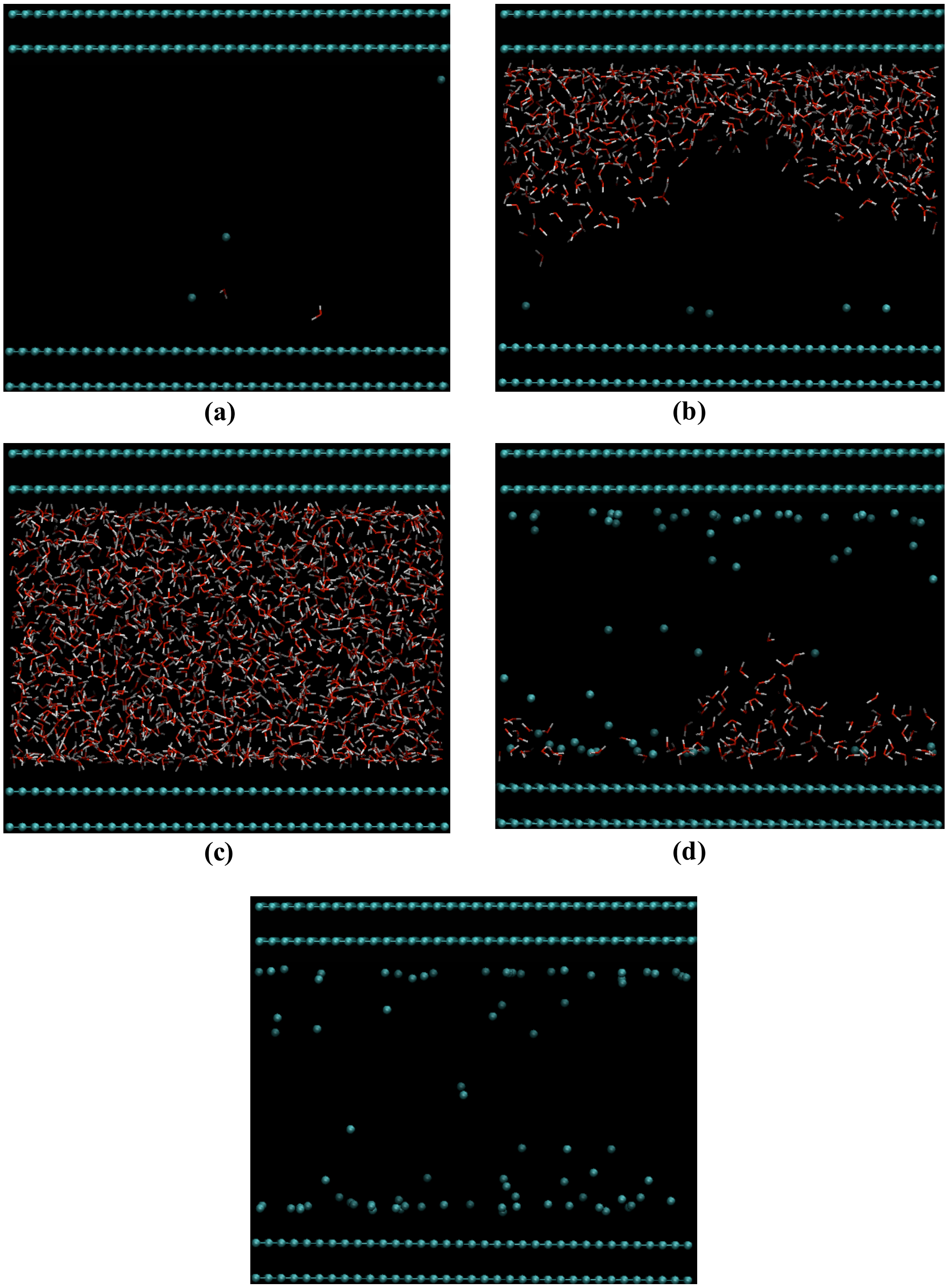
(a) (b) (c) (d) (e)

Figure 7-9 – Final configurations of confined methane-water binary mixture in a slit graphite pore with 3.0 of separation from GCMC simulations: (a) at p = 80 kPa and x_{Bulk,CH_4} = 0.35, (b) at p = 280 kPa and x_{Bulk,CH_4} = 0.78, (c) at p = 1000 kPa and x_{Bulk,CH_4} = 0.92, (d) at p = 1920 kPa and x_{Bulk,CH_4} = 0.965, and (e) at p = 3100 kPa and x_{Bulk,CH_4} = 0.985.

Based on the phase diagrams and analysis of the final configurations from the simulations, we can conclude that the methane-water binary mixture is an immiscible fluid in our confined system for the pressure range we specified in our simulations. However, we may observe methane dissolved in water in extreme conditions such as extremely high pressure or extremely low temperature. For immiscible fluids, temperature has a greater influence on the solubility of a mixture than pressure. As a result, a *T*-*x* phase diagram is more interesting than a *P*-*x* phase diagram.

7.2.2 *T-x* Phase Diagram

To derive a *T*-*x* phase diagram of a confined methane-water binary mixture in a slit graphite pore with 3.0 nm of separation at p = 1 atm, or 101.325 kPa, we varied the molar composition of the bulk mixture as shown in **Figure 7-10**. The temperature of the system is varied from 100 K to 500 K, and the methane mole fraction of the bulk mixture is varied from 0.05 to 0.999375. As mentioned earlier, fluid properties including the fluid composition in a confined space differs from the bulk properties because of the effect of confinement. Therefore, for each sampling point, we need to compute the mole fraction of each component of the confined fluid and the average confined fluid density from isotherms obtained from the GCMC simulation using equations (7-4) and (7-5), respectively.

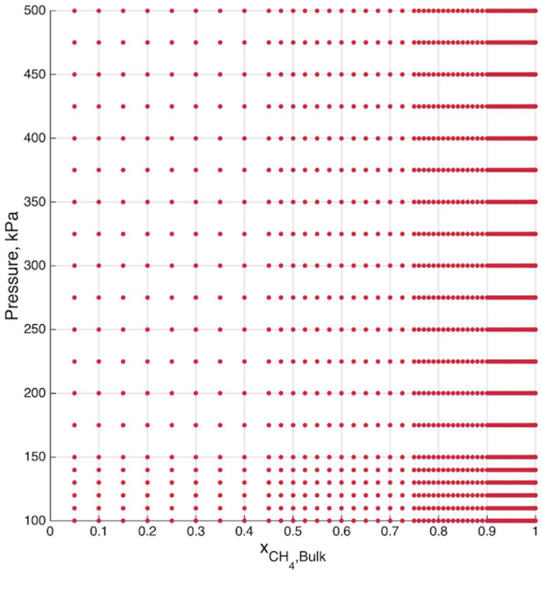

Figure 7-10 – Bulk molar fluid composition of methane-water binary mixture used in our study.

Figures 7-10a and **7-10b** are 2D- and 3D-*T*-*x* phase diagrams of a methane-water binary mixture in a slit graphite pore with 3.0 nm of separation at p = 1 atm. As seen in the color bar, the blue color represents low density, meaning that the mixture is in the vapor phase, and the red color represents high density. The level of the point in the 3D-phase diagram also represents the mixture density.

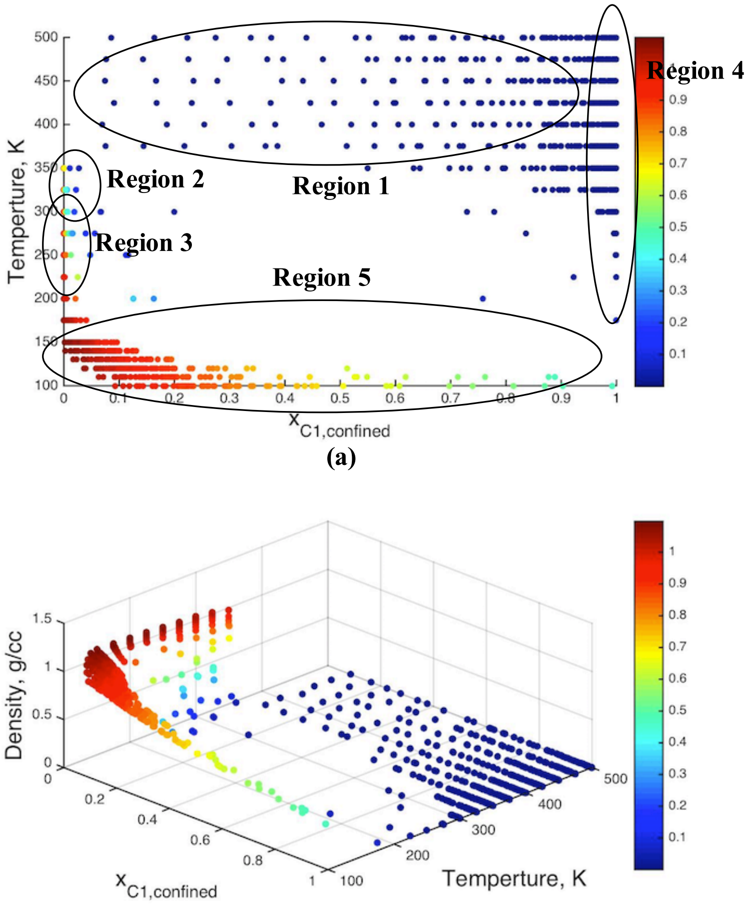

(a)

(b)

Figure 7-11 – Density plots on (a) 3D – and (b) 2D – *T-x* phase diagrams of the confined methane-water binary mixture at *p* = 1 atm.

Examples of final configurations of the confined fluid at room temperature for different bulk fluid composition are shown in **Figure 7-12**. According to **Figure 7-12a**, the confined system is filled with water molecules only, although the bulk mixture contains 50% methane. When the chemical potential increases as the bulk methane mole fraction increase to 0.9, methane starts occupying the confined space as illustrated in **Figure 7-12b**. As a result, the confined fluid contains both water and methane. However, water molecules and methane molecules accumulate separately in the confined system; water is in a liquid phase and methane is in a vapor phase. When the chemical potential of methane in the bulk mixture or the methane mole fraction is very high (x_{Bulk,CH_4} = 0.975) compared with those of water component (x_{Bulk,H_2O} = 0.025), we observe only methane molecules in our confined system as shown in **Figure 7-12c**. Methane molecules in the system tend to be adsorbed near the pore walls, as expected.

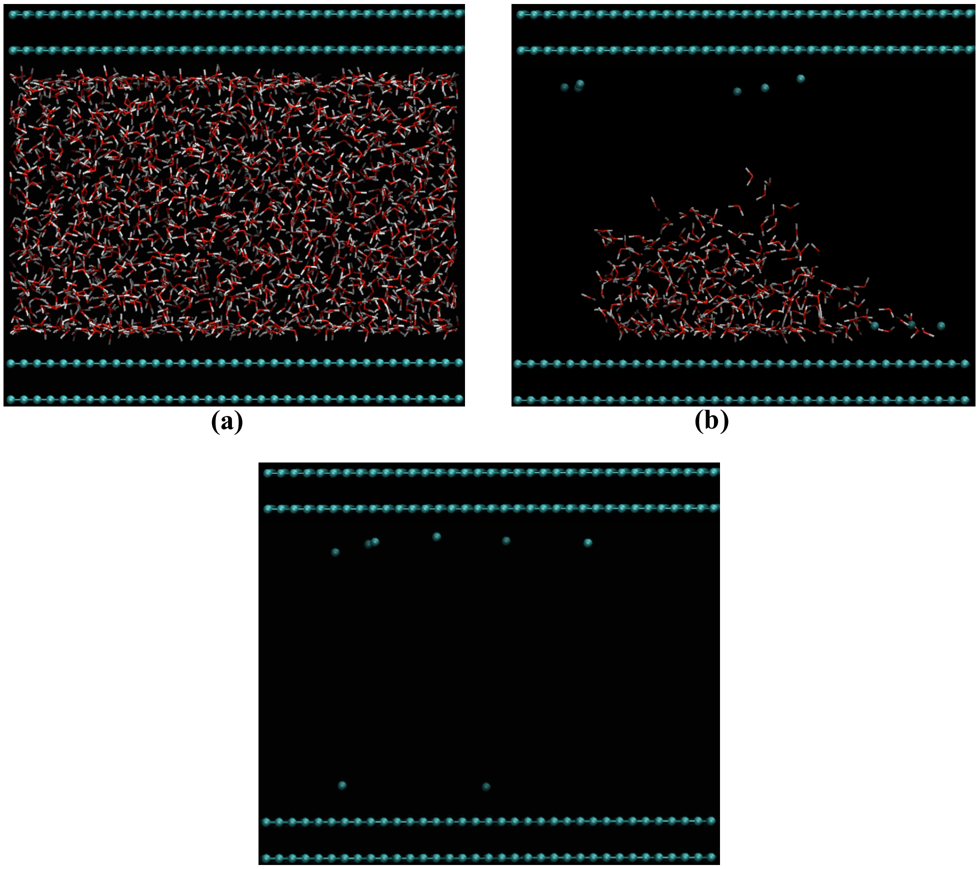
(a) (b)

(c)

Figure 7-12 – Final configurations of confined methane-water binary mixture in a slit graphite pore with 3.0 of separation from GCMC simulations at room condition (p = 80 kPa and T = 300K): (a) x_{Bulk,CH_4} = 0.50, (b) x_{Bulk,CH_4} = 0.90, and (c) x_{Bulk,CH_4} = 0.975.

There are five interesting regions in the 2D-*T*-*x* phase diagram as shown in **Figure 7-11a**.

- Region 1: At high temperature, the confined mixture is in a vapor phase for any fluid compositions. The confined mixture contains a few of both the methane and water molecules scattered in the system. This case is similar to the region 1 in **Figure 7-8a** where the bulk pressure is low.

- Region 2: Similar to the region 2 in the *p-x* phase diagram as shown in **Figure 7-8a**, as the temperature decreases, water may form a liquid phase in the confined system. In this region, the confined fluid comprises of two different phases of two different components, which are pure liquid water and pure methane vapor. Water molecules and methane molecules accumulate separately in the confined system, meaning that water and methane are immiscible under this condition. Moreover, it is noticeable that methane molecules tend to reside near the graphite wall. The configuration as shown in **Figure 7-12b** falls in this category.
- Region 3: This case is similar to region 3 in **Figure 7-8a**. The methane mole fraction of the confined fluid is almost zero, although the bulk mixture contains a methane component. This is because the liquid water dominates our confined system as shown in the final configuration, where only water molecules accumulate in the confined space.
- Region 4: When the temperature is higher than 200 K and the chemical potential of methane in the bulk mixture or the methane mole fraction is very high compared with the water component, we mostly observe only methane molecules in our confined system. This case is similar to the region 5 in the *p-x* phase diagram.
- Region 5: When the temperature is lower than 200 K, we found that methane was dissolved in water. This phenomenon cannot be observed in the *p-x* phase diagram as shown in **Figure 7-8a**. Examples of final configurations of confined fluid in this region are shown in **Figure 7-13**. **Figure 7-13a** is the final configuration at equilibrium for T = 150 K and a bulk methane mole fraction of 0.05. At this condition, only water molecules accumulate in the confined space. When the bulk methane mole fraction increases to 0.999375, methane molecules occupy the confined system and are dissolved in water as shown in **Figure 7-13b**. Most of the methane molecules in the confined fluid are adsorbed near the pore wall. **Figure 7-13c** is the final configuration at equilibrium for T = 100 K and a bulk methane mole fraction of 0.05. Even though the bulk methane mole fraction is only 5%, we found that methane molecules occupy the confined system and are dissolved in water. Again, methane molecules reside near the pore walls. When the bulk methane mole fraction increases to 0.975, methane is dissolved in water for both the adsorbed phase and the bulk phase in the confined space.

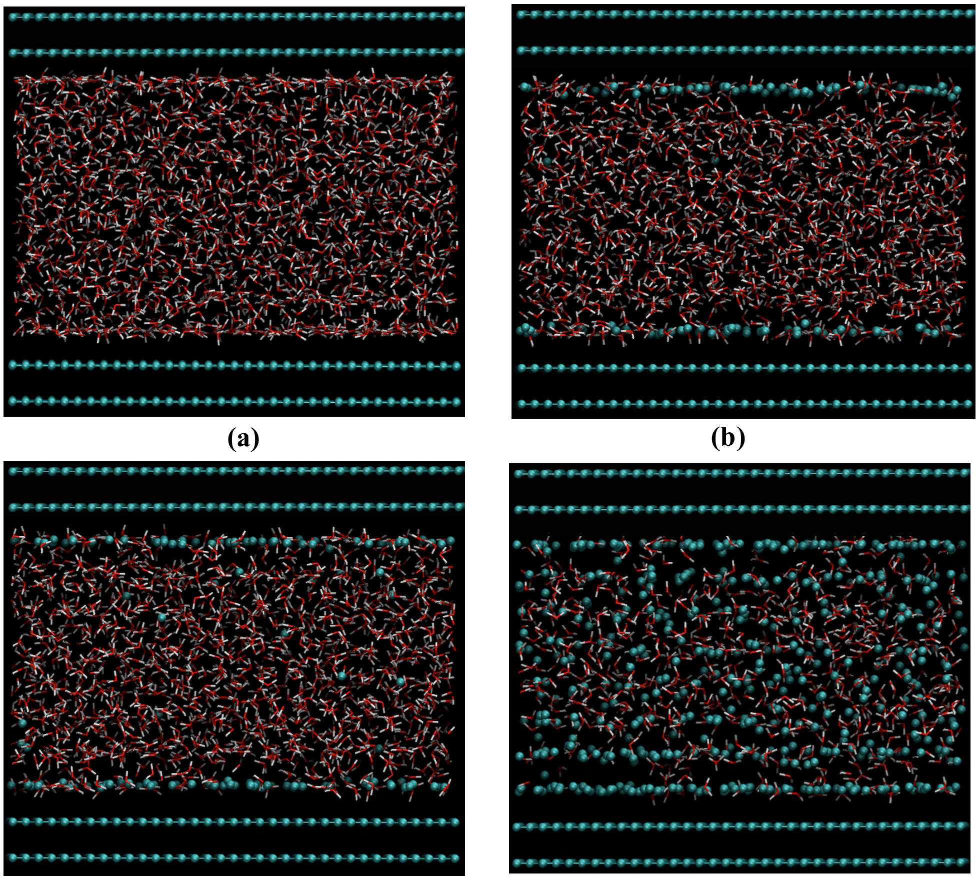

(a) (b) (c) (d)

Figure 7-13 – Final configurations of confined methane-water binary mixture in a slit graphite pore with 3.0 of separation from GCMC simulations: (a) at T = 150 K and x_{Bulk,CH_4} = 0.05, (b) at T = 150 K and x_{Bulk,CH_4} = 0.975, (c) at T = 100 K and x_{Bulk,CH_4} = 0.05, and (d) at T = 100 K and x_{Bulk,CH_4} = 0.975.

7.3 Conclusion

In conclusion, water is usually involved in unconventional reservoir fluid systems. Unlike hydrocarbons, water is a polar molecule. As a result, the Lennard-Jones potential equation is not enough to obtain reasonable accuracy for potential energy in the computation. For the petroleum fluid system with water, we need to include the Coulombic potential to account for electrostatic forces. The Coulombic potential is a long-range potential, thus we need to consider interactions due to molecules in periodic boxes. The Ewald summation method was implemented in our molecular simulations for computing long-range interactions in our periodic confined system.

For a pure component of water, the results from the classical MD simulations show that the water structure in the confined space differs from bulk water. The water molecules in the slit graphite pore form layers parallel to the graphite wall, whereas the water molecules in the bulk have no specific form. This change of water structure in the confined space caused changes to the water's properties. According to the GCMC simulation results, the confined water density is greater than the bulk water density, and the vapor pressure is lower in the confined space.

For methane-water binary mixture, we found that the confined fluid composition differs from the bulk fluid composition and it is dependent on the pressure, temperature, and bulk fluid composition. As known, methane and water are immiscible at room condition. This statement is also true in our confined system. As a result, *T-x* diagram is more useful than *P-x* diagram to describe phase behavior of the confined mixture. At high temperatures, the confined mixture is in the vapor phase for any bulk fluid compositions. The confined mixture contains a few of both the methane and water molecules scattered in the system. As the temperature decreases, water may form a liquid phase in the confined system. The confined fluid consists of two different phases of two different components, which are pure liquid water and pure methane vapor. Water molecules and methane molecules accumulate separately in the confined system, meaning that water and methane are immiscible under this condition, including room condition. For T = 200 – 325 K, there are some cases that the confined mole fraction of methane is almost zero, although the bulk mixture contains methane components. This is because the liquid water dominates our confined system. Consequently, only water molecules accumulate in the confined space. For T < 200K, we found that methane can be dissolved in water in our confined system. Methane molecules tend to be adsorbed to the pore walls. As the chemical potential of methane in the bulk mixture increases, methane molecules dissolve in both the adsorbed phase and the bulk phase in the confined space.

CHAPTER VIII

SUMMARY, CONCLUSIONS, AND RECOMMENDATIONS FOR FUTURE WORK

8.1 Summary

By and large, this research provides a detailed study of fluid behavior and changes in fluid properties – vapor pressures, critical properties, and densities – of hydrocarbons in slit graphite pores, representing kerogen pores in shale reservoirs, using molecular simulations. The conventional GCMC and CB-GCMC simulations were used to determine isotherms of pure component hydrocarbons and their mixtures. After analyzing the isotherms, the new vapor pressures, critical properties, and phase diagrams of the confined fluid were yielded. In addition, the results from the conventional GCMC and CB-GCMC simulations may be used to study selective environments in our confined system. This may help us understand how hydrocarbons populate and occupy kerogen pores in shale reservoirs. The primary use of the MD simulation for our research was to confirm the conclusions that we obtained from the conventional GCMC and CB-GCMC simulations. Moreover, the results from the MD simulations may give us an idea of the fluid molecule movement in the confined system and the exchanges of fluid molecules between the bulk and confined space.

For this study, we delivered the new phase diagrams and critical properties of pure hydrocarbons (up to C_6H_{14}) as well as the new phase diagrams of their binary and ternary mixtures in the confined system. These new properties may be implemented in numerical simulation to enhance the accuracy of reservoir performance prediction and reserve estimation. As secondary contributions of this work, we presented calculated *P-x* phase diagrams of binary systems and ternary phase diagrams of ternary systems in confined environments from isotherms of the mixtures obtained from the conventional GCMC and CB-GCMC simulations for the first time.

Furthermore, we performed a study of the effect of confinement on the structure of water and its properties including vapor pressure and density and derivations of density plots on *P-x* and *T-x* phase diagrams of a methane-water binary system in confined environments. The final configurations of the confined mixture at equilibrium also allows us to understand how water in shale reservoirs (i.e. reservoir water and injected water) interacts with hydrocarbons in the confined system.

A by-product of this work is an elucidation on the storage and transport phenomena of fluid in shale reservoirs that are yet to be evidently explained. The knowledge obtained from this work may be a stepping-stone of well stimulation efficiency improvement and production enhancement in shale reservoirs.

8.2 Conclusions

In this work, we derived critical properties and phase diagrams of hydrocarbons in shale reservoirs. Common pore sizes of shale reservoirs are at the nanoscale level. Therefore, production forecasts and reserve estimations obtained from a conventional reservoir simulator are inaccurate. In such confined spaces, continuum mechanics, which are the fundamentals of the conventional reservoir simulator, are no longer valid. To enhance accuracy of the reservoir simulator, we need to first understand how fluids behave in confined spaces. Molecular simulation is a useful technique for a study at the molecular level. The concept of GCMC simulation was introduced in this study. A combination of the Monte Carlo simulation and molecular thermodynamics are used in the GCMC simulation. The GCMC simulation seeks ensembles whose chemical potentials equal the bulk chemical potentials at a given pressure and temperature. The chemical potential, volume, and temperature of the ensembles that we obtained from the simulation must be constant. Thermodynamic properties (e.g. potential energy and density) of the confined fluid are an average of those properties of the ensembles. The acceptance rule for the GCMC simulation is a function of the chemical potential, which is dependent on the bulk pressure and temperature. At high pressure, pressure needs to be replaced by fugacity. The Peng-Robinson equation of state is used to calculate the fugacity that is then used as input in the GCMC simulation.

The Lennard-Jones potential equation and force fields are used to describe interactions (dispersion forces) between molecules in the system containing only hydrocarbons. Since we focus only on organic pores in this study, slit graphite pores were used to represent the kerogen pores in shale reservoirs. Periodic boundary conditions were applied in the simulation to extend our simulation box to a pore network.

We validated our adsorption model with experimental data for methane adsorption isotherms in a 2.34 nm slit graphite pore at 113 K, 123 K, 133 K, and 143 K, provided by Avgul and Kiselev (1970). We obtained a very good agreement between the simulation results and the experimental data, thus validating the model used for the interactions between the fluid and slit walls.

For long chain alkane molecules, intramolecular forces must be included in the calculation because their bond bending angles and bond torsion angles may alter at reservoir conditions. The CB-GCMC simulation was employed to account for intramolecular forces. A chain growth technique – first atom sampling, sphere sampling and disc sampling – is used to insert a long chain molecule into the confined system. The internal potential energy due to the molecular configuration of the inserted molecule is added to the acceptance rule of the CB-GCMC simulation.

We found that the confined environment of slit graphite pores affects fluid molecular behavior. As we observed from the GCMC simulation results, interactions between the surface walls and the fluid molecules caused changes in the thermodynamic behavior of the hydrocarbon phases. Our simulations also showed that the critical temperature and pressure of pure component methane and ethane are *reduced* as the pore size decreases. In short, the larger the pore size, the less significant the effect of confinement and the more the critical properties approach the bulk properties (as expected).

We compared our simulation results with the approximation models for shifts in critical properties of confined pure hydrocarbons commonly used in the petroleum industry and found that the Jin et al. and Ma et al. models gave very good estimations of the shifts in critical temperatures. On the other hand, none of these models provided a good approximation of the shifts in critical pressures of the confined pure hydrocarbons. We remark that the shifts in the critical properties from Zarragoicoechea and Kuz's model, Jin et al. and Ma et al.'s models, and the GCMC simulations approach zero as the pore size increases. It implies that the confined fluids tend to behave as the bulk fluid when the pore is large. However, there is a large discrepancy for the magnitude of the critical shift in pressure of the approximated models with the simulation results in small pores, especially for heavier molecules.

Moreover, according to the deviations of the confined hydrocarbon densities from the bulk densities at the reservoir conditions, they may cause intolerable errors in reserves estimation and production forecast calculation if the bulk densities are used instead of the proper densities. The confined pure component of methane, ethane, propane, butane, pentane, and hexane densities can deviate from their bulk properties by up to 69.8%, 35.5%, 19.9%, 18.8%, 19.6%, and 18.8%, respectively.

As we observed from the GCMC, CB-GCMC, and the classical MD simulation results, the slit graphite pore prefers to adsorb a heavier component more than a lighter component. In particular, the confined hexane mole fraction is higher than the confined butane mole fraction, and the confined butane mole fraction is higher than the confined methane mole fraction for a ternary system with 1/3 molar fluid composition of each component in bulk mixture. This is called selective environment in confined space due to different interactions of the pore walls with different fluid molecules. The selective environment is dependent on the temperature, reservoir (bulk) pressure, and bulk fluid composition. We also found a jump or discontinuity in the trend of molar composition of the confined fluid at the phase transition, while the trend is continuous for the supercritical fluid. This concept was used to generate *P-x* diagrams. A phase envelope is created from a collection of *P-x* diagrams. The effect of confinement causes deviations in the shapes and magnitudes of phase diagrams from the bulk. The critical properties and the phase envelope shapes are substantially different from those of the bulk mixture. As the pore size decreases, both critical pressure and temperature tend to decrease, as similarly observed with the pure component. According to the *P-T* diagrams of methane-ethane binary mixtures, both the critical pressure and temperature of the confined mixture are lower than those of the bulk fluid. The confined mixture has a higher dew point pressure than the bulk mixture with the same fluid composition, while the bubble point pressure of the confined mixture may be either lower or higher than that of the bulk mixture, depending on the temperature.

Based on the observations obtained from the binary and ternary mixture systems, the fluid composition of the produced hydrocarbon mixture may not be a good representation of the original fluid in the reservoir. The mole fraction of the heavy component of the contained mixture is higher than that of the produced fluid. At the beginning of production, shale reservoirs tend to release lighter components (e.g. methane) while the heavier components are left behind. Once the lighter components are almost completely drained from the shale reservoirs, the reservoirs will start releasing the heavier components. This phenomenon may cause changes in the produced fluid composition over the production time.

As known, water is usually involved in unconventional reservoir fluid systems. The Coulombic potential was included in our simulation to account for electrostatic forces. For confined pure water, the water density is greater and the vapor pressure is lower than bulk water. Based on the *T-x* diagram, the confined mixture is in the vapor phase for any bulk fluid composition at high temperature and a few of both the methane and water molecules are scattered in the system. As the temperature decreases, water may form a liquid phase in the confined system. The confined fluid then consists of two different phases of two different components, which are pure liquid water and pure methane vapor. Water and methane molecules accumulate separately in the confined system, meaning that water and methane are immiscible under this condition, which includes room temperature. For T = 200 – 325 K, there are some cases where the methane mole fraction of the confined fluid is almost zero, although the bulk mixture contains methane components. For *T* < 200 K, we found that methane can dissolve in water in our confined system. Methane molecules tend to be adsorbed to the pore walls. As the chemical potential of methane in the bulk mixture increases, methane molecules become dissolved in both the adsorbed phase and bulk phase in the confined space.

8.3 Recommendations for Future Work

In this work, we derived phase diagrams and critical properties of confined pure hydrocarbons from C_1H_4 to C_6H_{14}. Petroleum fluid systems usually contain hydrocarbons heavier than C_6H_{14}. Thus, I recommend extending our molecular simulation work to C_7H_{16}+.

In reality, kerogen is not as simple as a grephene sheet. It has functional groups that may change the wettability of the system. To enhance the accuracy of confined fluid properties, I strongly recommend adding functional groups in graphene sheets for a more realistic model to represent kerogen pores. Furthermore, as known, shale reservoirs consist of organic matter (kerogen) and inorganic matter (e.g. clay). We may need to include inorganic material in our molecular simulations to mimic a complex network of shale reservoirs.

We have studied up to only three fluid components in our confined system. However, reservoir fluid systems usually contain more than three components. More components need to be added in molecular simulation fluid systems to achieve more precise results.

We concluded that different interactions of the pore walls with various fluid molecule mixtures caused a selective environment in the confined system. In particular, kerogen adsorbs heavier components more readily than lighter components. This phenomenon affects the shape and size of the phase diagram and critical properties of hydrocarbon mixtures in shale reservoirs. However, we still need experimental data to validate our results and conclusions. Therefore, I strongly recommend performing an experiment to support our simulation results.

Last, but not least, it is very important to find a practical way to incorporate our results from molecular simulations into numerical reservoir simulators (e.g. adding a modification term to a conventional equation of state to account for the effect of confinement).

NOMENCLATURE

A = Helmholtz free energy, *kJ/mol*

A_p = Transversal section area of the pore, *m*^{2}

d_{ia} = Distance between the center of subparticle *a* and the center of mas of particle *i*, *Å*

$\boldsymbol{d_{ia}^s}$ = Distance vector of the subparticle *a* relative to the center of mass of particle *i*, *Å*

$\boldsymbol{d_q}$ = Displacement vector pointing from the negative charge to the positive change

D = Pore diameter, *Å*

D_e = Bond dissociation energy, *kcal/mol*

e = Electron charge

$\boldsymbol{e^s}$ = Unit vector along the particle axis

E_f = External electric field

$\boldsymbol{f}$ = Forces vector due to intermolecular forces, *N·m*

fug = Fugacity, *kPa*

fug° = Fugacity at standard condition, *kPa*

f_i = Total force acting on particle *i*, *N*

f_{ia} = Total force acting on subparticle *a* in particle *i*, *N*

$\boldsymbol{g}$ = Constraint force vector, *N·m*

$\boldsymbol{g_a^{(r)}}$ = Approximation of constraint force vector, *N·m*

$\boldsymbol{g^s}$ = Moment of force on a particle, *N·m*

$\boldsymbol{g^{\perp}}$ = A component of moment of force perpendicular to the particle axis, *N·m*

$\boldsymbol{g^{\parallel}}$ = A component of moment of force parallel to the particle axis, *N·m*

Q = Surface excess, *mol/m*^{2}

$\bar{G}$ = Molar Gibbs energy, *kJ/mol*

G° = Standard molar Gibbs energy, *kJ/mol*

h = Planck constant, *kJ·s*

H = Distance or separation between two graphite layers, *Å*

I = Moment of inertia, *kg·m*^{2}

I_p = The first ionization potential

k_B = Boltzmann Constant, *kJ/K*

k_C = Electric Constant, *Å·kJ/mol*

k_{ij} = Binary interaction parameter

k_r = Force constant in the harmonic oscillator model for bond length calculation

k_θ = Force constant in the harmonic oscillator model for bond bending angle calculation
K = Total kinetic energy, *kJ/mol*
L = Length of box, *m*
L_z = Pore length, *m*
$\mathcal{L}$ = Lagrangian function
M = Number of particles in ideal gas
MW = Molecular weight, *amu*
m_i = Mass of particle *i*, *kg*
n = Number of molecules
n_{SS} = Number of regions for the sphere sampling
N = Number of particles in restricted volume
N_A = Avogadro's number
N_θ = Number of regions of bond bending angle for the disc sampling
N_ϕ = Number of regions of bond torsion angle for the disc sampling
$p_{i\alpha}$ = α component of momentum on particle *i*, *N·s*
p = Pressure, *kPa*
p_c = Bulk critical pressure, *kPa*
p_{cp} = Pore critical pressure, *kPa*
p_r = Reduced pressure, *kPa*
p_{zz} = Axial pressure, *kPa*
p° = Pressure at standard condition, *kPa*
$\mathcal{P}$ = Probability density
q_e = Particle charge
q_k = Generalized coordinates
$\dot{q}_k$ = Generalized velocities
$\boldsymbol{q}^{\boldsymbol{N}}$ = Coordinates of *N* particles
Q = Partition function
r = Distance, *Å*
r_e = Equilibrium bond length, *Å*
r_i = Distance between the particle i and the reference point, *Å*
r_{ia} = Distance between the subparticle a in the particle *i* and the reference point, *Å*
r_j = Distance between the particle j and the reference point, *Å*
r_k = Distance between the particle k and the reference point, *Å*
r_{ij} = Distance between the two particles, *Å*

r_p = Pore radius, *m*
R = Gas constant, *kJ/mol/K*
$\ddot{r}_\imath$ = Acceleration of particle *i*, *m/s*
$\boldsymbol{s}^{\boldsymbol{N}}$ = Scaled coordinates of *N* particles
$\boldsymbol{s}^{\boldsymbol{N+1}}$ = Scaled coordinates of *N*+1 particles
$S_{C2/C1}$ = Selectivity of ethane over methane
t = Time, *s*
T = Temperature, *K*
T_c = Bulk critical temperature, *K*
T_{cp} = Pore critical temperature, *K*
T_r = Reduced temperature, *K*
u_1 = Potential energy of a particle due to external forces exerted on the system, *kJ/mol*
u_2 = Pair potential energy, *kJ/mol*
u_2^{eff} = Effective pair potential energy, *kJ/mol*
u_3 = Potential energy involving triplets of particles
U^{id} = Potential energy of ideal gas, *kJ/mol*
U = Potential energy, *kJ/mol*
U_I = Potential energy of state *I*, *kJ/mol*
U_{II} = Potential energy of state *I*, *kJ/mol*
$\boldsymbol{v}^{\boldsymbol{s}}$ = Angular velocity vector, s^{-1}
$\dot{\boldsymbol{v}}^{\boldsymbol{s}}$ = Angular acceleration vector, s^{-2}
v_c = Bulk critical specific volume, m^3/kg
v_{cp} = Pore critical specific volume, m^3/kg
v_e = Harmonic vibrational frequency
V = Volume of restricted system, m^3
V_p = Pore Volume, m^3
V_0 = Volume of ideal gas, m^3
$V_{Unit\ Cell}$ = Volume of simulated unit cell excluding the volume occupied by the graphite slab, cm^3
$\bar{V}$ = Molar volume, m^3
x = Mole fraction
x_{Bulk} = Mole fraction in the bulk system
$x_{Confined}$ = Mole fraction in liquid phase in the confined system
$y_{Confined}$ = Mole fraction in vapor phase in the confined system
z = Particle charge relative to the charge of the electron

Z = Compressibility factor

$\mathbb{Z}$ = Configuration Integral

α = Acceptance probability

α_p = Polarization of the molecule

β = Thermodynamic beta, kJ^{-1}

$\delta U_{I \rightarrow II}$ = Potential energy difference between State *I* and State *II*, *kJ/mol*

ε_{ii} = Depth of potential trough for the interaction between the two type *i* particles, *kJ/mol*

ε_{ij} = Depth of potential trough for the interaction between the type *i* and type *j* particles, *kJ/mol*

ε_{jj} = Depth of potential trough for the interaction between the two type *j* particles, *kJ/mol*

λ = Lagrange multiplier

μ = Chemical potential, *kJ/mol*

μ_{bulk} = Chemical potential of the bulk system, *kJ/mol*

μ_{bulk}^{vapor} = Chemical potential in vapor phase of the bulk system, *kJ/mol*

$\mu_{confined}$ = Chemical potential of the confined system, *kJ/mol*

$\mu_{confined}^{vapor}$ = Chemical potential in vapor phase of the confined system, *kJ/mol*

$\mu_{confined}^{liquid}$ = Chemical potential in liquid phase of the confined system, *kJ/mol*

$\boldsymbol{\mu_e}$ = Electric dipole moment

ξ = Random number from 0 to 1

ρ = Density, *kg/m*^{3}

ρ_{Bulk} = Density of bulk fluid, *g/cc*

$\rho_{Confined}$ = Density of confined fluid, *g/cc*

σ_A = Collision diameter of the molecule, *Å*

σ_e = Effective diameter of the molecule, *Å*

σ_{ii} = Distance between the two type *i* particles at which the inter-particle potential is zero, *Å*

σ_{ij} = Distance between the type *i* and type *j* particles at which the inter-particle potential is zero, *Å*

σ_{jj} = Distance between the two type *j* particles at which the inter-particle potential is zero, *Å*

$\boldsymbol{\tau}$ = Torque vector on a particle, *N·m*

τ_i = Torque about the center of mass of particle *i*, *N·m*

θ_e = Equilibrium bond bending angle

ϕ = Bond torsion angle

ϕ_f = Fugacity coefficient

ω = Acentric factor

Λ = Thermodynamic beta, m

Ω = Phase space volume of the molecule

Π = Acceptance rule

ψ = Eulerian angle

REFERENCES

Al Ismail, M.I. and Horne, R.N. 2014. Modeling Adsorption of Gases in Nanoscale Pores Using Grand Canonical Monte Carlo Simulation Techniques. Paper SPE 170948 presented at the SPE Annual Technical Conference and Exhibition, Amsterdam, The Netherlands, 27–29 October. http://dx.doi.org/10.2118/170948-MS.

Allen, M.P. and Tildesley, D.J. 1987. *Computer Simulation of Liquids*. Oxford University Press, Oxford.

Ambrose, R.J., Hartman, R.C. and Akkutlu, Y.I. 2011. Multi-component Sorbed-phase Considerations for Shale Gas-in-place Calculations. Paper SPE 141416 presented at the SPE Production and Operations Symposium, Oklahoma City, OK, USA, 27-29 March. http://dx.doi.org/10.2118/141416-MS.

Ambrose, R.J., Hartman, R.C., Diaz-Campos, M., Akkutlu, Y.I. and Sondergeld, C.H. 2012. Shale Gas-in-place Calculations Part I: New Pore-Scale Considerations. *J. Pet. Tech.* **17** (1): 219-229. SPE-131772-PA. http://dx.doi.org/10.2118/131772-PA.

Avgul, N.N., and Kiselev, A.V. 1970. Physical Adsorption of Gases and Vapors on Graphitized Carbon Blacks. *Chemistry and Physics of Carbon.* **6**: 1-124. Dekker. New York.

Barendsen, H.J.C., Grigera, J.R. and Straastsma, T.P. 1987. The Missing Term in Effective Pair Potential. *J. Phys. Chem.* **91**: 6269-6271. http://dx.doi.org/10.1021/j100308a038.

Bloomer, O.T., Gami, D.C. and Parent, J.D. 1953. Physical-Chemical Properties of Methane-Ethane Mixtures. *Research Bulletin, Institute of Gas Technology* **22**: 1-39.

Brusllovsky, A.L. 1992. Mathematical Simulation of Phase Behavior of Natural Multicomponent Systems at High Puressure with An Equation of State. *SPE Reservoir Engineering*. **7** (1): 117-122. http://dx.doi.org/10.2118/20180-PA.

Chalmers, G.R., Bustin, R.M. and Power, I. 2009. A Pore by Any Other Name Would Be as Small: the Importance of Meso and Microporosity in Shale Gas Capacity. Presented at the AAPG Annual Conventional and Exhibition, Denver, CO, USA, 7-10 June.

Coquelet, C., Chareton, A. and Richon, D. 2004. Vapour–Liquid Equilibrium Measurements and Correlation of the Difluoromethane (R32) + Propane (R290) + 1,1,1,2,3,3,3-Heptafluoropropane (R227ea) Ternary Mixture at Temperatures from 269.85 to 328.35 K. *Fluid Phase Equilibria* **218**: 209-214. http://dx.doi.org/10.1016/j.fluid.2003.12.009.

Cracknell, R.F., Nickolson, D. and Quirke, N. 1993. A Grand Canonical Monte Carlo Study of Lennard-Jones Mixtures in Slit Shaped Pores. *Molecular Physics* **80** (4): 885–897. http://dx.doi.org/10.1080/00268979300102741.

Curtis, M.E., Ambrose, R.J., Sondergeld, C.H. and Rai, C.S. 2010. Structural Characterization of Gas Shales on Micro- and Nano-Scales. Paper SPE 137693 presented at the Canadian Unconventional Resources and International Petroleum Conference, Calgary, AB, Canada, 19-21 October. http://dx.doi.org/10.2118/137693-MS.

Darabi, H., Ettehad, A., Javadpour, F. and Sepehrnoori, K. 2012. Gas Flow in Ultra-tight Shale Strata. *J. Fluid Mech.* **710**: 641-658. http://dx.doi.org/10.1017/jfm.2012.424.

Devegowda, D., Sapmanee, K., Civan, F. and Sigal, R. 2012. Phase Behavior of Gas Condensates in Shales Due to Pore Proximity Effects: Implications for Transports, Reserves and Well Productivity. Paper SPE 160099 presented at the SPE Annual Technical Conference and Exhibition, San Antonio, TX, USA, 8-10 October. http://dx.doi.org/10.2118/160099-MS.

Didar, B.R. and Akkutlu, Y.I. 2013. Pore-Size Dependence of Fluid Phase Behavior and Properties in Organic-Rich Shale Reservoirs. Paper SPE 164099 presented at the International Symposium on Oilfield Chemistry, The Woodlands, TX, USA, 8 – 10 April. http://dx.doi.org/10.2118/164099-MS.

Didar, B.R. and Akkutlu, Y.I. 2013. Pore-Size Dependence of Fluid Phase Behavior and the Impact on Shale Gas Reserves. Paper SPE 168939 / URTeC 1624453 presented at the Unconventional Resources Technology Conference, Denver, CO, USA, 12 – 14 August. http://dx.doi.org/10.1190/URTEC2013-183.

Dunfield, L.G., Burgess, A.W. and Scheraga, H.A. 1977. Energy Parameters in Polypeptides. 8. Empirical Potential Energy Algorithm for the Conformational Analysis of Large Molecules. *J. Phys. Chem.* **82**: 2609-2616. http://dx.doi.org/10.1021/j100513a014.

Fathi, E., Tinni, A. and Akkutlu, Y.I. 2012. Shale Gas Correction to Klinkenberg Slip Theory. Paper SPE 154977 presented at the Americas Unconventional Resources Conference, Pittsburgh, PA, USA, 5-7 June. http://dx.doi.org/10.2118/154977-MS.

Frankel, D. and Smit, B. 1996. *Understanding Molecular Simulation from Algorithms to Applications*. Academic Press, Chestnut Hill, MA.

Freeman, C.M. 2010. A Numerical Study of Microscale Flow Behavior in Tight Gas and Shale Gas Reservoir Systems. Paper SPE 141125-STU presented at the SPE International Student Paper Contest at the SPE Annual Technical Conference and Exhibition, Florence, Italy, 19-22 September. http://dx.doi.org/10.2118/141125-STU.

Hirunsit, P. and Balbuena P.B. 2007. Effects of Confinement on Water Structure and Dynamics: A Molecular Simulation Study. *J. Phys. Chem.* **111** (4): 1709-1715. http://dx.doi.org/10.1021/jp063718v.

Honarpour, M.M., Nagarajan, N.R., Orangi, A., Arasteh, F. and Yao, Z. 2012. Characterization of Critical Fluid, Rock, and Rock-Fluid Properties-Impact on Reservoir Performance of Liquid-Rich Shales. Paper SPE 158042 presented at the SPE Annual Technical Conference and Exhibition, San Antonio, TX, USA, 8-10 October. http://dx.doi.org/10.2118/158042-MS.

Jin, L., Ma, Y. and Jamili, A. 2013. Investigating The Effect of Pore Proximity on Phase Behavior And Fluid Properties in Shale Formations. Paper SPE 166192 presented at the SPE Annual Technical Conference and Exhibition, New Orleans, LA, USA, 30 September–2 October. http://dx.doi.org/10.2118/166192-MS.

Jorgensen, W.L., Madura, J.D. and Swenson, C.J. 1984. Optimized Intermolecular Potential Functions for Liquid Hydrocarbons. *J. Am. Chem. Soc.* **106** (22): 6638-6646. http://dx.doi.org/10.1021/ja00334a030.

Kanda, H., Miyahara, M. and Higashitani, K. 2004. Triple Point of Lennard-Jones Fluid in Slit Nanopore: Solidification of Critical Condensate. *J. Chem. Phys.* **120** (13): 6173-6179. http://dx.doi.org/10.1063/1.1652431.

Kuila, U. and Prasad, M. 2010. Pore Size Distribution and Ultrasonic Velocities of Compacted Na-Montmorillonite Clays. Paper SEF-2010-2590 presented at the SEG Annual Meeting, Denver, CO, USA, 17-22 October.

Kurniawan, Y., Bhatia, S.K. and Rudolph, V. 2006. Simulation of Binary Mixture Adsorption of Methane and CO_2 at supercritical conditions in carbons. *AIChE J.* **52** (3): 957-967. http://dx.doi.org/10.1002/aic.10687.

Lemmens, H.J., Butcher, A.R. and Botha, P.W. 2010. FIB/SEM and Automated Mineralogy for Core and Cuttings Analysis. Paper SPE 136327 presented at the SPE Russian Oil & Gas Technical Conference and Exhibition, Moscow, Russia, 26-28 October. http://dx.doi.org/10.2118/136327-MS.

Lemmens, H.J., Butcher, A.R. and Botha, P.W. 2011. FIB/SEM and SEM/EDX: a New Dawn for the SEM in the Core Lab?. *Petrophysics* **52** (6): 452-463.

Lewis, R., Singer, P., Jiang, T., Rylander, E., Sinclair, S. and Mclin, R.H. 2013. NMR T2 Distributions in the Eagle Ford Shale: Reflections on Pore Size. Paper SPE 164554 presented at the Unconventional Resources Conference, The Woodlands, TX, USA, 10-12 April. http://dx.doi.org/10.2118/164554-MS.

Li, B., Mezzatesta, H., Thern, H., Zhang, B., Wu, J. and Zhang, H. 2014. The Condition of Capillary Condensation and Its Effects on Gas-In-Place of Unconventional Gas Condensate Reservoirs. Paper SPE 170837 presented at the SPE Annual Technical Conference and Exhibition, Amsterdam, The Netherlands, 27–29 October. http://dx.doi.org/10.2118/170837-MS.

Li, Z., Jin, Z. and Firoozabadi, A. 2014. Phase Behavior and Adsorption of Pure Substances and Mixtures and Characterization in Nanopore Structures by Density Functional Theory. *SPE Journal*, December 2014: 1096-1109. http://dx.doi.org/10.2118/169819-PA.

Ma, Y., Jin, L. and Jamili, A. 2013. Modifying van der Waals Equation of State to Consider Influence of Confinement on Phase Behavior. Paper SPE 166476 presented at the SPE Annual Technical Conference and Exhibition, New Orleans, LA, USA, 30 September–2 October. http://dx.doi.org/10.2118/166476-MS.

Machida, K. 1999. *Principles of Molecular Mechanics*. John Wiley & Sons, Hoboken, NJ.

McQuarrie, D.A and Simon, A.D. 1999. *Molecular Thermodynamics*. University Science Books, Sausalito, CA.

Melèndez-Pagán, Y. and Ben-Amotz, D. 2000. Intermolecular Forces and Bond Length Changes in High-Pressure Fluids. Vibrational Spectroscopic Measurement and Generalized Perturbed Hard Fluid Analysis. *J. Chem. Phys.* **104** (32): 7858-7866. http://dx.doi.org/ 10.1021/jp0016479.

Metropolis, N., Rosenbluth, A.W., Rosenbluth, M.N., Teller, A.H. and Teller, E. 1953. Equation of State Calculation by Fast Computing Machines. *J. Chem. Phys.* **21**: 1087-1092. http://dx.doi.org/10.1063/1.1699114.

Moore, E.B., Ezequiel de la Llave, Welke, K., Scherlisb, D.A. and Molinero, V. 2010. Freezing, Melting and Structure of Ice in a Hydrophilic Nanopore. *Physical Chemistry Chemical Physics* **12** (16): 4124-4134. http://dx.doi.org/10.1039/B919724A.

Nagarajan, N.R., Honarpour, M.M. and Arasteh, F. 2013. Critical Role of Rock and Fluid – Impact on Reservoir Performance on Unconventional Shale Reservoirs. Paper SPE 168864 presented at the Unconventional Resources Technology Conference, Denver, CO, USA, 12-14 August. http://dx.doi.org/10.1190/URTEC2013-194.

National Institute of Standards and Technology. 2011. NIST Chemistry WebBook: Thermophysical Properties of Fluid Systems, http://webbook.nist.gov/chemistry/fluid (accessed October 2014).

Nohabaei, B., Johns, R.T. and Chu, J. 2013. Effect of Capillary Pressure on Fluid Density and Phase Behavior in Tight Rocks and Shales. *SPE Reservoir Evaluation & Engineering*, August 2013: 281-289. http://dx.doi.org/10.2118/159258-PA.

Orangi, A., Nagarajan, N.R., Honarpour, M.M. and Rosenzweig, J. 2011. Unconventional Shale Oil and Gas-Condensate Reservoir Production, Impact of Rock, Fluid, and Hydraulic Fractures. Paper SPE 140536 presented at the SPE Hydraulic Fracturing Technology Conference and Exhibition, The Woodlands, TX, USA, 24-26 January. http://dx.doi.org/10.2118/140536-MS.

Orbey, H. and Sandler, I.S. 1998. *Modeling Vapor-Liquid Phase Equilibria: Cubic Equations of State and Their Mixing Rule*. Cambridge University Press, New York, NY.

Panagiotopoulos, A.Z., Quirke, N., Stapleton, M. and Tildesley, D.J. 1987. Phase-Equilibria by Simulation in The Gibbs Ensemble - Alternative Derivation, Generalization and Application to Mixture and Membrane Equilibria. *Mol. Phys*. **63** (4): 527-545. http://dx.doi.org/10.1080/00268978800100361.

Peng, D. and Robinson, D.B. 1975. A New Two-Constant Equation of State. *Industrial & Engineering Chemistry Fundamental* **15** (1): 59-64. http://dx.doi.org/10.1021/i160057a011.

Ping, G., Liangtian, S., Li, S. and Lei, S. 1996. A Theoretical Study of the Effect of Porous Media on the Dew Point Pressure of a Gas Condensate. Paper SPE 35633 presented at the SPE Gas Techmology Symposium, Calgary, Alberta, Canada, 28 April – 1 May. http://dx.doi.org/10.2118/35644-MS.

Pitakbunkate, T., Balbuena, P.B., Moridis, G.J. and Blasingame, T.A. 2014. Effect of Confinement on PVT Properties of Hydrocarbons in Shale Reservoirs. Paper SPE 170685 presented at the SPE Annual Technical Conference and Exhibition, Amsterdam, The Netherlands, 27–29 October. http://dx.doi.org/10.2118/170685-MS.

Prausnitz, J.M., Lichtenthaler, R.N. and Gomes de Azevedo, E. 1999. *Molecular Thermodynamics of Fluid-Phase Equilibria*. Prentice-Hall, Upper Saddle River, NJ.

Sanaei, A., Jamili, A., Callard, J. and Mathur, A. 2014. Production Modeling in the Eagle Ford Gas Condensate Window: Integrating New Relationships between Core Permeability, Pore Size, and Confined PVT Properties. Paper SPE 169493 presented at the SPE Western North American and Rocky Mountain Joint Regional Meeting, Denver, CO, USA, 16–18 April. http://dx.doi.org/10.2118/169493-MS.

Shabro, V., Torres-Verdin, C. and Javadpour, F. 2011. Numerical Simulation of Shale-Gas Production: from Pore-Scale Modeling of Slip-Flow, Knudsen Diffusion, and Langmuir Desorption to Reservoir Modeling of Compressible Fluid. Paper SPE 144355 presented at the 2011 SPE North American Unconventional Gas Conference and Exhibition, The Woodlands, TX, USA, 14-16 June. http://dx.doi.org/10.2118/144355-MS.

Singh, S.K. and Singh, J.K. 2011. Effect of Pore Morphology on Vapor–liquid Phase Transition and Crossover Behavior of Critical Properties from 3D to 2D. *Fluid Phase Equilibria* **300** (1-2): 182-187. http://dx.doi.org/10.1016/j.fluid.2010.10.014.

Singh, S.K., Sinha, A., Deo, G. and Singh, J.K. 2009. Vapor–liquid Phase Coexistence, Critical Properties, and Surface Tension of Confined Alkanes. *The Journal of Physical Chemistry C* **113** (17): 7170-7180. http://dx.doi.org/10.1021/jp8073915.

Sisk, C., Diaz, E., Walls, J., Grader, A. and Suhrer, M. 2010. 3D Visualization and Classification of Pore Structure and Pore Filling in Gas Shales. Paper SPE 134582 presented at the SPE Annual Technical Conference and Exhibition, Florence, Italy, 19–22 September. http://dx.doi.org/10.2118/134582-MS.

Smith, J.M., Ness, H.V. and Abbott, M.M. 2005. *Introduction to Chemical Engineering Thermodynamics*. Mc-Graw Hill, New York, NY.

Stanley, M.W. 1984. *Phase Equilibria in Chemical Engineering*. Butterworth Publishers, Boston, MA.

Steinfeld, J.I., Francisco, J.S. and Hase, W.L. 1998. *Chemical Kinetics and Dynamics*. Prentice Hall; 2nd edition, Upper Saddle River, NJ.

Sun, H., Chawathé A., Hoteit, H., Shi, X. and Li, L. 2015. Understanding Shale Gas Flow Behavior Using Numerical Simulation. *SPE Journal*, February 2015: 142-150. http://dx.doi.org/10.2118/167753-PA.

Swami, V., Clarkson, C., and Settari, A. 2012. Non-Darcy Flow in Shale Nanopores: Do We Have a Final Answer?. Paper SPE 162665 presented at the SPE Canadian Unconventional Resources Conference, Calgary, Alberta, Canada, 30 October – 1 November. http://dx.doi.org/10.2118/162665-MS.

Teklu, T.W., Alharthy, N., Kazemi, H., Yin, X., Graves, R.M. and Alsumaiti, A.M. 2014. Phase Behavior and Minimum Miscibility Pressure in Nanopores. *SPE Journal*, August 2014: 396-403. http://dx.doi.org/10.2118/168865-PA.

Thommes, M. and Findenegg, G.H. 1994. Pore Condensation and Critical-Point Shift of a Fluid in Controlled-Pore Glass. *Langmuir* **10** (11): 4270-4277. http://dx.doi.org/10.1021/la00023a058.

Travalloni, L., Castier, M., Tavares, F.W. and Sandler, S.I. 2010. Critical Behavior of Pure Confined Fluids from an Extension of the van der Waals Equation of State. *The Journal of Supercritical Fluids* **55** (2): 455-461. http://dx.doi.org/10.1016/j.supflu.2010.09.008.

Vandenbroucke, M. 2006. Kerogen: from Types to Models of Chemical Structure. *Oil & Gas Science Technology – Rev.* IFP **58** (2): 243-269. http://dx.doi.org/10.2516/ogst:2003016.

Vishnyakov, A., Piotrovskaya, E.M., Brodskaya, E.N., Votyakov, E.V. and Tovbin, Y.K. 2001. Critical Properties of Lennard-Jones Fluid in Narrow Slit-Shaped Pores. *Langmuir* **17** (14): 4451-4458. http://dx.doi.org/10.1021/la001641a.

Wang, L., Persa, E., Gao, Y., Ok, J.T., Neeves, K.B., Yin, X. and Ozkan, E. 2014. Experimental Study and Modeling of the Effect of Nanoconfinement on Hydrocarbon Phase Behavior in Unconventional Reservoirs. Paper SPE 169581 presented at the SPE Western North American and Rocky Mountain Joint Regional Meeting, Denver, CO, USA, 16–18 April. http://dx.doi.org/10.2118/169581-MS.

Zarragoicoechea, G.J. and Kuz, V.A. 2002. van der Waals Equation of State for a Fluid in a Nanopore. *Physical Review E.* **65** (2): 1-4. http://dx.doi.org/10.1103/PhysRevE.65.021110.

Zarragoicoechea, G.J. and Kuz, V.A. 2004. Critical Shift of a Confined Fluid in a Nanopore. *Fluid Phase Equilibria* **220** (1): 7-9. http://dx.doi.org/10.1016/j.fluid.2004.02.014.

Zeigermann, P., Dvoyashkin, M., Valiulin, R. and Karger, J. 2009. Assessing the Pore Critical Point of the Confined Fluid by Diffusion Measurement. *Diffusion-fundamental.org* **11** (41): 1-2.

Zhang, H., Bai, B., Song, K. and Elgmati, M. 2012. Shale Gas Hydraulic Flow Unit Identification Based on SEM-FIB tomography. Paper SPE 160143 presented at the SPE Annual Technical Conference and Exhibition, San Antonio, TX, USA, 8-10 October. http://dx.doi.org/10.2118/160143-MS.

APPENDIX A

CRITICAL PROPERTIES OF HYDROCARBONS IN DIFFERENT PORE SIZES

A.1 Methane (1.0 nm – 7.0 nm)

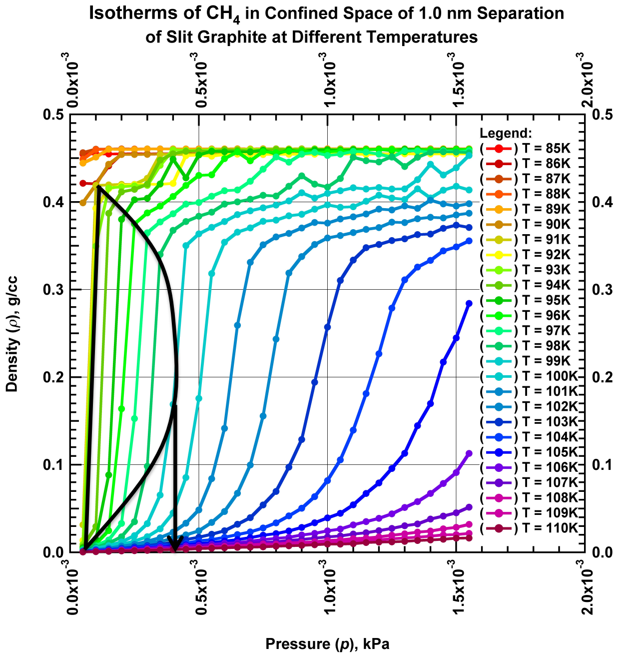

Figure A-1 – Phase diagram of confined methane in 1.0 nm of separation of a slit graphite pore (representing kerogen in shale reservoir).

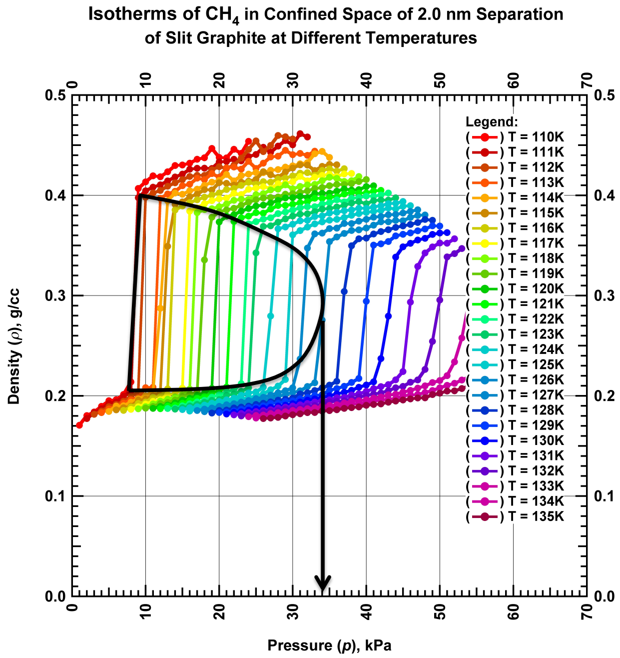

Figure A-2 – Phase diagram of confined methane in 2.0 nm of separation of a slit graphite pore (representing kerogen in shale reservoir).

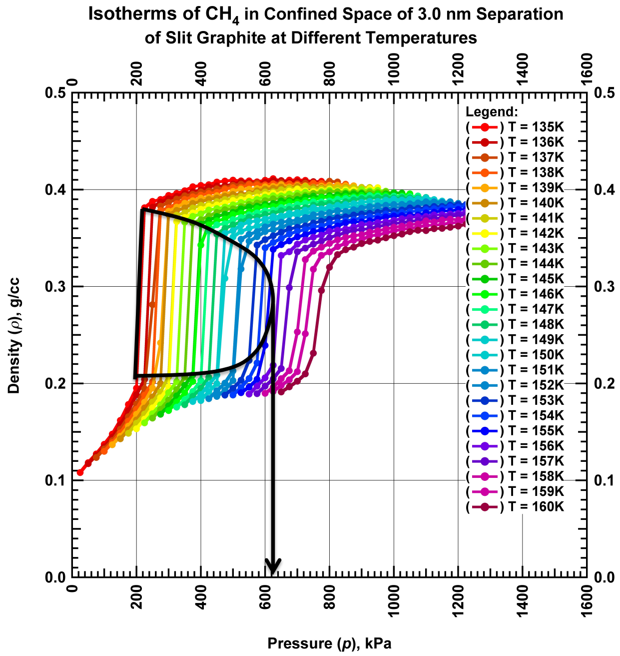

Figure A-3 – Phase diagram of confined methane in 3.0 nm of separation of a slit graphite pore (representing kerogen in shale reservoir).

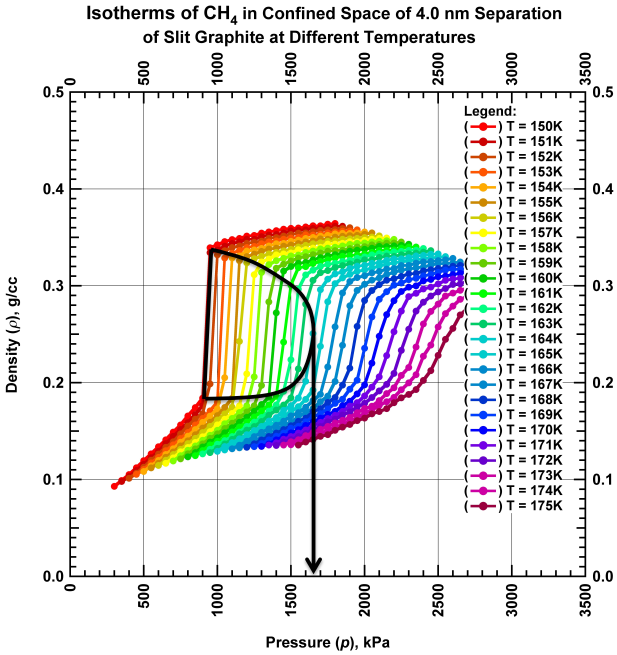

Figure A-4 – Phase diagram of confined methane in 4.0 nm of separation of a slit graphite pore (representing kerogen in shale reservoir).

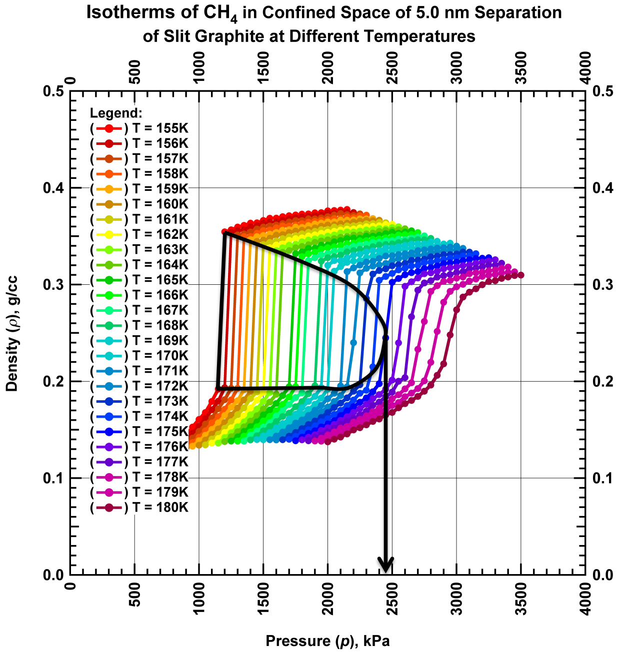

Figure A-5 – Phase diagram of confined methane in 5.0 nm of separation of a slit graphite pore (representing kerogen in shale reservoir).

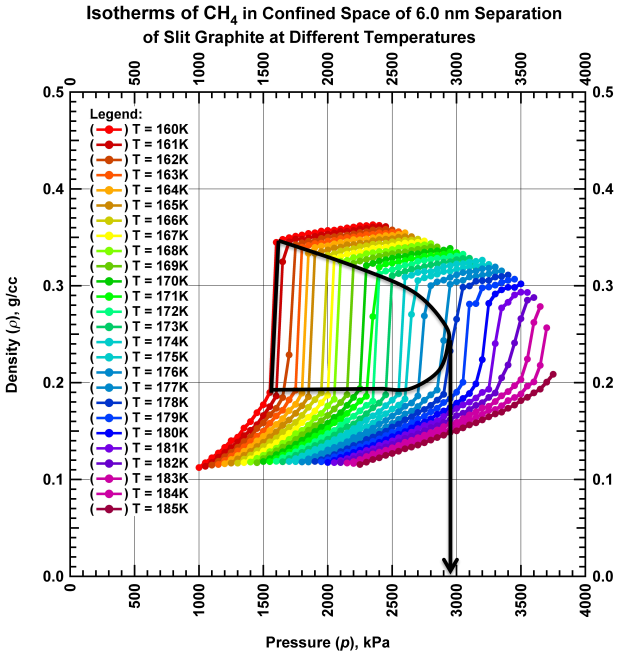

Figure A-6 – Phase diagram of confined methane in 6.0 nm of separation of a slit graphite pore (representing kerogen in shale reservoir).

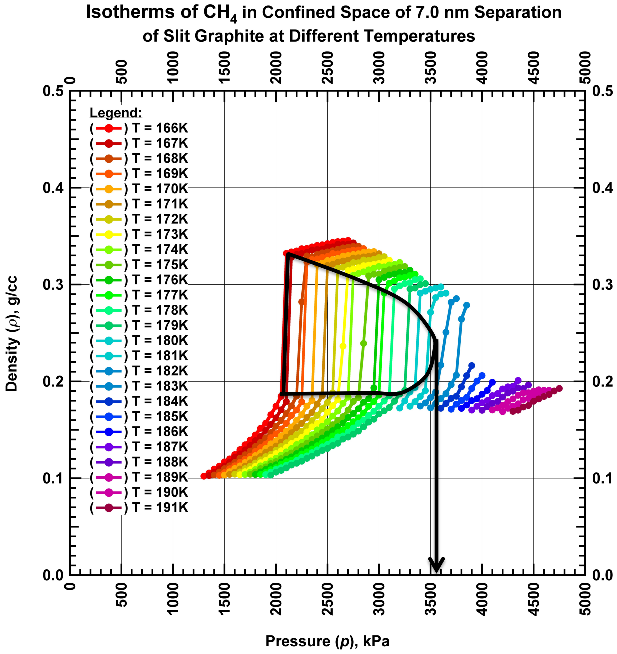

Figure A-7 – Phase diagram of confined methane in 7.0 nm of separation of a slit graphite pore (representing kerogen in shale reservoir).

A.2 Ethane (2.0 nm – 10.0 nm)

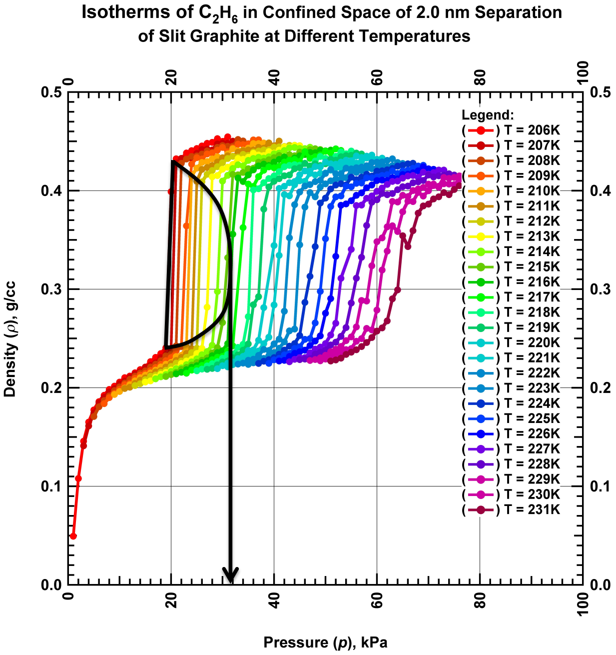

Figure A-8 – Phase diagram of confined ethane in 2.0 nm of separation of a slit graphite pore (representing kerogen in shale reservoir).

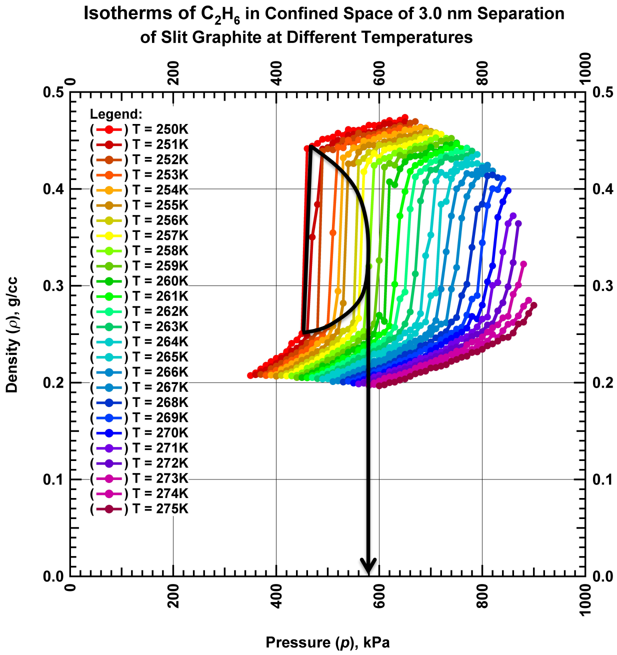

Figure A-9 – Phase diagram of confined ethane in 3.0 nm of separation of a slit graphite pore (representing kerogen in shale reservoir).

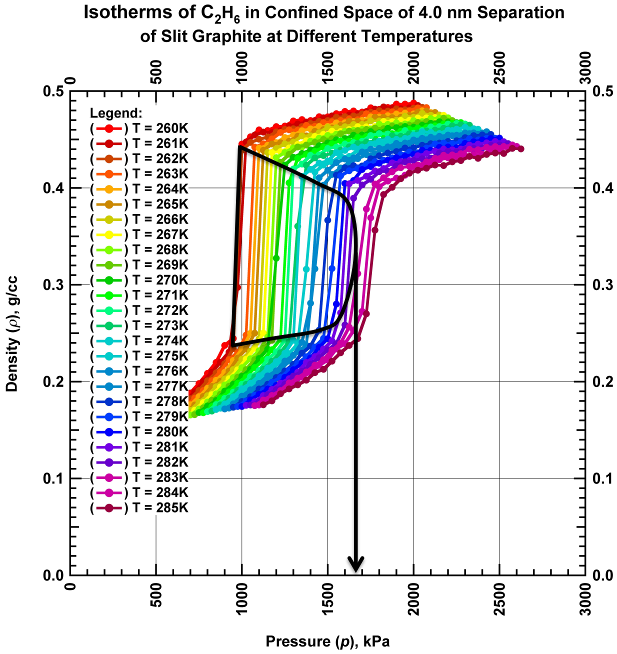

Figure A-10 – Phase diagram of confined ethane in 4.0 nm of separation of a slit graphite pore (representing kerogen in shale reservoir).

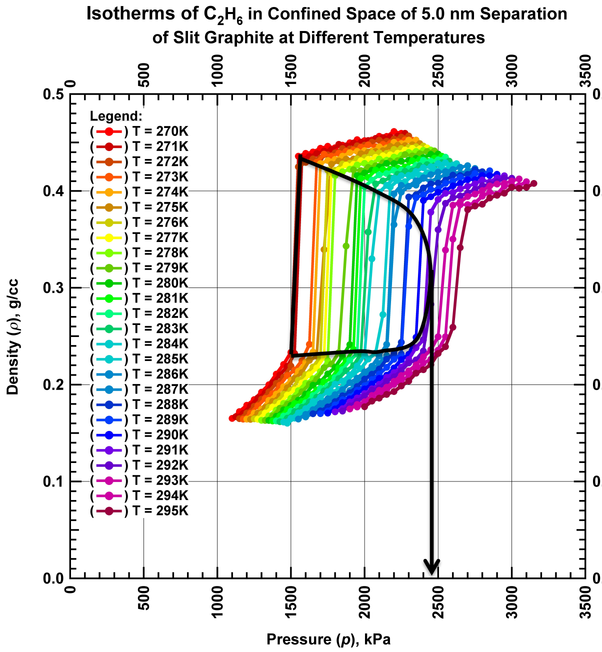

Figure A-11 – Phase diagram of confined ethane in 5.0 nm of separation of a slit graphite pore (representing kerogen in shale reservoir).

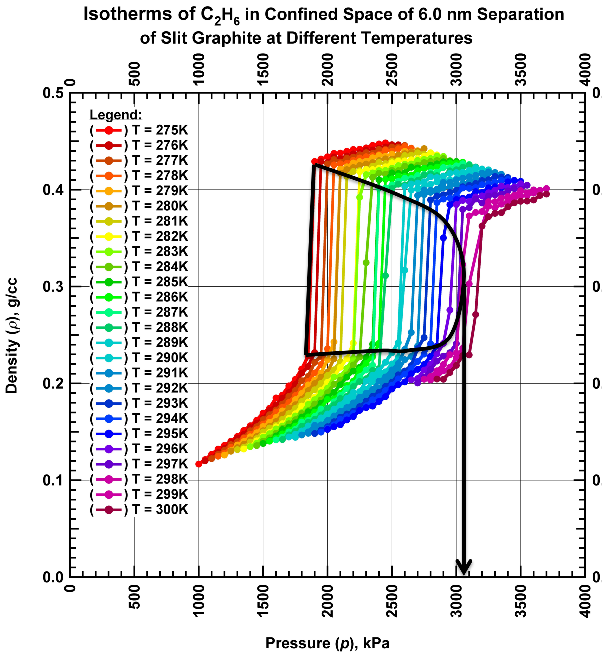

Figure A-12 – Phase diagram of confined ethane in 6.0 nm of separation of a slit graphite pore (representing kerogen in shale reservoir).

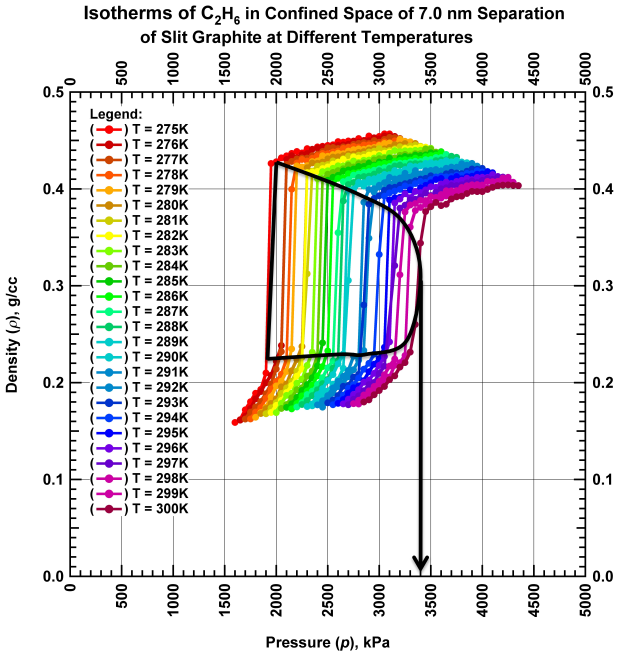

Figure A-13 – Phase diagram of confined ethane in 7.0 nm of separation of a slit graphite pore (representing kerogen in shale reservoir).

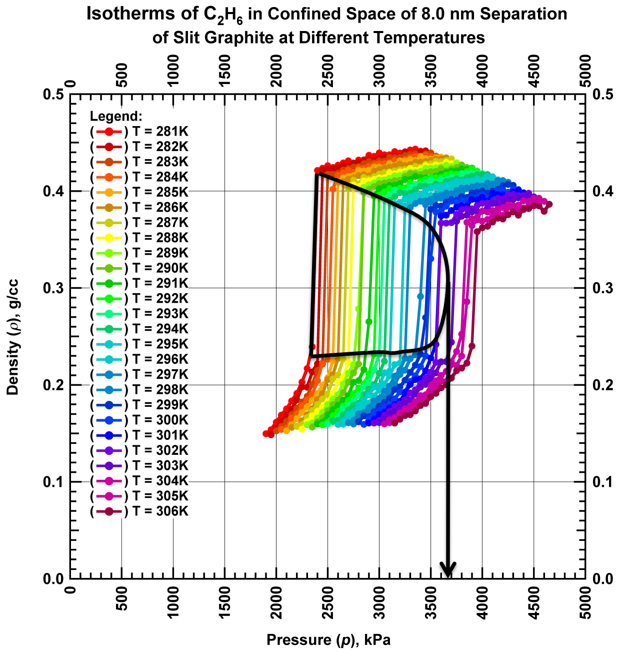

Figure A-14 – Phase diagram of confined ethane in 8.0 nm of separation of a slit graphite pore (representing kerogen in shale reservoir).

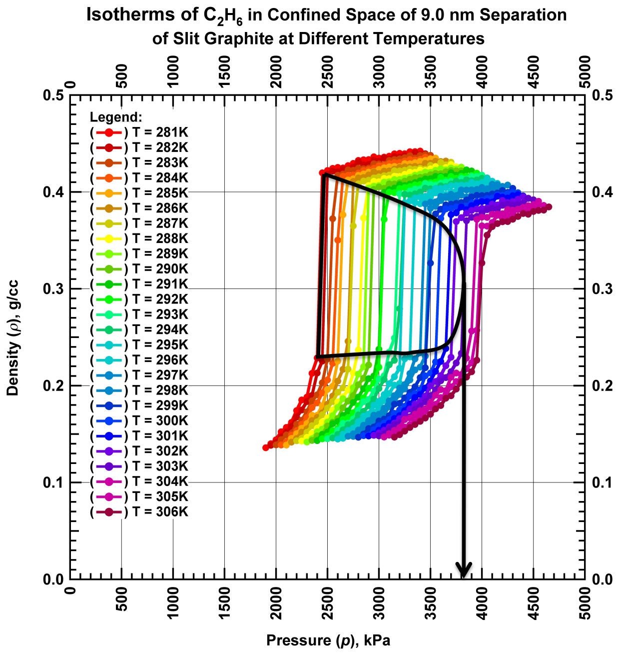

Figure A-15 – Phase diagram of confined ethane in 9.0 nm of separation of a slit graphite pore (representing kerogen in shale reservoir).

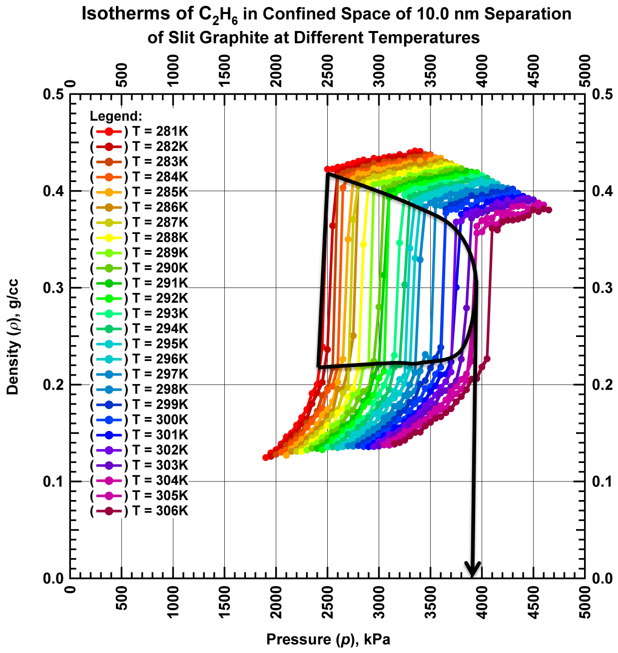

Figure A-16 – Phase diagram of confined ethane in 10.0 nm of separation of a slit graphite pore (representing kerogen in shale reservoir).

A.3 Propane (2.0 nm – 10.0 nm)

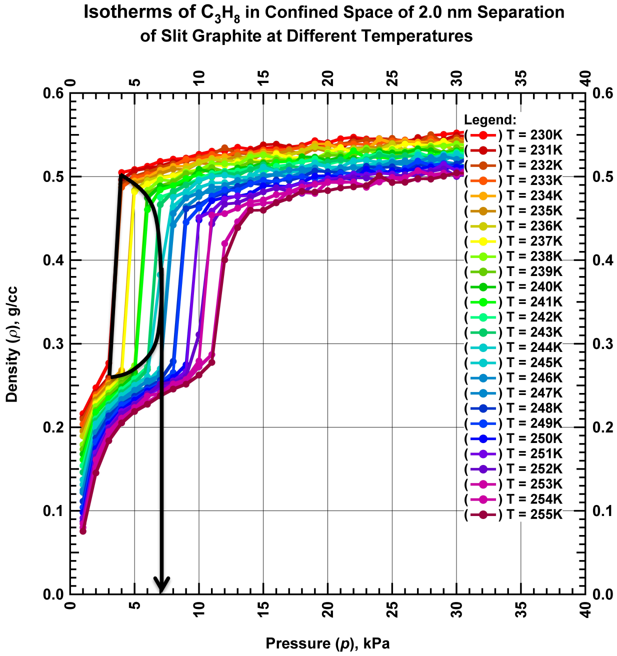

Figure A-17 – Phase diagram of confined propane in 2.0 nm of separation of a slit graphite pore (representing kerogen in shale reservoir).

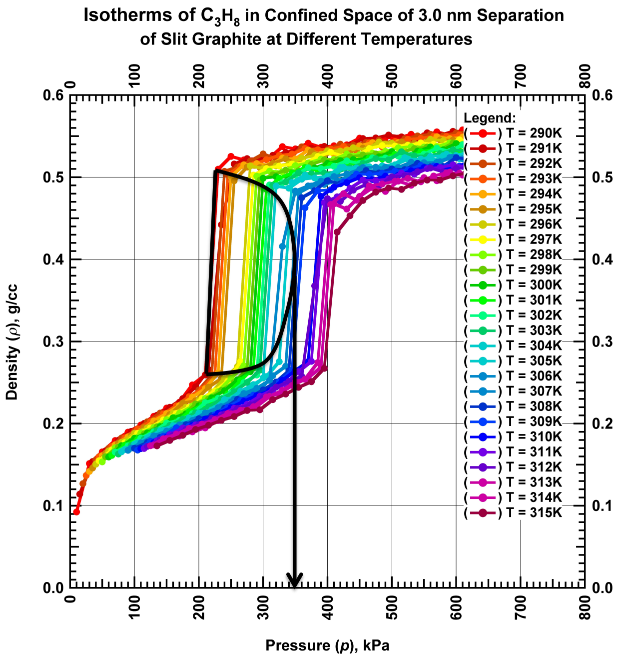

Figure A-18 – Phase diagram of confined propane in 3.0 nm of separation of a slit graphite pore (representing kerogen in shale reservoir).

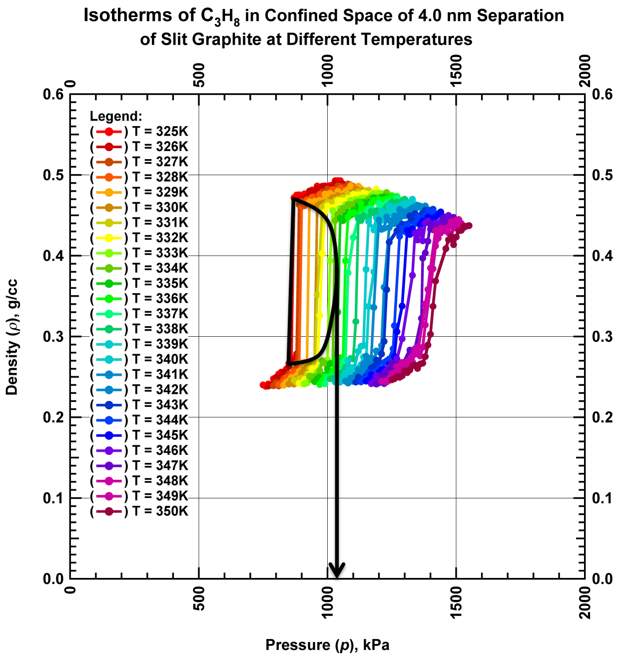

Figure A-19 – Phase diagram of confined propane in 4.0 nm of separation of a slit graphite pore (representing kerogen in shale reservoir).

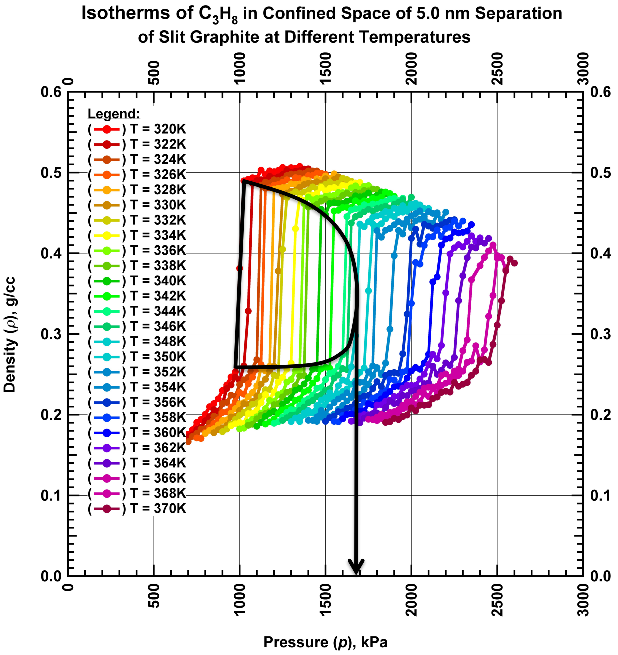

Figure A-20 – Phase diagram of confined propane in 5.0 nm of separation of a slit graphite pore (representing kerogen in shale reservoir).

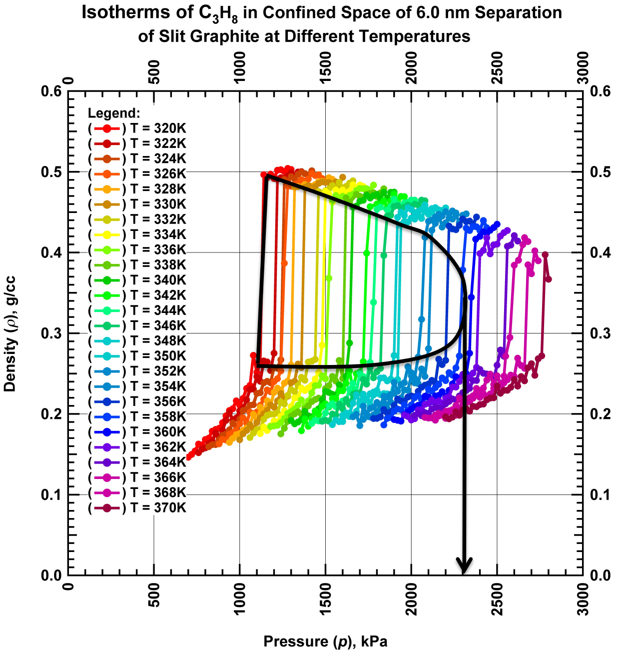

Figure A-21 – Phase diagram of confined propane in 6.0 nm of separation of a slit graphite pore (representing kerogen in shale reservoir).

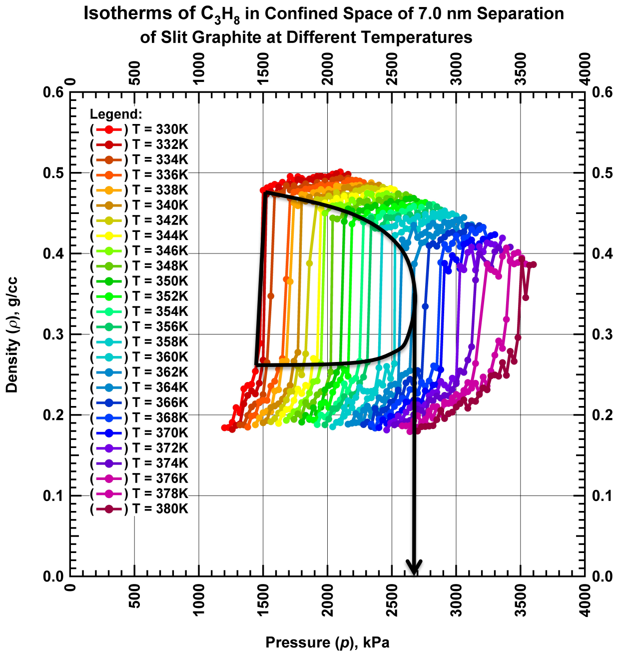

Figure A-22 – Phase diagram of confined propane in 7.0 nm of separation of a slit graphite pore (representing kerogen in shale reservoir).

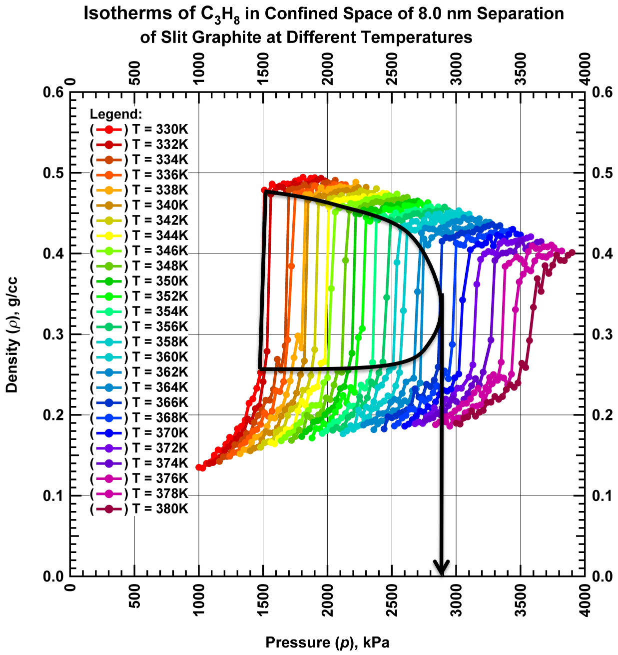

Figure A-23 – Phase diagram of confined propane in 8.0 nm of separation of a slit graphite pore (representing kerogen in shale reservoir).

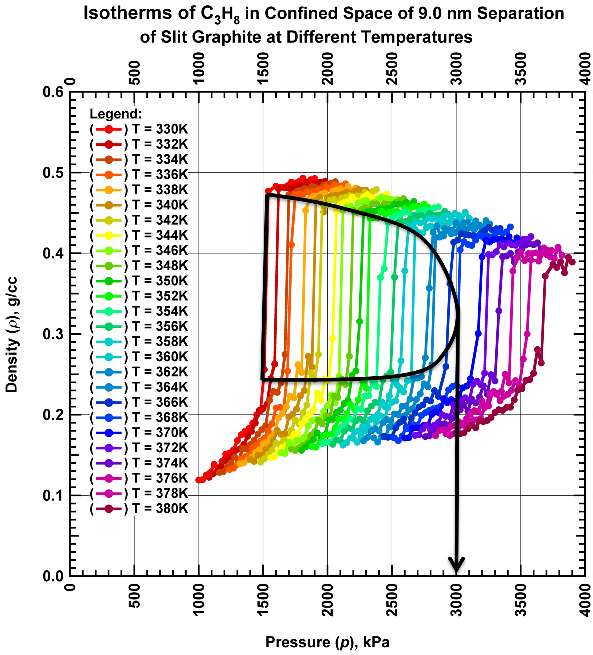

Figure A-24 – Phase diagram of confined propane in 9.0 nm of separation of a slit graphite pore (representing kerogen in shale reservoir).

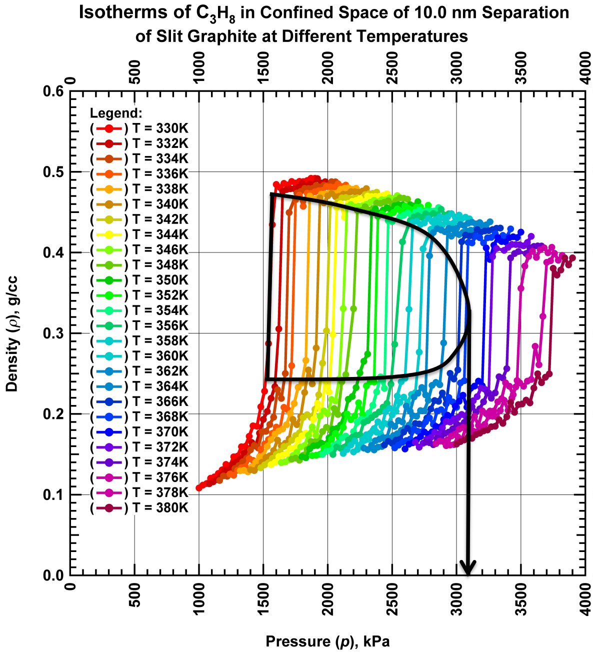

Figure A-25 – Phase diagram of confined propane in 10.0 nm of separation of a slit graphite pore (representing kerogen in shale reservoir).

A.4 Butane (2.0 nm – 10.0 nm)

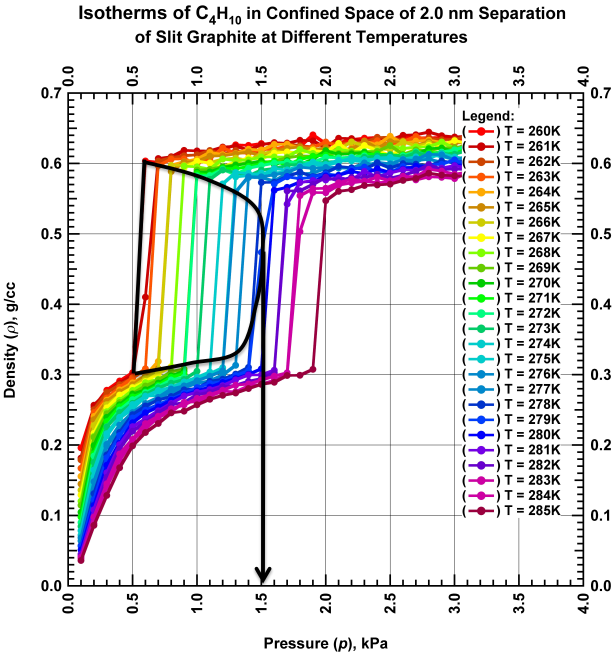

Figure A-26 – Phase diagram of confined butane in 2.0 nm of separation of a slit graphite pore (representing kerogen in shale reservoir).

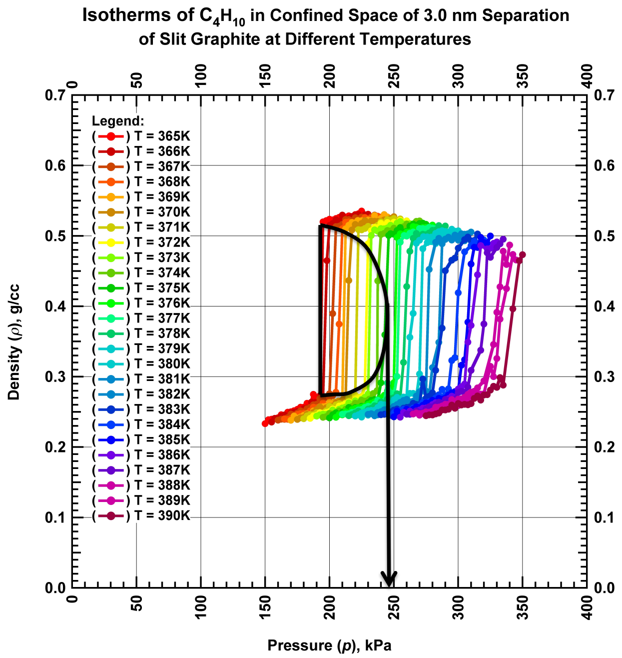

Figure A-27 – Phase diagram of confined butane in 3.0 nm of separation of a slit graphite pore (representing kerogen in shale reservoir).

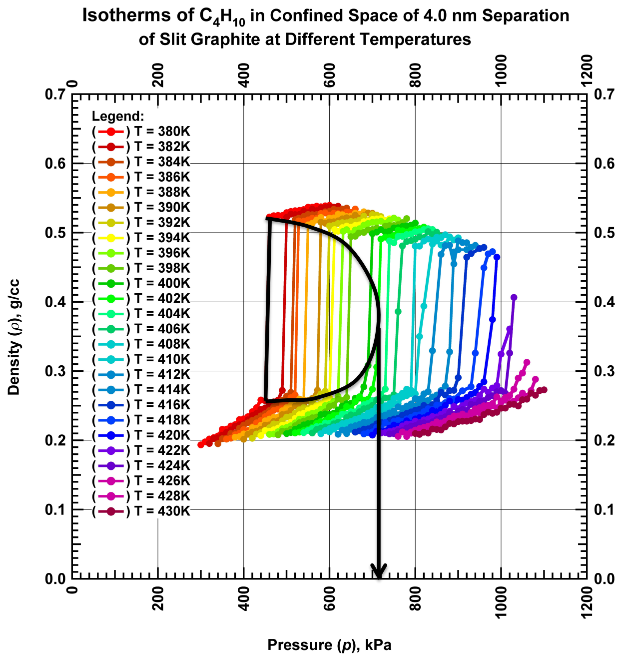

Figure A-28 – Phase diagram of confined butane in 4.0 nm of separation of a slit graphite pore (representing kerogen in shale reservoir).

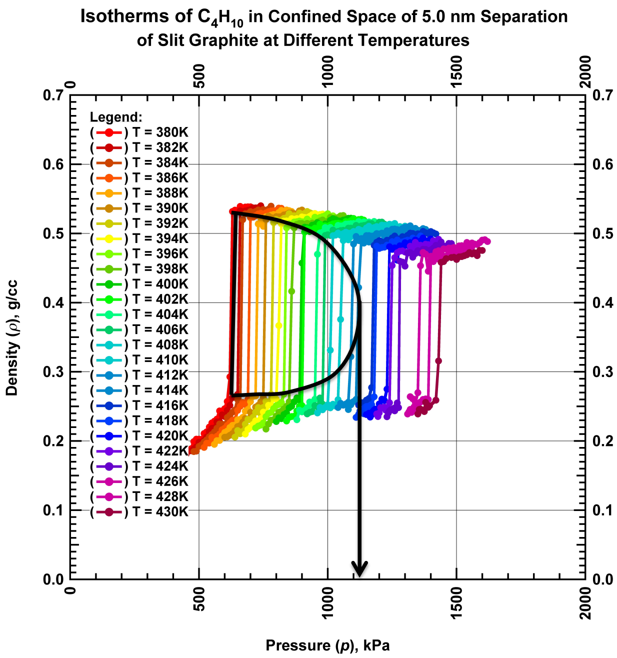

Figure A-29 – Phase diagram of confined butane in 5.0 nm of separation of a slit graphite pore (representing kerogen in shale reservoir).

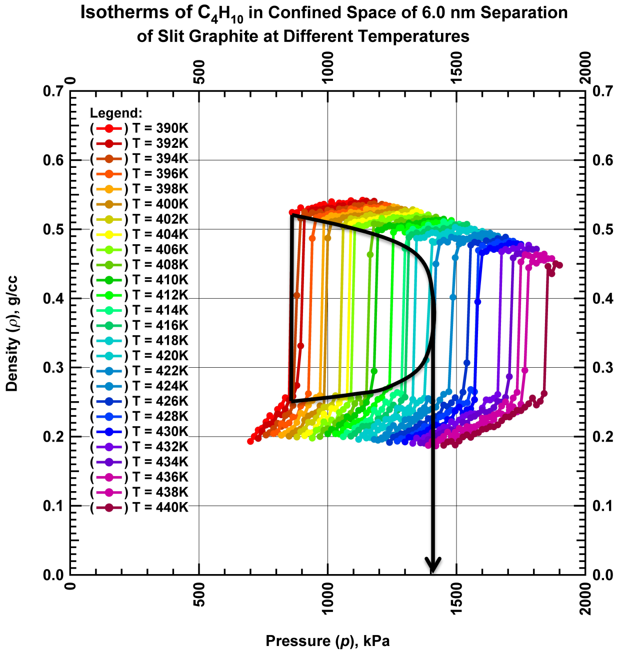

Figure A-30 – Phase diagram of confined butane in 6.0 nm of separation of a slit graphite pore (representing kerogen in shale reservoir).

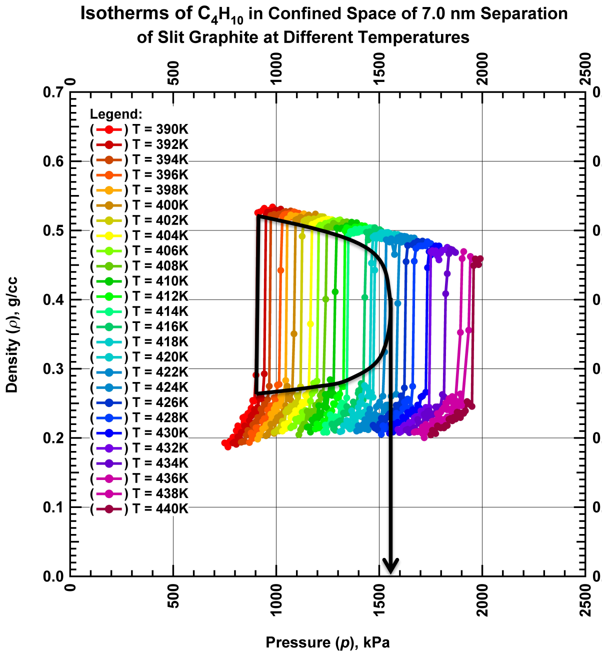

Figure A-31 – Phase diagram of confined butane in 7.0 nm of separation of a slit graphite pore (representing kerogen in shale reservoir).

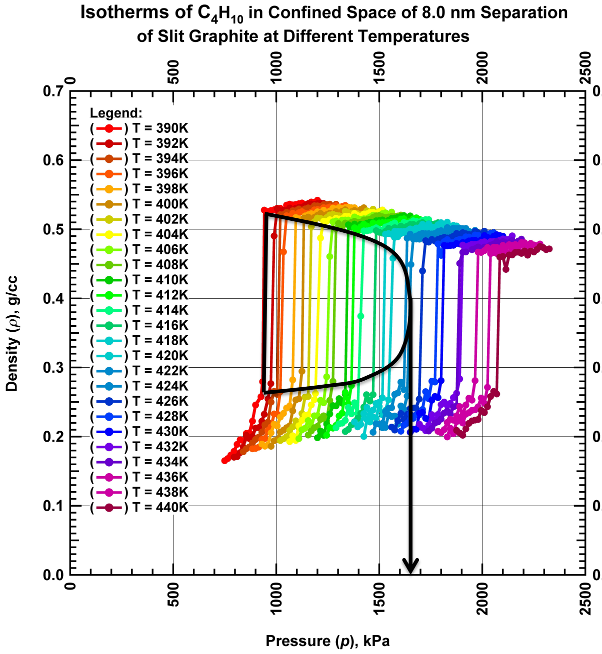

Figure A-32 – Phase diagram of confined butane in 8.0 nm of separation of a slit graphite pore (representing kerogen in shale reservoir).

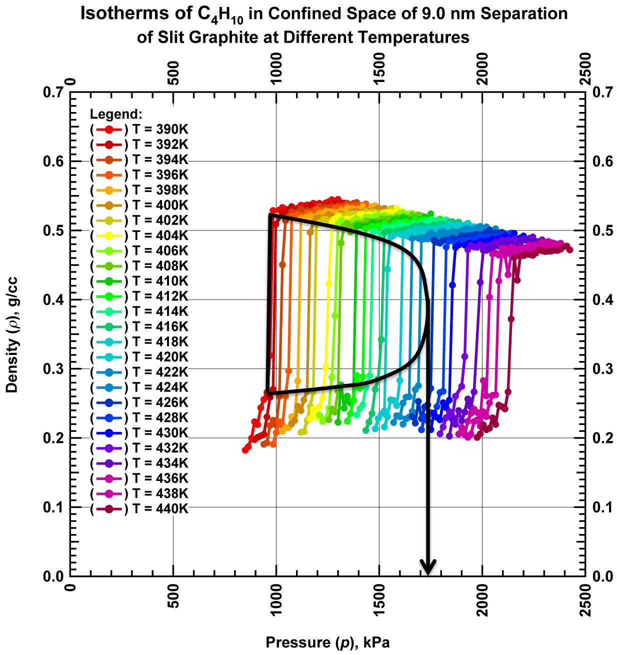

Figure A-33 – Phase diagram of confined butane in 9.0 nm of separation of a slit graphite pore (representing kerogen in shale reservoir).

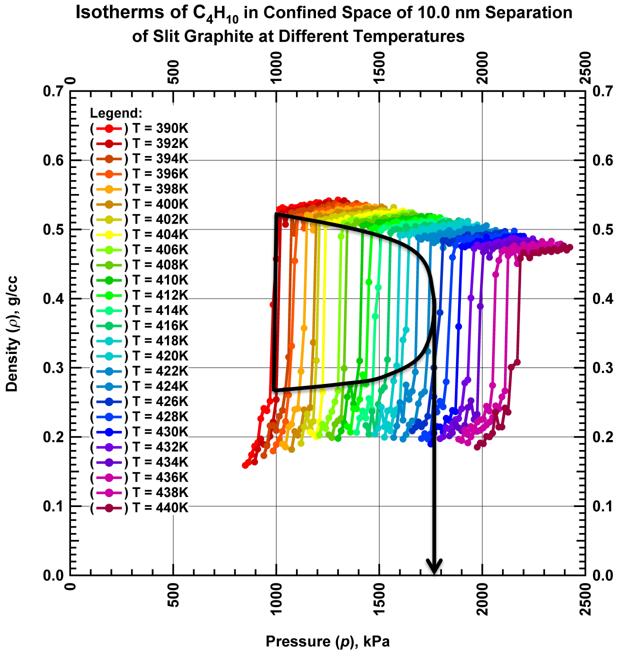

Figure A-34 – Phase diagram of confined butane in 10.0 nm of separation of a slit graphite pore (representing kerogen in shale reservoir).

A.5 Pentane (2.0 nm – 10.0 nm)

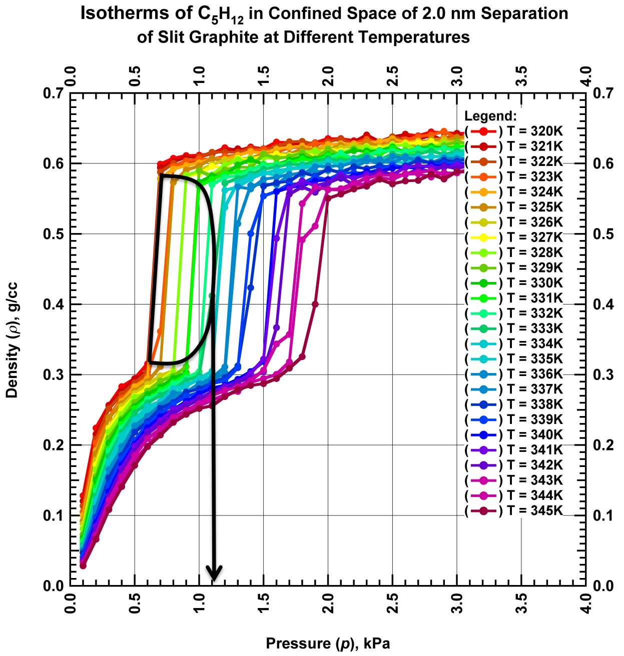

Figure A-35 – Phase diagram of confined pentane in 2.0 nm of separation of a slit graphite pore (representing kerogen in shale reservoir).

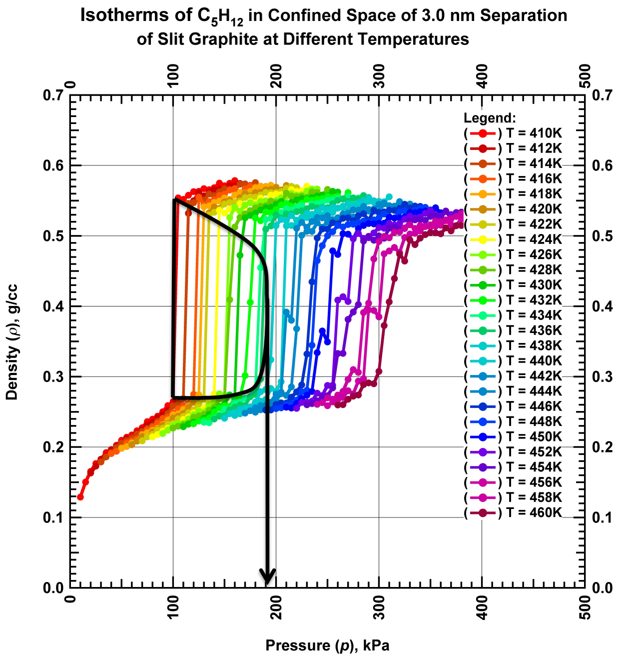

Figure A-36 – Phase diagram of confined pentane in 3.0 nm of separation of a slit graphite pore (representing kerogen in shale reservoir).

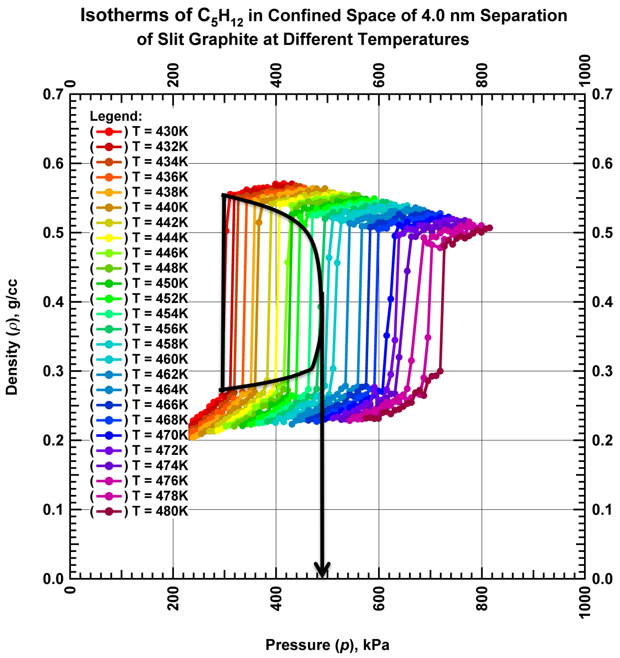

Figure A-37 – Phase diagram of confined pentane in 4.0 nm of separation of a slit graphite pore (representing kerogen in shale reservoir).

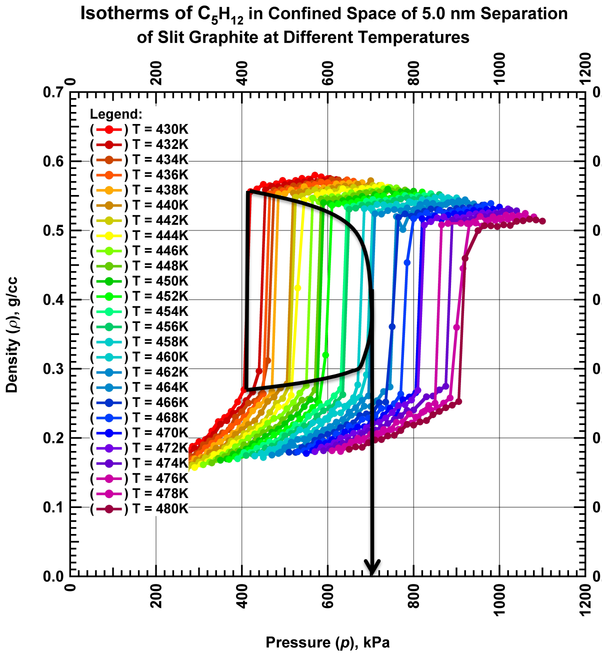

Figure A-38 – Phase diagram of confined pentane in 5.0 nm of separation of a slit graphite pore (representing kerogen in shale reservoir).

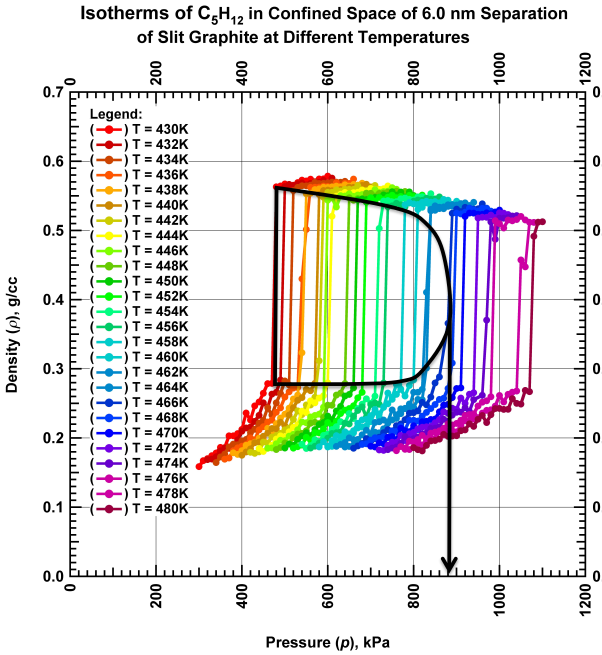

Figure A-39 – Phase diagram of confined pentane in 6.0 nm of separation of a slit graphite pore (representing kerogen in shale reservoir).

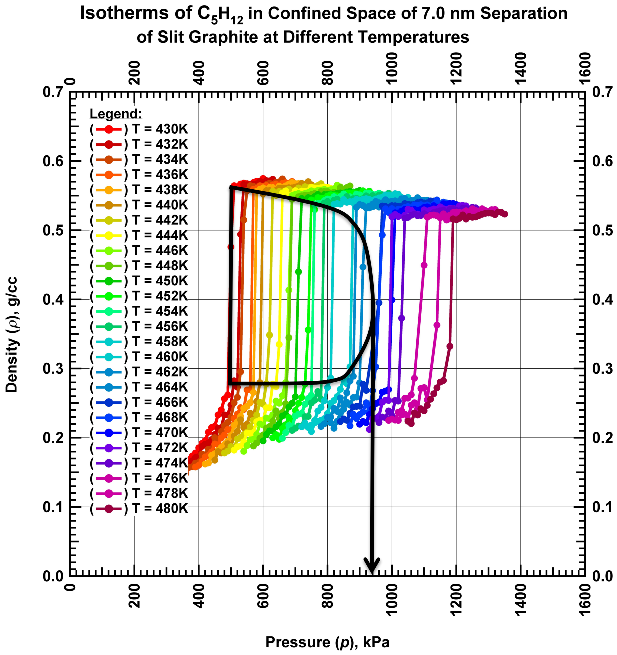

Figure A-40 – Phase diagram of confined pentane in 7.0 nm of separation of a slit graphite pore (representing kerogen in shale reservoir).

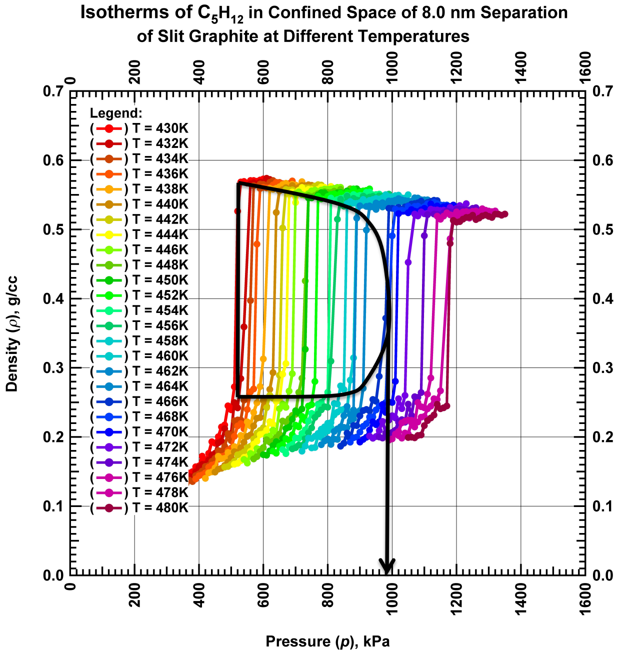

Figure A-41 – Phase diagram of confined pentane in 8.0 nm of separation of a slit graphite pore (representing kerogen in shale reservoir).

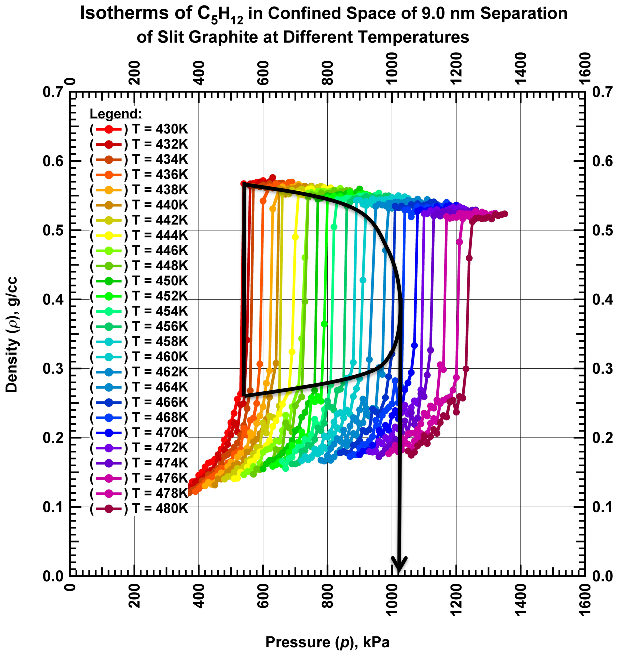

Figure A-42 – Phase diagram of confined pentane in 9.0 nm of separation of a slit graphite pore (representing kerogen in shale reservoir).

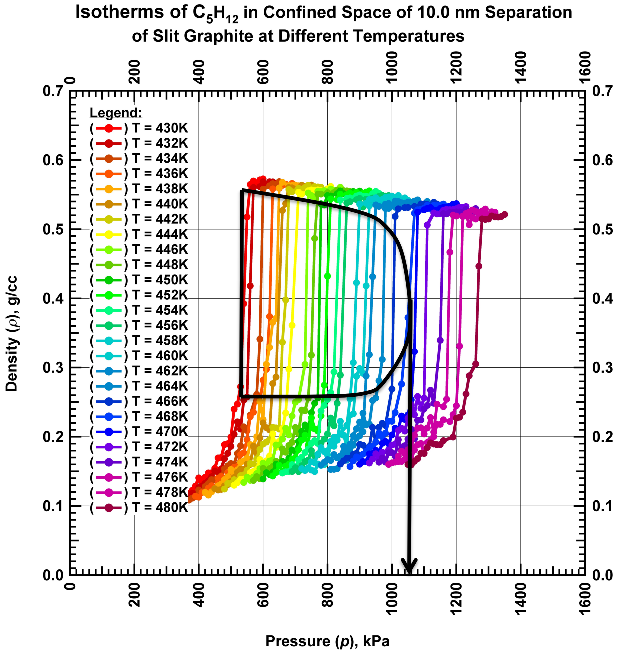

Figure A-43 – Phase diagram of confined pentane in 10.0 nm of separation of a slit graphite pore (representing kerogen in shale reservoir).

A.6 Hexane (2.0 nm – 10.0 nm)

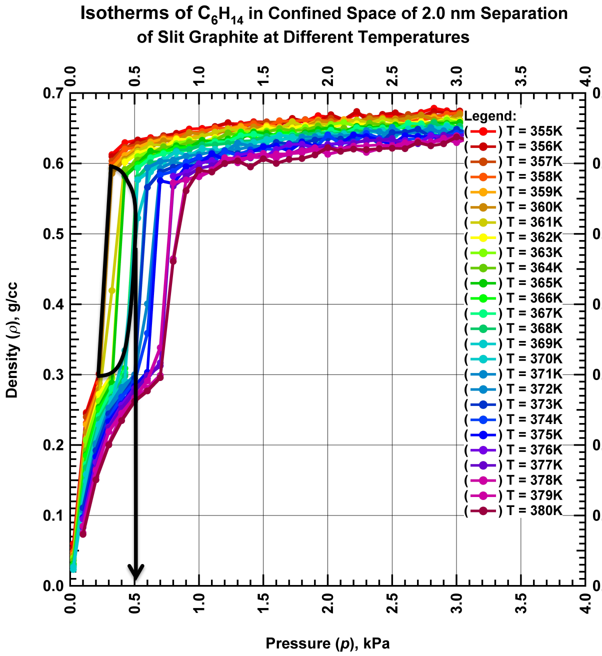

Figure A-44 – Phase diagram of confined hexane in 2.0 nm of separation of a slit graphite pore (representing kerogen in shale reservoir).

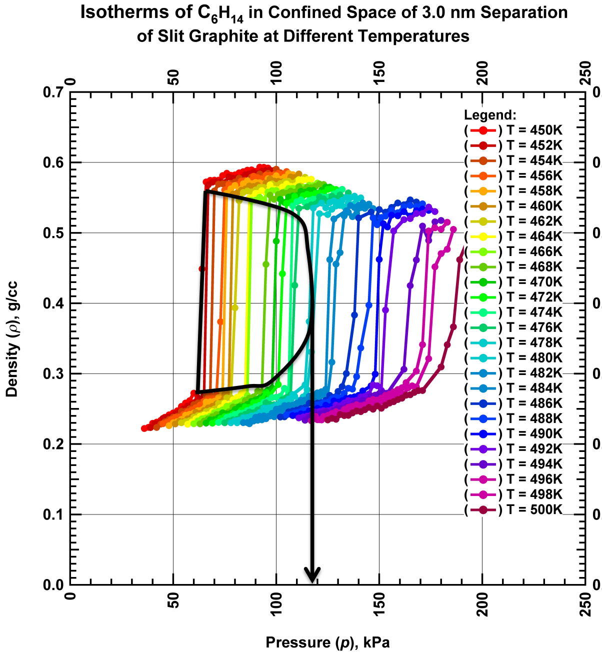

Figure A-45 – Phase diagram of confined hexane in 3.0 nm of separation of a slit graphite pore (representing kerogen in shale reservoir).

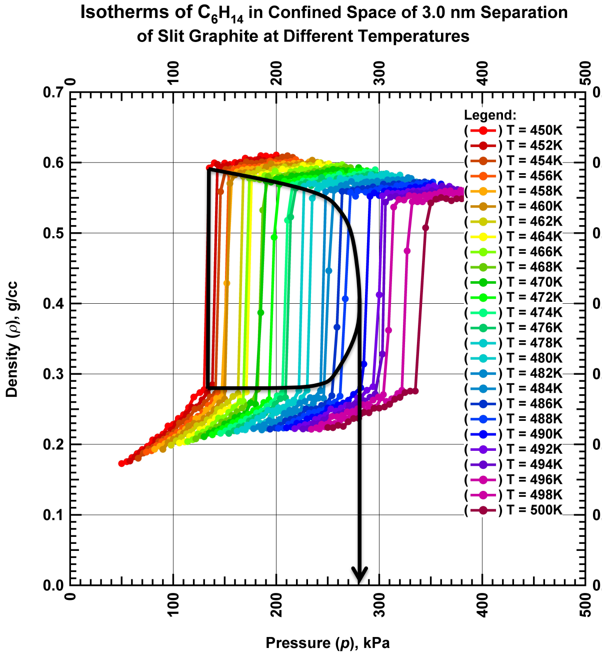

Figure A-46 – Phase diagram of confined hexane in 4.0 nm of separation of a slit graphite pore (representing kerogen in shale reservoir).

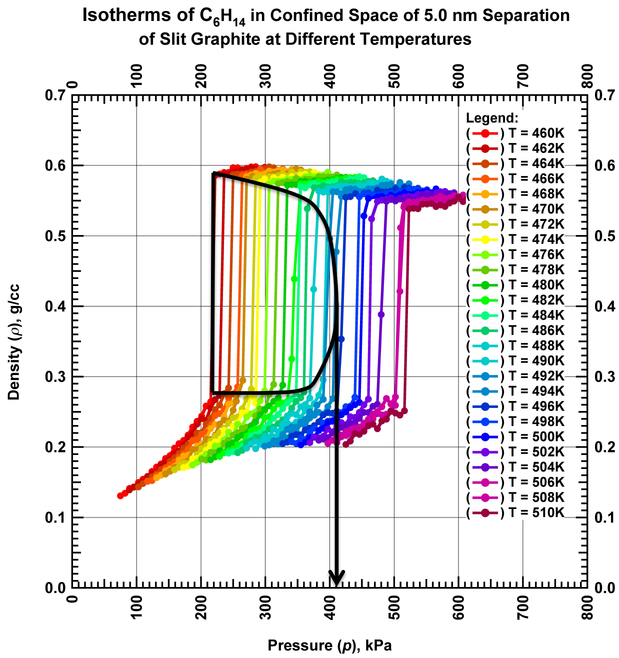

Figure A-47 – Phase diagram of confined hexane in 5.0 nm of separation of a slit graphite pore (representing kerogen in shale reservoir).

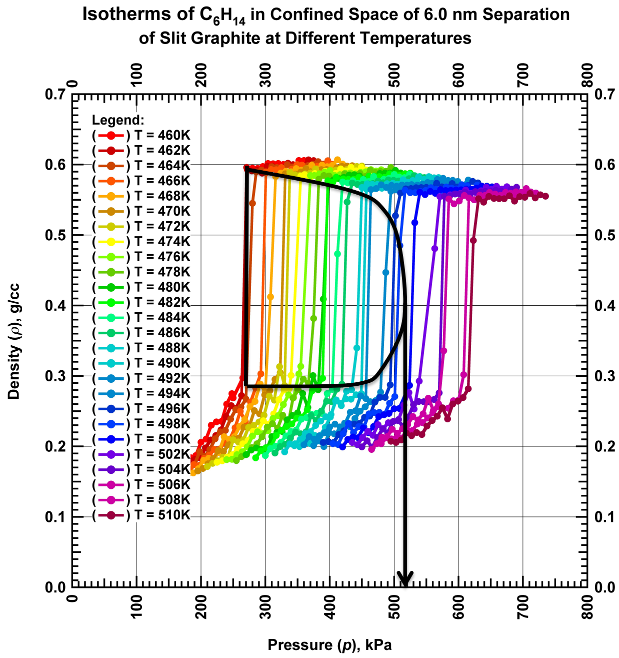

Figure A-48 – Phase diagram of confined hexane in 6.0 nm of separation of a slit graphite pore (representing kerogen in shale reservoir).

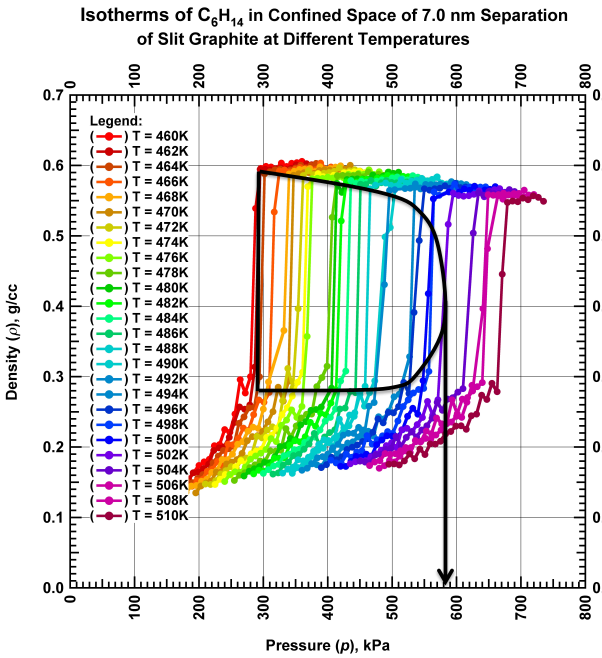

Figure A-49 – Phase diagram of confined hexane in 7.0 nm of separation of a slit graphite pore (representing kerogen in shale reservoir).

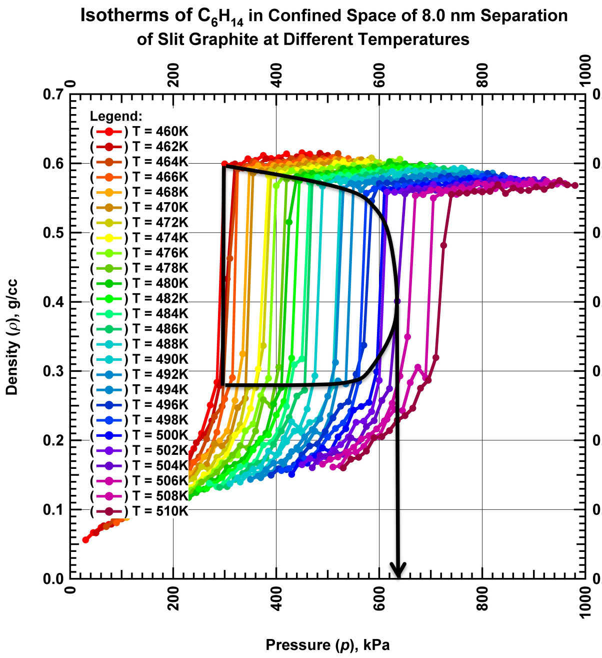

Figure A-50 – Phase diagram of confined hexane in 8.0 nm of separation of a slit graphite pore (representing kerogen in shale reservoir).

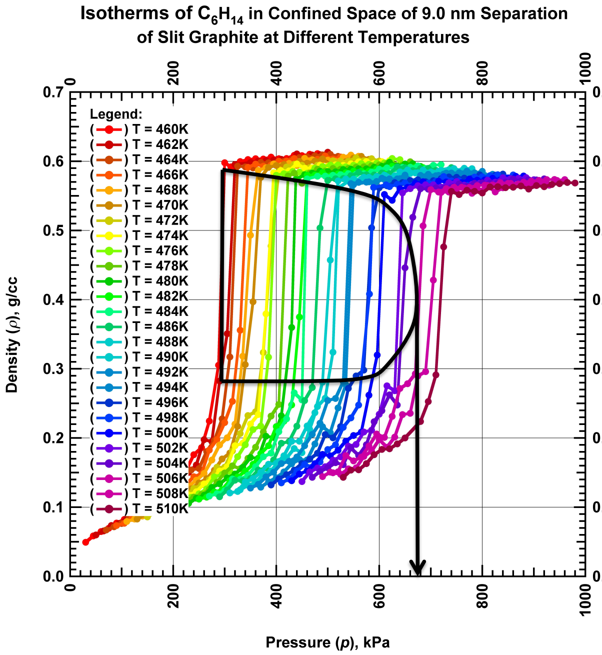

Figure A-51 – Phase diagram of confined hexane in 9.0 nm of separation of a slit graphite pore (representing kerogen in shale reservoir).

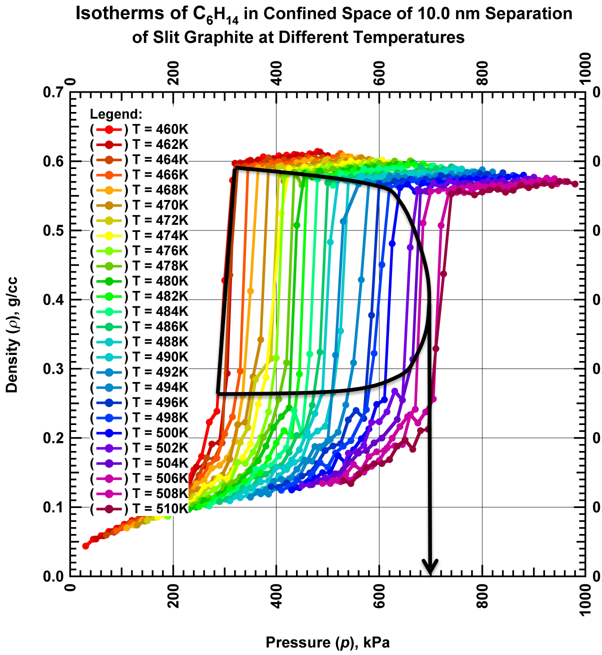

Figure A-52 – Phase diagram of confined hexane in 10.0 nm of separation of a slit graphite pore (representing kerogen in shale reservoir).

APPENDIX B

PHASE DIAGRAMS OF CONFINED METHANE-BUTANE-HEXANE TERNARY MIXTURE

B.1 At *T* = 350 K

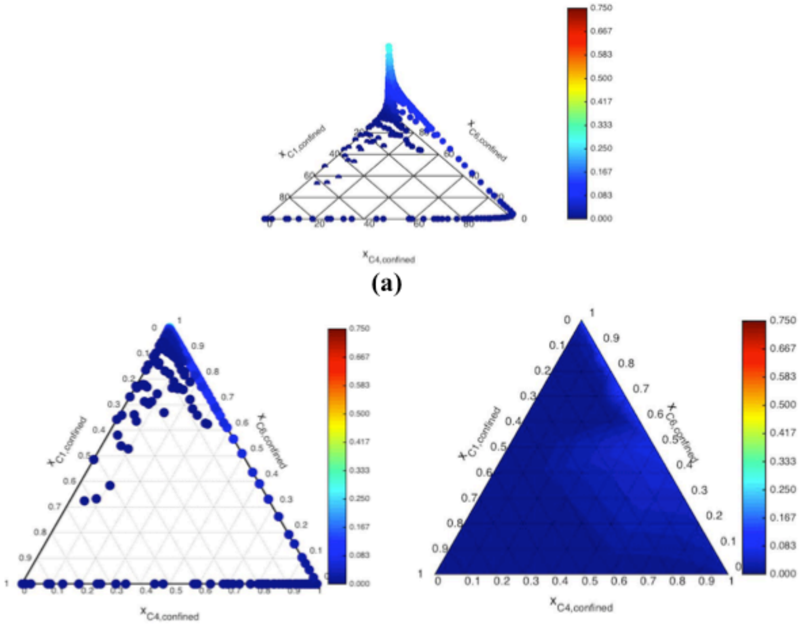

(a)

(b)

(c)

Figure B-1 – Density plots on (a) 3D – and (b) 2D – phase diagrams, and approximation of complete 2D – phase diagram of the C1-C4-C6 confined mixture at *T* = 350 K and *p* = 10 kPa.

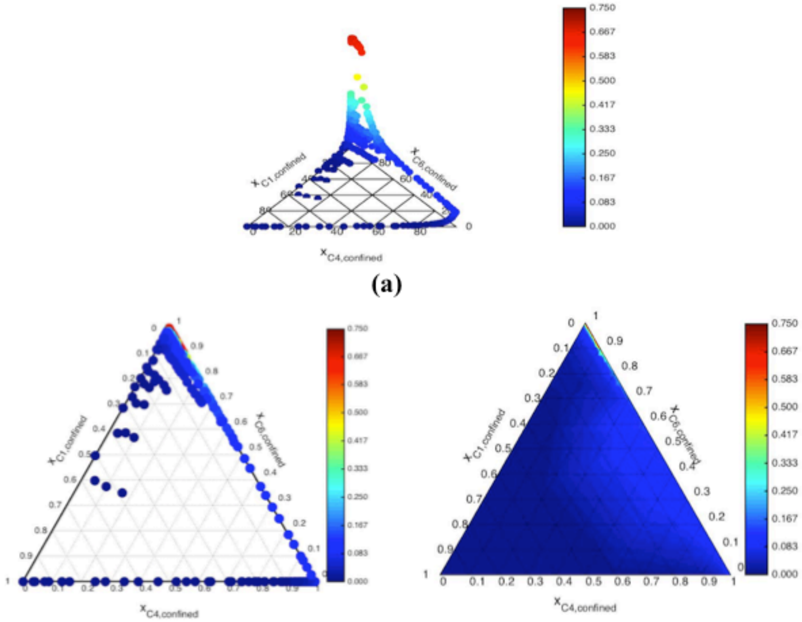

(a)

(b)

(c)

Figure B-2 – Density plots on (a) 3D – and (b) 2D – phase diagrams, and approximation of complete 2D – phase diagram of the C1-C4-C6 confined mixture at *T* = 350 K and *p* = 50 kPa.

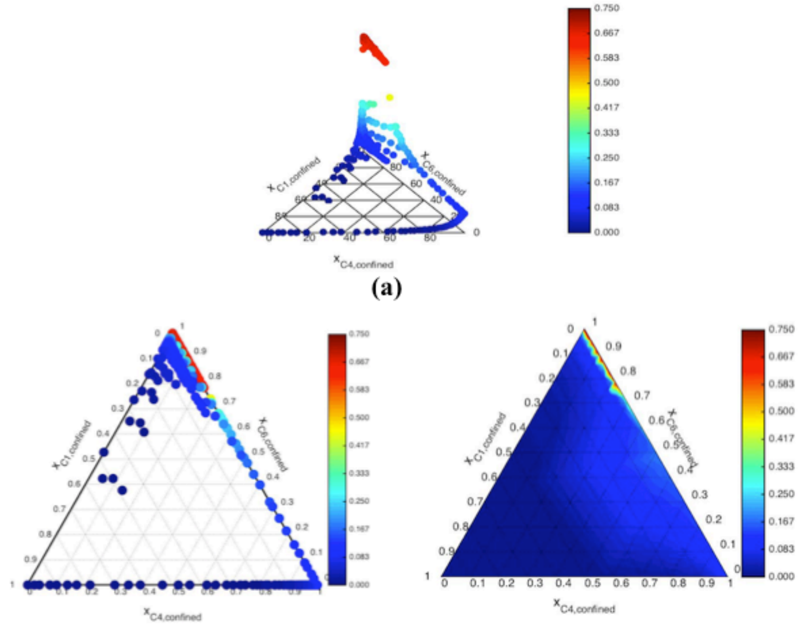

(a)

(b)

(c)

Figure B-3 – Density plots on (a) 3D – and (b) 2D – phase diagrams, and approximation of complete 2D – phase diagram of the C1-C4-C6 confined mixture at *T* = 350 K and *p* = 100 kPa.

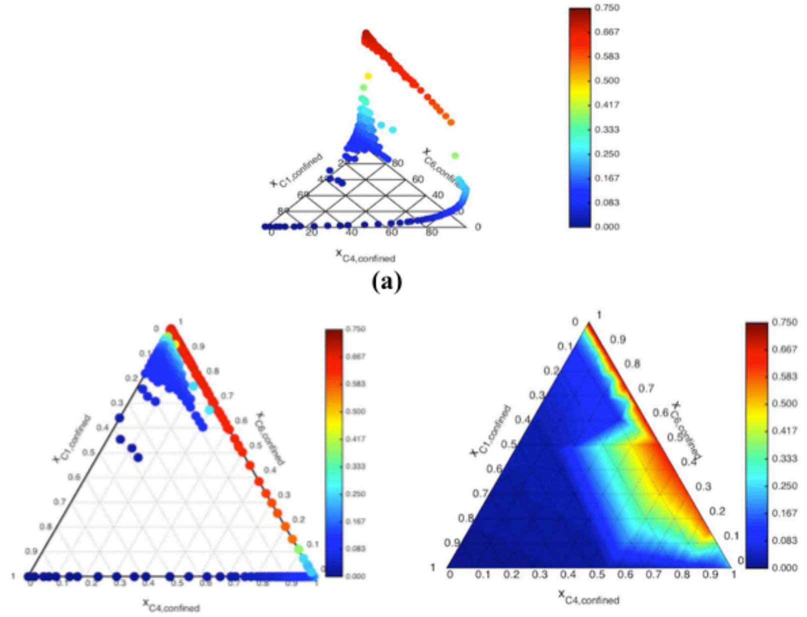

(a)

(b)

(c)

Figure B-4 – Density plots on (a) 3D – and (b) 2D – phase diagrams, and approximation of complete 2D – phase diagram of the C1-C4-C6 confined mixture at T = 350 K and p = 300 kPa.

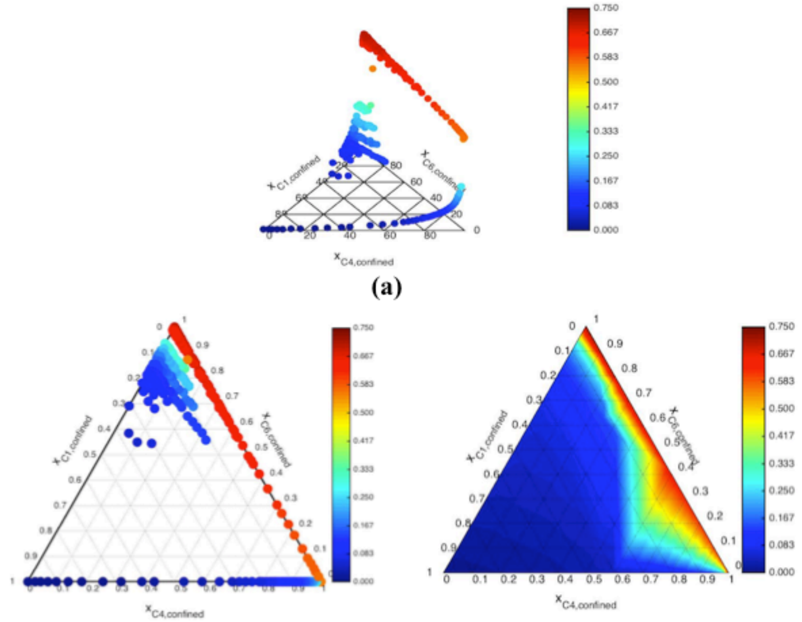

(a)

(b)

(c)

Figure B-5 – Density plots on (a) 3D – and (b) 2D – phase diagrams, and approximation of complete 2D – phase diagram of the C1-C4-C6 confined mixture at T = 350 K and p = 500 kPa.

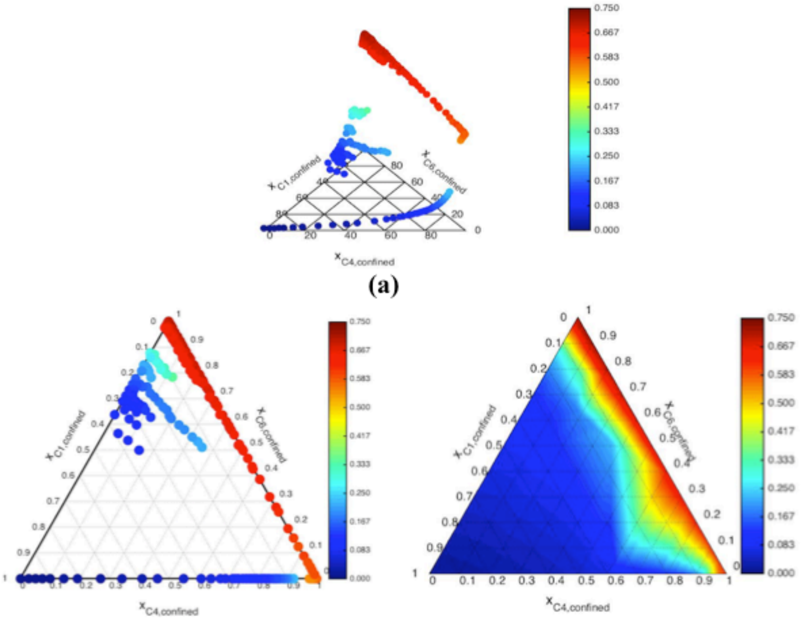

(a)

(b) (c)

Figure B-6 – Density plots on (a) 3D – and (b) 2D – phase diagrams, and approximation of complete 2D – phase diagram of the C1-C4-C6 confined mixture at T = 350 K and p = 1000 kPa.

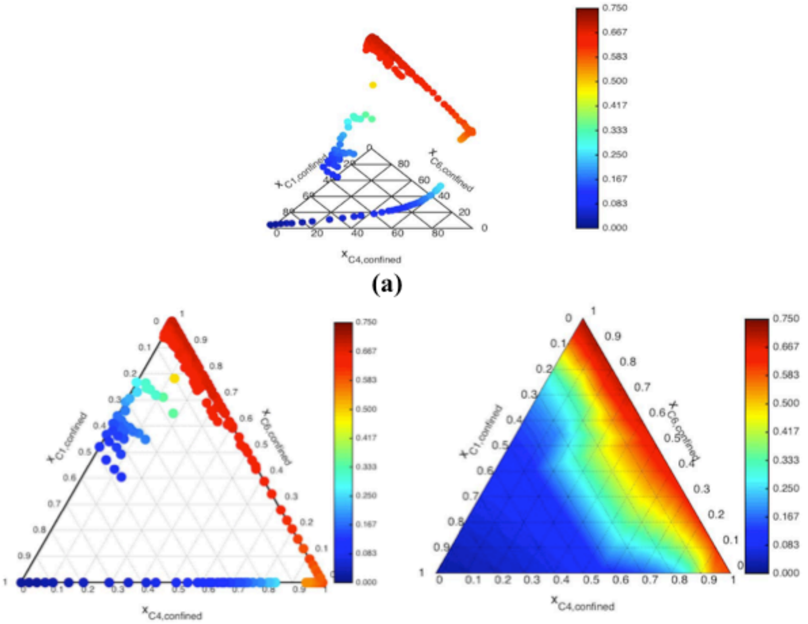

(a)

(b) (c)

Figure B-7 – Density plots on (a) 3D – and (b) 2D – phase diagrams, and approximation of complete 2D – phase diagram of the C1-C4-C6 confined mixture at T = 350 K and p = 2000 kPa.

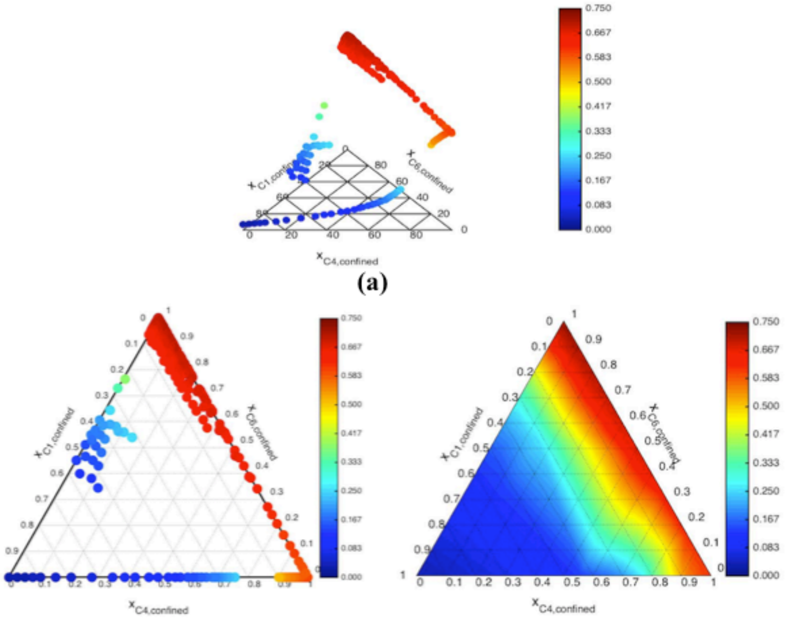

(a)

(b) (c)

Figure B-8 – Density plots on (a) 3D – and (b) 2D – phase diagrams, and approximation of complete 2D – phase diagram of the C1-C4-C6 confined mixture at *T* = 350 K and *p* = 3000 kPa.

B.2 At *T* = 400 K

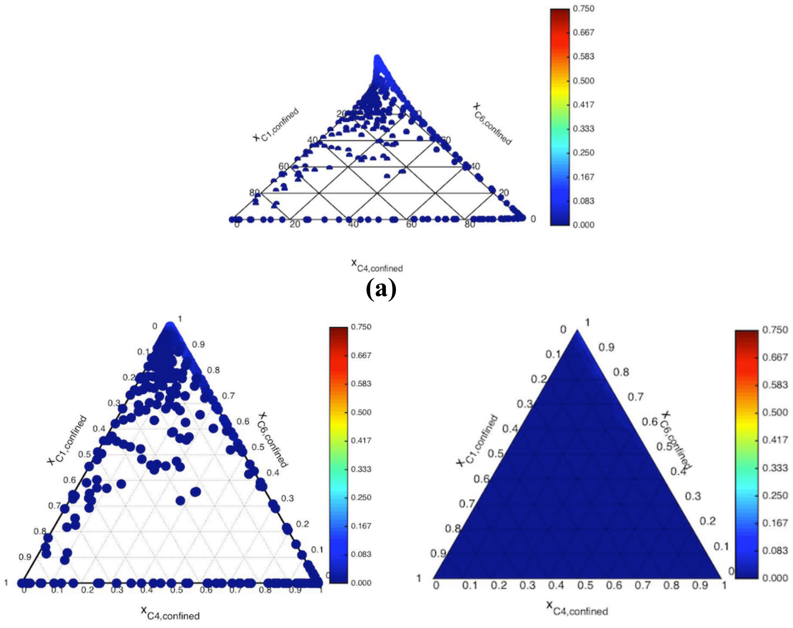

(a)

(b) (c)

Figure B-9 – Density plots on (a) 3D – and (b) 2D – phase diagrams, and approximation of complete 2D – phase diagram of the C1-C4-C6 confined mixture at *T* = 400 K and *p* = 10 kPa.

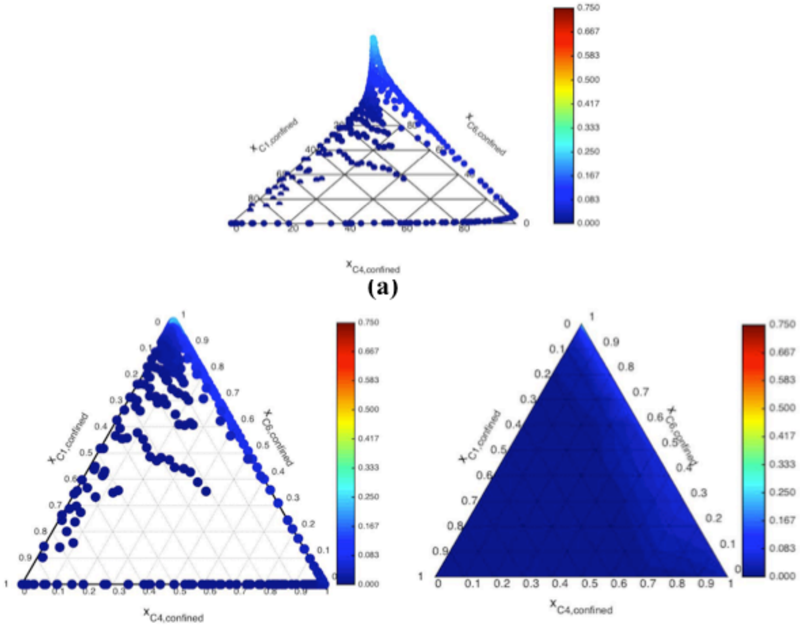

(a)

(b) (c)

Figure B-10 – Density plots on (a) 3D – and (b) 2D – phase diagrams, and approximation of complete 2D – phase diagram of the C1-C4-C6 confined mixture at *T* = 400 K and *p* = 50 kPa.

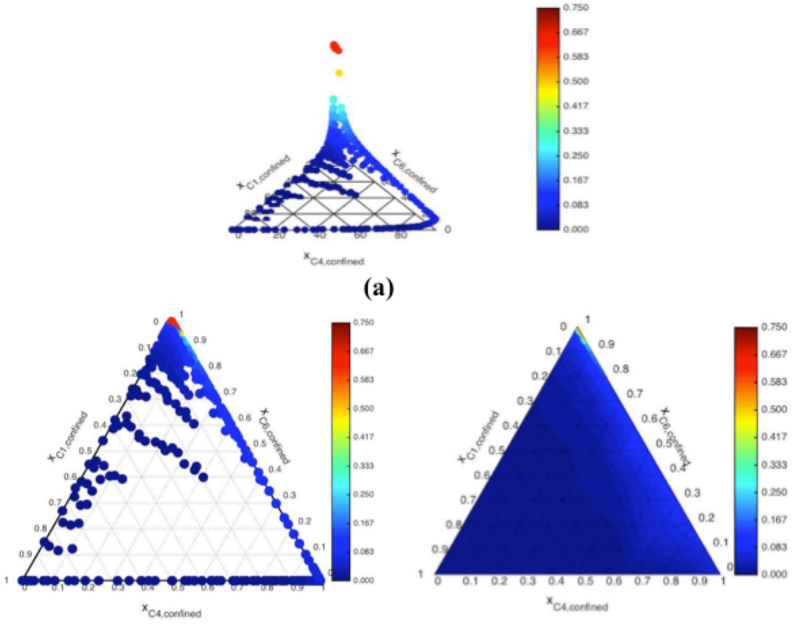

(a)

(b) (c)

Figure B-11 – Density plots on (a) 3D – and (b) 2D – phase diagrams, and approximation of complete 2D – phase diagram of the C1-C4-C6 confined mixture at *T* = 400 K and *p* = 100 kPa.

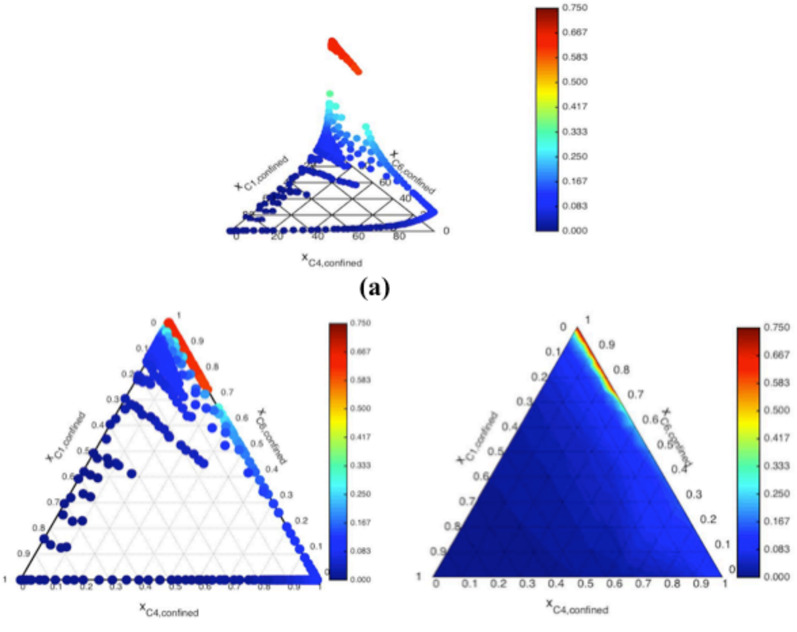

(a)

(b) (c)

Figure B-12 – Density plots on (a) 3D – and (b) 2D – phase diagrams, and approximation of complete 2D – phase diagram of the C1-C4-C6 confined mixture at *T* = 400 K and *p* = 300 kPa.

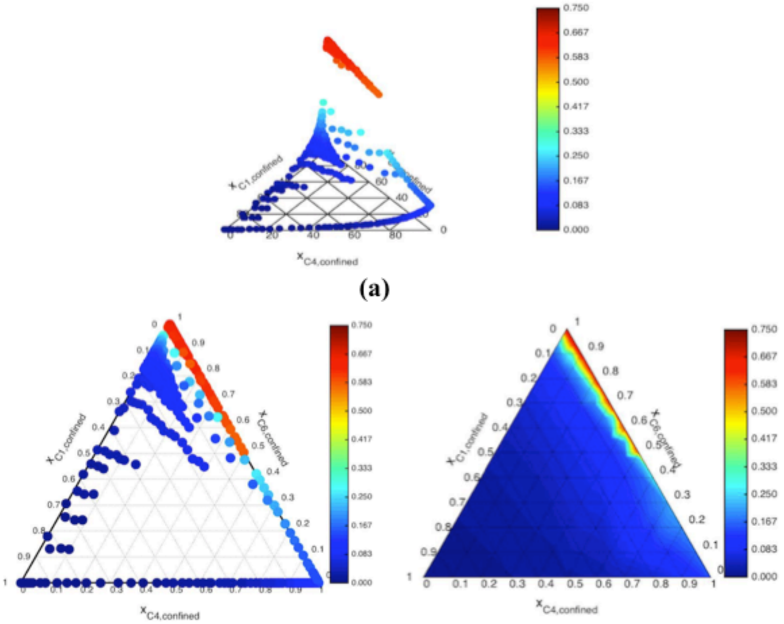

(a)

(b) (c)

Figure B-13 – Density plots on (a) 3D – and (b) 2D – phase diagrams, and approximation of complete 2D – phase diagram of the C1-C4-C6 confined mixture at T = 400 K and p = 500 kPa.

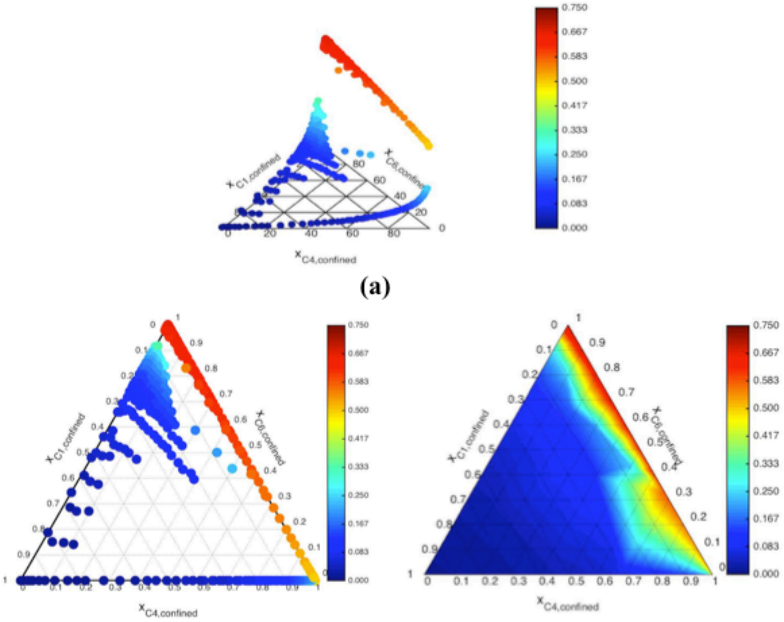

(a)

(b) (c)

Figure B-14 – Density plots on (a) 3D – and (b) 2D – phase diagrams, and approximation of complete 2D – phase diagram of the C1-C4-C6 confined mixture at T = 400 K and p = 1000 kPa.

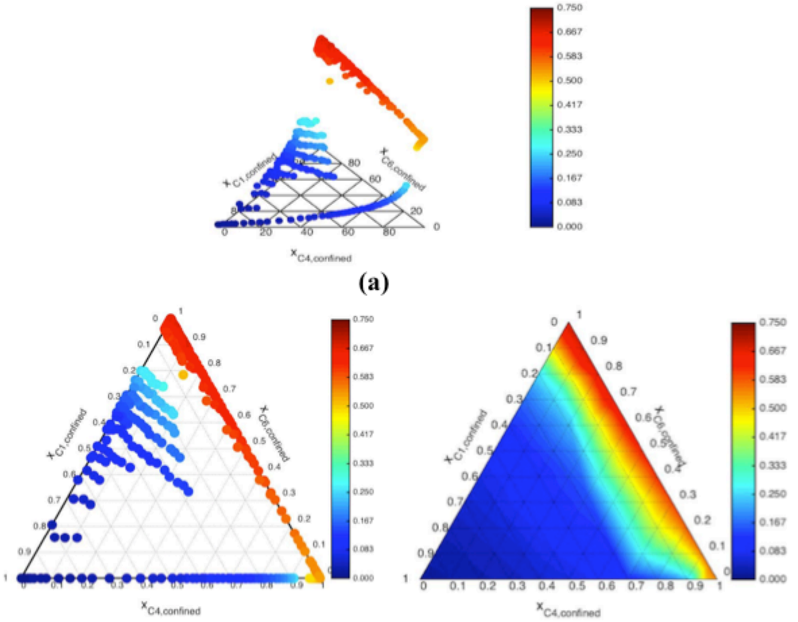

(a)

(b) (c)

Figure B-15 – Density plots on (a) 3D – and (b) 2D – phase diagrams, and approximation of complete 2D – phase diagram of the C1-C4-C6 confined mixture at *T* = 400 K and *p* = 2000 kPa.

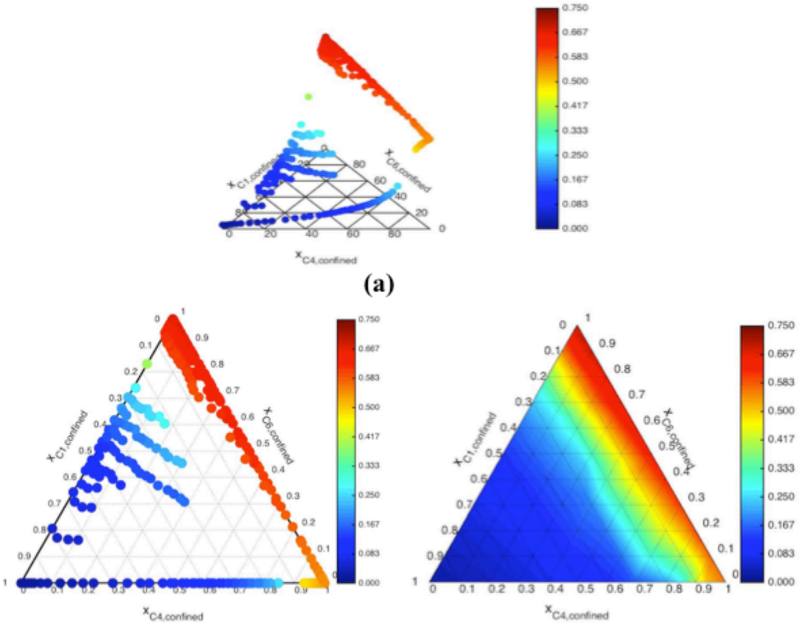

(a)

(b) (c)

Figure B-16 – Density plots on (a) 3D – and (b) 2D – phase diagrams, and approximation of complete 2D – phase diagram of the C1-C4-C6 confined mixture at *T* = 400 K and *p* = 3000 kPa.